The Spring of Life – Cosmological Matter Flows and Their Multiscale Effects

Benjamin Andreas Seidel



Munich 2026

Massenflüsse von Kosmologie bis Galaxienphysik

Benjamin Andreas Seidel



München 2026

The Spring of Life – Cosmological Matter Flows and Their Multiscale Effects

Benjamin Andreas Seidel

Dissertation
an der Fakultät für Physik
der Ludwig-Maximilians-Universität
München

vorgelegt von
Benjamin Andreas Seidel
geboren in München

München, 19. 05. 2026

Erstgutachter: Apl. Prof. Klaus Dolag
Zweitgutachter: Prof. em. Rolf-Peter Kudritzki
Tag der mündlichen Prüfung: 30. 06. 2026

Abstract

The formation and evolution of structures in the Universe is a highly multi-scalar process. While galaxies and clusters of galaxies generally form bottom-up, they are embedded in even larger structures like filaments and superclusters. In this work we will study the mass flows connecting the these large-scale structures with clusters and galaxies.

The flow field can be generally separated into inflows of dark matter and gas, driven by the gravitational forces, and outflows, coupled to the hydrodynamics of the gas. These flows are a key ingredient to a number of baryonic processes. In galaxies, the balance of inflow, outflow, and conversion of gas into stars determines the ability of a galaxy to maintain its star formation rate. For galaxy clusters, the inflow and accretion of substructure drives turbulence in the intra-cluster medium and can modify the hydrostatic pressure balance.

Due to their highly detailed modelling of processes on many different scales, cosmological simulations, like the hydrodynamical MAGNETICUM PATHFINDER suite provide the ideal theoretical tool to quantify and analyse these flows. We introduce this simulation suite and show that the environment and flow structure are key elements for accurately modelling galaxy formation, especially at higher redshifts $z > 2$. We demonstrate the simple mass scaling behaviour of accretion flows, while their spatial configuration is highly diverse. The self-similarity found for the inflowing component is broken by outflows from galaxies being more efficient than those from clusters. As a consequence, we show that galaxies impact the gas distribution in their environment to relatively large scales compared to their size.

This highlights a dichotomy between in- and outflows, which we explore further. To this end we introduce a spherical harmonics based method to quantify the anisotropy of a given accretion field. We show that, while accretion flows are highly anisotropic, the feedback-driven outflows are generally more spherically symmetric. Applying this formalism to simulated galaxies, we show that the flow field is closely tied to their star formation properties and evolution.

The peculiar motions of galaxies in the linear regime make it possible to reconstruct the local density field in our cosmic neighbourhood. Such reconstructions are the basis for constrained cosmological simulations, where the initial conditions are perturbed in a way consistent with the constraints in order to reproduce the observed Local Universe at the present time. In this work, we introduce and analyse one such simulation, the SLOW (Simulating the LOcal Web) project, which we show to reproduce the Local Universe, and especially its superclusters, to an unprecedented degree.

Using these superclusters and their predicted bound regions, derived from an N-Body extrapolation of the SLOW simulation into the far future, we propose a physically motivated method to derive zoom-in initial conditions for massive galaxy clusters. We show that this method results in very stable zoom-in regions, which is numerically advantageous.

The resulting high resolution full-physics simulations of local galaxy clusters – the LOWERDECKS set – are a valuable tool for limiting selection biases in comparing simulations to observations. Since the simulated clusters resemble their real-world counterparts in terms of environment and formation history, this facilitates the pinpointing of discrepancies or shortcomings in the modelled physical processes compared to observations.

Zusammenfassung

Die Entstehung von Strukturen im Universum findet gleichzeitig auf vielen verschiedenen Größenskalen statt. Gebundene Strukturen wie Galaxien und Galaxienhaufen sind dabei stark an die großskaligen Strukturen wie Filamente und Superhaufen, die sie umgeben, gekoppelt. Diese Arbeit beschäftigt sich mit diesen Flüssen, die großskalige Strukturen mit Galaxien und Galaxienhaufen verbinden.

Generell können Flussbewegungen in gravitativ hervorgerufene Zuflüsse von dunkler Materie und Gas und Ausströmungen, die durch die hydrodynamische Wechselwirkung des Gases getrieben sind, unterteilt werden. Diese Flüsse sind ein wichtiger Bestandteil einer Reihe astrophysikalischer Prozesse: Die Balance zwischen Zuflüssen und Ausströmung bestimmt das Gasreservoir, das einer Galaxie für die kontinuierliche Sternentstehung zur Verfügung steht. Im heißen diffusen Gas innerhalb von Galaxienhaufen erzeugen Gaszuflüsse beispielsweise Turbulenzen, die das hydrostatische Gleichgewicht der Atmosphäre beeinflussen können.

Da sie eine Vielzahl physikalischer Prozesse auf verschiedenen Größenskalen modellieren können, sind kosmologische Simulationen wie Magneticum Pathfinder ein ideales Werkzeug, um diese Massenflüsse aus einer theoretischen Perspektive zu verstehen. Anhand dieser Simulation erläutern wir, wie Strukturen im Universum entstehen und sich entwickeln. Insbesondere die Sternentstehung in Galaxien hängt dabei stark von den oben genannten Massenflüssen und Strukturen in ihrer Umgebung ab. Es kann gezeigt werden, dass diese Faktoren insbesondere im frühen Universum ($z > 2$) eine wichtige Rolle bei der Regulierung der Sternentstehung massiver Galaxien spielen.

Die Flussraten an den Grenzen gebundener Strukturen zeigen eine einfache Massenabhängigkeit, wie sie von der analytischen Theorie vorhergesagt wird. Dabei ist die geometrische Struktur der Flussfelder komplex und divers. Darüber hinaus ist bei den Ausströmungen keine vergleichbare Selbstähnlichkeit zu finden. Wir zeigen, dass Galaxien effizienter Masse ausstoßen als massereichere Objekte. Dies resultiert in ausgedehnteren Einflussgebieten von galaktischen Ausströmungen.

Um diesen Einfluss genauer zu betrachten, quantifizieren wir die Struktur des Zuflussfeldes mithilfe einer Zerlegung in Kugelflächenfunktionen. Grundsätzlich sind die Ausströmungen sphärisch symmetrischer angeordnet als die Massenzuflüsse, welche, der filamentösen Struktur der Umgebung folgend, auf einige Regionen mit starken Zuflüssen konzentriert sind. Zudem zeigen wir, dass diese Struktur der Zuflüsse und Ausströmungen direkt mit der Sternentstehungsgeschichte individueller Galaxien verbunden ist.

Die linearen Pekuliargeschwindigkeiten von Galaxien, verursacht durch großskalige Überdichten, können dazu verwendet werden, das lokale Universum zu modellieren: Das beobachtete Geschwindigkeitsfeld wird dabei als Randbedingung auf die statistische Realisierung der Anfangsbedingungen für kosmologische Simulationen angewendet. Die resultierende Simulation, SLOW (Simulating the LOcal Web), reproduziert lokale Galaxienhaufen bis zirka 100 Mpc Entfernung. Da insbesondere das großskalige Dichtefeld von den Beobachtungen gut reproduziert werden kann, sind auch die geometrischen Anordnungen der simulierten Superhaufen in guter Übereinstimmung mit den realen Regionen. Dies ermöglicht direkte

Vergleiche der Dynamik und Zusammensetzung lokaler Strukturen zwischen Modell und Beobachtung.

In Erweiterung der SLOW-Simulationen stellen wir eine Reihe sogenannter Zoom-in-Simulationen vor – die LowerDecks-Simulationen – welche lokale Galaxienhaufen in verbesserter Auflösung resimulieren. Dabei verwenden wir insbesondere die Kernregionen lokaler Superhaufen, welche durch ihre gravitativen Eigenschaften numerisch vorteilhafte Grenzvolumina darstellen. Abschließend legen wir dar, wie die mit dieser Methode erstellten digitalen Zwillinge der lokalen Galaxienhaufen Beobachtungen ihrer realen Gegenstücke unterstützen und das Verständnis der baryonischen Physik in und um diese Galaxienhaufen erweitern und ergänzen können.

Contents

I Introduction **1**

1 The Origins of Structure **3**
1.1 The Canvas of Structure Formation: Space–Time . . . 3
1.2 Complexity on Top of Simplicity – The CMB and the Beginning of Everything 6
1.3 The Primordial Gaussian Random Field . . . 7
1.4 Linear Theory . . . 8
1.5 From Linear Growth to Haloes: Press-Schechter . . . 10
1.5.1 Press-Schechter Formalism . . . 10
1.5.2 Beyond Press-Schechter . . . 11
1.6 From Bottom-Up to Top-Down: The Zeldovich Approximation . . . 11
1.7 The Cosmic Web . . . 12
1.8 The Moving Web: Local Cosmography . . . 13

2 The Highly Non-Linear Universe **17**
2.1 Preface – Virialization . . . 17
2.2 The Stars of the Show – Galaxies . . . 18
2.2.1 Morphology . . . 18
2.2.2 Structure . . . 19
2.2.3 The Baryon Cycle . . . 20
2.2.4 Galaxies and their Environment . . . 21
2.3 The Giants – Galaxy Clusters . . . 22
2.3.1 Stellar Component . . . 22
2.3.2 Intra Cluster Medium . . . 22
2.4 Dynamical State . . . 23
2.5 Sunyaev Zeldovich Effect - Imprints from the Neighbourhood . . . 24
2.6 Non-Linearity and the Argument for Simulations . . . 24

II Characterizing accretion flows of halos in cosmological simulations **27**

3 Flows in a Box: Cosmological Simulations **29**
3.1 Numerical Schemes: General . . . 29
3.2 Gravity . . . 29
3.3 Hydrodynamics . . . 30
3.4 The Magneticum Suite . . . 31
3.5 Sub-Grid Modelling . . . 33
3.6 (Sub-)Structure Identification . . . 35
3.7 Fundamentals: Scaling Relations in Numerical Simulations . . . 35
3.8 High(-z) Noon: Early Quenching in the Magneticum Simulations . . . 39
3.8.1 Shape of the Gravitational Environment . . . 40

3.8.2 Case Study . . . 42
3.8.3 Conclusions . . . 43
3.9 Sunrise over Magneticum: The DAWN Simulations . . . 43
3.10 Tackling the Multi-Scalarity of Flows . . . 44

4 Feeding Flow: Accretion, Outflows and Shocks in the Outskirts of Simulated Haloes 47
4.1 Introduction . . . 47
4.2 Methods . . . 48
4.2.1 Identifying the Systems . . . 48
4.2.2 Reconstructing the Peculiar Mass Flow from Simulation Data . . . 49
4.2.3 Geometry . . . 50
4.2.4 Flowmaps . . . 50
4.2.5 Discerning In- And Outflows . . . 51
4.2.6 Theoretical Accretion Model . . . 51
4.3 Characterising the Mass Flows in the Outskirts of Magneticum Haloes . . . 53
4.3.1 Accretion . . . 53
4.3.2 Outflow . . . 55
4.3.3 Flow Geometry . . . 56
4.3.4 Redshift Evolution of the Measured Flows . . . 58
4.4 Shocks in the Outskirts of Magneticum Haloes . . . 59
4.5 Case Study: Cluster 20 . . . 64
4.6 Global Phase Properties of the Flowing Gas . . . 68
4.6.1 Temperature . . . 68
4.6.2 Metallicity . . . 71
4.6.3 Redshift Evolution of Temperature and Metallicity . . . 72
4.7 Conclusions . . . 73

5 The Inflow Asphericity 75
5.1 Introduction . . . 75
5.2 Introducing the Asphericity Parameter . . . 77
5.2.1 Spherical Harmonics Decomposition . . . 77
5.2.2 Asphericity . . . 79
5.2.3 Logarithmic Versus Linear Asphericity . . . 79
5.3 Idealized Test Cases . . . 80
5.3.1 Test Setup . . . 80
5.4 Tests on Simulated Flow Fields . . . 83
5.4.1 Reconstructing the Peculiar Mass Flow from Simulation Data . . . 84
5.5 Summary and Conclusions . . . 86

6 Asphericity in Practice: Accretion at Cosmic Dawn and Beyond 89
6.1 The Global Evolution of the Flow Field Morphology . . . 90
6.2 Connecting Asphericity and Galaxy Properties . . . 91
6.3 Conclusions . . . 94

7 Intermission: Further Testing of the Asphericity Parameter 95
7.1 Flow Resolution: Sensitivity to the Discretization . . . 95
7.2 DAWN of Asphericities: Model Dependence of the Parameter . . . 96
7.3 Summary . . . 99

8 Further Flowing **101**
8.1 Die Aspherically: Galaxy Classes and Asphericity. 101
8.2 Shaped by the Flow: Galaxy Halo Shapes and Asphericity 103
8.3 Summary and Conclusions 104

III Flows in the Local Universe **107**

9 Going Local: From Cosmological Simulations to Constrained Simulations **109**
9.1 Constrained Simulations 110
9.2 The SLOW Simulation Suite 110
9.2.1 Initial Conditions 110
9.2.2 Simulation Runs 111
9.3 Looking Ahead: The Clairvoyant Suite 112

10 SLOW-ly Growing Giants: Superclusters in Constrained Simulations **113**
10.1 Introduction: Superclusters 113
10.2 Methods 114
10.2.1 Cross-identification of Structures 114
10.2.2 Quality Assessment of the Crossmatches 115
10.2.3 Simulating Ahead: The Clairvoyant N-body Forward Simulation Suite 116
10.3 Results 117
10.3.1 Superclusters in the SLOW Simulations 117
10.3.2 The Future of Bound Structures 121
10.3.3 Collapse Regions 124
10.4 Summary and Conclusions 126

11 Local Safari: Comparing Unique Structures between Simulations and Observations **137**
11.1 Local Imprints on the CMB 138
11.2 A3667-A3651 Bridge 141
11.3 Fornax 143
11.4 Conclusions 145

12 Level Up: Re-Building the Local Universe in High Definition **147**
12.1 Introduction 147
12.2 A Brief History of Cluster Zoom-In Simulations 148
12.3 Methods: SLOW Cluster ICs 151
12.3.1 Clairvoyant - The Parent Simulation 151
12.3.2 Cluster target selection 152
12.3.3 Constructing the High-Resolution Volume 152
12.3.4 Multimass Layering 153
12.4 Results 154
12.4.1 Cleanliness 154
12.4.2 Mixing Layer 155
12.5 Conclusions 156

13 Graduating from the LowerDecks: Combining High-Resolution Zoom-In Simulations of the Local Universe with State-of-the-Art Observational Data **159**
13.1 Turbulent pressure fractions 161
13.2 ICL+BCG: A Dynamical Tracer 163

13.3 The Galaxy Population of the Coma Cluster . . . 165
13.4 Cold Gas in the Fornax Region . . . 168
13.4.1 Methods: Post-Processing the HI Content . . . 169
13.4.2 The HI Distribution in the Fornax Region . . . 171
13.5 Conclusions . . . 172

IV Conclusion 173

14 Confluence: Summary and Conclusions 175
14.1 In and out of the Box: Accretion and Outflows . . . 175
14.1.1 How Self-Similar Are In- and Outflows? . . . 175
14.1.2 How Can the Morphology of the Accretion Field Be Quantified? . . . 176
14.1.3 How Is the Evolution of the Flow Field Connected to Galaxy Properties? . . . 176
14.2 SLOW Flow: The Local Universe . . . 177
14.2.1 Can Peculiar Local Structures Explain Observed CMB Anomalies? 177
14.2.2 How Well Are Local Superclusters Reproduced by SLOW? . . . 177
14.2.3 How Bound Are Local Superclusters? . . . 177
14.2.4 How Can We Construct Stable and Clean Initial Conditions for Cluster Zoom-Ins? . . . 178
14.3 Future Flows: Outlook . . . 178

A Asphericities 180
A.1 Calibrating the absolute values for normalization . . . 180
A.2 Truncation of the sum . . . 180
A.3 Variation of the parameters . . . 182
A.4 Special Cases . . . 182
A.4.1 Impact of the configuration on the asphericity parameter . . . 182
A.5 Spherical harmonics and filament connectivity . . . 183
A.6 Orthogonality of the Spherical Harmonics . . . 184

B Superclusters 186
B.1 Local supercluster members . . . 186
B.2 The Coma supercluster region . . . 187
B.3 The Centaurus supercluster region . . . 188
B.4 The Local Supercluster . . . 188
B.5 The Hercules Supercluster Region . . . 189
B.6 A2147 . . . 190
B.7 Comparison of geometric significance and one-point significance . . . 190
B.8 Selecting from the local halo distribution. . . . 192
B.9 Constraint tracer distribution . . . 193

C Zoom-in Initial Conditions 195
C.1 The SLOW cluster zoom-IC suite . . . 195

Acknowledgements 229

Part I

Introduction

Chapter 1

The Origins of Structure

Wenn die Wellen über mir
zusammenschlagen
tauche ich hinab um nach Perlen zu
suchen

–Mascha Kaléko

One of the most central dichotomies in the large-scale dynamics and structure of the Universe as well as this work is that between homogeneity and inhomogeneity. The isotropy and homogeneity of the Universe on large scales, summarized in the so-called **Cosmological Principle**, is one of the basic assumptions for almost all modern theoretical descriptions of the cosmos. Because we, as observers, only have reasonable access to a sub-volume of the Universe due to causality, our measurements are necessarily limited. The assumption that the matter-energy content of the Universe is well described by some average density $\overline{\rho}$ is therefore critical to our ability to describe the very fabric of our space-time. Nonetheless it is precisely the **deviations** from this cosmic homogeneity at smaller scales, that give rise to the rich structures we find everywhere in the cosmos. These structures, that is the galaxies (and the groups, clusters and filaments they make up), are the main focus of this thesis. But, as will be demonstrated throughout this work, their properties are often closely tied to the dynamics of the cosmos as a whole. Therefore it is necessary to first consider the large homogeneous scales of the cosmological background to be able to work towards the rich structures that grow on spatial scales far below them.

1.1 The Canvas of Structure Formation: Space–Time

After Einstein's paradigm-shifting publications on his theory of general relativity (Einstein, 1916), it soon became clear that this would have far-reaching implications for attempts at describing the cosmos as a whole. A critical result of the musings of de Sitter (1917) and Einstein (1917) was the realization that for a universe to be static and closed (i.e. spatially finite), a consistent general relativistic description of the system was possible upon introduction of a constant extra term in the **Einstein Field Equations**:

$$T_{\mu\nu} = R_{\mu\nu} - 1/2 g_{\mu\nu} R + \lambda g_{\mu\nu}, \tag{1.1}$$

where $T_{\mu\nu}$ is the stress-energy tensor, describing the energetic contents of the Universe, $R_{\mu\nu}, R$ are the Ricci Tensor and Scalar respectively and $g_{\mu\nu}$ is the metric tensor. The λ-term was, in an ironic twist in scientific history, introduced by Einstein exactly to allow the Universe to be static. Much later, this extra term would be a key element to explain the accelerated

expansion of the Universe (Riess et al., 1998). Nevertheless, this form of the equation is the cornerstone of modern cosmology. It assumes that the geometry of the Universe, while it might be complex on small scales, can be sufficiently accurately described by a single metric, in other words that as mentioned above, the matter within it is distributed sufficiently homogeneously on large scales.

While Einstein described a spatially spherical world, with a constant curvature determined by its matter content, de Sitter credibly demonstrated (de Sitter, 1917) that this extended version of Einsteins formula did not even need any matter to be solved. The resulting flat **de Sitter** space-time remains a useful tool to this day in modelling the dynamics of the late time Universe, as will be discussed later on in this thesis.

From Static to Dynamic However both descriptions still imagined the Universe as a static system. It took the efforts of Alexander Friedmann (Friedmann, 1922, 1924) to generalize these ideas in order to allow for a universe with a dynamic scale. This work was in part motivated by growing evidence towards a systematic radial motion of nearby astronomical objects (dubbed as nebulae at the time) (e.g. Slipher, 1917). The equations derived by Friedmann, employing a metric with a time-dependent scale radius for the first time are named the **Friedmann Equations**:

$$\left(\frac{\dot{R}}{R}\right)^2 = \alpha\rho - \frac{k}{R^2} + \frac{\Lambda}{3} \tag{1.2}$$

$$\frac{\ddot{R}}{R} = \frac{\alpha}{2}(\rho + 3p) + \frac{\Lambda}{3}, \tag{1.3}$$

where k is the intrinsic curvature ($k = [-1, 0, 1]$ indicates a hyperbolic, flat and spherical curvature respectively). Λ is Einstein's additional constant from Eq. (1.1), while $\alpha = \frac{8\pi G}{3}$ and ρ, p describe the density and pressure of a perfect fluid. This ρ accounts for the matter and radiation content of the Universe. In his actual derivations, Friedmann additionally assumed a pressureless fluid with $p = 0$, but the derivation is identical up to the extra $3p$ from the diagonal terms in the trace of $T_{\mu\nu}$. In modern cosmology the physical scale R is often replaced by the dimensionless scale factor $a(t) = R(t)/R_0$ (where the subscript 0 indicates the value today), but in principle these two dynamical equations constitute humanity's current best understanding of the fabric of space-time.

Observables of Expansion In concrete terms, Eq. (1.2) and Eq. (1.3) relate the speed and acceleration of the expansion of the Universe to its matter and energy content. Historically,

$$\frac{\dot{R}}{R} = \frac{\dot{a}}{a} = H(t) \tag{1.4}$$

is called the **Hubble Function**, with its present day value H_0 being one of the first measurements from the recession velocities of galaxies as a function of their distance. This velocity manifests itself as an observed **redshift** of the light from these galaxies:

$$z = \frac{\lambda - \lambda_0}{\lambda_0} = \frac{1}{a(t)} - 1, \tag{1.5}$$

where λ_0 is the intrinsic wavelength of the light and λ the observed wavelength. For cosmologically small distances, measuring galaxy velocities via the redshift yields a linear relation $v_r = H_0 d$ (Hubble, 1929). The value of H_0 poses one of the biggest tensions in modern cosmology, as early time measurements, extrapolated by the current standard model to the present day consistently yield lower values $H_0 = 67.77$ km/s/Mpc (Planck Collaboration et al., 2016c) than local measurements of the current day expansion $H_0 = 73.04$ km/s/Mpc (Riess et al., 2022).

At the far end of the velocity-distance diagram the linear relation no longer holds. Using distances inferred from the apparent brightness of distant type Ia supernovae, Riess et al. (1998) demonstrated early evidence for an accelerated expansion, which essentially constrained $q = -\ddot{a}a/\dot{a}^2$, the deceleration parameter, to be negative.

Rest in Motion: Co-Moving Space The evolving scale factor due to expansion makes it convenient to re-write equations for large-scale processes in **co-moving** units. Here, one defines

$$\mathbf{x} = \mathbf{r}/a(t), \tag{1.6}$$

where $\mathbf{x}$ is the co-moving position and $\mathbf{r}$ is the real-space position. For the velocity of objects it is similarly convenient to consider only the velocity in the co-moving frame. From Eq. (1.6):

$$\frac{d}{dt}\mathbf{r} = \dot{a}\mathbf{x} + a\dot{\mathbf{x}}, \tag{1.7}$$

where the first term is simply the change in physical coordinate due to expansion, the so-called **Hubble Flow**. The second term is the perturbative velocity, also referred to as the **peculiar velocity**

$$\mathbf{v}_p = a\dot{\mathbf{x}}. \tag{1.8}$$

Unless stated otherwise, velocities in this work are exclusively the peculiar velocities. For the cosmological simulations introduced in this work, co-moving units are especially convenient.

The Standard Model of Cosmology The exact evolution of space-time, as determined by Eq. (1.2) and Eq. (1.3), depends on its contents encoded in the components of ρ_m, the (mass-)energy density of the Universe, and Λ, a cosmological constant associated with the phenomenological **Dark Energy**, responsible for the aforementioned accelerated expansion. Together, these form the modern standard model of cosmology, the so-called ΛCDM Universe, containing dark energy (ρ_Λ), radiation (ρ_r) and matter (ρ_m), the latter dominated by a collisionless mass component, the so called **Cold Dark Matter** (CDM).

This ingredient to the cosmological model was introduced upon early observations that the dynamics in nearby clusters of galaxies (Zwicky, 1937) and galaxies (Roberts & Whitehurst, 1975) did not match what the visible mass of these objects could account for. It is currently still unclear what this component is comprised of, however one can reasonably assume it to be "cold" or at most "warm", i.e. characteristic velocities are in the non-relativistic or intermediate range. If the dark matter is "hot" there would be a strong suppression of small scale structure from the additional pressure and this has not been observed (Bond et al., 1982). Possible candidates for cold dark matter from particle physics are for example axion-like particles (Duffy & van Bibber, 2009) or even more exotic combinations like axion-quark nuggets (Sommer et al., 2024). Throughout this work and all discussed simulations, we will assume a cold dark matter component as in the standard ΛCDM model.

If the Universe has a flat geometry, the k-term in Eq. (1.2) vanishes. In the additional limit of a vanishing cosmological constant $\Lambda = 0$ and a purely matter dominated Universe (Einstein-de-Sitter universe), this leaves $(\frac{\dot{a}}{a})^2 = H^2 = \frac{8\pi G}{3}\rho$. This is why $\rho_c = \frac{3H^2}{8\pi G}$ is referred to as the **critical density**. Modern cosmological probes (Komatsu et al., 2011, Planck Collaboration et al., 2016c) have indeed determined the density to be very close to this value, indicating an almost flat geometry.

The critical density allows to bring Eq. (1.2) into its most commonly used form: We replace ρ_x, the density of each species of the model with $\Omega_X(t) = \rho_X(t = t_0)/\rho_c(t = t_0) \times f(t)$, where t_0 is the present epoch and $f(t)$ encodes the time evolution of each mean density. We

will discuss this time evolution in the next paragraph. This replacement results in

$$H^2(t) = H_0^2(\Omega_m(t) + \Omega_\Lambda(t) + \Omega_k(t) + \Omega_r(t)), \tag{1.9}$$

where, by construction at $t = t_0$

$$\Omega_k = 1 - (\Omega_m + \Omega_\Lambda + \Omega_r). \tag{1.10}$$

For the standard flat Λ-CDM we have therefore:

$$\Omega_m + \Omega_\Lambda + \Omega_r = 1 \tag{1.11}$$

at $t = t_0$.

Equations of State and Evolution The balance between individual components of the model is not fixed. In fact, dark energy, dark matter and radiation evolve very differently across time. This is because each component follows a different equation of state, connecting the density to the pressure. The dependency is often parametrized with the so-called equation of state parameter w, such that $p = \mathrm{w}\rho$. For a pressureless fluid, $w = 0$ so from conservation of energy, as the Universe expands, $\rho_m = \rho_{\mathrm{ini}} a^{-3}$. In general, $\rho_X \propto a^{-3(1+\mathrm{w_X})}$. For the dark energy, behaving like a cosmological constant, therefore $\mathrm{w} = -1$, such that $\rho_\Lambda = const$. As the universe expands, the ratio ρ_m/ρ_Λ declines with a^3. This means, that in the limit of large a, the matter content of the Universe can be neglected and therefore we have $(\frac{\dot{a}}{a}) = \sqrt{\frac{\Lambda}{3}}$ and $a(t) \propto exp(\frac{\sqrt{\Lambda}}{3}t)$. Similarly, for a matter dominated era (due to the extra a^{-3} factor) $a(t) \propto t^{2/3}$. Radiation scales even more rapidly with time $\rho_r \propto a^{-4}$ due to the additional red-shifting of individual photons by expansion ($\mathrm{w_r} = 1/3$). This also means that, going back in time, not only do both the energy density of matter and radiation grow, leading to the standard concept of a "Big Bang" origin of the Universe, but the relativistic radiation component actually outgrows the matter component. The consequence is an early epoch of radiation domination with $a(t) \propto \sqrt{t}$. From this early period, shortly after matter-radiation equality ($z_{\mathrm{eq}} \approx 3400$, Planck Collaboration et al. (2016c)), it is also where we receive one of the most important cosmological signals: The relic radiation from the chaotic and hot beginning of the Universe – the **Cosmic Microwave Background** (CMB).

1.2 Complexity on Top of Simplicity – The CMB and the Beginning of Everything

The previously discussed cosmological principle – the hypothesis that the Universe is homogeneous on large scales – was in part validated by a serendipitous discovery by Penzias & Wilson (1965): In the microwave band the sky does indeed look perfectly smooth and homogeneous in every direction. The radiation that Penzias & Wilson (1965) detected originates from the so-called epoch of recombination, where due to the expansion of the Universe for the first time the hot plasma of the Universe was cold enough for electrons and protons to form neutral atomic hydrogen. As a result, the photons decoupled from the baryonic component, allowing the former to stream freely. Because the photons and the baryons were coupled before, the early structure of the baryons is still reflected in the temperature of the received photons. Modern space-based microwave instruments like WMAP (Bennett et al., 2003) and Planck (Planck Collaboration et al., 2016a, 2020) make it possible to measure this radiation temperature to outstanding precision.

The CMB has a blackbody temperature of $T_0 = 2.7255$ K (Fixsen, 2009) with only very small deviations from this temperature ($O(10^{-5})$) across the sky. Both the robust mean temperature as well as the small fluctuations are cosmologically very meaningful.

The fact that the temperature is uniform across the sky implies that the entirety of the last scattering surface (the surface from which we currently measure the light that decoupled at $z = z_{\rm rec}$) implies that the entirety of the region must have been in thermal equilibrium. Extrapolating the expansion history back to the recombination epoch however, one arrives at the result that regions with an angular separation $\gtrapprox 2^\circ$ cannot have been in causal contact with each other. This "horizon problem" had been known already from theoretical considerations (Rindler, 1956) pre-dating the discovery of the CMB, but its uniform temperature highlights this issue further. One proposed solution to this issue (along with the so-called "flatness problem", related to the previously discussed very small deviation of the matter content of the Universe from $\rho/\rho_c \approx 1$) was an inflationary period (e.g. Guth, 1981). In this model, the Universe undergoes an extremely brief period of rapid exponential growth at very early times (first few 10^{-32} s). This rapid expansion would then stretch the causality horizons to the sizes observed in the CMB today.

The modern version of inflationary theory, developed by e.g. (Linde, 1982), was then shown not only to reconcile the homogeneity of the Universe with our understanding of causality but also predict the anisotropies in the CMB as well as their statistical properties from initial quantum fluctuations in the inflationary field (Mukhanov & Chibisov, 1981, 1982). Curiously, our attempts to explain the homogeneity of the CMB temperature also provided an explanation for the tiny fluctuations in that temperature. These initial fluctuations in the density field are the seeds of all structures we can observe in our Universe today.

1.3 The Primordial Gaussian Random Field

A key prediction of the modern inflationary model is that the perturbations resulting from the inflationary epoch are Gaussian in nature (Mukhanov, 2007). As scalar perturbations in the metric are connected to the energy-density distribution, this means that a sample of N points has overdensity values $\zeta = \{\delta_1, \delta_2, \ldots, \delta_N\}$ (where $\delta_i = \delta(\mathbf{x}_i) = \frac{\rho(\mathbf{x}_i)-\bar{\rho}}{\bar{\rho}}$) according to the multivariate Gaussian distribution

$$p(\zeta) = \frac{\exp(-\frac{1}{2}\zeta^i {M^{-1}}_{ij} \zeta^j)}{\sqrt{(2\pi)^N \det M}} \tag{1.12}$$

where $M_{ij} = \langle \delta_i, \delta_j \rangle$ is the covariance matrix. In the limit of continuous sampling with large N, this covariance is identical to the **two-point correlation function** defined by

$$\xi(|\mathbf{x_i} - \mathbf{x_j}|) = \langle \delta_i, \delta_j \rangle, \tag{1.13}$$

which completely characterises the Gaussian random field. A measure of the total variance of the field is given by the diagonal terms of the matrix or correspondingly the one-point correlation

$$\sigma^2 = \xi(|\mathbf{x_i} - \mathbf{x_i}|) = \xi(0) = \langle \delta_i \delta_i \rangle. \tag{1.14}$$

A more intuitive way to think about the initial Gaussian random field is in terms of its *power spectrum* $P(k)$, the Fourier transform of the correlation function, expressing the power in fluctuations with scale $\lambda = \frac{2\pi}{k}$. Most theoretical descriptions yield a power law shape (e.g. Harrison (1970), Mukhanov (2007))

$$P(k) = Ak^n \tag{1.15}$$

where n defines the slope of the power spectrum.

This initial **matter power spectrum** can be directly inferred from the angular temperature fluctuations in the CMB and provides the starting point for numerical simulations, as we will further elucidate in the following chapters. Similarly, it is possible to infer the matter power spectrum at the present time from the clustering of visible structures (i.e. galaxies). Fig. 1.1 shows this power spectrum inferred from late time probes like galaxy clustering

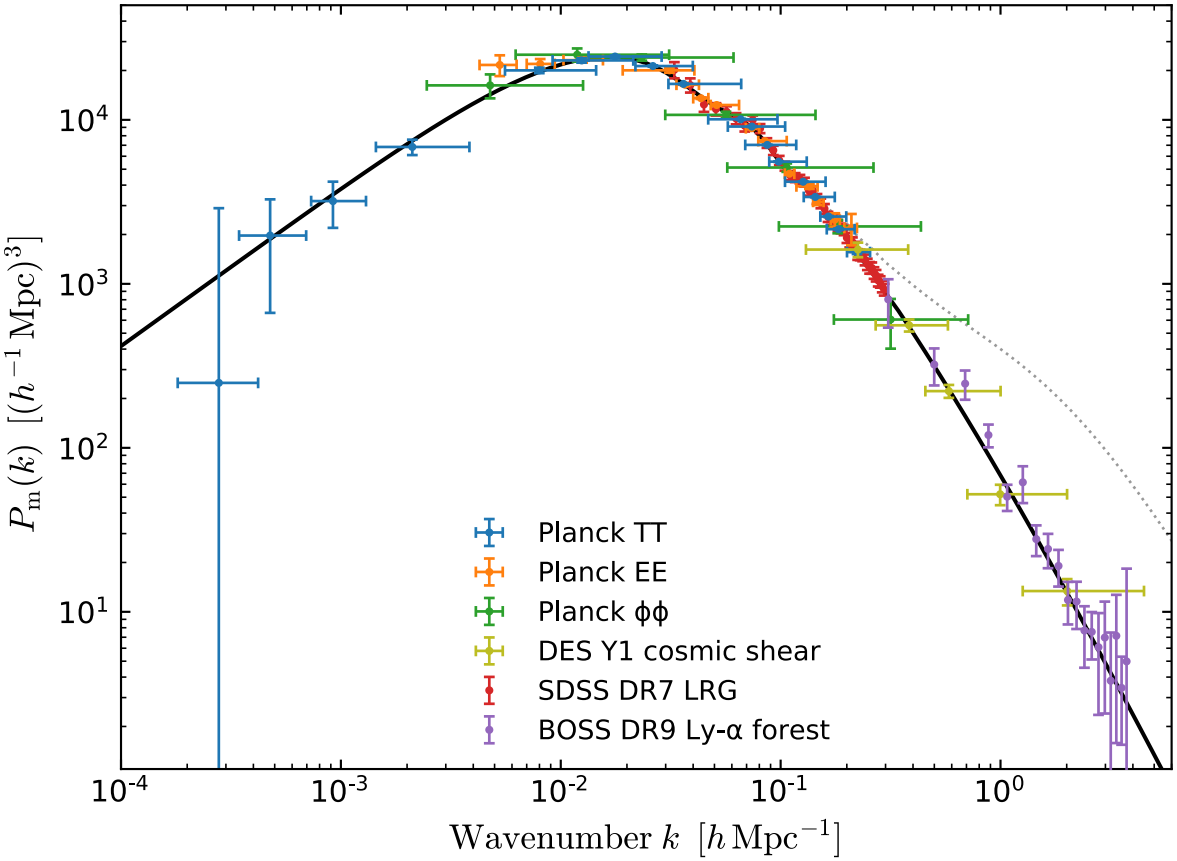


Figure 1.1: The matter power spectrum as measured by various different early and late-time probes (CMB power spectrum by Planck, Galaxy clustering by SDSS and BOSS, with additional lensing data from DES). The black line is a theoretical model power spectrum. All power spectra were transformed to $z = 0$ assuming linear evolution. The grey dashed line shows the impact of non-linear clustering at small scales. Figure 19 from Planck Collaboration et al. (2020).

as well as the recombination epoch from the angular temperature fluctuations in the CMB. A large scales (small k), this power spectrum is a pure power law with a spectral slope $n_S = 0.9649 \pm 0.0042$ (Planck Collaboration et al., 2020), very close to unity. Connecting these measurements from the present-day Universe to data from its very early epoch is possible, as on large scales, the density perturbations evolve linearly. This fact, in combination with the Gaussian nature of density perturbations, allows for a number of powerful and simple predictions, so we will briefly outline the linear theory of structure formation in the following.

1.4 Linear Theory

The evolution of density perturbations that give rise to the structures observed today is largely dominated by the perturbations in the pressureless dark matter component. We will therefore focus on such a pressureless fluid.

Fluid Equations The linearized fluid equations in co-moving coordinates read

$$\frac{\partial \delta_{dm}}{\partial t} = -\frac{1}{a}\nabla \cdot \mathbf{v} \qquad \text{(Continuity)} \tag{1.16a}$$

$$\frac{\partial \mathbf{v}}{\partial t} = -\frac{\dot{a}\mathbf{v}}{a} - \nabla\phi a^{-1} \qquad \text{(Euler Equation)} \tag{1.16b}$$

$$\nabla^2\phi = 4\pi G a^2 \overline{\rho}_{dm}\delta_{dm} \qquad \text{(Poisson Equation)} \tag{1.16c}$$

In Eq. (1.16), $\mathbf{v}$ and ϕ are the peculiar velocity and the potential perturbation i.e. those are already perturbative quantities without the uniform backgrounds ($\dot{a}\mathbf{x}$, the Hubble flow and $1/2a\ddot{a}x^2$, the background potential).

The Growth of Linear Perturbations of Dark Matter During Matter Domination Taking the divergence of the Euler equation and combining it with the Poisson and the continuity equation leads to a second order differential equation in time:

$$\frac{\partial^2\delta}{\partial t^2} = \frac{3}{2}\Omega_0 a^{-3} {H_0}^2\delta - 2H(t)\frac{\partial\delta}{\partial t} \tag{1.17}$$

This second-order differential equation only contains differentials with respect to time, allowing for a separation of the temporal and spatial part of the density perturbation field: $\delta(\mathbf{x}, t) = D(t) * f(\mathbf{x})$, where $D(t)$ depends on the cosmology but not on the point in space, consequently growing the density perturbations universally. Generally the growth factor can be written as (e.g. Peebles, 2020)

$$D(t) = H(t)\int \frac{dt}{a(t)^2 H(t)^2}, \tag{1.18}$$

where by Eq. (1.2) it depends directly on the matter density and the dark energy component. In the aforementioned matter dominated universe with negligible dark energy $a(t) \propto t^{2/3} \Rightarrow H(t) = \dot{a}/a \propto t^{-1}$, this reduces to the very simple relationship

$$D(t) \propto t^{2/3}, \tag{1.19}$$

or $D(a) \propto a = 1/(1+z)$. In other words, the density contrast in a matter dominated Einstein-de-Sitter universe just grows linearly with the scale factor.

Relating the Fields in Fourier space A very insightful little calculation to understand how the velocity field is related to the density field can be performed by looking at the Fourier transformed version of the continuity equation, Eq. (1.16a). Firstly, we write the fields in terms of their Fourier transformed counterparts:

$$[\delta, v, \phi](\mathbf{x}) = \int \frac{d\mathbf{k}}{2\pi}[\delta, v, \phi](\mathbf{k})e^{-i\mathbf{kx}} \tag{1.20}$$

Switching to Fourier space in Eq. (1.16a) yields

$$\frac{\partial\delta_{dm}(\mathbf{k})}{\partial t} = \frac{1}{a}i\mathbf{k}\cdot\mathbf{v}(\mathbf{k}) \tag{1.21}$$

which can be re-written by multiplying both sides with $\mathbf{k}$ as

$$\mathbf{v}(\mathbf{k}) = \frac{a\mathbf{k}}{ik^2}\frac{\partial\delta_{dm}(\mathbf{k})}{\partial t}. \tag{1.22}$$

Due to the temporal evolution of the density perturbations being separable (recall $\delta(\mathbf{x}, t) = D(t)\delta(\mathbf{x})$ with the same being true for the Fourier transformed density perturbations) this directly implies the velocity field $\mathbf{v}(\mathbf{x})$ to be a Gaussian random field as well in the linear regime (since Fourier transforms do not change the gaussianity property). More interestingly, since the power spectrum $P(k)$ of a Gaussian random field is the Fourier transform of its two-point correlation function, the extra $1/k$ term relating the density field to the velocity field in Fourier space implies directly

$$P_\delta(k) \propto P_{\mathbf{v}(k)}(k)k^{-2}. \tag{1.23}$$

In other words, smaller-scale fluctuations are suppressed in the velocity field compared to the density field. This property makes the linear velocity field a great tool to constrain the large-scale environment, as we will see in Chapter 9 and the following chapters.

An additional observation from the Fourier transformed fields is, that the modes do not mix in the linear regime. Adding non-linear terms (such as the $(\mathbf{v} \cdot \nabla)\mathbf{v}$ term that appears in the general Euler Equation) would mix the modes, transferring power between the scales and complicating the analysis significantly.

1.5 From Linear Growth to Haloes: Press-Schechter

The two ingredients of a Gaussian random field and the linear growth of initial perturbations allow analytical calculations to reach surprisingly far into the non-linear regime: As we will briefly discuss in the following, from these two assumptions it is possible to infer how the mass in the Universe is distributed among the gravitationally bound haloes that host the galaxies and clusters we observe.

1.5.1 Press-Schechter Formalism

Press & Schechter (1974) developed an analytical model for the so-called **Halo Mass Function** (HMF), which quantifies how mass is distributed among collapsed haloes. Its assumptions are almost exclusively built on the assumptions of linear theory we introduced in the previous section. We showed how the density contrast grows as ($\delta(t, \mathbf{x}) \propto D(t)\delta(t_i, \mathbf{x})$). Overdense regions will eventually reach a certain threshold density δ_c (the exact value of this threshold is derived from the spherical collapse model by Gunn & Gott (1972)), start to collapse and eventually form a halo. We will discuss this collapse in more detail in Chapter 2. For now we just associate collapsed haloes with critical overdensities.

In order to determine the mass of such an object, one can smooth the initial Gaussian density field by averaging the density with a spatial filter (usually the spatial spherical top hat filter $W(\mathbf{x}, R) = \frac{3}{4\pi R^3}\Theta(R - r)$). This associates a smoothed overdensity field to the filter scale R, which can be readily converted into a filter mass M, given by multiplying the mean density with the volume of the filter $M = \frac{4\pi}{3}\bar{\rho}R^3$. This operation, with the right choice of filter, ensures that the smoothed field δ_M is still a Gaussian random field. The quantities defined in section 3.1 will have their corresponding partners for these smoothed fields. The variance of the smoothed field is defined analogously to the variance of the original field:

$$\sigma_R^2 = \sigma_{M(R)}^2 = \langle \delta_R \delta_R \rangle. \tag{1.24}$$

As an important side note, this variance, when computed at a scale $R = 8$ Mpc/h (where h is dimensionless and defined by $h = H_0/100$ km/s) is called σ_8 and is a key observable of the density field from galaxy clustering statistics.

Moving along, the Gaussianity of the smoothed field ensures that the probability for a single point in space reaching the threshold δ_c at a Mass scale M i.e. that the region

around the point collapses into a halo of this mass is given by the Gaussian integral (compare Eq. (1.12)):

$$P(\delta_M > \delta_c)(x) \propto \int_{\delta_c}^{\infty} \frac{e^{-\frac{\delta_M{}^2}{2\sigma_M{}^2}}}{\sqrt{2\pi\sigma_M{}^2}} \tag{1.25}$$

. From this basic assumption, Press & Schechter (1974) derived the following mass function:

$$\frac{dn}{dln(M)}(M,z)dM = \sqrt{\frac{2}{\pi}}\bar{\rho}\frac{\delta_c(z)}{\sigma^2 M}exp\Big(-\frac{\delta_c{}^2(z)}{2\sigma^2(M)}\Big)d\sigma \tag{1.26}$$

It marked an important milestone in our understanding of cosmic structure and can make surprisingly good predictions to this day. Taking this equality to the extreme however, a paradox arises: Setting $M \to 0$, σ_M diverges and the integral in Eq. (1.25) evaluates to 1/2. So according to the PS formalism only 1/2 of all mass is contained in haloes. This was initially fixed by introducing a "fudge factor" of 2.

1.5.2 Beyond Press-Schechter

Bond et al. (1991) further formalized the approach of Press and Schechter to accurately account for the artificial factor of 2: By considering the radial overdensity structure at individual locations as Markovian random walks in σ_M, δ, the factor arises naturally from symmetry arguments. Another extension of the formalism, introduced by Sheth et al. (2001), further improved the accuracy of the resulting halo mass functions by extending the model from (Bond et al., 1991) to allow for a variable δ_c to be coupled to statistics of the tidal field. This accounts for the fact that haloes do not collapse perfectly spherically, as the previous fixed threshold assumed, because the initial perturbations themselves are not spherical to begin with. Modern models additionally account for baryonic effects and at the present time theoretical mass functions are in excellent agreement with numerical simulations (Tinker et al., 2008, Bocquet et al., 2016).

1.6 From Bottom-Up to Top-Down: The Zeldovich Approximation

Historically speaking, the approach described in the previous section represents the **bottom-up** view of structure formation: Since the function $\sigma(M)$, which determines the shape of the HMF, is a decreasing function of mass (e.g. van den Bosch, 2002), lower mass haloes will form first and then hierarchically merge into larger structures. The opposing perspective is the **top-down view** on structure formation which we will discuss in the following. If dark matter would indeed have relativistic velocities (in a "warm" or even "hot" dark matter scenario, e.g. sterile neutrinos), this would be the preferred way structures form in general. Large-scale perturbations would collapse first, due to the suppression of density fluctuations on small scales. For a direct comparison to CDM, see Knebe et al. (2003). Nonetheless even in the CDM case the top-down philosophy can help understand the largest observed structures in our Universe:

In his early theoretical work on structure formation, Zel'dovich (1970) developed an approximate mapping between a fluid elements initial (Lagrangian) position in co-moving space and its Eulerian position at time t via

$$\mathbf{x}(\mathbf{q},t) = \mathbf{q} + D(t)\mathbf{s}(\mathbf{q}). \tag{1.27}$$

Here $\mathbf{s}(\mathbf{q})$, the initial displacement critically only depends on the initial coordinates and the motion of the fluid element continues along the direction of initial displacement, where the time dependence is encoded in the linear growth factor $D(t)$. The so-called **Zel'dovich approximation** then assumes the displacement vector to solely depend on the linear gravitational potential perturbation at the initial position (extrapolated to time t):

$$\mathbf{s}(\mathbf{q}) \propto -\nabla\phi_{lin}(\mathbf{q}) \tag{1.28}$$

From mass conservation, one can derive (Hidding et al., 2014)

$$\rho(\mathbf{x}, t)d\mathbf{x} = \overline{\rho}(t)d\mathbf{q} \tag{1.29}$$

leading to

$$\frac{\rho(\mathbf{x}, t)}{\overline{\rho}(t)} = \det\left(\frac{\partial x_i}{\partial q_j}\right)^{-1}, \tag{1.30}$$

in other words, the density contrast depends of the Jacobian of the mapping between x and q, the Eulerian and Lagrangian coordinates. This mapping is defined by Eq. (1.27), so inserting this dependency and rewriting in terms of the Eigenvalues λ_i of the deformation tensor $-\frac{\partial s_i}{\partial q_j}$ one arrives at:

$$\delta(\mathbf{x}, t) + 1 = \frac{1}{(1 - D_+(t)\lambda_1)(1 - D_+(1)\lambda_2)(1 - D_+(t)\lambda_3)} \tag{1.31}$$

It can be shown (Hidding et al., 2014), that the Eigenvalues $\lambda_1, \lambda_2, \lambda_3$ will almost never be equal. As a result the density contrast will grow anisotropically with the fastest enhancement along the shortest initial axis of the deformation, forming a "pancake"-like structure. Depending on the exact balance of the eigenvalues, this process can produce a diverse range of anisotropic elongated patterns. This provides an intuitive interpretation of the observed large-scale structure, the so-called **Cosmic Web** (see next section). In fact, from the singularities of the mapping it is possible to derive the structure of the cosmic web almost entirely (Hidding et al., 2014).

1.7 The Cosmic Web

From this anisotropic collapse at large scales, a beautiful and complex density pattern emerges: Massive clusters sit at the **nodes** of an intricate web, where they collapse almost spherically ($\lambda_1 \approx \lambda_2 \approx \lambda_3$). These node points are connected by elongated **filaments** of all sizes, where there is one clear compression axis ($\lambda_1 \approx \lambda_2 \gg \lambda_3$). These filaments are often themselves embedded into 2-dimensional **sheets**, the pancake structure from the previous section, with the collapse happening in a single preferred spatial direction $\lambda_1 \gg \lambda_2 \approx \lambda_3$. Finally, the regions where everything is outflowing (like the node case but with inverted signs for the Eigenvalues) are called the **cosmic voids**. These regions present a rather unique environment for the few haloes forming within them due to the low ambient density and super-Hubble expansion (Sheth & van de Weygaert, 2004), which leads to an overall suppression of structure formation (Kreckel et al., 2010, Kuutma et al., 2017). This effect can be quantified in numerical simulations using the Void Halo Mass Function (Schiller et al. in prep inc. Seidel).

Fig. 1.2 shows the cosmic web structure in Magneticum Pathfinder *Box4/uhr* (Dolag et al., 2025). As can be seen, the pattern evolves across time with filaments merging into larger structures, and is visible in both the gas component as well as in the arrangement of the galaxies within the simulation volume. As is evident by the hot gas represented with the magma colour map, along major filaments, there is also significant shock heating causing the gas distribution in these filaments to become multi-phase, while smaller filaments remain predominantly cold. This is the reason why the **warm-hot phase of the intergalactic**

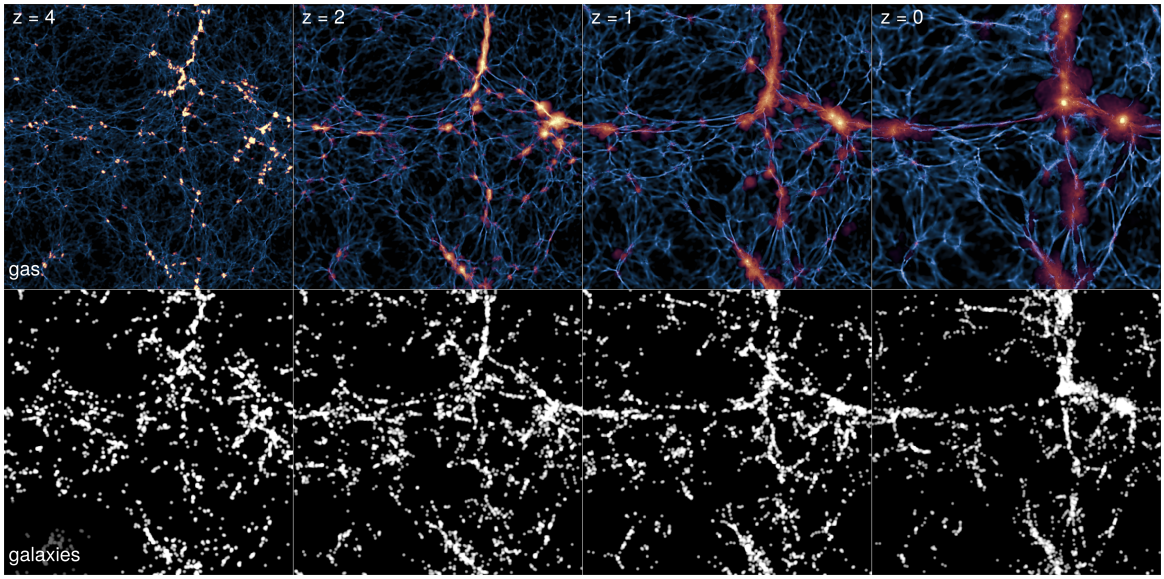


Figure 1.2: The evolution of the cosmic web in the MAGNETICUM PATHFINDER simulation visualized in the gas component (top row), with the colours differentiating between hot (red-yellow) and cold (blue) gas, and the galaxy distribution (bottom row) at different points in time. The side length of the simulation volume is 48 Mpc/h and the thickness of the slice is 2 Mpc/h.

medium (WHIM), an observationally elusive gas component suspected to make up $30-50\%$ of the total baryon budget of the Universe, is usually searched for in these regions (Churazov et al., 2023, Zhang et al., 2024a). The complex gas structure additionally makes filaments a rather unique environment for galaxy evolution, since, as seen in the lower panels, galaxies align along them and they present a preferred direction of anisotropic gas accretion.

The two major nodes in the top right of the $z = 0$ panels highlight another structure component, as it is comprised of two large clusters together, the region resembles an elongated filamentary **Supercluster**, a cluster of clusters (even though the volume of the simulation is not large enough at 48 Mpc/h to accurately reproduce such structures). These regions were actually the first elements in the cosmic web to be actually observed due to their significant overdensity in the galaxy distribution (Abell, 1961, Jôeveer & Einasto, 1978, Jõeveer et al., 1978). In part III, this work will study these fascinating regions in greater detail and answer the question whether, or to what degree, they are gravitationally bound.

The imprint of the structure in the galaxy distribution also allows us to observe the cosmic web, even though the dark matter and cold gas that make up a large part of it are not directly observable. Large modern spectroscopic galaxy surveys like the Sloan Digital Sky Survey and the eBOSS follow-up (York et al., 2000, Ahumada et al., 2020) or the DESI survey (DESI Collaboration et al., 2026) make the cosmic web accessible for studies and comparison to numerical predictions. Fig. 1.3 shows an example of such a galaxy distribution from the DESI survey. The cosmic web structure from the simulation with its complex, multi-scale morphology clearly reproduces the observed cosmic web. The figure further demonstrates how the cosmic web pattern fades into homogeneity, when viewed at large enough scales, in agreement with the aforementioned cosmological principle.

1.8 The Moving Web: Local Cosmography

In our immediate cosmic neighbourhood (out to a few 100 Mpc), it is even possible to reveal the cosmic web dynamically using galaxies. While for distant galaxies the Hubble

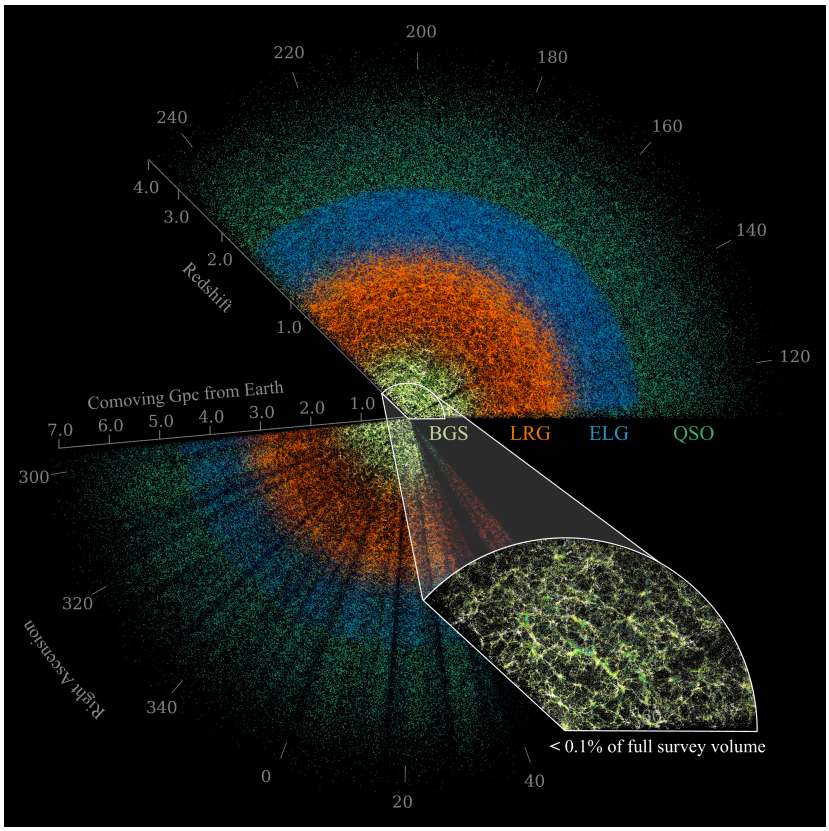


Figure 1.3: Slice through a DESI map of the Universe out to $z = 4$. The colour groups represent different subsamples of the survey–The bright galaxy survey (BGS) galaxies, luminous red galaxies (LRG), emission– line galaxies (ELG), and QSOs are shown with yellow, orange, blue, and green points, respectively. Figure from DESI Collaboration et al. (2026).

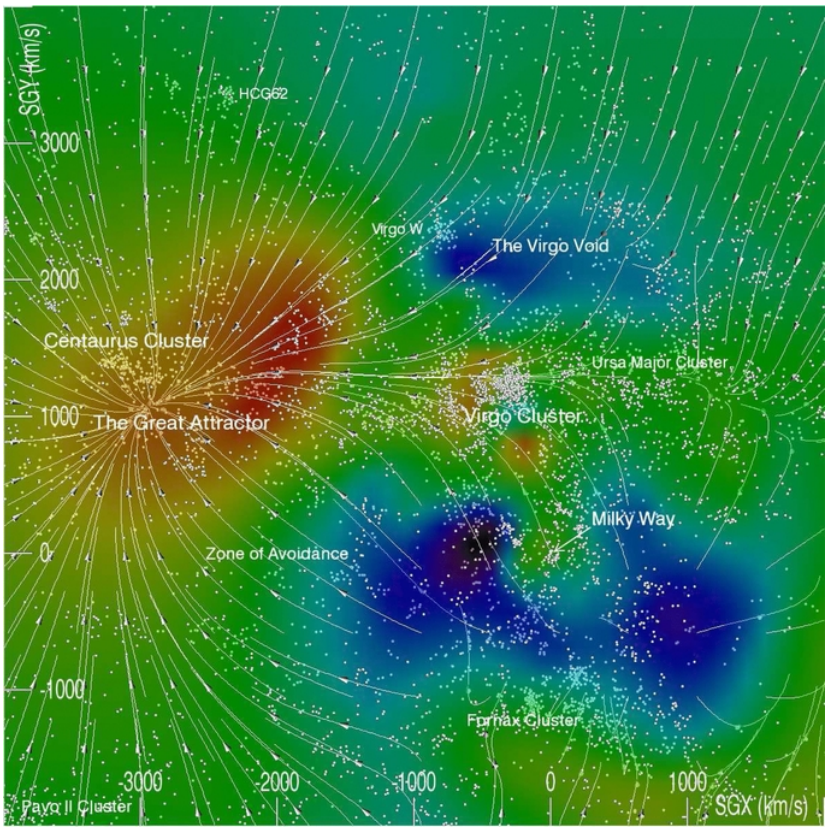


Figure 1.4: The local linear velocity field as streamlines. Colours show the underlying density field, like the velocity field inferred from the Wiener Filter. The Milky Way position and some of the prominent local clusters and groups are indicated. The slice is in the supergalactic x-y plane, with a thickness of 3000 km/s (≈ 43 Mpc) centred on SGZ=0. Figure taken from (Courtois et al., 2013).

Flow (first term in Eq. (1.7)) by far dominates the peculiar velocities of galaxies (recall $H_0 \approx 70$km/s/Mpc), for nearby galaxies this is not the case. Additionally, the proximity of these objects makes it possible to very precisely measure their distances. This is done by calibrating their luminosities independently from known scaling relations, for example the Tully-Fisher scaling relation between the neutral hydrogen line profile and the absolute magnitude of a galaxy (Tully & Fisher, 1977). This can then used to calculate the distance to the galaxy via the **distance modulus**

$$\mu = m - M = 5 \log_{10}(d) - 5 \tag{1.32}$$

i.e. the difference between the absolute magnitude M, which is inferred from the relation and the apparent magnitude m which is measured. From Eq. (1.7) this distance then means that it is possible to calculate the peculiar velocity by subtracting the Hubble flow term. Compilations of such distance moduli for nearby (up to $z \approx 0.05$) galaxies, for example the Cosmicflows project (Tully et al., 2013, 2016, 2023) make it possible to reconstruct the local 3D velocity field using statistical methods like Wiener Filtering to infer the missing components (Zaroubi et al., 1999, Hoffman et al., 2015, Courtois et al., 2013). These reconstructions (including corrections) allow us to directly access the linear velocity field from Eq. (1.23). It is an excellent tracer of the local large-scale structure. Such reconstructions are therefore the foundations for the constrained simulations Part III of this work is based on. Fig. 1.4 shows streamlines from the Local Universe reconstructed with this method (Courtois et al., 2013). Most of the streamlines in the map are dominated by the so called ”Great Attractor”, the centre of the speculated Laniakea supercluster (Tully et al., 2014), which subsumes most

of the nearby galaxy clusters such as Virgo and Centaurus (as well as an apparent connecting flow system between the clusters). We will introduce some of these clusters in more detail in the following chapter, where we finally move on from the (quasi-) linear regime and mainly gravitational dynamics into the non-linear regime of structure formation.

Chapter 2

The Highly Non-Linear Universe

The previous chapter showed how it is possible to describe the evolution of density perturbations to astonishing detail using relatively simple assumptions. To fully describe the richness of structures in the Universe, one has to, however, consider the non-linear regime where baryonic effects additionally complicate a wholistic analytic description.

2.1 Preface – Virialization

In Section 1.5, we described how it is possible to derive halo statistics purely by analysing the peak structure of the primordial overdensity field. One of the key assumptions in the approach by Press & Schechter (1974) was that there is a universal density threshold δ_c, above which peaks in the density field can collapse into haloes. Once an overdensity decouples from the Hubble Flow, it stops expanding, reaches a maximal size in physical space and turns around to collapse. The required densities for this decoupling to occur can be derived from **spherical collapse theory** (Gunn & Gott, 1972, Gunn, 1977, Peebles, 2020), which assumes a spherical top-hat profile for the initial overdensity (in reality, as previously discussed, this is likely not the case but a good general approximation). While the spherical top-hat profile homologously collapses to infinite density, one can extrapolate the required initial density for turnaround to occur linearly instead, using $\delta t = D(t)\delta_i$. This yields $\delta_c = 1.686$, the value commonly used as the density threshold for the Press-Schechter formalism.

Contrary to a theoretical spherical top-hat density profile, in a real collapsing spherical overdensity, eventually shell-crossing occurs (i.e. the mass inside a given radius $M(r < R)$ is no longer constant). Through the resulting energy exchange between individual shells of the overdensity, the system will eventually relax towards **virial equilibrium**, which means that

$$2\langle T\rangle = -\langle U\rangle, \tag{2.1}$$

in other words the kinetic energy of the system,U, is half of the potential energy T. From simple energy conservation considerations, it is possible to estimate the radius in virial equilibrium to be half the maximal radius. In the simple case of an Einstein-de-Sitter cosmology (recall $\Omega_m = 1, \Omega_\Lambda = 0$), the density contrast at virialization is $\Delta_{\rm vir} = \delta_{\rm vir} + 1 \approx 178$, while in a ΛCDM cosmology this will depend on the cosmological parameters as well as time (Kravtsov & Borgani, 2012). This leads to the most commonly used definition of halo mass

$$M_{\rm vir} = 4/3\pi r_{\rm vir}^3 \Delta_{\rm vir} \rho_{\rm crit} \tag{2.2}$$

the **virial mass** of a halo. Inside the ellipsoidal halo formed by the dark matter, the collisional gas that collapses along with the dark matter can dissipate and radiate away energy. Therefore it can concentrate even further than the dark matter and form complex structures called galaxies.

2.2 The Stars of the Show – Galaxies

Since cold dark matter does not emit light (exceptions might apply depending on the specific dark matter model), the cosmic web described in the previous chapter can only be observed via the distribution of luminous matter in the Universe. In fact, it was the distribution of galaxies around massive clusters and superclusters (e.g. Jôeveer & Einasto, 1978, Bond et al., 1996a), which first confirmed the cell-like structure of the cosmic web. Within their ellipsoidal dark-matter haloes, galaxies come in a rich variety of dynamical and morphological structure.

2.2.1 Morphology

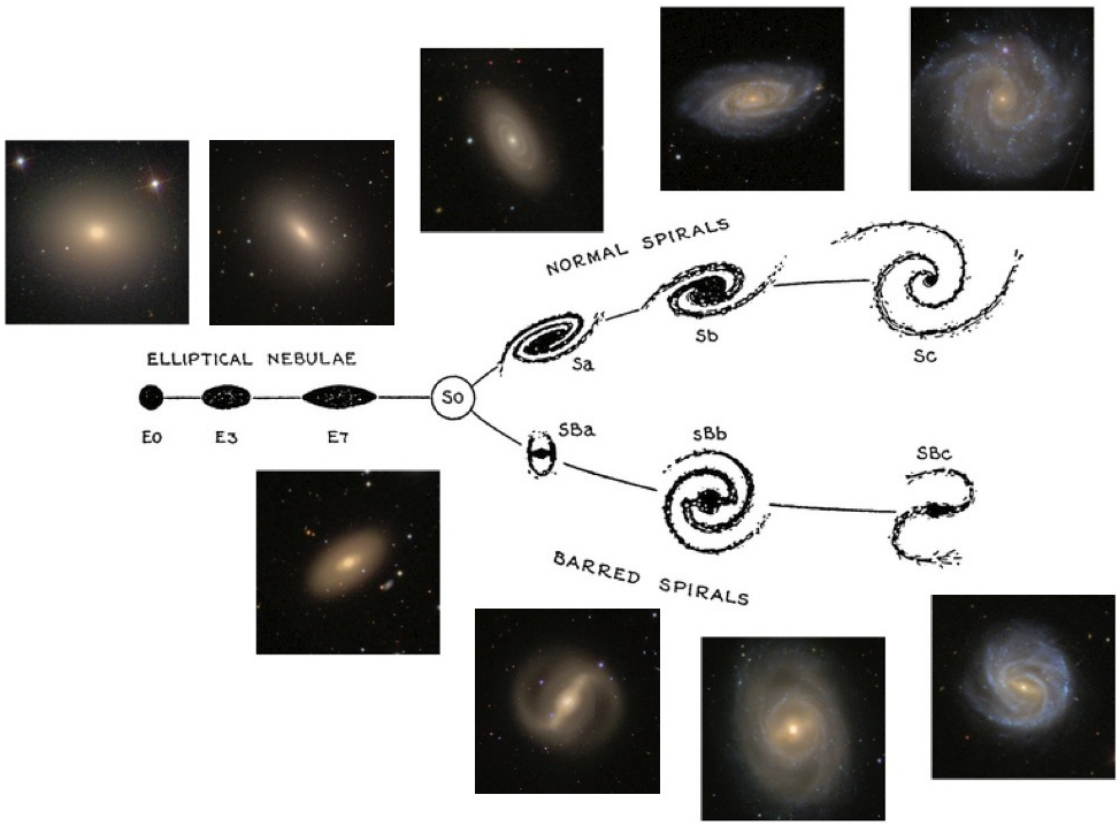


Figure 2.1: The Hubble tuning fork as a morphological classification scheme. Ellipticals are characterized from E0 to E7 accoring to their ellipticity. Spirals are split according to whether they have a bar (SB) or not (S). Image from Masters (2015).

Galaxies form bottom-up from the density fluctuations discussed in the previous chapter and can also combine into groups or even clusters via merging. From a purely morphological perspective, as defined by Hubble (1926) and later refined by Sandage (1961), they can be classified into categories: The simplest type are **Elliptical Galaxies**. These galaxies are completely characterized by their elliptical appearance in optical light and have no distinguishable features. These galaxies are often found as the most massive galaxies dominating the central regions of galaxy clusters or groups, where they are referred to as brightest cluster galaxies (**BCGs**) or brightest group galaxies (**BGGs**) respectively. Hubble erroneously referred to this class of galaxies as ”early-type” galaxies (ETGs), believing them to be the progenitors of the second of galaxies he defined. Today it is established that these ellipticals

are most likely the result of many galaxy mergers erasing the dynamical features found in the other subtypes (González-García & Balcells, 2005, Bournaud et al., 2007). As a consequence, these galaxies mostly have no gas reservoir left to form stars from and show very low star formation rates (e.g. Clemens et al., 2009).

Spiral Galaxies on the other hand, or late-type galaxies (LTGs), are very actively forming stars from a rich gas reservoir. As the name suggests, these galaxies are characterised by their spiral structure, commonly thought to be caused by density waves across a central disk composed of stars and gas (Shu, 2016). They can be further distinguished by their central regions into normal spiral galaxies (S) and barred spiral galaxies (SB), as well as the strength of their central spheroidal component – the bulge – from a to c. All of these categories are summarized in the **Hubble tuning fork** shown in Fig. 2.1. In the following we will outline a more detailed model for a Milky-Way like galaxy. The mass range for galactic haloes spans from $10^9 M_\odot$ for dwarf galaxies to $10^{15} M_\odot$ for the BCGs of galaxy clusters, so there is a large variety in galaxy types and not all galaxies will fit this basic model description.

2.2.2 Structure

The typical dimensions of the galactic halo of Milky-Way-mass ($M_{\text{halo}} \approx 10^{12} M_\odot$) galaxy is on the order of a few hundred kiloparsecs. A general universal profile for a dark matter halo is given by the so-called NFW profile (Navarro et al., 1997):

$$\rho(r) = \frac{\rho_0}{r/r_S(1 + r/r_S)^2} \tag{2.3}$$

where ρ_0 and the scale radius r_S are free parameters of the model. In the presence of baryons however, which can cool and concentrate in the centre, the NFW profile will be modified by the gas and stellar densities within the galaxy itself (Cautun et al., 2020). In the central regions of a Milky Way-like galaxy, the gas (and as a result also the stellar component) has settled into an angular-momentum dominated disc through energy losses from dissipative processes, while the initial angular momentum imparted by the non-spherical gravitational was conserved (e.g. Peebles, 1969, Porciani et al., 2002). The baryonic components of galactic discs can often be modelled using exponential profiles

$$\rho(r, z) \propto exp(-r/r_S - z/z_H), \tag{2.4}$$

again dependent on some characteristic scale radius r_S and a scale height z_H. Usually one distinguishes between an inner stellar disc, a thick outer stellar disc and a gas disk (mostly neutral and molecular hydrogen), each with its own exponential profile.

Modelling the stellar bulge components of disc galaxies is interestingly similar to modelling ellipticals, in that the surface brightness (or correspondingly the projected density) follows a so-called Sérsic law (Sérsic, 1963)

$$I(r) \propto exp(-Ar^{n^{-1}}), \tag{2.5}$$

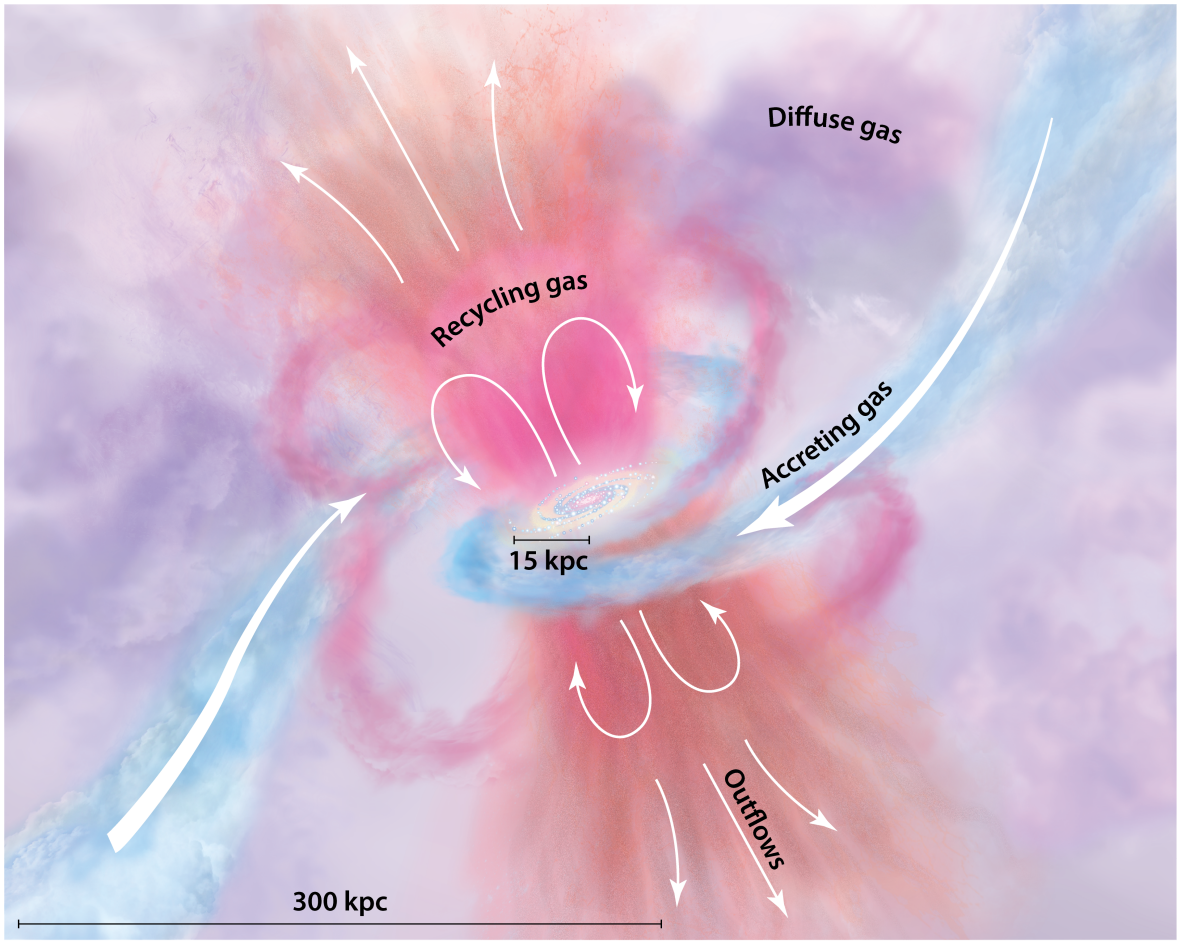
where the Sérsic index $\frac{1}{n}$ sets the curvature of the profile. This is a generalization of the exponential profile. Models of the galactic bulge of the Milky Way often employ such a model for the central component (McMillan, 2017). In the outer haloes of galaxies, in addition to the dominant dark matter profile, the diffuse stellar component can be described by the mathematically equivalent Einasto profile (Remus et al., 2016). There is evidence that this profile even fits the dark matter haloes better than the NFW profile in the better resolved modern cosmological simulations (e.g. Baes et al., 2011, Retana-Montenegro et al., 2012). In larger halos, usually this region contains a number of satellite galaxies, smaller galaxies that still

live in their own potential well within the dark matter halo. There is also a diffuse gas component in the outer region of the galactic halo. The so-called **circum-galactic medium** (CGM) is a complex multi-phase gas environment, with temperatures ranging from $10^4 K$ up to a hot ionized plasma component shock heated to the virial temperature in massive galaxies,

$$T = T_{\rm vir} = \frac{G M_{\rm vir} m_p}{k_B R_{\rm vir}}, \tag{2.6}$$

which is $\approx 10^6 K$ for a Milky Way-mass halo (Tumlinson et al., 2017). These temperatures make this component partially available to X-Ray observations for high mass galaxies (e.g. Zhang et al., 2024b). It forms the boundary layer between the galaxy and its environment. As such, understanding the physics of the CGM is key to understanding how a galaxy forms its stars and how this star formation can be quenched.

2.2.3 The Baryon Cycle



Tumlinson J, et al. 2017.
Annu. Rev. Astron. Astrophys. 55:389–432

Figure 2.2: Schematic of the galactic baryon cycle, showing recycling fountain flows, inflows from the environment and outflows as well as the CGM around a typical active galaxy. The colours distinguish the cold, inflowing gas from the hotter phases in the CGM and the outflows. Figure 1 from Tumlinson et al. (2017).

As a galaxy acquires cold gas, either through cooling from the CGM or from the environment, this gas settles into the aforementioned gas disc due to its angular momentum, where local instabilities fragment the neutral hydrogen into even denser cold clouds. The

enhanced densities, in turn, allow for the formation of molecular hydrogen (Krumholz et al., 2008). As a result, the gas cools even more efficiently through the additional energy states and de-excitation pathways from the molecular structure. Eventually, the gas cloud exceeds a critical mass threshold (Ebert, 1955) and collapses into multiple stars, due to further fragmentation during the collapse. These stars then undergo a mass-dependent evolution, during which they can inject heavier elements $Z > Z_{He}$, or as astrophysicists call them "metals", as well as energy into the surrounding medium. Additionally, massive stars ($8 - 10 M_{\odot}$) can explode as core-collapse supernovae (Janka et al., 2007) at the end of their short (≈5-50 Myr according to e.g. Zapartas et al. (2017)) lifetimes. The supernova events from massive stars drive large and hot outflowing bubbles in the interstellar medium (ISM) (Romano et al., 2025) and re-inject energy on very brief delay timescales due to the short lifetimes. This couples the energy output to the star formation rate. The outflows, in combination with radiative heating from an active galactic nucleus driven by a central black hole, then add to the depletion of the gas reservoir caused by the conversion of gas into stars. In order for the galaxy to maintain a continuous star formation rate, it therefore needs to establish a balance between the gas mass losses and accretion from either the CGM, where previously ejected gas can precipitate back onto the disc by cooling efficiently (Voit et al., 2015), or the cold intergalactic medium (IGM).

This interconnection of star formation, outflows, cooling, and inflows leads to the standard picture established by (Tumlinson et al., 2017), of the so-called "galactic fountain". We show the famous illustration, which admittedly has been used in countless works and presentation for its conciseness in Fig. 2.2. The balance can be disrupted by a number of processes: Galaxies can undergo mergers, which disrupt their gas reservoir, fall into larger structures like groups or clusters, which removes gas via ram pressure stripping or they can be cut off from cold inflows by their hot atmosphere. The latter is especially true for large halo masses, where an accretion shock can effectively stabilize, leading to the picture of hot mode accretion for massive haloes at late times (Birnboim & Dekel, 2003, Dekel & Birnboim, 2006). How efficiently the hot atmosphere builds up and can stop the cold inflows can also depend on the density of the surrounding cosmic web, with dense inflows potentially even penetrating the hot atmospheres of massive galaxies (Brooks et al., 2009). This couples the baryon cycle sensitively to the large-scale environment (among other factors like feedback efficiency).

2.2.4 Galaxies and their Environment

Both theoretical and observational studies have shown the distance of galaxies from the cosmic web filaments to affect stellar masses and star formation rates (e.g. Laigle et al., 2018) as well as the metal content of galaxies. However, the degree to which the complex gas flows in the outskirts of galactic haloes are dictated by the large-scale density field is still not completely understood. In particular the removal of gas via outflows is highly model dependent from a theoretical perspective (e.g. Tanner et al., 2025). Additionally, how hot outflows interact with the inflows from the cosmic web is a key puzzle piece to constraining galactic feedback models and baryon fractions as they directly affect the galaxies' gas reservoirs. One of the key questions this work aims to address is therefore how the structure of the inflow field of galaxies can be quantified from a numerical perspective and how this field evolves with time. In Chapter 6, we will also explore how these flow fields are connected to the star formation rate and kinematical properties of field galaxies. For galaxies already infalling into a node of the cosmic web, their proximity to the structure can furthermore affect the amount of mergers they undergo during infall as well as the amount of ram pressure their gas is subjected to from the hot group or cluster atmosphere.

From a purely gravitational perspective, the angular momentum of a collapsing halo is

tied to the large-scale structure around it. Tidal torque theory connects the spin of a galactic halo, and with it the galaxy itself, to the tidal fields from the environment torquing the halo as it collapses (Porciani et al., 2002, Neyrinck et al., 2020, López et al., 2025). However it is still a matter of debate how clear this signal really is in terms of the galactic spin and disc orientation, because baryonic processes and off-axis mergers can gradually erode this primordial signal.

2.3 The Giants – Galaxy Clusters

At the nodal intersections of the largest filaments of the cosmic web sit the most massive bound structures in the Universe: Galaxy clusters are commonly defined at halo masses $10^{14} - 10^{15} M\odot$, which from Eq. (2.6) implies that they are also host to some of the hottest gas ($T_{\rm vir} = 10^7 - 10^8 K$). These cosmic giants can contain up to thousand member galaxies of different sizes and types. Their physical dimensions are in the Megaparsec range with $r_{\rm vir} \approx 1 - 2$ Mpc for the largest of these objects.

2.3.1 Stellar Component

At the centre of a galaxy cluster sits one, or even multiple, BCGs, which are usually giant elliptical galaxies, or, to be more precise, the cD subtype (Zhao et al., 2015), which shows a more diffuse stellar morphology than conventional elliptical galaxies. Their stellar masses are in the $M_\star = 10^{12}$ range (Lidman et al., 2012, Ragone-Figueroa et al., 2018). This BCG is additionally enveloped in a similarly diffuse, but dynamically distinct component, the intra-cluster light or **ICL**, also known from theory as the diffuse stellar component (DSC) (Dolag et al., 2010, Remus et al., 2017). The stellar component of clusters contains important information about their formation history, as the fraction of mass in this component compared to the total stellar mass in the region is a direct indication of how much time the cluster environment had to destroy and cannibalize infalling galaxies (Kimmig et al., 2023, 2025a).

2.3.2 Intra Cluster Medium

Due to its high temperatures, the gas atmosphere of galaxy clusters, the intra-cluster medium (**ICM**) is readily available to X-Ray observations from the thermal Bremsstrahlung emitted by the hot plasma (Merloni et al., 2012, Hitomi Collaboration et al., 2018, XRISM Science Team, 2022). Like the CGM, this is a complex dynamical environment governed by physical processes on vastly different scales:

The interaction of a galaxy cluster with its environment, and especially the mergers such a system undergoes to reach its high mass, continuously perturb the ICM, generating strong shocks even in the inner regions of the halo. In the outskirts of a cluster, massive mergers can significantly push the accretion shock beyond the virial radius (Zhang et al., 2020). Additionally the gravitational perturbations from mergers create sloshing motions in the gas, which causes sharp discontinuities in temperature and, consequentially, X-Ray surface brightness called **cold fronts** (Roediger et al., 2012). In combination with jets from **active galactic nuclei** (AGN) in the central BCG and ram-pressure stripped gas from infalling galaxies, these processes make the ICM very rich in structure. This is usually highlighted by subtracting the simple β-model (Cavaliere & Fusco-Femiano, 1976, Ettori, 2000) from observed surface brightness maps, which describes the general density (respectively surface brightness) profile of the cluster. The presence of non-thermal plasma from the central AGN jets, as well as jets from infalling galaxies, further enhance this complexity. Fig. 2.3 shows these components for the Perseus cluster in the Local Universe. In the X-Ray composite, which shows

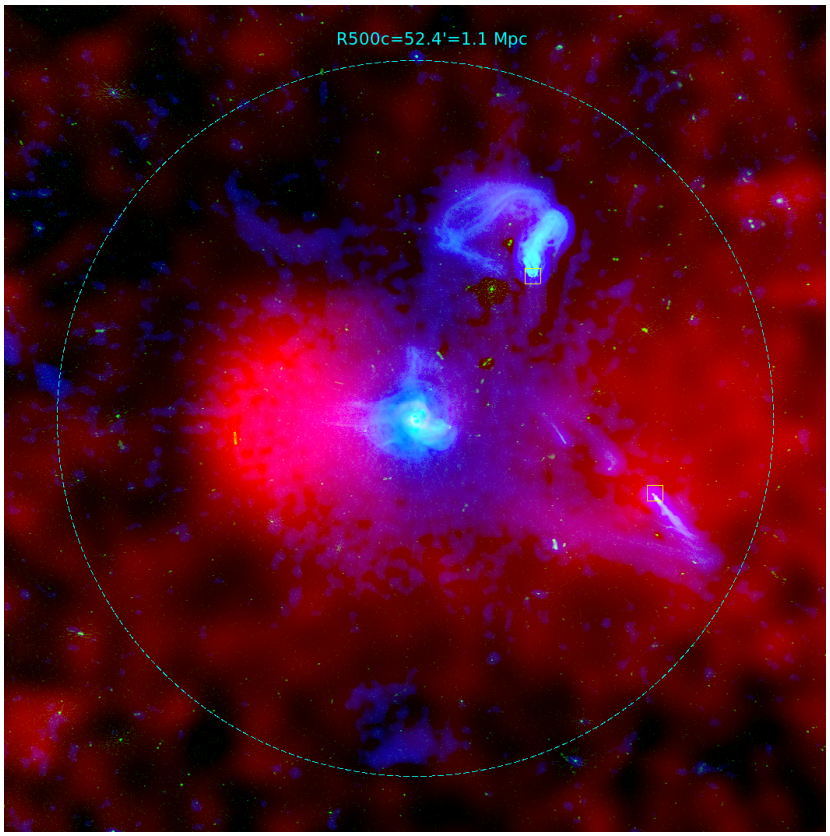


Figure 2.3: Composite image of the Perseus cluster, combining X-Ray data from eROSITA, Chandra, XMM Newton in red (a smoothed equal weighted composite, with a radial weight to ensure the center is dominated by the Chandra image and a background profile already subtracted) and the LOFAR radio emission ovelayed in blue. Figure 7 from Churazov et al. (2026).

the X-Ray surface brightness excess in red, one can see prominent substructures enveloping the core of the cluster to the east and the west. These are possibly remnants of past mergers along this direction, triggering a sloshing spiral of displaced ICM gas. Two infalling radio galaxies and their ram-pressure stripped radio tails can be seen in the blue colours indication radio brightness. The stripped tails form complex patterns, indicating the motion of the infalling structures relative to the cluster gas. Finally, in the dense centre of the cluster the activity of the central AGN can be seen in both radio and X-Ray emission, with prominent X-Ray cavities from the AGN, as well as a diffuse radio halo enveloping the centra BCG (NGC 1275) (van Weeren et al., 2024). The merging activity, as well as the central AGN, can be expected to inject turbulence at small scales as well as at larger scales into the ICM. Understanding the degree of turbulence in galaxy clusters, as well as how the turbulence cascades and dissipates, is an important endeavour for astrophysics and cosmology, because cluster masses are usually inferred from hydrostatic equilibrium assumptions. Non-thermal pressure components, such as turbulence and bulk flows from sloshing, can significantly bias the observed masses (Ettori & Eckert, 2022, Wicker et al., 2022, Lebeau et al., 2024b). We will revisit the turbulent structure of the ICM briefly in Chapter 13.

2.4 Dynamical State

Despite the plentiful activity in Fig. 2.3, the Perseus cluster has been historically counted among the **cool-core** clusters (Churazov et al., 2003, Sanders et al., 2004). These clusters are

characterised by a very dense core region (the ICM density increases from $n_e = 10^{-4}\text{cm}^{-2}$ to 10^{-2}cm^{-2} towards the central region (Ota et al., 2013)), allowing the cooling times to become short enough ($O(Gyr)$) for the gas to cool efficiently via X-Ray continuum emission. This also triggers a steady cooling flow into the cluster centre, with cooling gas contracting and lowering pressure support for the surrounding gas. This, in turn, allows the external gas to sink closer to the core and cool (Sarazin & White, 1987, Fabian, 1994). Galaxy clusters with these properties are usually assumed to be more dynamically relaxed, having formed most of their mass at early times and encountered no major mergers in recent times (Hudson et al., 2010). These hydrodynamic properties can be expected to coincide with other tracers of a cluster's dynamical histories, like the aforementioned intra cluster light fraction (Kimmig et al., 2025a).

Overall, the rich physics from gravitational dynamics to cooling, star-formation, non-thermal processes, turbulence and viscosity make galaxy clusters ideal laboratories to test current astrophysical models.

2.5 Sunyaev Zeldovich Effect - Imprints from the Neighbourhood

Galaxy clusters also impact the relic radiation from the CMB: Due to their high temperatures and pressures, cold photons from the CMB can be Compton up-scattered off of energetic ICM electrons. This process causes spectral distortions in the CMB power spectrum and is called the **Sunyaev Zeldovich** (SZ) effect (Zeldovich & Sunyaev, 1969, Sunyaev & Zeldovich, 1970). It is parametrized by the Compton-y parameter, which depends on the line of sight integral of the electron pressure:

$$y(\Omega) = \frac{\sigma_T}{m_e c^2} \int_0^{r_{\text{CMB}}} dr\, p_e(\Omega, r), \tag{2.7}$$

where σ_T is the Thomson cross section and m_e the electron mass. The induced temperature change in the CMB is then given by

$$\frac{\Delta T^{\text{tSZ}}}{T_{\text{CMB}}}(\nu, \Omega) = g(\nu) y(\Omega), \tag{2.8}$$

with $g(\nu)$ encoding the spectral dependence and constant across the sky. Due to the direct pressure dependence, this allows for X-Ray independent studies of the ICM structure (Cavaliere & Lapi, 2014, Salvati et al., 2019, Walker et al., 2019), superclusters (Aghanim et al., 2024) and even hot filaments connecting galaxy clusters (Bonjean et al., 2018). When there is a bulk motion in the gas (e.g. due to peculiar motion of the whole system or intrinsic rotation), there is the secondary kinematic Sunyaev-Zeldovich effect (**kSZ**) quantified by

$$\frac{\Delta T^{\text{kSZ}}}{T_{\text{CMB}}}(\Omega) = -\frac{\sigma_T}{c} \int_0^{r_{\text{CMB}}} dr\, \Omega \cdot v_e(\Omega, r). \tag{2.9}$$

The kinematic effect is mostly subdominant, but it allows for direct measurements of cluster peculiar velocities (Haehnelt & Tegmark, 1996). As we will discuss in more detail in Chapter 13, the Sunyaev-Zeldovich effect is especially sensitive to nearby galaxy clusters due to their large angular size on the sky.

2.6 Non-Linearity and the Argument for Simulations

The observations of fluctuations in the CMB discussed in Section 1.2 provide an accurate statistical description of the starting conditions for structure formation in the Universe. Since

the initial conditions of the Universe are Gaussian Random fields to very good accuracy, knowledge of the power spectrum $P(k)$ of density and velocity fluctuations (which are linearly related on large scales and at early times) constrains realistic density and velocity fields at a starting time $z_{\rm ini}$. At early times and on large scales, the perturbations in the density fields and velocity fields evolve in a linear fashion and the quasi-linear Zeldovich approximation (Zel'dovich, 1970) allows an analytical description even beyond the linear scale (see Part I). Even higher order dynamics can be included using Lagrangian Perturbation Theory (Buchert, 1993a,b). However to accurately model the full multi scalar evolution of the Universe and capture structure formation processes from the cosmic web to the formation of galaxies with all their rich dynamics simultaneously, it is necessary to discretize the problem and solve the dynamics numerically. Additionally, the hydrodynamical interactions of the baryonic component cannot be neglected at smaller scales. Techniques like baryon pasting (e.g. Osato & Nagai, 2023), which semi-analytically model baryons on simulated dark matter haloes, cannot account for the fact that baryons are tightly coupled to the gravitational evolution on larger scales. In order to study the motions of matter across scales from superclusters to galaxies, as this work aims to do, **Hydrodynamical Cosmological Simulations** are an important theoretical tool.

Part II

Characterizing accretion flows of halos in cosmological simulations

Chapter 3

Flows in a Box: Cosmological Simulations

Gleich mit jedem Regengusse
Ändert sich dein holdes Tal,
Ach, und in demselben Flusse
Schwimmst du nicht zum Zweitenmal.

–Goethe, *Dauer im Wechsel*

In Part I, we have highlighted the degree to which it is possible to understand multi-scale structure formation analytically and where the usefulness of feasible approximations ends. This emphasized the need for highly resolved cosmological simulations as a tool to study non-linear structure formation and the coupling of physical processes at vastly different scales. In this chapter, we discuss the successes and challenges of such simulations using the Magneticum Pathfinder suite, the mainstay of the numerical analysis in the first part of this thesis.

3.1 Numerical Schemes: General

In order to solve the coupled differential equations describing the full non-linear evolution of a patch of the universe, one needs to discretize them. Temporal integration is introduced by updating the state of the system in intervals given by a discrete time step Δt. To ensure numerical stability, this time step needs to be sufficiently small. The gravitational evolution of the system is then usually computed by discretizing the mass within the simulation volume (set by Ω_m) into N pseudo particles.

3.2 Gravity

The dynamics of the collisionless stellar and dark matter particles can then be computed by numerically integrating either the direct Newtonian particle-particle forces

$$F_i = \sum_{j \neq i} \frac{m_i m_j}{|\mathbf{r_i} - \mathbf{r_j}|^2}, \tag{3.1}$$

or by computing a grid-based gravitational acceleration by solving the Poisson equation

$$\nabla^2 \Phi(\mathbf{r}) = 4\pi G \rho(\mathbf{r}), \tag{3.2}$$

where Φ is the gravitational potential, in Fourier space. OpenGadget3 and P-GADGET3, the codes used in this work, combine these two approaches into a so-called Tree-Particle Mesh (PM) approach (Springel, 2005, 2010). In this method, the gravitational forces are split into long-range and short-range forces. The short-range forces are calculated by putting the particles on an oct-tree (Barnes & Hut, 1986) for efficient computation. The simulation volume is recursively split into cubes until the lowest level, where each sub-cube only contains a single particle. To compute the force on a single particle from a given subdomain it is then decided via a force accuracy estimation, whether the subdomain needs to be "opened". This ensures that the sum in Eq. (3.1) has as few terms as possible since the contributions from distant particles are summarized by the contribution of a higher-level subdomain.

The long-range forces are computed by putting the particles on a grid or mesh and solving Eq. (3.2) via

$$k^2\Phi(\mathbf{k}) = 4\pi G\rho(\mathbf{k}). \tag{3.3}$$

The transition between long range and short-range forces is set by a specific truncation scale $r_{\rm cut}$ (e.g. Bagla & Ray, 2003).

3.3 Hydrodynamics

Additionally it is necessary to account for the hydrodynamical forces for the baryonic component, specifically the gas. Solving for the hydrodynamical forces can be achieved with two approaches: **Grid-based** hydro-solvers solve the (inviscid) fluid equations in their Eulerian form:

$$\frac{\partial\rho}{\partial t} = -\nabla\cdot\rho\mathbf{v} \qquad \text{(Continuity)} \tag{3.4a}$$

$$\frac{\partial\rho\mathbf{v}}{\partial t} = -\nabla\cdot(\rho\mathbf{v}\times\mathbf{v} + p) \qquad \text{(Euler Equation)} \tag{3.4b}$$

$$\frac{\partial\rho e}{\partial t} = -\nabla\cdot(\rho e + p)\mathbf{v} \qquad \text{Energy Conservation} \tag{3.4c}$$

where ρ and p are the density and pressure of the fluid and the energy density, e, is given by the sum of the kinetic and internal energy densities $e = u + \mathbf{v}^2/2$ (see Groth et al., 2023, and references therein). Since this is an underdetermined system of equations (6 variables, 5 equations), additionally an equation of state is assumed. For an ideal gas, this is $p = (\gamma-1)\rho u$, where γ is the polytropic index (5/3 for a monoatomic gas). Eulerian codes solve these equations on a discrete grid. Examples for such codes are the adaptive mesh refinement code RAMSES (Teyssier, 2002) or Athena (Stone et al., 2008) and the follow-up Athena++ (Stone et al., 2020).

The other philosophy is **Lagrangian Hydrodynamics**. Here instead of computing the hydrodynamics on a grid, one follows the evolution of individual fluid parcels instead. This approach is easily combined with the N-Body approach for gravity, since the Lagrangian hydrodynamical formalism just adds hydrodynamical accelerations to the gas particles. Transforming between the two formalism amounts to a simple transformation of the differential $d/dt_L = \partial/\partial t_E + \mathbf{v}\cdot\nabla$, where the subscripts indicate the Lagrangian and Eulerian derivative respectively. Inserting this into Eq. (3.4) yields the Lagrangian version of these equations.

The simulation codes employed in this work use a **Smoothed Particle Hydrodynamics** (SPH) prescription to calculate the hydrodynamical forces in a Lagrangian way. In this formulation, the density at each Lagrangian particle position $\mathbf{x_i}$ is smoothed using a kernel function via

$$\rho(\mathbf{x_i}) = \sum_j m_j W(\mathbf{r}_{i,j}, h_i), \tag{3.5}$$

	Box0	*Box1a*	*Box2b*	*Box2*	*Box3*	*Box4*	*Box5*
Volume [Gpc^3]	56.35	2.06	0.75	0.125	0.006	0.00032	0.000017
Boxlength [Mpc]	3820	1300	910	500	180	68	26
Boxlength [h^{-1}Mpc]	2688	896	640	352	128	48	18
mr	2×4536^3	2×1512^3		2×594^3	2×216^3	2×81^3	
hr			2×2880^3	2×1564^3	2×576^3	2×216^3	2×81^3
uhr					2×1536^3	2×576^3	2×216^3
xhr							2×576^3

Table 3.1: Overview of the different box sizes and resolutions for the Magneticum Pathfinder runs. The particle number is given as $N_{\rm dm}+N_{\rm gas}$, hence the factor of 2. Unfilled boxes around a given resolution indicates a run that has not run until $z = 0$. Table 1 from (Dolag et al., 2025).

where $\mathbf{r}_{i,j}$ is the separation between particle i and j, $W(..)$ is the smoothing kernel and h_i is the characteristic smoothing scale. The smoothing scale is computed from the average neighbour density via

$$\frac{4\pi}{3}\rho_i h_i = \langle m\rangle_{\rm Ngb} N_{\rm Ngb}, \tag{3.6}$$

where the subscript Ngb indicates a fixed number of neighbours. This is a simulation parameter. The Magneticum Pathfinder suite discussed in this work uses $N_{\rm Ngb} = 295$ (Dolag et al., 2025). The smoothing function employed is the so called Wendland C^6 function, a polynomial function with compact support and numerically advantageous Fourier properties (Dehnen & Aly, 2012).

There are also hybrid approaches between Eulerian and Lagrangian hydrodynamics like the mesh-less finite mass method (**MFM**) which was implemented into OpenGadget3 by Groth et al. (2023). As we focus on the runs using SPH in this work, we will discuss exclusively these simulation methods in the following.

3.4 The Magneticum Suite

The work presented in Sections 3.4-3.7 has been partially submitted and accepted as Dolag et al. (inc. Seidel) 2025, "Encyclopedia Magneticum: Scaling Relations from Cosmic Dawn to Present Day"

The Magneticum Pathfinder suite is comprised of seven cosmological volumes ranging from a volume of $V \approx (3.8\text{Gpc})^3$ to $V \approx (26\text{Mpc})^3$. Fig. 3.1 provides an overview of these volumes by mapping the dark matter density within a slice trough each box. The smallest volume, *Box5*, was omitted due to its extremely small size relative to the largest volume, *Box0*. For the largest simulation, *Box0*, we additionally show the gas density in the bottom half of the upper panel of the figure. Each of these volumes were then run in a dark matter-only version at multiple different resolutions as well as a full physics simulation including hydrodynamics and star formation physics. Table 3.1 provides an overview of all available runs in the suite listing the Box properties as well as the particle numbers for each available resolution. The particle masses resolution is set by the cosmology: For dark matter and baryons respectively, the box contains a mass of $M_x = \Omega_x \times \rho_{crit} \times V_{\rm Box}$, resulting in a particle mass of $m_x = M_x/N_x$. Throughout the Magneticum Pathfinder suite, the assumed cosmology is adapted from the WMAP-7 parameters (Komatsu et al., 2011): $h = 0.704$, $\Omega_m = 0.272$, $\Omega_\Lambda = 0.728$, $\sigma_8 = 0.809$, $n = 0.963$ (excluding the multi-cosmology realizations of *Box1a*). Magneticum Pathfinder uses an equal number of gas and dark matter particles, in contrast to cosmological simulation projects like the Flamingo simulations (Schaye et al., 2023). For a discussion of potential drawbacks of the resulting unequal masses, see Ludlow et al. (2019). The particle

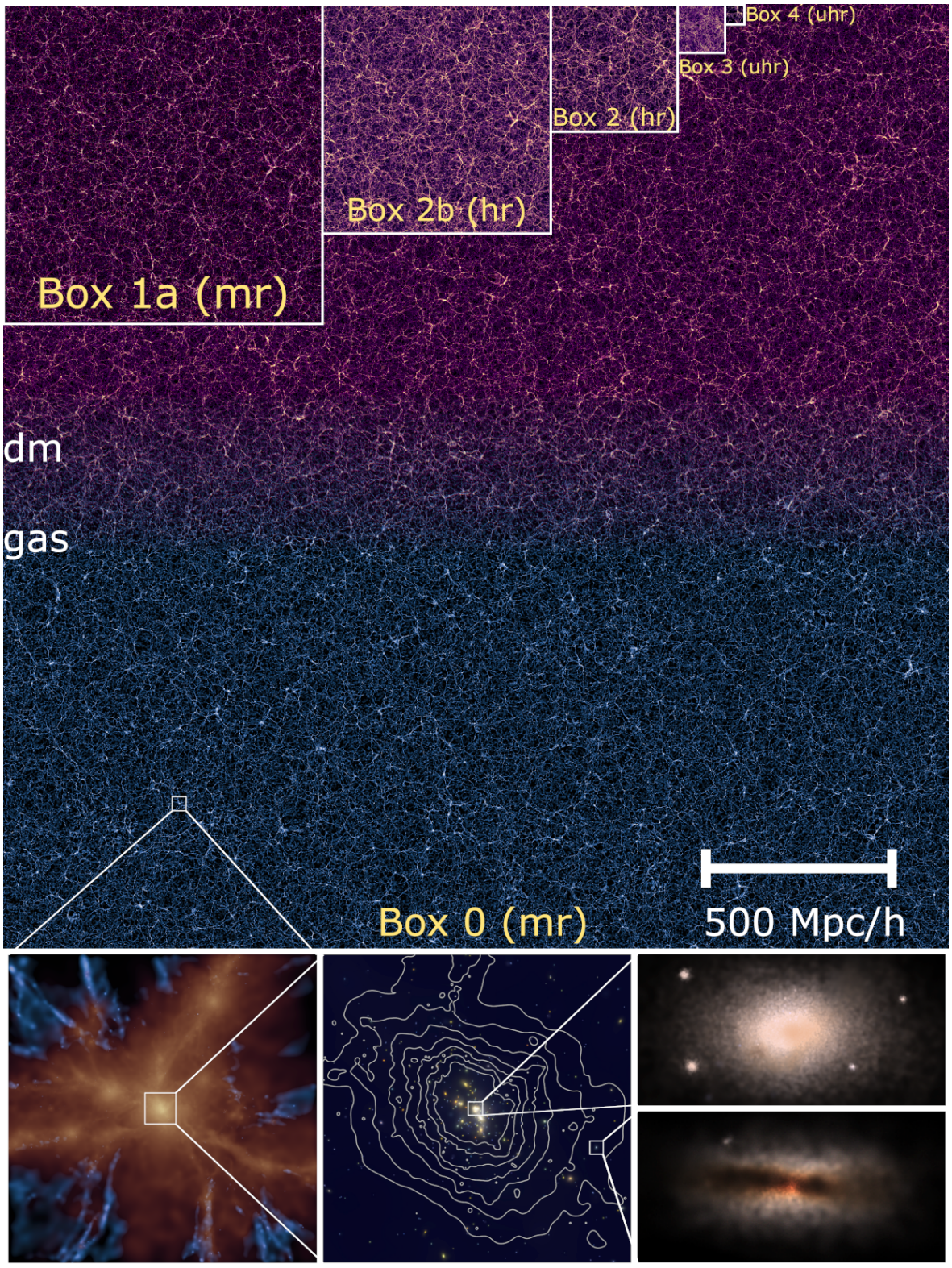


Figure 3.1: Overview over the scales covered by the MAGNETICUM PATHFINDER suite of cosmological simulations from Gpc to kpc scales. *Top panels:* The simulation volumes of MAGNETICUM PATHFINDER to scale. *Box0* transitions from dm density to gas density at the border between the magma colour-map and the blue colours. *Bottom left:* Zoom-in into a massive galaxy cluster in *Box2b*. Hot gas is shown with the red-yellow colours and cold gas in blue ($T_{\rm cut} = 10^4 K$). *Bottom middle:* The same galaxy cluster, showing the stellar density visualized with Splotch (Dolag et al., 2008) and the gas density indicated by the white contours. *Bottom right:* Two galaxies from *Box4* generated with the dust radiative transfer code SKIRT (Baes et al., 2011). Part of my personal contribution to Dolag et al. (2025).

	$\epsilon_{\mathrm{gas/DM}}$ $[h^{-1}\mathrm{kpc}]$	ϵ_* $[h^{-1}\mathrm{kpc}]$	m_{DM} $[h^{-1}M_\odot]$	m_{gas} $[h^{-1}M_\odot]$	m_* $[h^{-1}M_\odot]$
mr	10	5	1.3×10^{10}	2.6×10^{9}	6.5×10^{8}
hr	3.75	2	6.9×10^{8}	1.4×10^{8}	3.5×10^{7}
uhr	1.4	0.7	3.6×10^{7}	7.3×10^{6}	1.8×10^{6}
xhr	0.45	0.25	1.9×10^{6}	3.9×10^{5}	1.0×10^{5}

Table 3.2: Softening lengths (ϵ_X) and masses (m_X) of dark matter, gas and stars in the Magneticum Pathfinder simulations. Table 2 from Dolag et al. (2025)

mass of each simulation, its **mass resolution** is the most important resolution characteristic of an SPH simulation. Additionally the gravitational **softening lengths** determine the scale to which the gravitational potentials are smeared out (see the discussion about Plummer Profiles in Section 3.2). These quantities are listed in Table 3.2 for each of the different resolutions in the Magneticum Pathfinder suite.

All Magneticum Pathfinder simulations were performed with an updated version of the parallel cosmological Tree-PM code GADGET-2 (Springel, 2005). The code P-GADGET3, has since been further evolved and is planned for a public release as OpenGadget3 (see also Groth et al., 2023).

Modifications to the hydro solver include a modified smoothed-particle hydrodynamics scheme, with modifications such as improved thermal conduction (Dolag et al., 2004) and a low-viscosity formulation of SPH (Dolag et al., 2005c, Beck et al., 2016) specifically to improve the modelling of ICM physics.

3.5 Sub-Grid Modelling

While gravitational and hydrodynamical forces can be computed at the particle level following the Lagrangian formulation in Section 3.2 and Section 3.3, galaxy formation involves physical processes that cannot be fully resolved at the current level of computational power. In order to simulate galaxy evolution in a cosmological box, it is therefore necessary to rely on **sub-grid modelling**. The general idea is to treat each gas and star particle as an ensemble representing a population of stars or baryons and couple the ensemble state variables, like temperature, pressure or chemical composition to physical processes on scales smaller than the hydrodynamical resolution (which depends on the smoothing h) via semi-analytical or numerical models. We give a brief summary here for the most important subgrid models, for an extensive overview refer to Dolag et al. (2025) and the references therein.

Cooling The cooling rate for each gas particle is calculated as a function of temperature and metallicity following Wiersma et al. (2009). Cooling rates for each element traced by the simulation are pre-tabulated from CLOUDY (Ferland et al., 1998) simulations of an optically thin gas in photo-ionization equilibrium, taking into account background radiation from the CMB and UV/X-ray emission from AGN and galaxies.

Star Formation Magneticum Pathfinder employs the two-phase model from Springel & Hernquist (2003): Each gas particle is treated as a combination of hot ISM and cold gas clouds, with the latter forming from the former when a set density threshold is reached. The cold clouds subsequently form stars on a timescale of 1.5 Gyrs. A big advantage of the Magneticum Pathfinder model is that not all of the cold gas is converted into a star particle

in a single event. To account for molecular clouds converting their mass into stars with imperfect efficiency, a single gas particle can undergo up to 4 separate star formation events, before its mass is completely transferred to the stellar component.

Stellar Populations Each star particle then represents a population of stars with a set initial mass function (Chabrier, 2003). This population is evolved in time, accounting for mass losses from AGB stars, SNIa, and SNII and releasing metals and supernova energy into the surrounding medium. The treatment of metals is extensively described by Tornatore et al. (2007) with extensions of the metal tracing described by Dolag et al. (2017).

Stellar Feedback The model introduced by (Springel & Hernquist, 2003) includes stellar winds driven by SNII as an effective stellar feedback mechanism. This model has effectively two free parameters. The mass gain rate of the wind is determined by

$$\dot{M}_W = \eta \dot{M}_\star \tag{3.7}$$

where η is the mass loading factor, determining the outflow rate as a function of the star formation rate. The second parameter is the velocity of the wind v_W. This determines the kinetic energy injected into the wind via

$$\frac{1}{2}\dot{M}_W {v_W}^2 = \chi \epsilon \dot{M}_\star \tag{3.8}$$

where $\chi\epsilon$ is assumed as an effective supernova energy per star formation rate at 10^{51} erg. Through the two equations, setting one of these parameters effectively sets the second one. For Magneticum Pathfinder the standard choice is to set the wind velocity to a fiducial value of $v_W = 350$km/s.

Black Hole Model The AGN model is based on the model described by Springel et al. (2005). BH particles themselves are collisionless and coupled to their surroundings via accretion of mass, injection of feedback energy and merging with other black hole particles. Accretion is described by the Bondi-Hoyle-Lyttleton approximation (Hoyle & Lyttleton, 1939, Bondi & Hoyle, 1944, Bondi, 1952):

$$\dot{M}_\mathrm{B} \propto \alpha \rho / (c_\mathrm{s}^2 + v^2)^{3/2} \tag{3.9}$$

with c_s, ρ, v the sound speed, density and relative velocity of the surrounding gas with respect to the black hole. α is a boost factor that accounts for the lack of resolution to describe the gas density around the actual black hole and is usually set to 100 (Springel et al., 2005). Additionally the black hole accretion rate is always limited by the Eddington accretion rate, i.e. the accretion rate at which the radiation pressure is equal to the gravitational force of the black hole. The energy output of the black hole is then parametrized as

$$\dot{E}_f = \epsilon_r \epsilon_f \dot{M_\bullet} c^2 \tag{3.10}$$

where ϵ_r, ϵ_f are the radiative efficiency and the thermal fraction respectively. ϵ_r is set to 0.2 in order to reproduce observations for large black hole masses (Davis & Laor, 2011) and ϵ_f is set to 0.15. Following Fabjan et al. (2010), when the accretion rate of the black hole is below a factor of 10^{-2} of the Eddington rate, the black hole switches into radio mode, which boosts ϵ_f by a factor of 4 to account for the efficient heating of AGN jets via hot bubbles. In further deviation from the model by Springel et al. (2005), the black hole mass growth is diminished by the feedback resulting from the accretion rate at each time step. Magneticum

Pathfinder also implements an explicit dynamical friction term based on the properties of the surrounding halo in order to physically keep the black hole in the center of galaxies.

For *Box3/uhr*, several improvements to the black hole model were introduced by Steinborn et al. (2015). The main strength of the model is the differing treatment of cold and hot gas. α is lowered to 10 for the hot gas, while the boost factor is kept at the original 100 for the cold gas, due to the more efficient accretion of cold gas from cold streams. Additionally, the transition between the two feedback modes described above is smoothed and coupled to the black hole mass instead of only the accretion rate. These changes better regulate the BH mass growth in galactic environments of differing thermodynamical and kinematic properties, and ultimately achieve more realistic stellar masses at high redshifts (see Section 3.8, Steinborn et al. (2015), Kimmig et al. (2025b), Remus & Kimmig (2025)).

3.6 (Sub-)Structure Identification

P-GADGET3 includes an on-the-fly structure finding toolkit, SubFind (Springel et al., 2001). The general idea is to run a so-called Friends-of-Friends (FOF) algorithm on particles within the simulation, grouping all particles within a linking length l into a group in a transitive fashion (hence the name). A standard value for the linking length is $0.2d_{\mathrm{part}}$, where d_{part} is the mean particle separation. Eke et al. (1996) showed that scaling this linking length by Δ_c/Ω_m, where Δ_c is the critical density and, together with Ω_m, factors in the cosmology, these FOF groups reproduce the overdensity predicted for virialized haloes in the spherical collapse model. Therefore, Magneticum Pathfinder uses this scaled linking length to obtain FOF haloes. Substructures are then identified within these FOF haloes according to Dolag et al. (2009) by identifying saddle points in the smoothed density field obtained from all particle species. An additional unbinding step based on the potential of each substructure ensures the persistence of the sub-haloes obtained this way. Because the density identifies not only dark matter systems but also stellar overdensities and gas-rich subhaloes, the subhalo catalog is analogous to the galaxy population of the simulation. The most massive subhalo is commonly referred to as the *main* sub-halo, in a cluster mass halo this corresponds to the BCG, for smaller haloes in the field, this can simply be considered an independent field galaxy. SubFind also computes a number of properties for subhaloes and haloes. An example is the virial mass M_{vir}, the mass within the sphere of radius R_{vir} around a halo which encloses a spherically averaged density corresponding to the virial density

$$\rho_{\mathrm{vir}} = \Delta_{\mathrm{vir}}(z) \times \rho_{\mathrm{crit}}. \tag{3.11}$$

Here, $\Delta_{\mathrm{vir}}(z)$ is obtained from the cosmology according to the fitting formula given by Bryan & Norman (1998). Unless stated otherwise, quantities like $M_{500,gas}$ refer to these outputs from the structure finding with the subscript indicating the density criterion used (in this example 500 times the critical density) as well as the particle species (in this case the gas mass). No particle type subscript indicates that the total mass within that density contour is used (e.g. M_{vir}). Using these tools we can now approach structure formation in the Magneticum simulations and test how well the simulations agree with observations as well as theory.

3.7 Fundamentals: Scaling Relations in Numerical Simulations

Scaling relations are a powerful tool to analyze how structure formation proceeds in a cosmological simulation. Where linear theory (see Section 1.5) gives useful predictions for the

expected distribution and growth of haloes in a cosmological volume over time, this provides a possibility to study the effects of non-linearities and baryonic effects on the global evolution of dark matter haloes. For the baryonic component, which can be directly observed, it can then be verified how well the hydrodynamical and especially sub-grid modelling actually reproduces the galaxy populations observed in the real Universe (assuming that the purely gravitational part is accurate enough, which is also dependent on the validity of the underlying cosmological assumptions). In this section, we therefore focus on the most general scaling relations in each of the particle species described in the previous section.

The Halo Mass Function

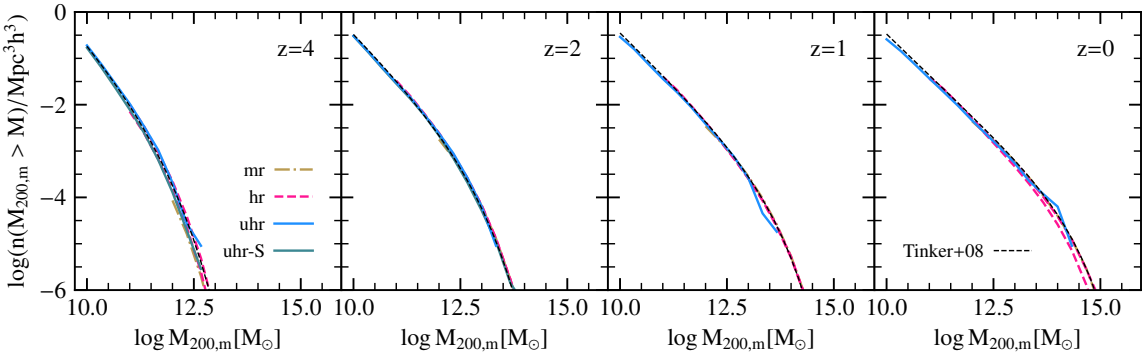


Figure 3.2: The evolution of the HMF for the different Magneticum Boxes compared to analytical expectations. For the simulated mass functions the line colours indicate the different runs at $z = 4, 2, 1, 0$ respectively. The gray dashed line shows the theoretical prediction given by the HMF defined by Tinker et al. (2008). Part of my personal contribution to Dolag et al. (2025) (see Fig. 8).

Among the most well established scaling relations used to assess structure formation in the Universe is the halo mass function (HMF). This function captures the purely gravitational part of structure formation in the Universe. It has a long theoretical history beginning with the Press-Schechter Mass Function Press & Schechter (1974) (see also Section 1.5), which was a surprisingly accurate prediction given the simplicity of its assumptions. A critical feature of this early model and is subsequent elaboration (Bond et al., 1991, Sheth et al., 2001) was the sensitivity on cosmological parameters, which makes it a powerful tool for inferring cosmological information from cluster samples (Bocquet et al., 2016). On the small scale end, the impact of baryonic physics has been significantly constrained using cosmological simulations and has resulted in even more accurate mass functions (Tinker et al., 2008, Bocquet et al., 2016). Reproducing these HMFs is a valuable first baseline test for any cosmological simulation.

Fig. 3.2 shows the HMF for the Magneticum Pathfinder simulations *Box0/mr* (gold dash-dotted lines), *Box2b* and *Box2/hr* (pink dashed lines), and *Box4/uhr* fiducial BH (blue solid lines) as well as *Box3/uhr* advanced BH (turquoise solid lines), in comparisons with the fitted model by Tinker et al. (2008, black dashed lines). We used the fitting parameters for $\Delta = 200$ in combination with computing the HMF from the simulations with the $M_{200,m}$ masses. As can be seen by the minuscule deviations between the different simulation boxes and the theoretical HMF, the simulations reproduce the theoretical expectations very well and mostly differ only with regards to the dynamic range of halo masses that can be found at each resolution and box size.

The Gas Mass Function

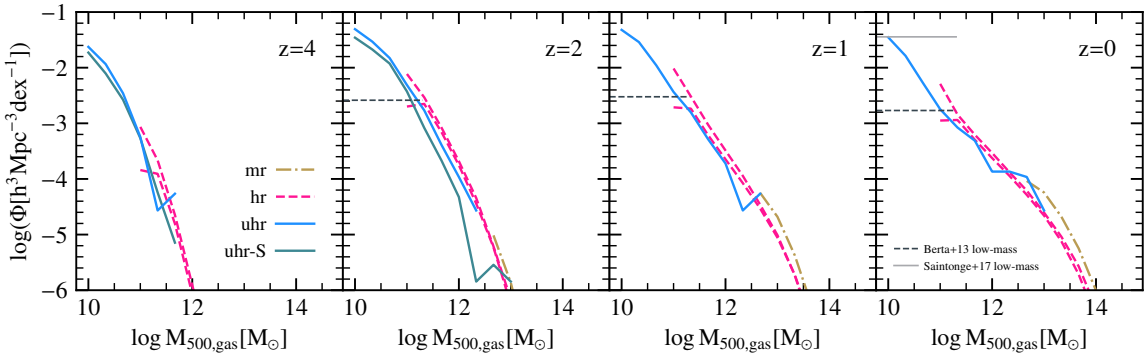


Figure 3.3: The evolution of the GMF for the different Magneticum Boxes. For the simulated mass functions the line colours indicate the different runs at $z = 4, 2, 1, 0$ respectively. As an observational comparison, we show the data from xCOLDGASS CO data (Saintonge et al., 2017) (grey horizontal line) and the PEP plus HerMES field from Herschel (Berta et al., 2013) (black dashed line). Figure 10 from Dolag et al. (2025).

The second step in the formation of galaxy beyond the purely gravitational mass assembly is the accretion of gas. As we will show in Chapter 4, while accreting onto haloes, the gas behaves fairly similar to the dark matter component in terms of its overall inflow. However as it falls onto galaxies and clusters, the gas component heats and forms shocks that fundamentally alter the dynamics from purely gravitational collapse. Additionally feedback from star formation and black holes can drive powerful outflows that further impact the thermodynamical state of the gas at intermediate scales. Observationally, it is very difficult to compute this function consistently across a large mass range, because different structures are dominated by different gas phases: For massive halos, most of the gas is present in the form of the hot ICM or IGM, while for galaxies the balance is tilted towards colder gas phases like neutral and molecular hydrogen. The former is usually measured utilizing the X-Ray and thermal Sunyaev-Zeldovich signal under the assumption of a hydrostatic equilibrium, while the latter is inferred from tracer line ratios, Lyman-alpha absorption or the 21-cm signal. Each of these methods suffer their own unique biases and in addition, cold gas and hot gas are very differently distributed in terms of spatial extent (e.g. Ayromlou et al., 2023).

All these factors, in addition with the intermediate stage, the warm-hot intergalactic medium, being even more difficult to observe (e.g. Nicastro et al., 2018), while most likely containing a large fraction of the cosmic baryon budget, make the observation of a unified cosmic GMF non-viable. It has been independently shown that Magneticum Pathfinder reproduces hot gas fractions obtained from state-of-the-art X-Ray data fairly well (Popesso et al., 2026). Here we only compare with cold gas data at the low-mass end, specifically data from the xCOLD GASS CO survey (Saintonge et al., 2017) and the combined PEP and HerMES field observed by Herschel (Berta et al., 2013). Both surveys find a Schechter-function like behaviour for the gas mass function with plateaus at the low-mass end. However, Berta et al. (2013) find this plateau to be at much lower values than Saintonge et al. (2017).

Fig. 3.3 shows the universal gas mass fractions obtained from the different simulation volumes. Because X-Ray and SZ gas densities are usually obtained within R_{200}, where densities are sufficient for detection and the cold molecular gas traced by our reference studies can be expected to be distributed even more centrally, we chose $M_{500,\mathrm{gas}}$ as a measurement for the total gas mass of each halo. This can then be roughly expected to be dominated by cold gas at $M_{\mathrm{gas}} < 10^{11} M_{\odot}$ and by hot gas at group masses $M_{\mathrm{gas}} > 10^{12} M_{\odot}$. The simulations with *uhr*, where galaxy physics can be expected to be reasonably resolved reach the masses

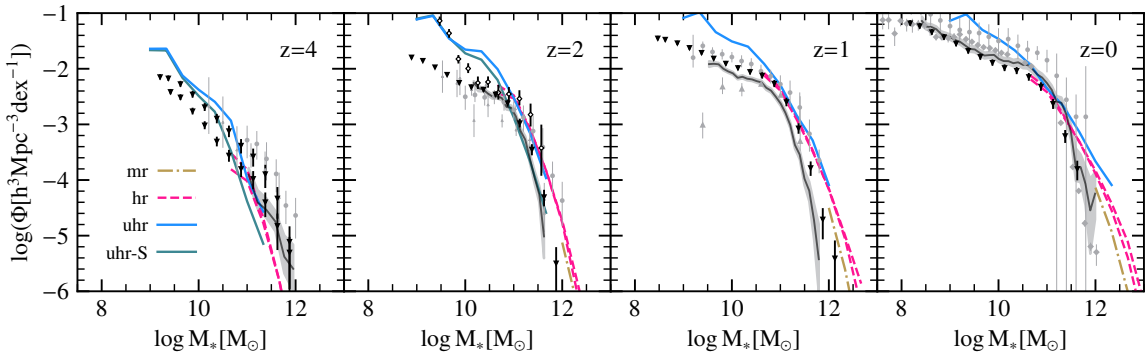


Figure 3.4: The evolution of the SMF for the different Magneticum Boxes compared to various observations. For the simulated mass functions the line colours indicate the different runs at $z = 4, 2, 1, 0$ respectively. The black lines with the grey shaded errors are taken from (Muzzin et al., 2013). Observations from the COSMOS survey (Weaver et al., 2022, 2023) are shown with the black downwards pointing triangles. Additional observational data from Pérez-González et al. (2008) (circles), Panter et al. (2004) (diamonds), Marchesini et al. (2009) (tri-down), Bundy et al. (2005) (upwards pointing triangles) are shown with grey symbols. For z=2 we include measurements from Santini et al. (2012) (blue diamonds). Part of my personal contribution to Dolag et al. (2025) (see Fig. 9).

and observed plateau values for both Berta et al. (2013) and Saintonge et al. (2017), however the fact that the former found a flat plateau at their lower GMF value means the simulation data is leaning towards a shape of the GMF more compatible with the xCOLD GASS field. In combination with reproducing the observed hot gas fractions for massive haloes, it can be concluded that the overall gas mass budget of Magneticum Pathfinder is fairly realistic.

The Stellar Mass Function

The flip side of the gas mass budget in a given halo is the stellar mass budget. As the gas in a system cools and forms dense clumps, it can be converted into stars. The exact evolution of the stellar mass of a given halo is subject to a complex interplay of physical processes: Star formation itself injects feedback energy into the surrounding medium, consequently reducing densities and regulating the star formation rate locally. Additionally, the overall heating of the medium can influence gas inflows from the environment. Once stars are formed, they can also be stripped away by tidal distortions from mergers or ultimately as a galaxy falls into a galaxy cluster or group. The SMF is therefore a key metric for calibrating galaxy formation and evolution between theory and observations. Since stellar masses are more readily accessible observationally, there are robust observational SMFs to directly compare how galaxy form stars in simulations with observed galaxies. Fig. 3.4 shows the stellar mass functions in the Magneticum Pathfinder simulations. By the general agreement between the simulation runs, it can be seen that the star formation prescription described in Section 3.5 is robust against different resolutions, with the lower resolution runs generally in agreement with the higher resolution runs at the stellar masses where they overlap. In contrast, the scatter between individual observed SMFs is larger, possibly due to selection effects and different systematics. Within this relatively large scatter, simulations and observations overlap well across almost the entire mass and redshift range. The largest disagreement can be found at the lowest stellar masses from $z = 2$ onward. Magneticum Pathfinder systematically over-predicts the abundance of galaxies from $M_\star \approx 10^{10.2} M_\odot$. A possible explanation for this is the lack of relative efficiency of stellar winds with respect to the AGN feedback. At the low-mass end the stellar feedback has been found to be much more important for

effective quenching of the star formation (Wang et al., 2015). Recent tests with the Magneticum Pathfinder model in preparation for the MagneticumDAWN (see Section 3.9) suite also showed that it is important **where** stars are formed in less massive galaxies: Increasing the density threshold for star formation resulted in an increase of more massive galaxies with a simultaneous decrease at the low-mass end due to the star formation activity being more centrally concentrated (Kimmig, 2026). Together with the improvements to the BH seeding, this simulation suite will deliver more insights into the evolution of the SMF across cosmic time.

At the high-mass end the Magneticum Pathfinder model produces an overabundance of massive galaxies at late times due to over-cooling in massive groups and cluster environments. Interestingly, the data from (Muzzin et al., 2013) (black line with grey error bars), which is taken at a slightly higher redshift than (Panter et al., 2004) ($z \approx 0.35$ vs. $z = 0$) indicates a slightly larger abundance at the high-mass end. This could indicate a local bias with the dynamically relatively active clusters in the Local Universe featuring smaller BCGs, due to their dynamical state (Kimmig et al., 2025a).

The impact of the improved model by Steinborn et al. (2015) with regards to producing quiescent galaxies at $z = 2$ and higher (Steinborn et al., 2015, Kimmig et al., 2025b) can be seen in the suppression at both the high and the low mass end and the resulting better fit to the observational data. However, this effect is much more apparent in the fraction of quiescent galaxies, which lead to the numerical study presented in the following section.

3.8 High(-z) Noon: Early Quenching in the Magneticum Simulations

This chapter highlights the large-scale analysis I contributed to Kimmig, Remus, Seidel et al., 2025, ApJ 979, 15, "Blowing Out the Candle: How to Quench Galaxies at High Redshift—An Ensemble of Rapid Starbursts, AGN Feedback, and Environment"

As shown in Fig. 3.4, the modified BH model from (Steinborn et al., 2015) manages to produce galaxies with better star formation properties at high redshifts in *Box3/uhr*. This proved to be of unforeseen consequentiality, when early observations from JWST (Carnall et al., 2023, Gould et al., 2023, Long et al., 2024, e.g.) were consistently finding higher volume fractions of massive quiescent galaxies at high redshifts ($z > 3$) than simulations had seemingly previously predicted (Remus & Kimmig, 2025, Weller et al., 2025). Fig. 3.5 shows both the evolution of the total and the quenched number density for *Box3/uhr* as a function of mass in the top row and compares these densities for massive galaxies to the observed densities in the bottom row. It can clearly be seen that the simulation (which was at the time almost 10 years old) reproduced these surprising findings with regards to the number of massive quiescent galaxies quite well. Its unique combination of *uhr* resolution and a much larger simulation volume compared to *Box4/uhr* allowed the star formation to be sufficiently resolved and provided enough opportunities for massive haloes to already be formed at high redshifts (Kimmig et al., 2025b). This presented the unique opportunity to investigate how and why these massive quiescent galaxies had managed to accrete enough gas, undergo a starburst, and subsequently quench on these surprisingly short timescales. In the following we consider especially the environments of these massive quiescents in order to assess whether their quenching behaviour is tied to the large-scale structure surrounding them.

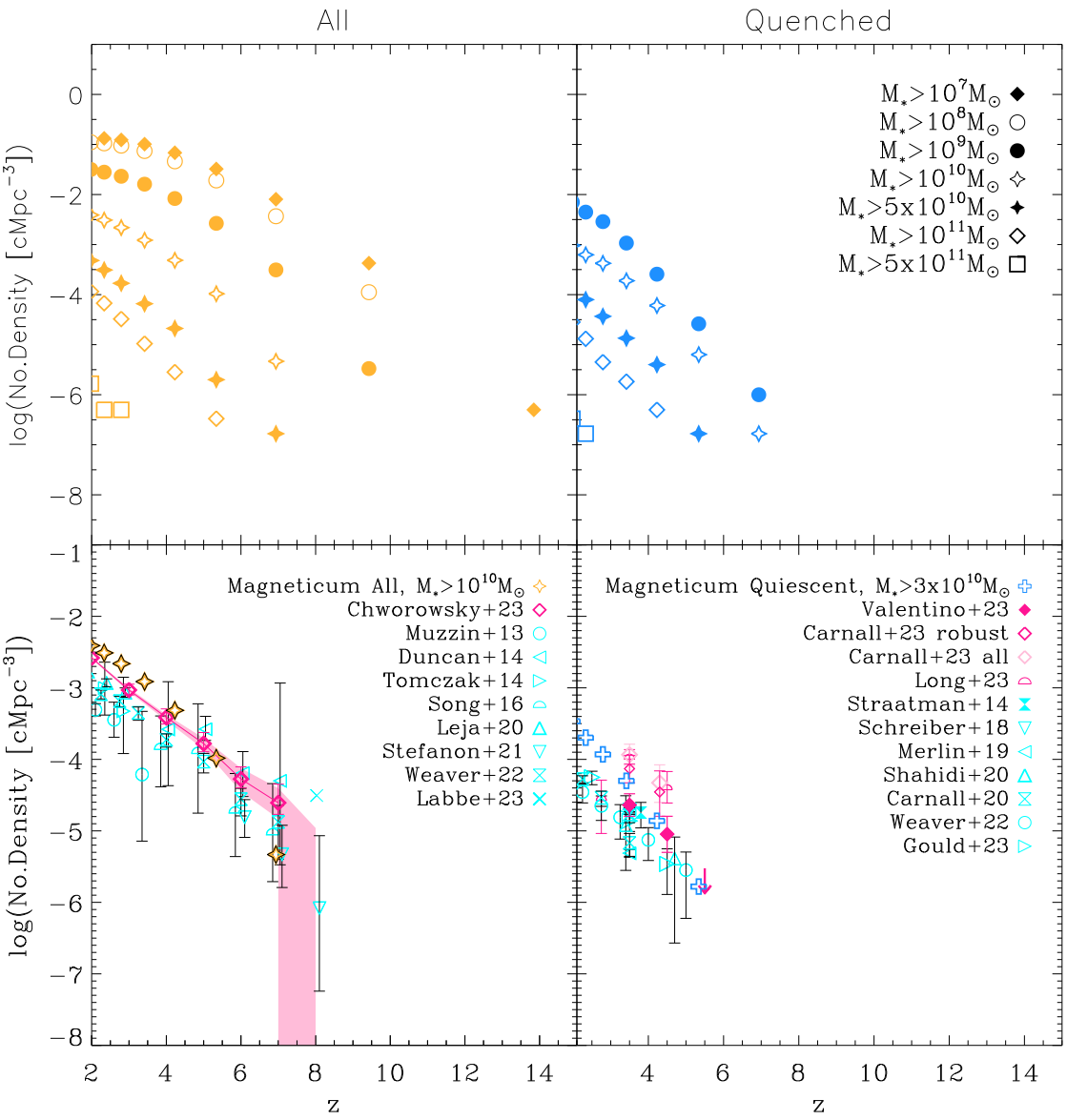


Figure 3.5: *Top row*: Time evolution of the number density of simulated galaxies from $z = 2$ to $z = 15$. Different symbols mark the different lower mass limits applied, as indicated in the legend. Galaxies are shown as all galaxies (*left*) and only the quenched galaxies (*right*). For the quenched number densities the lower two mass cuts are omitted due to resolution. *Bottom row*: Comparison to observations (JWST spectroscopy in pink, others in cyan). The total sample includes all galaxies above $M_* > 10^{10} M_\odot$ (*left*, yellow stars) and the quiescent sample galaxies above $M_* > 3 \times 10^{10} M_\odot$ (*right*, blue pluses). Observed total values are taken from Chworowsky et al. (2023), Muzzin et al. (2013), Duncan et al. (2014), Tomczak et al. (2014), Song et al. (2016), Leja et al. (2020), Stefanon et al. (2021), Weaver et al. (2022), Labbé et al. (2023), while quiescent values are from Long et al. (2024), Carnall et al. (2023), Valentino et al. (2023), Straatman et al. (2014), Schreiber et al. (2018), Merlin et al. (2019), Shahidi et al. (2020), Carnall et al. (2020), Weaver et al. (2022), Gould et al. (2023). Figure 2 from Kimmig et al. (2025b).

3.8.1 Shape of the Gravitational Environment

By measuring the relative overdensity of these massive quiescents, Kimmig et al. (2025b) were able to show that especially after they have been quenched, these galaxies live in comparatively underdense environments out to relatively large scales ($r \lesssim 2$ cMpc), in conflict

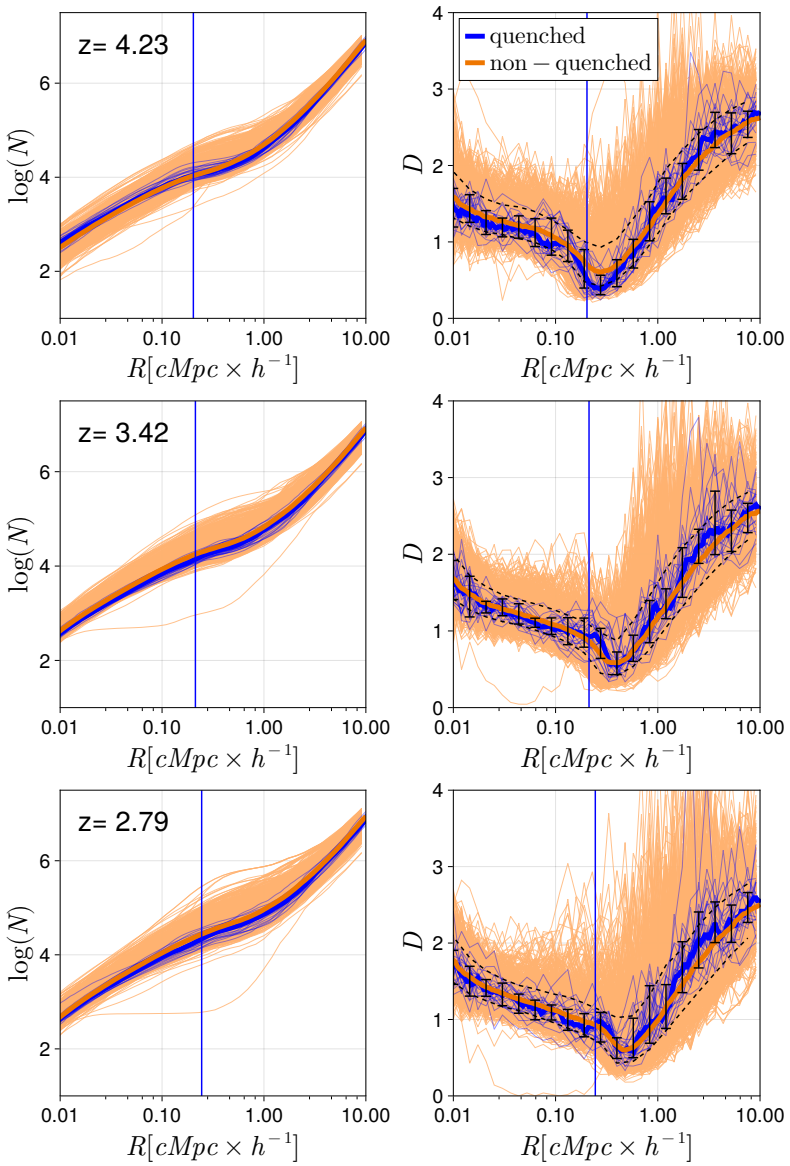


Figure 3.6: Number of dark matter particles N (*left panels*) and resulting dimensionality parameter D (*right panels*) as a function of radius around the quenched (blue lines) and non-quenched (sand lines) centrals, for three redshifts ($z = 4.23$ to $z = 2.79$, top to bottom). Median behaviors are given by the fat solid lines. In the right panels, the thin dashed lines show the 1σ bounds of the non-quenched sample, while the quenched samples 1σ bounds are shown as black errorbars. Also shown are the median virial radii of the quenched centrals (vertical blue line). Part of my personal contribution to Kimmig et al. (2025b) (Fig. 12).

with findings for massive quiescent galaxies from other simulations, which found them to rather favour overdense environments (Weller et al., 2025). Beyond the density of the gravitational environment, where a galaxy sits in the cosmic web paradigm, i.e. whether it inhabits a node, sheet, filament or void, can impact the tidal fields that affect its growth. This can ultimately also shape the mass inflow onto the galaxy. In order to estimate the geometry of the environment, we computed the so-called local dimensionality parameter (Sarkar & Bharadwaj, 2009), which quantifies how quickly the density grows locally as a function of scale. It can be computed via

$$D \propto \frac{d\log(N)}{d\log(R_{\text{filter}})}, \tag{3.12}$$

with N being the number of dark matter particles (due to all particles having the same mass m_{dm}, this is essentially the dark matter mass within the sphere of radius $R_{\rm filter}$). We determined D within 100 logarithmically spaced ($\Delta \log(R[\mathrm{cMpc/h}]) = 1.05$) spherical filters with radii ranging from 0.1 cMpc/h to 10 cMpc/h. The idea of this parameter is as follows: How fast the mass inside a spherical volume of $R_{\rm filter}$ grows with increasing volume is essentially determined by the spatial configuration of the density (assuming an otherwise homogeneous mass distribution), in other words it grows with R^D. If $D = 3$ it is simply distributed in a homogeneous spherically symmetric configuration, $D = 2$ represents a sheet-like configuration, where the mass increases in two spatial dimensions and $D = 1$ represents a 1D filamentary structure. These scenarios are clearly distinguished if the density is not at all radially dependent, which is of course an oversimplification. Nonetheless, the dimensionality can give an idea of the spatial configuration of matter around these quiescent galaxies.

Fig. 3.6 shows both the dark matter counts as a function of radius in the left panel as well as the dimensionality D in the right panel. The generally lower relative density, that quenched galaxies reside in is, reflected by the fact that, at radii larger than the median virial radius (vertical blue lines), the spherically averaged mass is consistently lower for quenched galaxies compared to the median of non-quenched galaxies. The most interesting region in the mass profiles is around these median virial radii, where, before the time of quenching ($z = 4.23$, upper row), the flattening of the profile is noticeably stronger for the quiescent sample. This is also reflected in the dimensionality with the median D among the quenched galaxies dropping significantly below 1 and outside of the 1-σ bounds of the non-quenched sample. This indicates a shell of very low density with a potentially weak filamentary connection as the preferred environment of these massive quenched galaxies. After these galaxies quench, they reside in a similar environment to their non-quenched counterparts with regards to the dimensionality, albeit the slight underdensity of their surroundings is even more pronounced at these times. To go from the purely dark matter density to a more complex view of the gaseous environment, which is ultimately much more sensitive to the feedback mechanisms responsible for the quenching, we consider as a case study, the exact environment of one of the galaxies from the quenched set.

3.8.2 Case Study

Fig. 3.7 shows the evolution gaseous environment of an example galaxy, one of the most massive galaxies from the quiescent set with $M_\star = 5.6 \times 10^{10} M_\odot$, with a quenching time around $z = 3.42$, the last snapshot in the figure. The galaxy evolves in a tenuous spider-web like environment at early times with many weak gas filaments connecting to the central halo. As the galaxy grows in mass, just ahead of quenching ($z = 5.34, z = 4.23$), many of these less dense filaments become more pronounced against the background due to merging together. At these times, a distinct lack of structure in the lower right from the halo also becomes noticeable, indicating a neighbouring underdensity, reminiscent of a cosmic void. This is even more apparent in the velocity field, where the infall velocities are relatively low in this area. Even though the galaxy accretes from all directions, the inflow from the lower right, where the density is lower has a much lower velocity and is directly connected to the divergence point associated with the underdensity. This discrepancy becomes even more apparent when the galaxy quenches in the final two snaps. First the shock surface from the bubble triggered by the starburst (black ring) and then the AGN bubble (high velocity zone in the final snapshot) both exhibit an asymmetry into the lower right direction, where they are much more extended. The gas flow lines curling around both surfaces show how these bubbles effectively stop the accretion and thus the supply onto the central halo, which prevents further star formation beyond the removal of the galaxy's gas. It should further be noted that both of the outflow systems happen at scales of the virial radius of the halo or

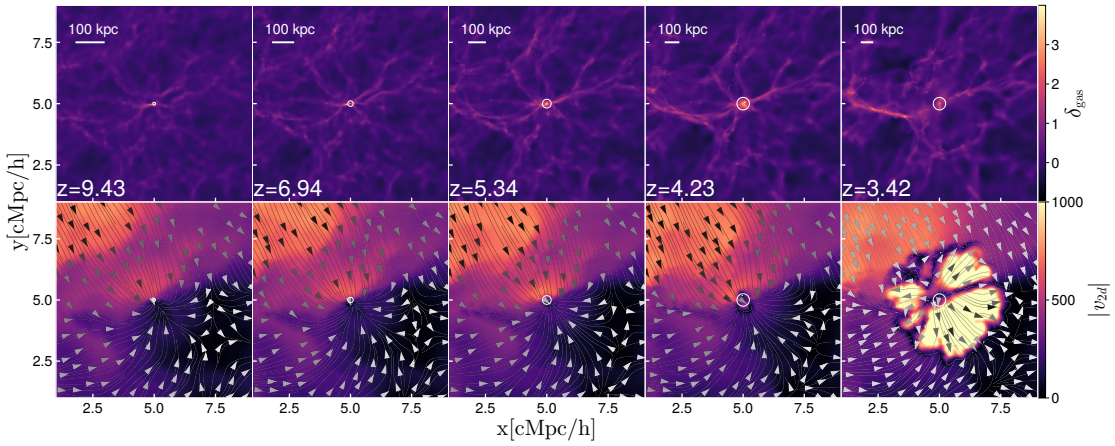


Figure 3.7: The cosmic web and flow structure shown as projected gas density (*top row*) and velocity (*bottom row*, heat map=amplitude, arrows=direction) around an example massive quiescent galaxy from *Box3/uhr*. Both quantities are computed in a slice of dimensions $10\text{cMpc}/h \times 1000\text{ckpc}/h$, centred on the galaxy. The white circle indicates its virial radius at each snapshot. Shown are snapshots at redshifts from $z = 9.43$ to $z = 3.42$ (*columns, left to right*). Part of my personal contribution to Kimmig et al. (2025b) (Fig. 3).

even beyond, so the feedback in Magneticum Pathfinder clearly has effects far beyond the galaxy itself. In the final snapshot, this is also manifested by the effective destruction of the filamentary system present before the quenching time, with only the densest parts of these region still visible close to the virial radius, where the feedback has visibly smoothed the entire immediate vicinity of the galaxy.

To summarize, analysing the evolution of the gaseous environment of an example massive quiescent galaxy, we have seen how the environment both shapes, and is shaped by the galaxy. The unique structure around the galaxy shapes the inflow structure around it, which is fairly isotropic in the sense that material is flowing in from everywhere but shows a clear bias with weakened inflows from a void like region adjacent to the halo. When the galaxy then quenches, this direction is also the axis of maximal extend of the outflow driven by the feedback, which reaches very large radii compared to the halo scale and disrupts both the cosmic web as well as the inflow structure. This shows that environment does indeed shape galaxy evolution, but it is also shaped by it.

3.8.3 Conclusions

From an environmental perspective, both the statistical evaluation of the dark matter density structure, as well as the gas density and flows have shown that the structure and dynamics of the mass outside a galaxy is closely tied to the internal evolution. We have shown especially the flow field to be profoundly affected by the outflows driven by the stellar feedback and AGN activity as well as the underlying cosmic web structure. This motivated the work on the flow fields around haloes, which we will present in the following chapters, where we will explore the structure of the motions on the outskirts of haloes from galaxy to cluster mass and through cosmic time.

3.9 Sunrise over Magneticum: The DAWN Simulations

The fact that the early massive quiescent galaxies observed by JWST could actually be produced by *Box3/uhr* presented an opportunity for a follow-up project: The Magneticum-

DAWN simulation suite (Kimmig, 2026) is in essence a re-run of two MAGNETICUM PATHFINDER simulation volumes, *Box2* and *Box3*, where the larger *Box2* is re-simulated at *uhr* resolution and the *Box3* volume is upgraded to *xhr* mass resolution. And additional calibration volume, *Box4/uhr* was run 44 times to redshifts $z \approx 2$ in order to test the impact of the sub-grid configuration. In addition to the models described in Section 3.5, the simulations employ a redshift-dependent black hole seeding according to

$$\frac{M_{bh}}{M_\star}(z) = A \times 0.00145 \times 10^{0.05z}, \tag{3.13}$$

where A is a free parameter (for further details see Kimmig (2026)). Furthermore, the simulations were and are performed with the newest version of the OPENGADGET3 code, including an improvement of the explicit dynamical friction scheme for black holes (Damiano et al., 2024), a black hole spin evolution model (Sala et al., 2024), an improved physical viscosity scheme (Marin-Gilabert et al., 2022) and an updated model for the UV background (Di Federico et al. in prep.). This simulation project is currently ongoing and aims to further shed light on the evolution of early galaxies. We will employ a specifically selected sample of the calibration runs in Section 7.2 to test specifically how the feedback model impacts galactic inflows.

3.10 Tackling the Multi-Scalarity of Flows

In the sections above we demonstrated that the overall growth of structure is well described by numerical simulations (see especially Fig. 3.2). There are however tensions between the observed and simulated galaxy stellar masses. The biggest challenge here is to modify the models in such a way that they best reflect the accretion of cold gas and subsequent star formation at all (sufficiently resolved) halo masses and all times simultaneously. How the black hole and stellar feedback models are tuned can be expected to have a profound impact on the stellar evolution of galaxies. Strong outflows from the galaxies themselves can also weaken or cut-off the gas inflow from the cosmic web, as we showed in Section 3.8.

The next two chapters will therefore focus on the flow fields around simulated halos and especially how the inflow rates and morphologies evolve. Similarly to the density field, the velocity field in a cosmological volume is highly multi-scalar. To illustrate this, Fig. 3.8 shows the peculiar velocity field computed on a grid in *Box4/uhr*. The left column shows a very linear flow field with very little bending of the streamlines even across the boundaries of complex gas filaments shown in the background. This also demonstrates an issue with small simulation volumes: The entire inflow-outflow structure of the simulation can be ascribed to a single overdensity (the "cross" structure in the upper right) and a corresponding void (lower left). There is, however more than meets the eye here. By applying a filter in Fourier space (in order to avoid artifacts we used a smoothly decreasing Butterworth filter (Butterworth, 1930), which yields better results than a sharp k-space cut) in order to filter out the large-scale component of the velocity field, the complex small-scale structure becomes visible. Many of the smaller substructures can be seen to exist within small peculiar flow systems of their own. The influence of feedback on these small scale components of the velocity field can also be observed in the form of turbulent flow-lines forming bubbles around these systems.

This picture of multi-scale flows, separated into gravitational inflows and hydrodynamical outflows is the motivation behind the numerical approach developed in the following chapters: In order to capture the gas motions around haloes from cluster masses to galaxy masses accurately, we quantify the scaled flows across their virial surface in the respective halo rest-frame. We will exploit this methodology in order to quantify the flow rate as well

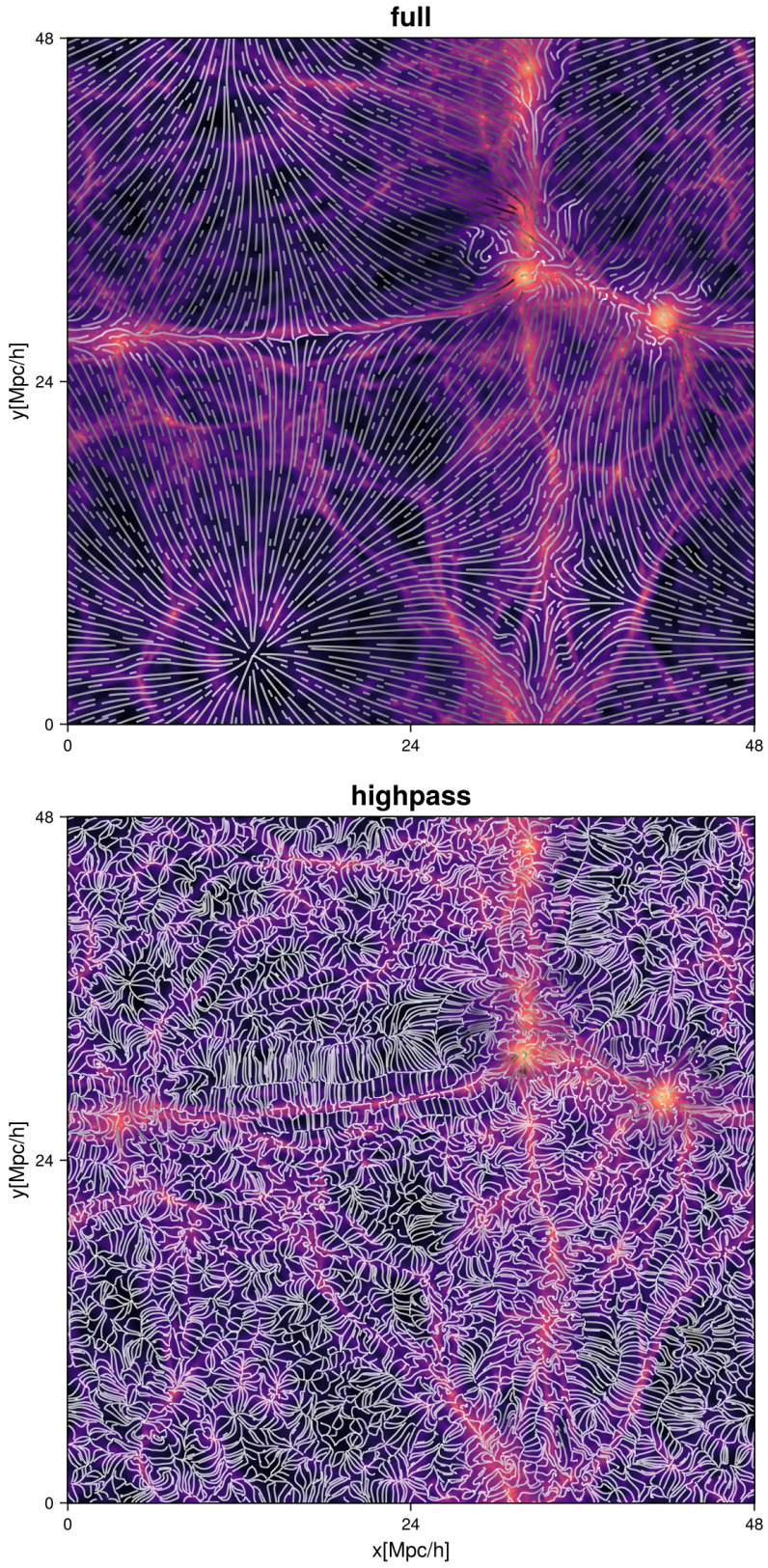


Figure 3.8: Gas density (heatmap) and velocity (streamlines) in a 1 Mpc/h slice through *Box4/uhr* from MAGNETICUM PATHFINDER. The left column shows the total peculiar velocity field. In the right column, large scale fluctuations of the velocity field have been filtered out in Fourier space, highlighting the small scale gas motions. The cutoff scale for the k-space filter is 5 Mpc/h. The grid units for the x-y grid are 48 kpc/h per grid cell.

as the spatial configuration of the flow field across cosmic time and show how these parameters impact and are impacted by the dynamics inside the haloes, connecting the large scale environment to galaxies and clusters of galaxies.

Chapter 4

Feeding Flow: Accretion, Outflows and Shocks in the Outskirts of Simulated Haloes

The content of this chapter has been published as Seidel et al. 2025, A&A, 701, A192, "Go with the flow: The self-similar and non-linear behaviour of large-scale in- and outflows and the impact of accretion shocks from galaxies to galaxy clusters". Parts of the analysis were already present in my master thesis with significant improvements and modification to the work.

4.1 Introduction

A detailed understanding of the multi-scalar process of structure formation remains a key objective for modern cosmology and astrophysics. Since the notion of the inter-connectivity of the large scale cosmic web was first conceived by Zeldovich in his seminal paper (Zel'dovich, 1970), it has become ever more clear that the large-scale assembly of matter into a complex web of filaments, sheets and nodes has consequences that proliferate well into the regime of non-linear structure formation and evolution in the galaxy regime (e.g. Papovich et al., 2018, Castignani et al., 2022). Especially the filamentary and smooth gas flows in close vicinity to galaxy clusters and galactic haloes are governed by a complex combination of the gravitational environment they arise in and the internal gas physics that predominantly drive the outflows. A comprehensive overview of the complex physics in the outskirts of galaxy clusters is presented by Walker et al. (2019).

On the galaxy scale, the make up of the large-scale environment is widely assumed to be a crucial factor in its star formation history, possible quenching and the galaxy's dynamical evolution (Galárraga-Espinosa et al., 2023). If the gravitational Universe is truly self-similar and the morphological differences at small scales arise purely from the increased importance of baryonic processes at smaller scales, the configuration of the gas and dark matter flow fields around galaxy clusters and galaxies must bear some residual resemblance in global properties, albeit scaled by the different gravitational energies involved. The outskirts of (quasi-) virialized structures, where infalling gas and smaller structures encounter the thermalized medium of the already assembled larger structure for the first time are a critical test bed for our understanding of how these structures form and accrete mass over time.

Both the hot components of the intra-cluster medium (ICM) in the outer regions of galaxy clusters and the multi-phase circum-galactic medium (CGM) have been the focus of large observational (e.g. Gatkine et al., 2019, Gatuzz et al., 2023) and theoretical (e.g. Churazov et al., 2023, Bogdán et al., 2023) efforts in the recent past.

In the standard self-similar assembly picture the radius at which the in-falling gas is shock-heated by the already virialized atmosphere (accretion shock radius, $r_{\rm sh}$), and the apoapsis of the first-infall orbit of dark matter (splash-back radius, $r_{\rm sp}$) are generally expected to coincide (Shi, 2016, Dekel & Birnboim, 2006). However, recent numerical simulations have demonstrated that encounters of merger driven shocks with the accretion shock and the resulting merger-accelerated shock (MA-shock) can drive baryonic shocks out to multiple virial radii in galaxy clusters, far exceeding $r_{\rm sp}$ (Zhang et al., 2020) and create complex non-spherical baryonic boundaries with gas properties rapidly changing across these surfaces.

The CGM is a key part in understanding how galaxies regulate their star formation in a complex interplay of large-scale gas accretion, cooling flows from the cold phase CGM and thermal feedback from star formation and active galactic nuclei (AGN) (Yu et al., 2021, Stuber et al., 2021, Hogarth et al., 2021). The balance between pristine inflowing gas from the cosmic web feeding the star formation in galaxies, and outflowing gas heated and enriched by feedback caused by the star forming activity and the central AGN is still not fully understood. Nevertheless, it is most crucial for understanding the evolution of galaxies and their properties through cosmic time.

A holistic theoretical understanding of structure formation and how collapsed structures are connected to their environment is in general crucial in the exploration and interpretation of the increasingly precise X-ray and SZ observations of the present and near future. A better understanding of the ICM specifically and its complex non-thermal physics, such as clumping, bulk flows and magnetic fields, is critical for improving mass estimates obtained from X-ray observations for cosmology. These non-thermal processes can introduce significant biases when assuming hydrostatic equilibrium to calculate masses. This can significantly impact the constraining power of cluster masses on cosmological parameters (Salvati et al., 2019, Lebeau et al., 2024c). Additionally with regards to galaxy formation a better understanding of the assembly of structures can aid in interpreting the highly resolved observations of inflows, outflows and feedback bubbles now resolved in many galaxy observations (Watkins et al., 2023).

From the purely gravitational perspective, structure formation is assumed to be self-similar, that is structures assemble the same way at all scales, owing to the scale-invariant nature of gravity. It is then precisely the deviation from self-similarity that encodes interesting information on the complex baryonic processes that set the evolution of massive and less massive haloes apart. Balancing the reproduction of observed CGM and ICM properties simultaneously poses a formidable challenge to numerical simulations, nevertheless it is integral to their predictive power. This work aims to tackle the mass assembly of organised structures in the Universe from a multi-scalar perspective and provide insights on the interaction of physical processes separated by several orders of magnitude. To this end we investigate the mass flows in the outskirts of objects from galaxy (group) to cluster masses and analyse their gravitational and thermodynamical properties in the framework of a state-of-the-art hydrodynamical cosmological simulation.

4.2 Methods

4.2.1 Identifying the Systems

We sampled a Catalogue of $29 \times 11 = 319$ randomly selected haloes in 11 logarithmic mass bins from $10^{12} - 10^{15} M_{\odot}$. The logarithmic width of each bin was was selected to ensure that at least 29 objects existed in each mass bin while keeping the width as small as possible [1].

[1] the number 29 was motivated by the 29 most massive clusters from the high-resolution box (*Box2b/hr*) as these are the haloes with mass $M_{\rm vir} > 10^{15} M_{\odot}$, see Kimmig et al. (2023) for further details

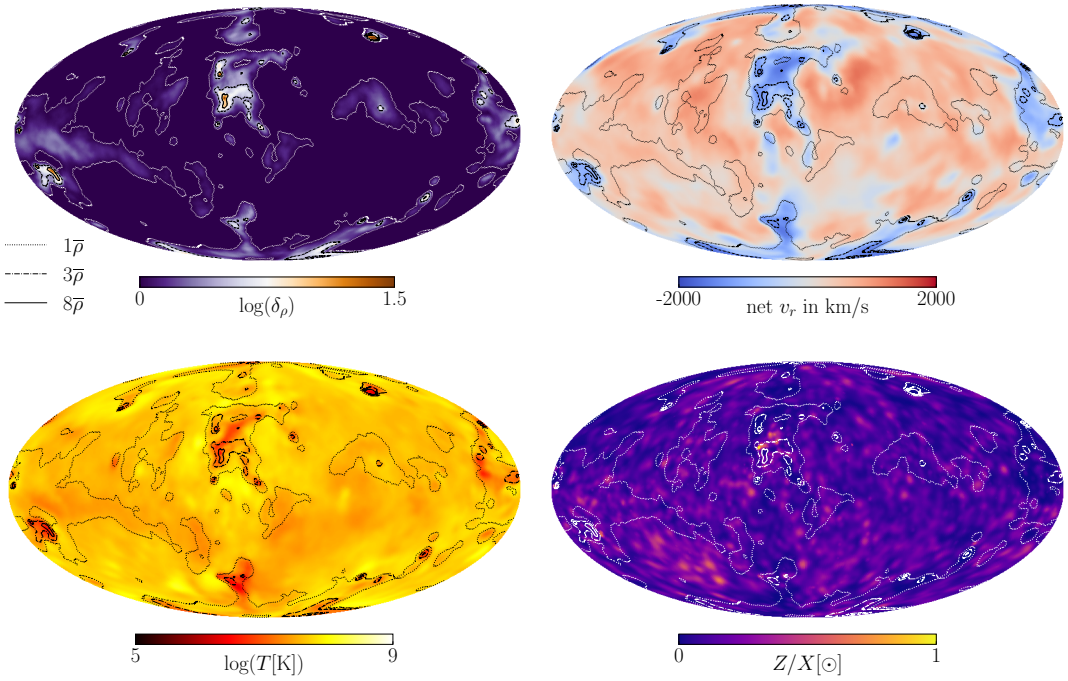


Figure 4.1: The four fields (density, radial velocity, temperature and metallicity) interpolated on the spherical shells just outside the virial surface ($r = 1.2r_{\mathrm{vir}}$) shown for an exemplary cluster from the highest mass bin ($10^{15} M_\odot$). The contours indicate relative to the mean density of the shell $\bar{\rho}$, $3\bar{\rho}$ and the $8\bar{\rho}$ level respectively.

We connect *Box2b/hr* and *Box4/uhr* at the $10^{13} M\odot$ mass bin, where *Box2b/hr* still has enough resolution to resolve the haloes sufficiently and *Box4/uhr* has enough haloes to build a mass bin with a sufficiently small mass spread. Dolag et al. 2025 show the resolutions to converge in the most relevant scaling relations for galaxies and clusters indicating that this mixing of resolutions is justified.

When selecting haloes at different timesteps, we did not trace individual haloes back in time but sampled new bins at each redshift, keeping the associated bin mass and not its constituents constant. The selected haloes are exclusively selected from the field, that is they are not bound to another, larger halo at some scale. This selection specifically excludes galaxies and groups evolving in a cluster environment, which are not the focus of this paper.

4.2.2 Reconstructing the Peculiar Mass Flow from Simulation Data

The flow through a surface given a continuous velocity field $\mathbf{v}(\mathbf{x})$ can be generally computed by either integrating its divergence over the enclosed volume or via the Gaussian theorem by

$$\int_V \nabla \cdot \mathbf{F}\, dv = \oint_{\partial V} \mathbf{F} \cdot \hat{n}\, da \tag{4.1}$$

. From a numerical perspective the latter method is the more sensible (integrating over a volume, scaling with r^3, vs. a surface, with r^2 scaling). The largest haloes in the sample reach several Mpc in virial radius or in other words scales where the expansion of the background cosmology becomes relevant, therefore we use peculiar velocities throughout this work. In SPH the gas discretisation is based on representative point particles that are smoothed over a volume of space with a density dependent kernel. To accurately model the gas flow given a set of gas "particles" it is therefore necessary to take into account the geometry and smoothing lengths of the kernels with the advantage that SPH will provide a continuous gas velocity

field without artificial clumpiness. This ensures that there are no holes in the density/velocity field due to the SPH particles' clustering leaving empty pixels, which would affect the computation of the geometrical properties of the flow fields in Section 4.3. To obtain a similarly smooth velocity field for the dark matter component, equivalent smoothing lengths are computed in post-processing for this species by calculating a weighted mean density at each particle position using a simple neighbour tree.

4.2.3 Geometry

Because dark matter haloes can to first order be considered as approximately spherically symmetric (deviations from this assumption wrt. to the matter configuration in the outskirts are discussed in section 4.3.3) for the purpose of this investigation, we compute the flow through spherical shells. We set up the computation of the inflow and outflow rates to be at spherical surfaces of $r \in [1.2, 1.4, ..., 5.0] \times r_{\rm vir}$. The peculiar particle velocities were corrected by subtracting the centre of mass motion of the main halo the shells are centered on.

4.2.4 Flowmaps

We use the program SMAC (Dolag et al., 2005b) to generate the flow maps. Our custom version of this post-processing software – adding a slice based computation of the quantities for flow computation as opposed to the standard radial binning method - uses a healpix (Gorski et al., 2005) based tessellation of the surface to compute the SPH based gas density at every pixel of the spherical shell. This density is calculated based on the contribution of each particle to the pixel:

$$\alpha_i \times \rho_i \times w(|\mathbf{r}_{i,j}|), \tag{4.2}$$

where α_i is a geometry factor encoding the overlap of the particle with the pixel [2], ρ_i is the nearest-neighbor density and w is the kernel function. We use the commonly employed cubic spline kernel for all SMAC calculations, where

$$w(\tilde{r}) \propto \begin{cases} 0, & \text{if } r > 1 \\ 2(1-\tilde{r})^3, & \text{if } 1/2 \leq \tilde{r} \leq 1 \\ 1 - 6\tilde{r}^2 + 6\tilde{r}^3 & \text{if } 0 \leq \tilde{r} \leq 1/2 \end{cases}, \tag{4.3}$$

where $\tilde{r} = \frac{r_{i,j}}{r_{\rm hsml}}$ and $r_{\rm hsml}$, the neighbour-density based smoothing length is a simulation output. The net flow through the i-th pixel is then the sum over all particle velocity contributions to that pixel, weighted with the respective particle density contribution. The total net flow is simply the sum over all pixels. For each net flow map we also generated pure inflow and pure outflow maps in order to identify the regions of in- and outflow and analyse the components separately. Additionally, temperature and metallicity weight maps are generated in order to select for hot stream components and processed matter streams. Here the metallicity of a particle is calculated as the mass fraction sum of all elements heavier (Z) than Helium (Y) divided by the particles hydrogen mass (X) $m_Z/m_H = (1 - \mathrm{X} - \mathrm{Y})/\mathrm{X}$. We then convert this value to solar metallicity, assuming the mass fractions from Wiersma et al. (2009).

[2] α_i is calculated with the ratio of the particles' smoothing length overlapping with the pixel $\frac{\mathrm{hsml}_{\rm proj,pixel}}{\mathrm{hsml}_{\rm proj}}$. Here $\mathrm{hsml}_{\rm proj}$ is the projected smoothing length of the particle given by $\mathrm{hsml}_{\rm proj} = \sqrt{\mathrm{hsml}^2 - dr^2}$, with dr being the particles radial distance to the pixel center.

4.2.5 Discerning In- And Outflows

To identify regions of inflow and outflow, we use two approaches that are outlined in the following.

Pixel-based philosophy Whenever referred to as pixel-based flows, pixels are selected by the projection of the mass-weighted net velocity vector onto the radial direction

$$\Phi_i = \mathbf{v_i} \cdot \hat{\mathbf{r}}_\mathbf{i} \tag{4.4}$$

through each pixel, where $\mathbf{v_i}$ is obtained with the kernel (and geometry)-weighted sum over all particle contributions in the pixel and $\hat{\mathbf{r}}_\mathbf{i}$ is the local normal radius vector. This is useful for determining the spatial configuration of the vector field and selecting inflow and outflow dominated pixels, respectively.

Particle-based philosophy The global quantities are computed by summing up particles with positive and negative radial velocity separately, generating pure inflow and pure outflow maps.

4.2.6 Theoretical Accretion Model

The fundamental theory of hierarchical structure formation can provide a theoretical first order estimate of the accretion flows one would expect in the vicinity of a halo with given mass. This work uses the relation for the universal mass accretion history (MAH) found by van den Bosch (2002) to compute a theoretical relationship between the halo mass and the expected accretion rate onto a halo of the given mass. Based on the excursion set extension of standard Press-Schechter theory, they construct randomly sampled mass accretion histories, which then are fit by the universal relation:

$$\log\langle\Psi(M_0, z)\rangle = -0.301\left[\frac{\log(1+z)}{\log(1+z_f)}\right]^\nu, \tag{4.5}$$

where M_0 is the mass of the halo today (at $z = 0$) and Ψ is the MAH (ratio of M to M_0) as a function of M_0 and redshift. The mass accretion rate can then be obtained by computing the derivative of this MAH with regard to time:

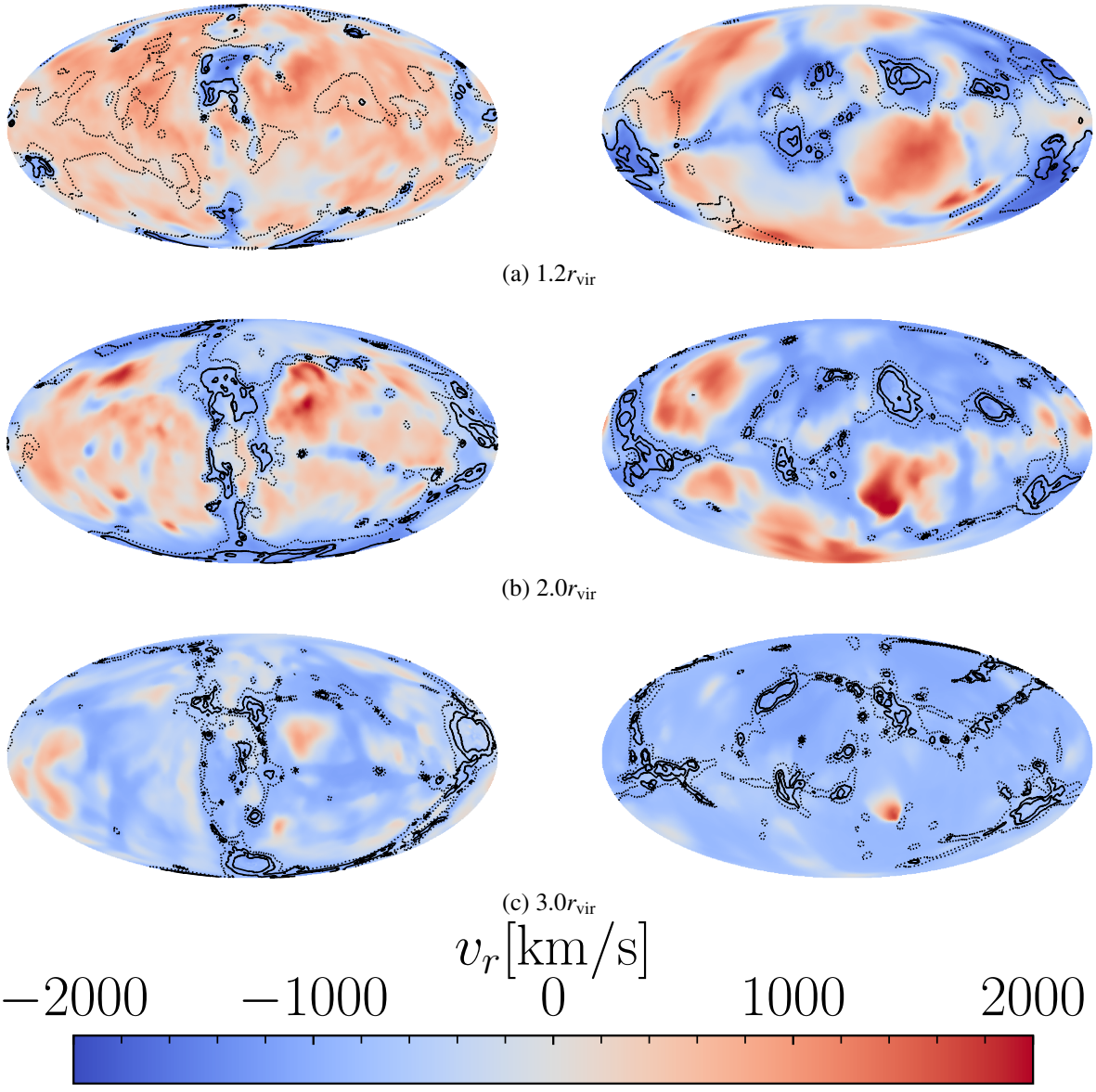
$$\dot{M} = M_0 \times \frac{d}{dt}\langle\Psi(M_0, z)\rangle. \tag{4.6}$$

The parameters z_f and ν are free fitting parameters in this model, but van den Bosch (2002) offers a recipe to directly compute them from cosmology and mass scale. Since from a simulation perspective all information about the cosmology is present, this prescription is used to calculate the curve. It should be noted that the van den Bosch (2002) approach is a backwards one: It calculates the MAH starting from the properties of the haloes today and reconstructs the assembly working towards higher redshifts. To compare the inflow of a general mass bin to the theoretical relation we therefore extrapolated the bin mass at $z = 0.25$ to an expected present-day mass using the linear growth factor

$$M_{\mathrm{bin},0} = \frac{M_{\mathrm{bin},z=0.25} D_0}{D(z = 0.25)}. \tag{4.7}$$

In this work $D_0 = D(z = 0)$ is calculated using the approximate formula found by Carroll et al. (1992) for simplicity

$$g(\Omega_\Lambda, \Omega_M) = D/a \approx \frac{5}{2}\Omega_M[\Omega_M^{4/7} - \Omega_\Lambda + (1 + \frac{\Omega_M}{2})(1 + \frac{\Omega_\Lambda}{70})]^{-1} \tag{4.8}$$



(a) $1.2r_{\mathrm{vir}}$

(b) $2.0r_{\mathrm{vir}}$

(c) $3.0r_{\mathrm{vir}}$

Figure 4.2: Exemplary total mass flow map generated with SMAC (Dolag et al., 2005b) for Cluster 05 (left column) and Cluster 20 (right column) in the sample. Red marks the outflow dominated pixels while the inflow dominated pixels are blue. Contours again mark the overdensity at the 1-δ and the 8-δ level.

We also employ an alternative approach, where the relationship between the halo mass at $z = 0.25$ and the halo mass today is left as a free-fitting parameter, that is parametrising

$$\dot{M} = \alpha \times M_{\rm bin} \times \frac{d}{dt}\langle\Psi(\alpha \times M_{bin}, z)\rangle. \tag{4.9}$$

The two methods are compared in the following section.

4.3 Characterising the Mass Flows in the Outskirts of Magneticum Haloes

In most conventional structure formation models, haloes are assumed to grow self-similarly and bottom-up with the additional assumption of spherical collapse as the main mechanism in the non-linear growth regime. Examples for this are the earlier described semi analytical MAH model from van den Bosch (2002) as well as the model from Dekel et al. (2009), both of which are built on the extended Press-Schechter formalism (EPS). However, the now well-studied cosmic web is already a manifestation of asphericities and non-linear effects arising in the large scale regime (Hidding et al., 2014), posing the questions whether accretion models based on sphericity and self-similarity hold in realistic cosmic environments such as fully hydrodynamical cosmological simulations, and whether self-similarity itself might already be broken at the large-scale flow level. Figure 4.1 shows the density, velocity, temperature and metallicity maps resulting from the scheme described in section 2.5 for an example halo with $M_{\rm vir} = 1.61 \times 10^{15} M_\odot$ (cluster 05). To illustrate the correlation between density and flow, temperature and metallicity, density contours in each panel indicate the regions with mean density and a factor of 3 and 8 times the mean density in the respective maps. As can clearly be seen, we find dense regions to be dominated by inflow and lower temperature gas indicating a cold filamentary inflow. In contrast underdense regions of higher temperature indicate an isotropic outflow most effectively expanding into underdense regions. To investigate this more closely, we split the maps into their inflowing and outflowing components and analyse them separately over a large range of radii and halo masses. For this we compute the instantaneous in- and outflow at five spherical radii ($r \in [1.2, 2.0, 3.0, 4.0, 5.0] \times r_{\rm vir}$) of increasing radius. An example of such a computation can be seen in Fig. 4.2 for two galaxy clusters from the $M_{\rm vir} > 10^{15} M_\odot$ bin, the 5-th (left column, also shown in Fig. 4.1) and 20-th (right column) most massive cluster in *Box2b/hr* respectively (hereafter referred to as cluster 5 and cluster 20) for the full radial range. As can be seen, the inflow (blue colour) follows the higher density regions radially, while the outflows (red colour) are distributed more isotropically across the underdense regions. For both haloes, the outflowing component fades at larger radii.

4.3.1 Accretion

To obtain a more statistical view of these observations, we compute the surface based in- and outflows for the complete sample (from $M_{\rm vir} = 10^{12} - 10^{15} M_\odot$). Figure 4.3 shows the flow rates versus halo mass at the five radial bins. The blue line in Fig. 4.3 shows the surface-based total gas inflow of the sample while the black solid line shows the DM accretion. For the gas inflow, we find an overall trend of rates increasing with halo mass that is consistent across the complete radial range from 1.2 to 5.0 $r_{\rm vir}$. This clearly demonstrates gas accretion to be a self-similar process from Milky Way-mass haloes to the most massive galaxy clusters, implicating halo internal processes to be the driver of the break in self-similarity, not the accretion flows. The comparison of dark matter (DM) inflow rates with the theoretical

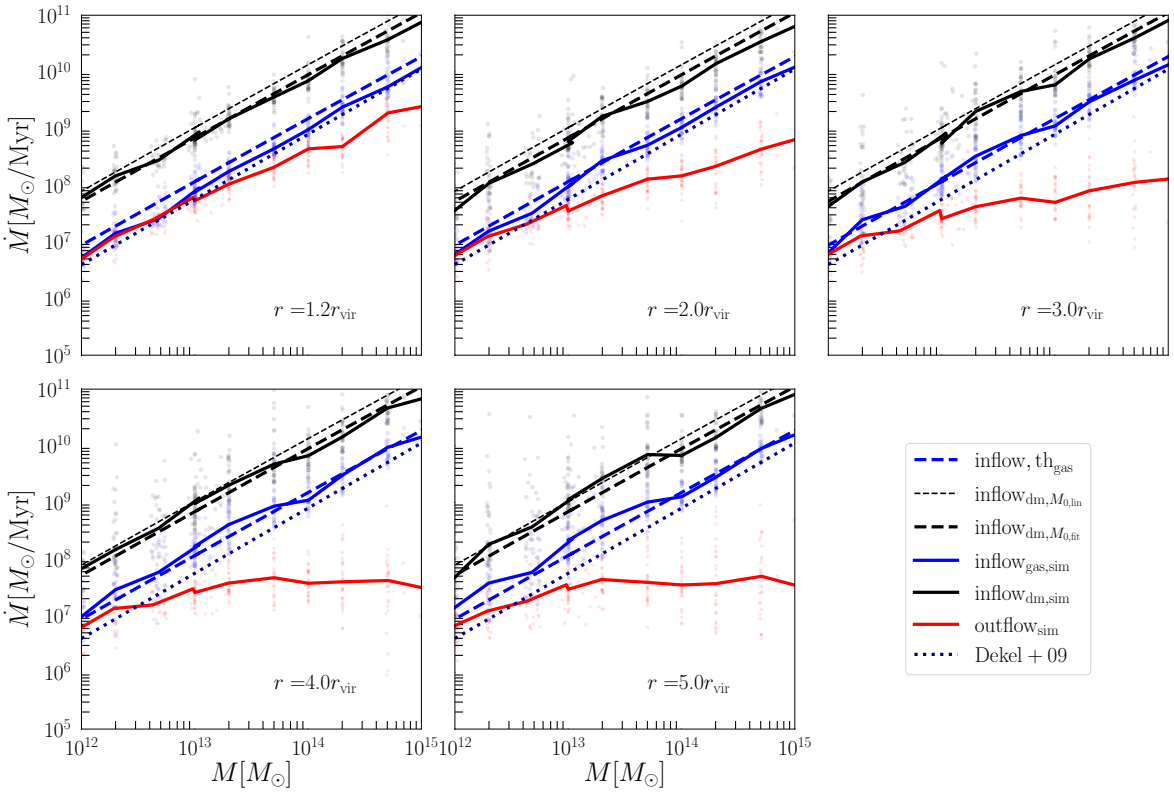


Figure 4.3: Comparison of the total in- (black and blue lines for DM and gas respectively) and outflow (red line for gas only) in the MAGNETICUM simulation to the van den Bosch (2002) model (dashed black lines, thin for the linearly extrapolated M_0, Eq. (4.7), bold for the fit M_0, Eq. (4.9)). The inflow component is decomposed into a DM accretion flow and a baryonic accretion flow using the baryon fraction and the Andreon (2010) model to compensate for the increasing stellar component at low masses. Additionally we show the gas accretion model presented by Dekel et al. (2009) as the dark blue dotted line. All flows are shown at 1.2,2,3,4 and 5 virial radii (different panels).

curves obtained from Eq. (4.7) (dashed black) demonstrates an over-estimation of accretion from dark-matter-only linear theory relative to full hydrodynamics. The overall shape of the linear infall scaling relation is nonetheless recovered well from the simulations. Strikingly, leaving the uncertainty about final halo masses to a fitting parameter according to Eq. (4.9) (dashed black) achieves an even better agreement between the DM infall relations, as the normalisation brings the curves to closer agreement with each other. This is remarkable when considering the simplicity of the underlying assumptions: The calculation of van den Bosch (2002) is based on a purely linear evolution of the DM density perturbation field, while the haloes considered here have significant amounts of gas and lie firmly in the non-linear regime. Additionally, as Fig. 4.2 shows, the infall is geometrically far from the spherical symmetry of the top-hat collapse model that the upcrossing thresholds of the excursion set formalism are obtained from (e.g. Navarro et al., 1997), but rather is organised into filamentary structures that dominate the overall accretion flow. Comparing the inflowing gas curves (blue) of Fig. 4.3 to the DM curves shows that even close to the virial surface of the halo the infalling gas is still tightly coupled to the DM accompanying it. Only upon encountering the pressure supported, hotter gas closer to the halo centre at the shock surfaces (for a further discussion on where these surfaces are located, see Section 4.4) that especially massive haloes drive in this region will this gas uncouple from the large-scale flow (Shi, 2016). The impact of this heating on the accretion flow can be seen in comparing the theoretical gas accretion rate (dashed blue line), obtained by multiplying the DM inflow with the cosmic baryon fraction, to the measured gas flow across the five radial bins. Purely gravitationally (as derived from the accretion model) the expected gas accretion rate is higher then the actual accretion achieved taking hydrodynamics into account. From $1.2 - 2r_{\mathrm{vir}}$, this discrepancy is consistent with mass, even though it is not present for the inflow computed with the model by Dekel et al. (2009). Beyond $3r_{\mathrm{vir}}$ the less massive haloes ($M < 2 \times 10^{13} M_{\odot}$) reach the theoretically predicted gas inflow rate, while the discrepancy in the high-mass bins persists to larger radii. This effect is visible in both the DM and the gas component. However, as can be seen by the thin dashed line in Fig. 4.3, this discrepancy can be almost entirely attributed to the linear extrapolation, leading to an overshooting in the theoretical estimate. Leaving the scaling as a fitting parameter (as described in Section 4.2) leads to much better agreement.

4.3.2 Outflow

There are two main channels that can drive outflowing motion in the outskirts of an assembling halo, namely the conversion of gravitational energy from mergers and accretion to thermal energy of the gas via virialization processes and heating from AGN and star formation in the galaxies present in the haloes. The outflowing component is shown in red in Fig. 4.3. In contrast to the accretion rate, the outflowing component flattens out with increasing radius, being almost completely flat at 5 r_{vir}, breaking the self-similarity. Figure 4.4 additionally shows the relative outflow strength (mass flow rate normalized to the halo mass) for each mass bin at the five radii. The breakdown of strong outflows at the high mass end can be seen even more pronounced in this figure, especially at large radii.

This is most likely a manifestation of the different effectiveness of feedback processes at different scales. At galaxy scales, processes like stellar feedback and AGN feedback can kick gas out to several virial radii, maintaining a high outflow rate to larger relative distances, while in galaxy clusters and massive groups the deeper potential well can balance out the impact of heating. Note that numerical simulations employing simplified AGN feedback schemes can additionally over-enhance the impact of the (in the case of Magneticum purely thermal) feedback at galaxy to group scales, which we will discuss further in Section 4.6.

Because of the contrast between the thermal nature of the outflow and the gravitational nature of the inflow, one would also expect a difference in the spatial distribution of the two

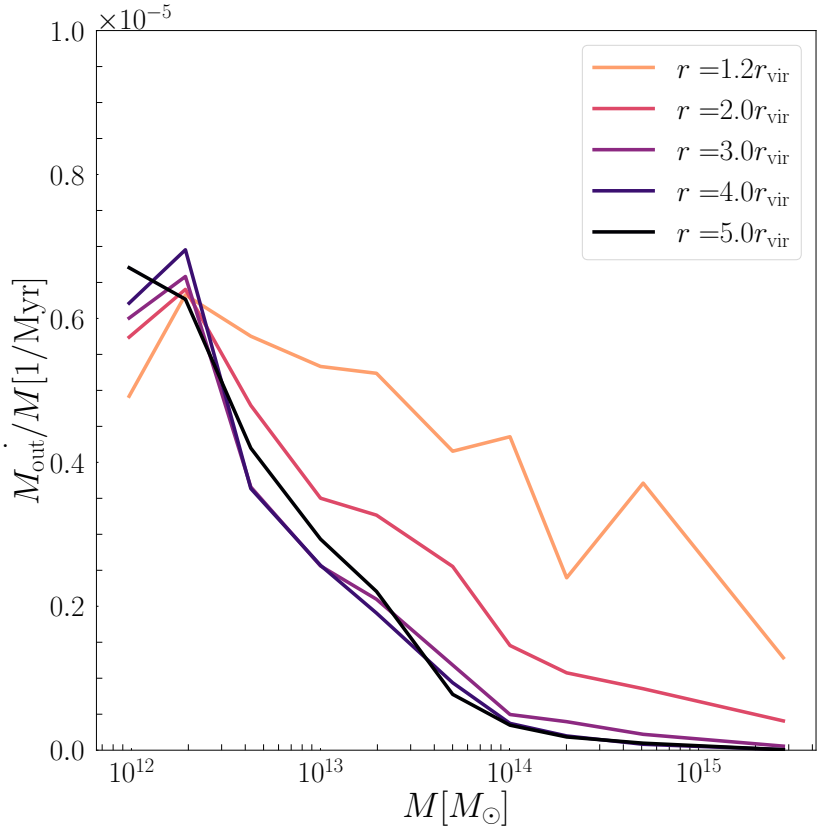


Figure 4.4: Relative outflow strength (the outflow rate divided by the respective halo mass, $\frac{\dot{M}}{M}$) as a function of mass. The line colours indicate the different radii the flow strength is measured at.

gas components with the outflows being more isotropically distributed than the inflows due to their thermal origin. The map-making scheme described in Section 4.2 provides the data to verify this for the numerically simulated haloes, which we will discuss in further detail in the following section.

4.3.3 Flow Geometry

In Figure 4.2 we showed the surface distribution of in- and outflow dominated pixels for two example haloes. It is apparent that inflowing gas is generally more concentrated than outflowing gas, consistent with the picture of a filamentary inflow driven by gravity versus thermally driven outflows. To obtain a more statistical measure of the geometrical properties of the gas distribution (or any distribution of a scalar quantity) the flow field can be reduced to a power spectrum by computing its harmonic decomposition. Comparable techniques have been used in the past to identify preferred directions of infall for satellite galaxies (Libeskind et al., 2011), to measure the degree of filamentary to isotropic accretion in isolated cluster simulations (Vallés-Pérez et al., 2020), and to study the correlation of the 2D-azimuthal symmetries in gas and DM to various halo properties (Gouin et al., 2022). We calculate the aspherical excess on the sphere, following closely the approach by Gouin et al. (2022). This excess is given by the sum of all multipole moments higher than the monopole normalized to the monopole power, truncating the sum at the 9-th order to ideally capture the large-scale anisotropic inflow modes:

$$\zeta = \frac{1}{C_0} \sum_{l=1}^{9} (2l+1) C_l. \tag{4.10}$$

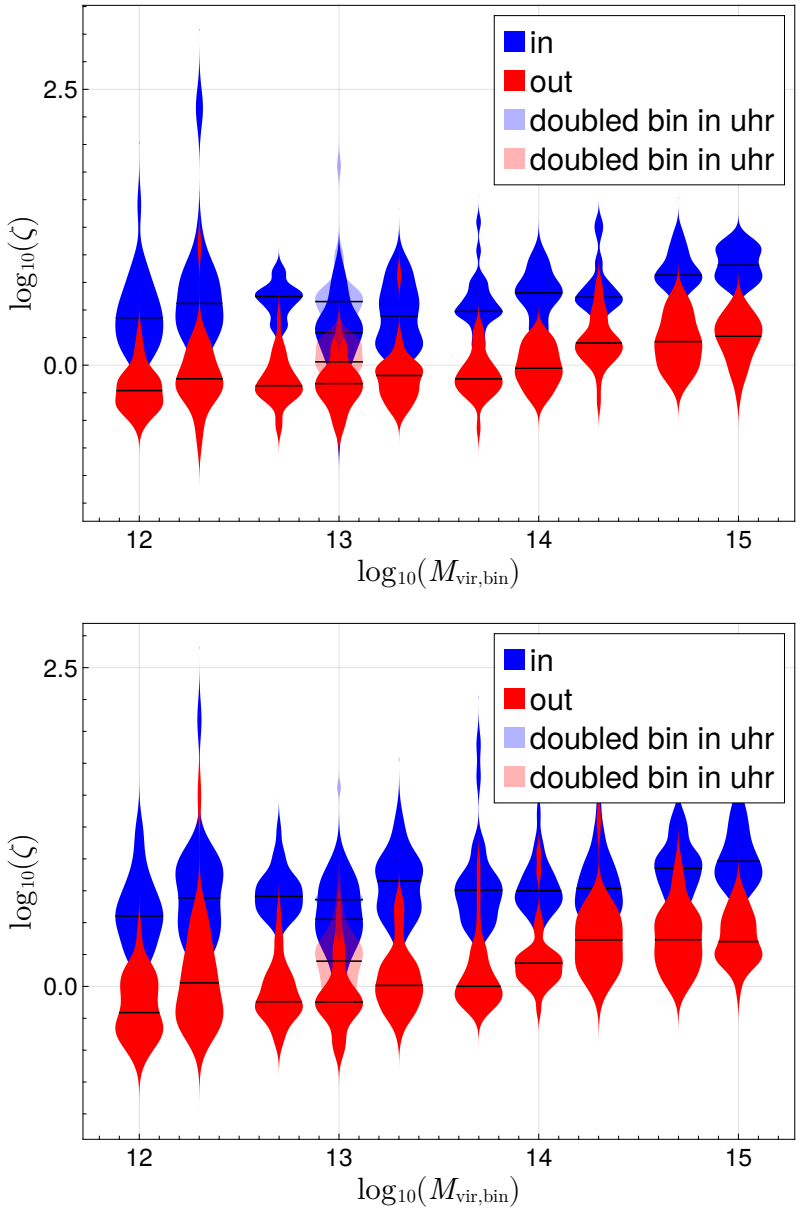


Figure 4.5: Aspherical excess of the flows parametrized by the asphericity parameter ζ at $1.2r_{\mathrm{vir}}$ (left) and $2.0r_{\mathrm{vir}}$ (right) for the in- and out-flowing components, respectively. The violins show the vertical distribution, while the black horizontal lines show the median for each bin. The bin present in both simulations (*Box2b/hr* and *Box4/uhr*) is plotted twice to indicate the transition in resolution.

A more spherically homogeneous field has less power in the non-isotropic angular modes, thus lowering ζ with a perfectly homogenous inflow field having a ζ of 0. For a more complex inflow field the exact value of ζ will depend on the spatial configuration (for example filament thickness and alignment), so to disentangle the exact structure the full spectrum of the spherical harmonics is necessary. A more detailed study on this parameter, the Asphericity ζ will be presented by Seidel et al. (in prep.)

Figure 4.5 shows the distribution of the asphericity for each mass bin at $1.2r_{\rm vir}$ (left panel) and $2r_{\rm vir}$ (right panel). In agreement with expectations, the distribution of inflowing gas is consistently more aspherical than the outflowing component. Additionally, the inflow asphericity exhibits a wider spread between systems. This clearly demonstrates the different mechanisms at play for the in- and outflowing component. While gravity organises the inflows into filaments according to the local environment of a halo, thus exhibiting a greater variance, the thermal processes that drive the outflows are more isotropic in nature and thus show less variance between haloes in different environments. The stability of this discrepancy across the mass range indicates, that groups and galaxies are indeed also connected to filamentary flows, similar to their more massive counterparts. This reflects the fractal nature of the cosmic web (Gaite, 2019), providing connectivity for galaxies and groups via low mass filaments.

Only a slight positive mass trend is apparent, indicating that the flow geometry outside of the virial radius is similar across the mass scales. Especially the lack of a low-mass end enhancement is striking as this implies that the outflows generated by baryonic feedback processes do not disturb the homogeneity of the hot gas outside of the virial surface even for small groups. This result is remarkable because feedback strength in a galaxy varies on small spatial scales, so one would expect more power in the high-frequency modes in the low mass bins, where these processes contribute more to the overall outflow. A potential reason for the missing signal here is the currently simplified sub-grid model for feedback in the Magneticum simulations with a distinct lack of directional kinetic feedback.

A discrepancy between the two simulation volumes can be seen at the mass bin with $10^{13} M_{\odot}$: In contrast to the mass flow rates, which are averaged over the entire spherical surface the asphericity is enhanced in the smaller, higher-resolution *Box4/uhr*. A possible explanation is that the highest mass bin of *Box4/uhr* by construction contains some of the largest collapsed haloes in the box, which tend to be very active and rather atypical in small volume cosmological simulations, so the bin value might simply not be representative for this mass bin. An additional possible factor is the difference of resolution, leading to a better resolved web structure around the haloes in the smaller *Box4/uhr*. This can be understood by considering how the total mass is split into discrete particles: In the higher-resolution box, particles have a smaller characteristic scale, which, when keeping the physical scale constant, will produce a fluctuation of the flow field with a smaller minimal scale than in the low-resolution case.

4.3.4 Redshift Evolution of the Measured Flows

In the hierarchical picture of structure formation haloes form bottom-up with low mass haloes forming early and then collapsing into larger structures at late times (Press & Schechter, 1974). As the cosmic web assembles we thus expect the accretion flow rates of our sample of isolated haloes to decrease with time overall. We consider the redshift evolution of the flows: Fig. 4.6 shows the inflow (left column) outflow (middle column) and the net accretion rate as a function of mass at different times, with the colour of the curves indicating the redshifts across all panels. We find that the inflow rates at all halo masses decrease self similarly with time. In contrast, the outflow is generally more stable over time than the inflow, showing an overall decrease by a factor of 2-4 vs. a factor of 5-8 for the inflow. Both flow modes

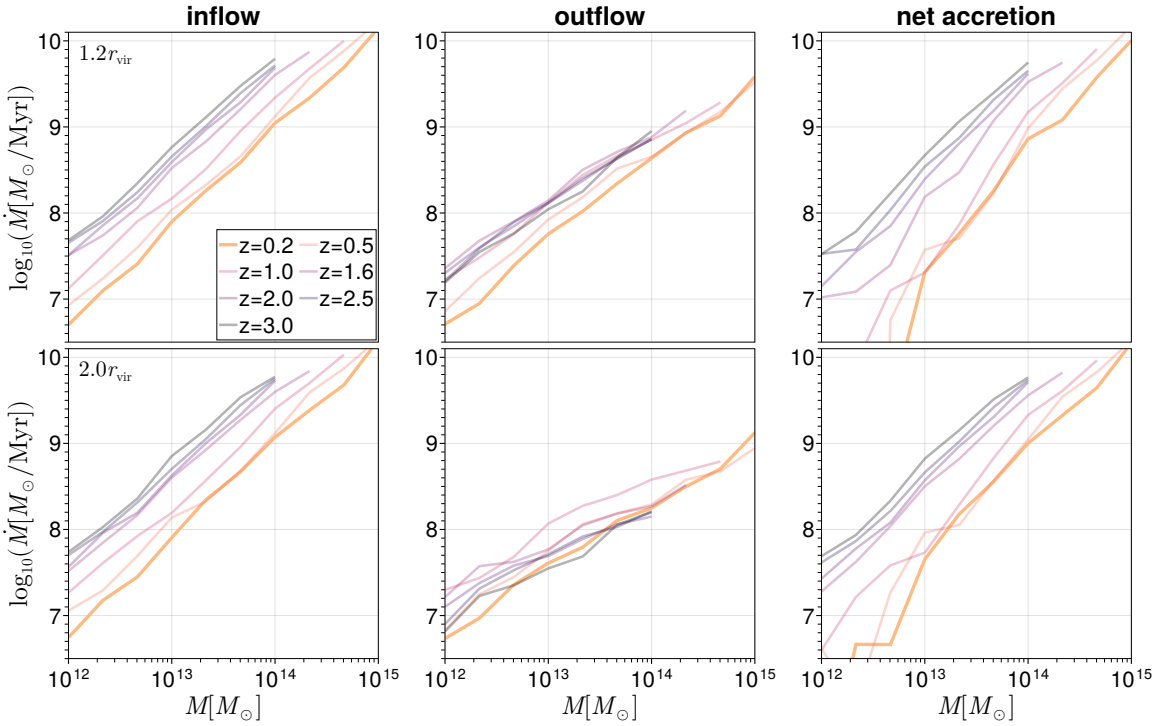


Figure 4.6: Redshift evolution of in-, out- and net flow (inflow − outflow) at $1.2r_{vir}$ (top row) and at $2.0r_{vir}$ (bottom row). The bin masses (x-axis) are identical to the ones used in Fig. 4.3. The colours indicate the redshift of the curve.

vary mostly self-similarly across the entire mass range with decreasing redshift, conserving the slope of the flow-mass relationships. The consequence of relatively stronger outflows at the low mass end, which was discussed in the previous section, can be seen in the rightmost panel: While all haloes experience a net inflow, its strength is proportional to halo mass, with the low-mass end exhibiting significantly lower net inflow than the massive clusters, which breaks the self-similarity in the net accretion rate. With decreasing redshift this relationship steepens, caused by a slight increase in the slope of the outflow-mass relationship, further highlighting the breakdown of self-similarity between the outflows in low and high mass haloes. Cluster-size objects at late times seem to be able to compensate the relatively weaker impact of thermal feedback more effectively at late times, steepening the outflow mass relationship.

One possible explanation for this is that at low redshifts most cluster-sized objects have undergone a massive merger through their assembly history and thus also have more energy injected into their outskirts as well as merger shocks or even MAH shock fronts where the gas is heated rapidly (Zhang et al., 2020). As this transition between feedback driven and shock propagation driven outflows (where the latter are sourced by gravitational heating and mergers) also impacts the chemical evolution of the gas, the following section will analyse the shocks more closely before the interacting thermal and chemical properties of the pre- and post-shock gas are considered.

4.4 Shocks in the Outskirts of Magneticum Haloes

Shocks play a central role in the formation of structures and the fragmentation of matter therein. In the simplest picture of a collapsing gas cloud (e.g. Rees & Ostriker (1977)) with even slight deviations from a perfectly spherical collapse, shock heating thermalises the

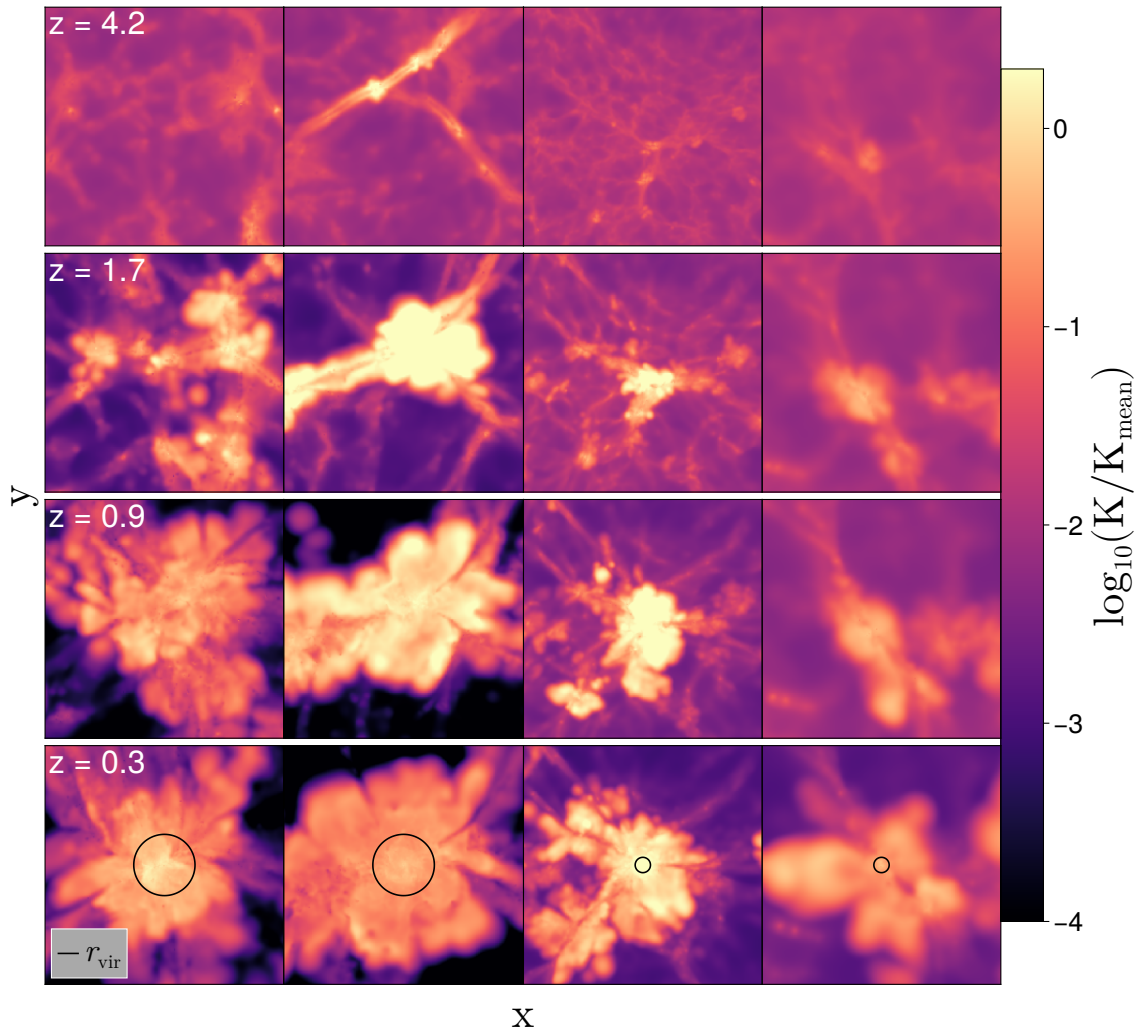


Figure 4.7: Entropy evolution of a $1.3 \times 10^{15} M_{\odot}$ mass non cool-core cluster, a $1.6 \times 10^{15} M_{\odot}$ cool-core cluster, a $1.6 \times 10^{13} M_{\odot}$ size group and a $0.91 \times 10^{12} M_{\odot}$ halo from left to right. The black circle indicates the virial radius of each object. The box lengths are scaled to 10 times the virial radius for the clusters and 40 times the virial radius for the groups/galaxies with a slice thickness of 1 Mpc/h for all images.

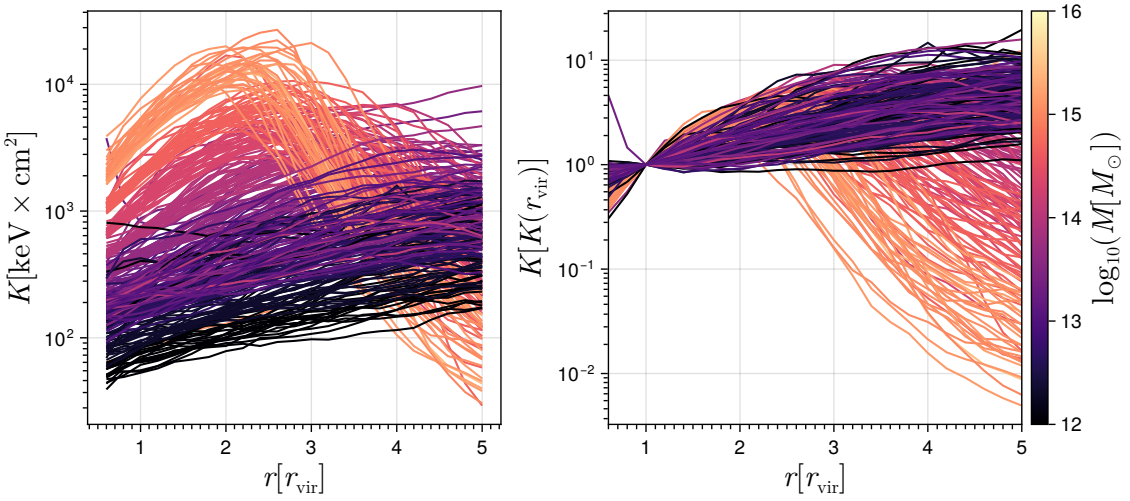


Figure 4.8: Absolute (left panel) and scaled ($K(r)/K(r_{\mathrm{vir}})$ right panel) radial entropy profiles for all haloes in the sample. The virial mass is indicated by the colour of the curve.

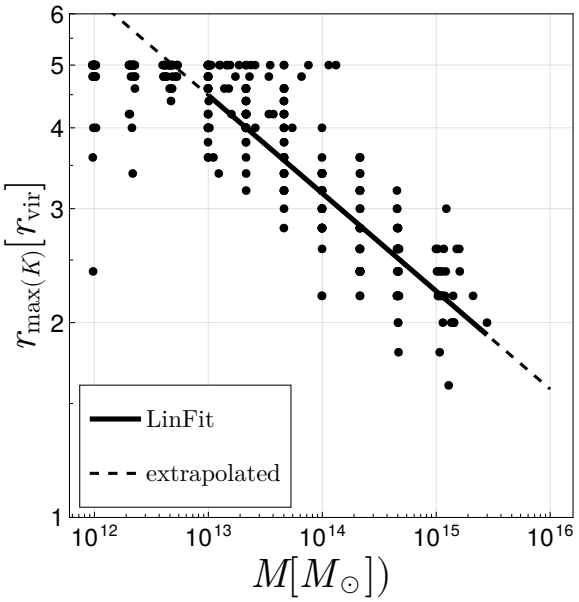


Figure 4.9: Mass dependence of the radius of maximal entropy. The dots represent the individual haloes of the sample. The line shows a Linear fit in log-log space obtained from the haloes in the range where there is a clear entropy peak visible. The obtained parameters are $t = 2.6193 \pm 0.1157$ and $m = -0.1513 \pm 0.0008$ using a $\log(r_{\mathrm{max}(K)}) = m \times \log(M/M_\odot) + t$ model. The tight spacing of the dots along the x-axis reflects the mass spread of the bins, which we have optimized to be as small as possible (see Section 4.2)

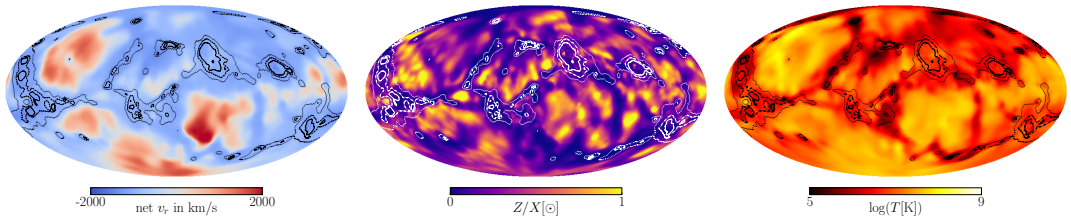


Figure 4.10: Comparison of the gas properties (Average radial velocity (left), Metallicity (middle) and Temperature (right)) at 2.0 $r_{\rm vir}$ for cluster 20. Contours the same as in Fig. 4.1

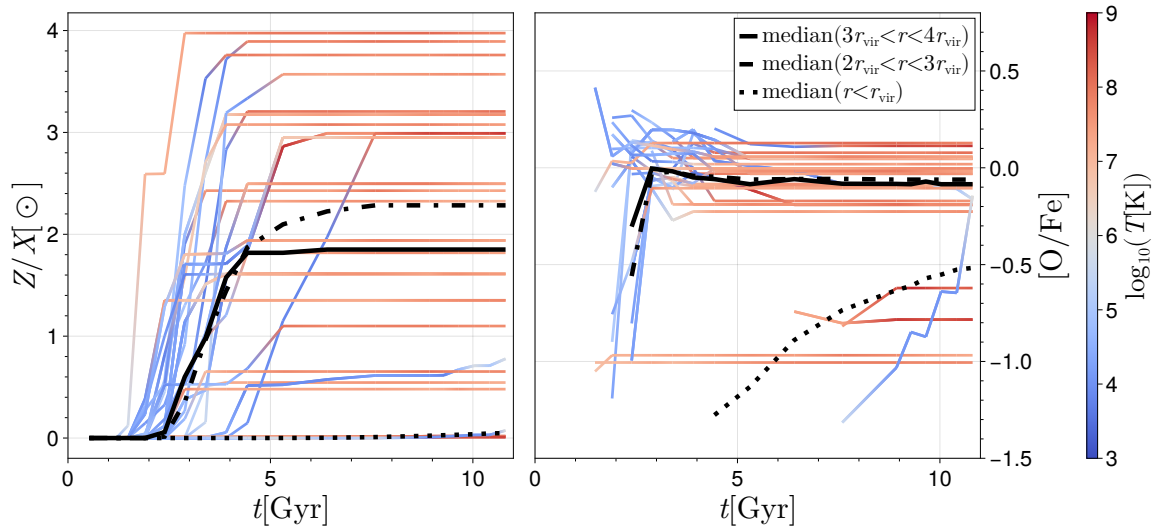


Figure 4.11: Evolution tracks of 40 individual particles in overall metallicity (left panel) and O/Fe ratio (right panel). Particles were selected randomly between $3r_{\rm vir}$ and $4r_{\rm vir}$ with a radial peculiar velocity exceeding 100 km/s (outflowing) and a final metal mass exceeding $m_Z/m_H = 10^{-4}$. The black lines show the medians of 1000 randomly selected particles each for three different radial ranges. The line colour indicates the temperature of the particle at the given scale factor.

kinetic energy and critically influences further mass accretion: Depending on the ratio of the (radiative) cooling time to the infall time $\frac{t_{\rm cool}}{t_{\rm dyn}}$, collapse might either continue in free-fall if cooling is efficient enough to diminish the pressure support from the heated gas (case I, $t_{\rm cool} < t_{\rm dyn}$) or enter a quasi-static contraction stage with a hot atmosphere (case II, $t_{\rm cool} > t_{\rm dyn}$) (Dekel et al., 2009). The distinction between these regimes is determined by the overall mass of the system, with the transitional regime traditionally in the range of $M_{\rm vir} = 10^{10} - 10^{12} M_\odot$ (Rees & Ostriker, 1977). An important distinction between the two modes of accretion is the radius at which the shock stabilises. In the low-mass case (I) the stabilisation radius is deep inside the DM halo ($r_{\rm shock} \ll r_{\rm vir}$) while more massive haloes are expected to have their accretion shocks stabilise on distances of the order of the virial radius or larger $r_{\rm shock} \geq r_{\rm vir}$.

In the complex environment of non-linear structure formation the transition between the rapid-cooling and slow-cooling accretion channels, namely the shock position, is significantly impacted by additional factors: Denser gas is organised into filaments at inflow and thus cools more efficiently and penetrates further into the halo unaffected by the shock (Dekel et al., 2009). Furthermore, as previously mentioned, merger shocks interact with the accretion shocks (Zhang et al., 2020) in the outskirts of massive clusters. Additionally the energy injected by feedback plays a more important role at the low mass end. This affects both the inflowing and the outflowing gas: The outflowing component is heated and can thus reach

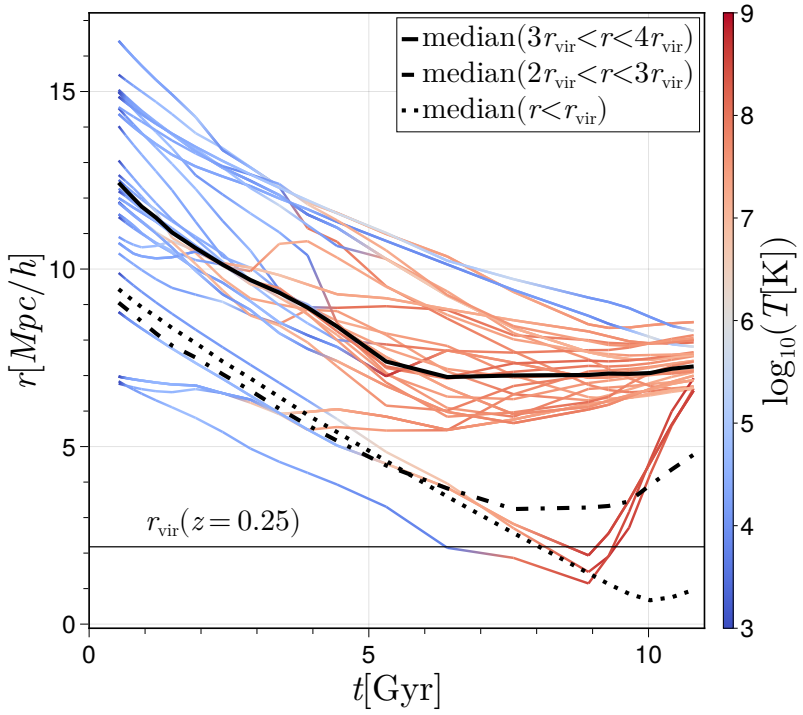


Figure 4.12: Evolution tracks of the same 40 particles as in Fig. 4.11 in radial distance to the cluster centre. The black lines again show the medians of 1000 randomly selected particles each for three different radial ranges. The line colour indicates the temperature of the particle at the given scale factor.

larger radii in the shallower potential of low-mass haloes. On the other hand feedback can also lead to a gentle heating of the infalling gas before being shocked (Murante et al., 2012), especially in low mass haloes. Hydrodynamical cosmological simulations like Magneticum therefore offer a unique laboratory to study the cluster shock dynamics in realistic environments and probe for the stability of simple mass-scaling arguments like the one outlined above.

One cannot draw precise conclusions about the position of the shocks themselves from the flow fields alone. To assess the scale dependence of shock strength and position, we calculate the pseudo-entropy (K), given by e.g. Zhang et al. (2020) as

$$K = \frac{T}{\rho^{\gamma-1}}, \tag{4.11}$$

averaged over radial shells across the complete sample, where usually an adiabatic index $\gamma = 5/3$ is assumed. Figure 4.7 shows the entropy environment in a quadratic slice of $10r_{\rm vir}$ side length for halo 20 ($10^{15} M_\odot$) and halo 5 ($10^{15} M_\odot$) from *Box2b/hr* as well as halo 31 ($10^{13} M_\odot$) and halo 538 ($10^{12} M_\odot$) from *Box4/uhr*. Generally it can be seen from the bright entropy edges, where the entropy peaks before dropping off, that the accretion shocks stabilise at much larger relative radii for the group size and galactic haloes, aided by the shallower potential of these haloes and the thermal feedback. This can also be seen in Fig. 4.4: The outflow strength relative to the halo mass is almost monotonically decreasing as a function of mass at larger radii. In general, Fig. 4.7 demonstrates that the radial peaks of entropy serve as a simplified tracer of where the outer shock surfaces lie.

We extend the radial profiles inwards to $0.6r_{\rm vir}$ in order to detect the entropy peaks if they are found at smaller halocentric distances. Figure 4.8 shows these radial entropy profiles for all haloes in the sample in absolute entropy (left column) and scaled to the entropy at the virial radius (right column). There is a clear evolution in the shape of these profiles with mass: The shocks (i.e. the entropy peaks) are smoothed out with decreasing mass of the central halo. For the haloes that exhibit an entropy peak within the probed radial range (up to $5r_{\rm vir}$), it is generally broader and peaked at greater radii with decreasing mass. This is in line with the general finding of the so-called closure radius (i.e. the radius at which the baryon fraction reaches the cosmic mean value) to scale with halo mass, as observed across various simulations in the group/cluster regime (Angelinelli et al., 2023). Most of the haloes that show a distinguishable peak have it in the region between $2 - 4r_{\rm vir}$. This is consistent with slow cooling accretion shocks and possibly additionally merger driven outwards shock propagation. To demonstrate this more quantitatively, Fig. 4.9 shows the radius of maximum entropy as a function of mass for our halo sample. We find a consistent trend of decreasing scaled radius of maximum entropy as a proxy for the approximate shock position with mass. A possible explanation is the relatively stronger potential the gas moves into these heavier haloes, allowing the hot post-shock gas to expand to relatively smaller radii overall. The general dynamics can be expected to be consistent across the total mass range. We will therefore now investigate the interaction of gas accretion and shocks specifically for a galaxy cluster from the highest mass bin.

4.5 Case Study: Cluster 20

The thermal properties of the infalling and outflowing gas and how the two components (in- and outflow) interact at the shock boundaries is of critical importance for many processes internal to the halo, for example replenishment of gas reservoirs for star formation in galaxies or the dynamical states of galaxy clusters. Because the jumps in the thermal properties of the gas are best resolved in the largest haloes (i.e. the shocks are the most pronounced), we will

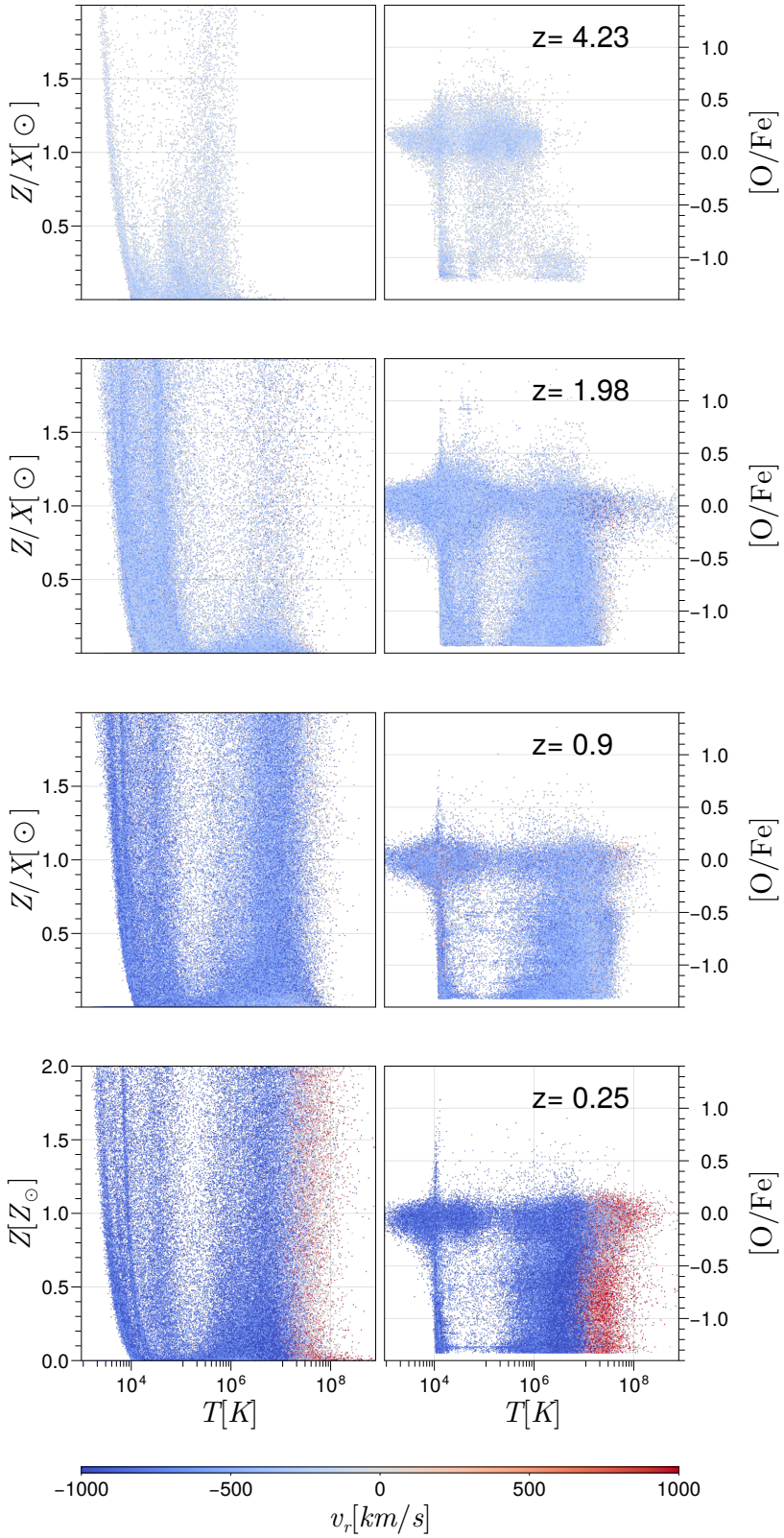


Figure 4.13: Particle temperature versus metallicity (left column) and oxygen/iron ratio (right column) evolution with redshift. Inflowing particles are shown in blue while outflowing particles are shown in red.

now focus on the gas properties in one of the biggest clusters in the MAGNETICUM simulations, cluster 20 which was shown to be an excellent match for the observed galaxy cluster Abell 2744 by Kimmig et al. (2023). Specifically we will focus on the infall and enrichment history of the gas that constitutes the outflowing component today. The abundance of heavy elements is routinely used in the literature to determine the origin and enrichment time of gas as well as potential mechanisms to strip it from its host galaxies in cluster environments (e.g. Biffi et al., 2018). The velocity, temperature and metallicity maps for this cluster are shown in Fig. 4.10. Consistent with expectations for an Abell 2744 counterpart, this cluster is fed by multiple filaments, mirroring the multiple mergers it is currently undergoing (Kimmig et al., 2023, see). We will therefore elucidate specifically the impact of the thermal structure and accretion on the metallicity of the outflowing gas. We will then assume a more global perspective on these gas properties in the final section.

The total metallicity of the gas found in the outskirts of clusters and its radial and azimuthal distribution can shed light on the overall dynamics of the infalling gas, that is where it is cold and dense enough to form stars that provide an influx of metals. This information can be further compounded by considering the enrichment type by analysing the mass ratios of different elements predominantly generated in different enrichment processes. One indicator for the type of enrichment and critically when it takes place is the ratio of oxygen to iron mass in the gas, as oxygen is the most common alpha element (Kobayashi et al., 2020). Early-type enrichment (i.e., enrichment from massive and short-lived stars on short timescales) is predominantly generated by core-collapse supernovae type II (e.g. Nomoto et al., 2013, Loewenstein, 2006), which produce lighter (alpha) elements in greater abundance and thus increase the ratio of oxygen to iron mass. Significant late-type enrichment, which is generated by thermonuclear supernovae type Ia, lowers this ratio if the gas is in contact with the stellar component on longer timescales (de Plaa et al., 2007). Extending the particle tracing method introduced by Biffi et al. (2018) to larger radii we follow the thermal and chemical evolution of the outskirt gas as it is accreted and heated by the central cluster.

Figure 4.11 shows the evolution tracks of gas particles that end up in the outflowing component of the cluster at the last snapshot ($z = 0.25$) with regards to total metallicity (left panel) and O/Fe ratio (right panel). Here O/Fe is defined as $[\mathrm{O/Fe}] = \log(\frac{m_\mathrm{O}}{m_\mathrm{Fe}}) - log(\frac{m_\mathrm{O}}{m_\mathrm{Fe}})_\odot$, using again the mass fraction from (Wiersma et al., 2009). Particles were selected from three radial bins (1000 particles per bin) within $1r_\mathrm{vir}$, between $2r_\mathrm{vir}$ and $3r_\mathrm{vir}$ and between $3r_\mathrm{vir}$ and $4r_\mathrm{vir}$. The coloured tracks show the evolution of 40 randomly selected particles from the outermost bin with blue indicating a cold particle temperature and red a hot temperature. Both panels demonstrate enrichment in the outflowing component to happen primarily early on, while the particles are infalling or in the halo centre before they are heated. Essentially all vertical movement in the left panel (increasing overall metallicity) occurs before $t \approx 6$Gyr and critically also before the particles are heated. Once the infalling particles are heated to the virial temperature, no new stars are formed in their surroundings as they become part of the diffuse cluster atmosphere, stopping also the influx of metals. This is also visible in the O/Fe ratio: Particles are first enriched by core-collapse supernovae, causing their oxygen mass to increase relative to their iron mass. At later times, type Ia supernovae decrease this ratio, but this process is eventually stopped once the particles are heated completely, leaving the particles stable at relatively high oxygen to iron ratios. A second population of particles, with a lower final oxygen to iron ratio can be seen in both panels. These particles are heated early on, remain at low metallicities and undergo almost no type Ia enrichment. Comparing the median lines at different radii, the difference between the enrichment processes in- and outside the virial surface become apparent: While the two radial regions in the outskirts are enriched early and settle on a high oxygen-to-iron ratio (see also Biffi et al., 2018), the gas particles inside the virial radius get enriched much later and do not reach the same O/Fe ratios due to metal influx predominantly from thermonuclear supernovae.

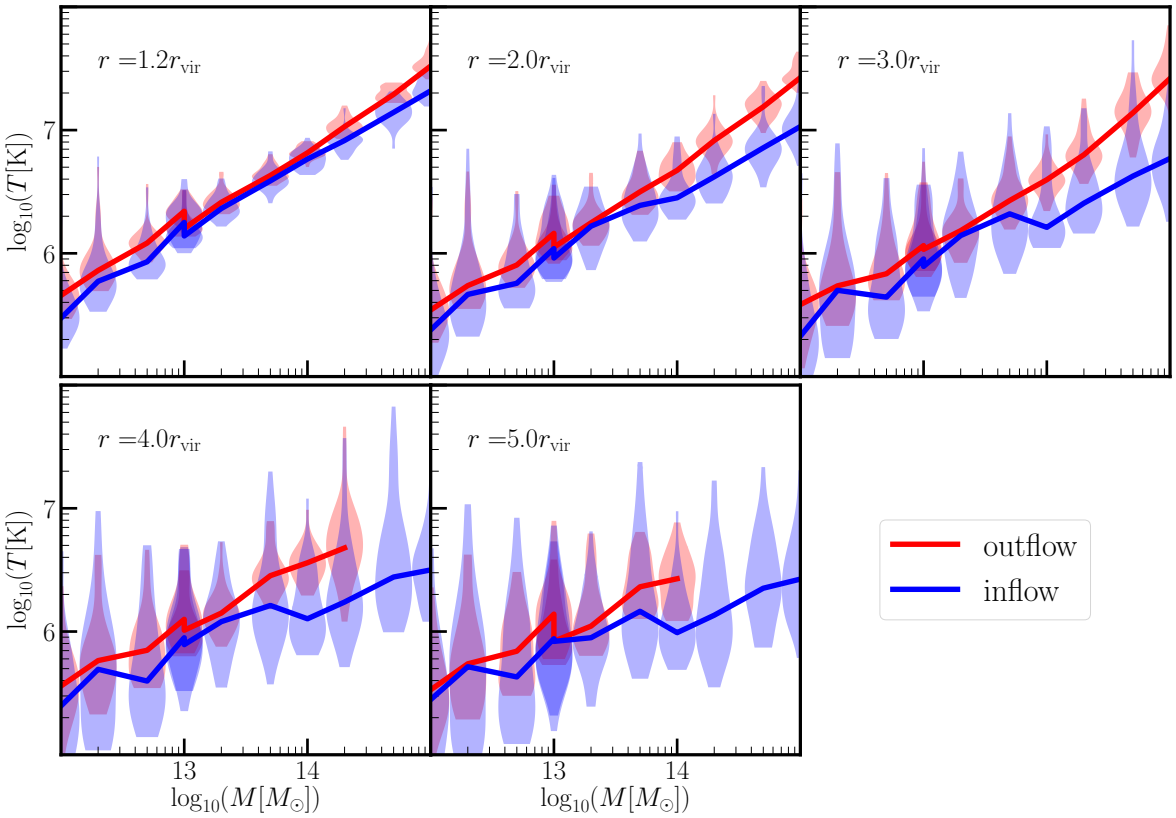


Figure 4.14: Temperature of net in- and outflow as a function of mass at five radii for the full halo sample. The spread of each bin is indicated by the red and blue vertical distributions. The cutoff at $10^{14} M_\odot$ for $r \geq 4.0 r_{\rm vir}$ stems from the fact that there are no pixels with net outflow at this scale and does not indicate zero outflow or zero temperature.

The radial evolution of these particles is shown in Fig. 4.12. It demonstrates a similar radial origin for the outflowing components at $3r_{\rm vir}$ to $4r_{\rm vir}$. There are, however, also particles that rapidly get kicked to these extreme halo-centric distances despite originally being accreted to well within $1r_{\rm vir}$ (see the lowest trajectories in the Fig. 4.12). These particles are most likely ejected by the massive merger that cluster 20 undergoes at late times (Kimmig et al., 2023) and demonstrates how even processes that happen on relatively long time scales – such as cluster mergers – can influence the dynamics on very short timescales and induce large velocities. This is also a channel through which halo-internal processes can directly influence the dynamics in the peripheral environments of these massive clusters and as such is an interesting subject for future work on dynamically very active cluster or supercluster regions.

To compound the information from the purely outflowing component, Fig. 4.13 shows the metallicity–temperature phase space for all particles in the outskirt of cluster 20 between $1.2r_{\rm vir}$ and $3.0r_{\rm vir}$ (using the final $r_{\rm vir}$ at $z = 0.25$) for different redshifts with blue indicating inflowing and red indicating outflowing particles. There is a clear temperature split between the hot and cold component of outskirt gas. In overall metallicity, the hot outflowing gas is slightly more spread out than the more pristine inflowing gas. (see also: Fig. 4.11). In the O/Fe-T plane the outflowing gas is distributed almost identically to the inflowing component, providing further evidence that the chemical evolution is largely stopped after infall. Note that in this cluster, which assembles rather late in time, none of the outskirt gas particles from z=0 show significant metal enrichment at z=4. We find that the evolution of the cluster gas elemental abundances starts out at high-redshift being strongly alpha enhanced, matching expectations also for the elements in the stars (Kimmig et al., 2023). As time passes, however, the gas is quickly enriched by SN Ia, strongly reducing [O/Fe] while also increasing [Z], especially within the hot gas phase. This is consistent with cluster 20 lacking a massive protocluster progenitor at z=4. Clusters with high $M_{\rm vir} > 10^{13} M_{\odot}$ in contrast, can already host a hot and metal enriched atmosphere, as shown by Remus et al. (2023).

In summary this study of cluster 20 largely confirms the standard picture of cluster accretion, with the gas infalling through dense and relatively cold filaments, enriching on infall and then being heated at the shock surface or below. Figure 4.11 clearly shows the chemical development being frozen in after the infalling phase and the subsequent heating is complete, with the final enrichment being dependent on the conditions during infall. We now test these findings across the whole mass sample to verify whether they generalise and are valid across the halo mass range probed in this study or if they might break down at the low-mass end, where the dynamics are more dominated by feedback.

4.6 Global Phase Properties of the Flowing Gas

We now extend the investigation of the thermal and chemical properties to the whole sample to verify consistency with the findings of the previous section and to analyse the mass scaling behaviour of these properties.

4.6.1 Temperature

Figure 4.14 depicts the mean temperature of the gas present in the halo outskirts for the full halo sample split into in- and outflowing gas (blue and red violins). The red and blue curves indicate the median of the respective mass bin. While Fig. 4.3 considered the total particle-based flow, as explained in Sect. 2.6, here only pixels with a net in- or outflow are considered for the blue and red curves, respectively. The linearity of the red and blue median curves in Fig. 4.14–in- and outflow respectively–demonstrates a clear mass-scaling behaviour of the

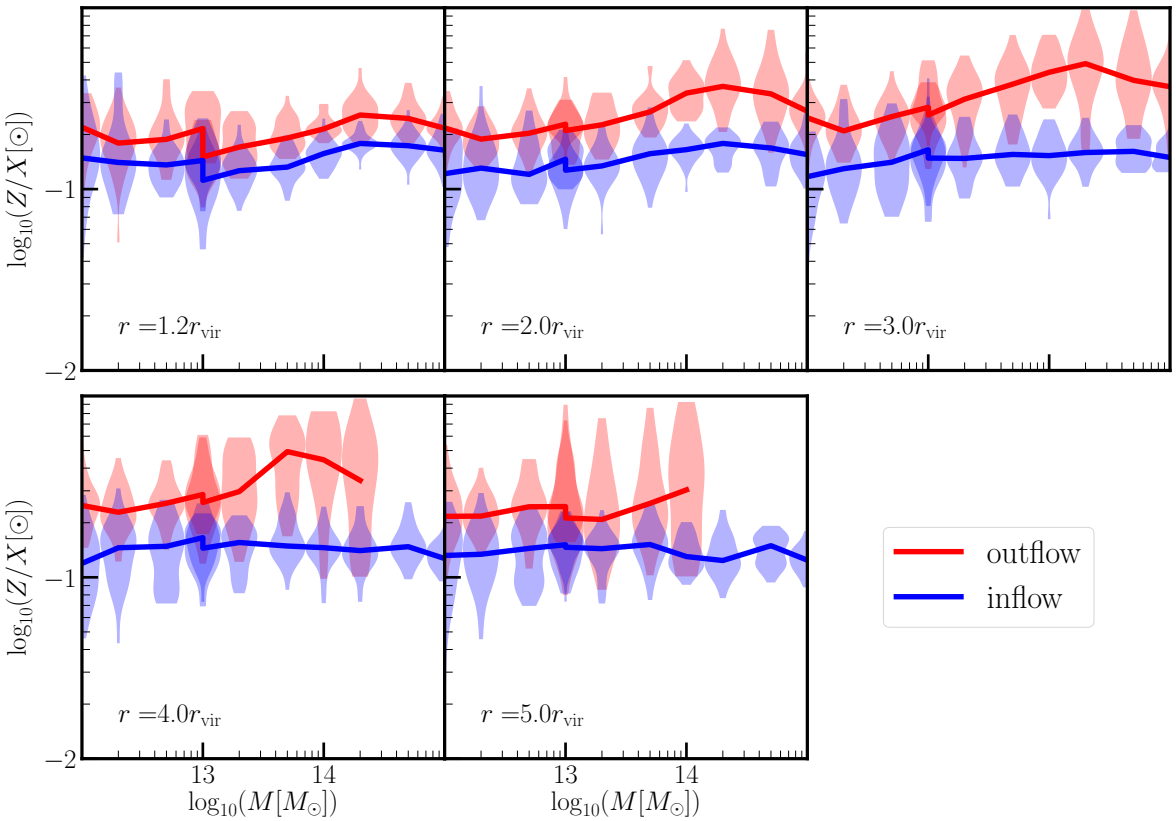


Figure 4.15: Metallicity of net (mean) in- and outflow as a function of mass at five radii for the full halo sample. As in Fig. 4.14, the spread within each mass bin is indicated by the vertical distributions. As in Fig. 4.14 the cut-off in the high-mass - large radius range does not indicate zero metallicity.

gas temperature close to the virial radius. However, there is a gap between the two curves that increases with radius and is more pronounced at the high-mass end. Notably, and inversely to the behaviour of the mass flow shown in Fig. 4.3, for the temperature it is the inflowing component that drops away from the mass-scaling relation at $\approx 10^{14} M_\odot$ for radii $> 1.2 r_{\rm vir}$, showing a downwards kink.

The outflow (red curve), in contrast, remains stable and linear out to large radii only decreasing slightly in temperature and showing a radial cut-off at large masses, where the outflows do not reach as far out in terms of scaled distance. This discrepancy in temperature can also be seen spatially in the right panel of Fig. 4.10, exemplary for cluster 20: The regions with a dense net in-flow that dominate the overall mass inflow – effectively the filaments – are significantly colder than the regions dominated by the thermally driven outflow. This is a direct manifestation of the shocks discussed in chapter 4. For the clusters of *Box2b/hr* and the high-mass group end, the gas falls in at a relatively cold temperature and is then heated when it encounters the pressure supported halo atmosphere. For the less massive haloes in both boxes however, in- and outflow are nearly in temperature equilibrium. This is possibly a manifestation of the mass hierarchy in the two different boxes: Less massive haloes (relative to the maximal halo mass in each box) tend to live in more active environments even when they have not yet been accreted by more massive haloes because there are more equal or higher mass haloes available in their vicinity to heat the surrounding gas. So the apparent drop-off of the inflow temperature at the high-mass end of the boxes should rather be thought of as a relative enhancement of inflow temperature for lower-mass haloes, responsible for the downwards kink in the mass-scaling relation.

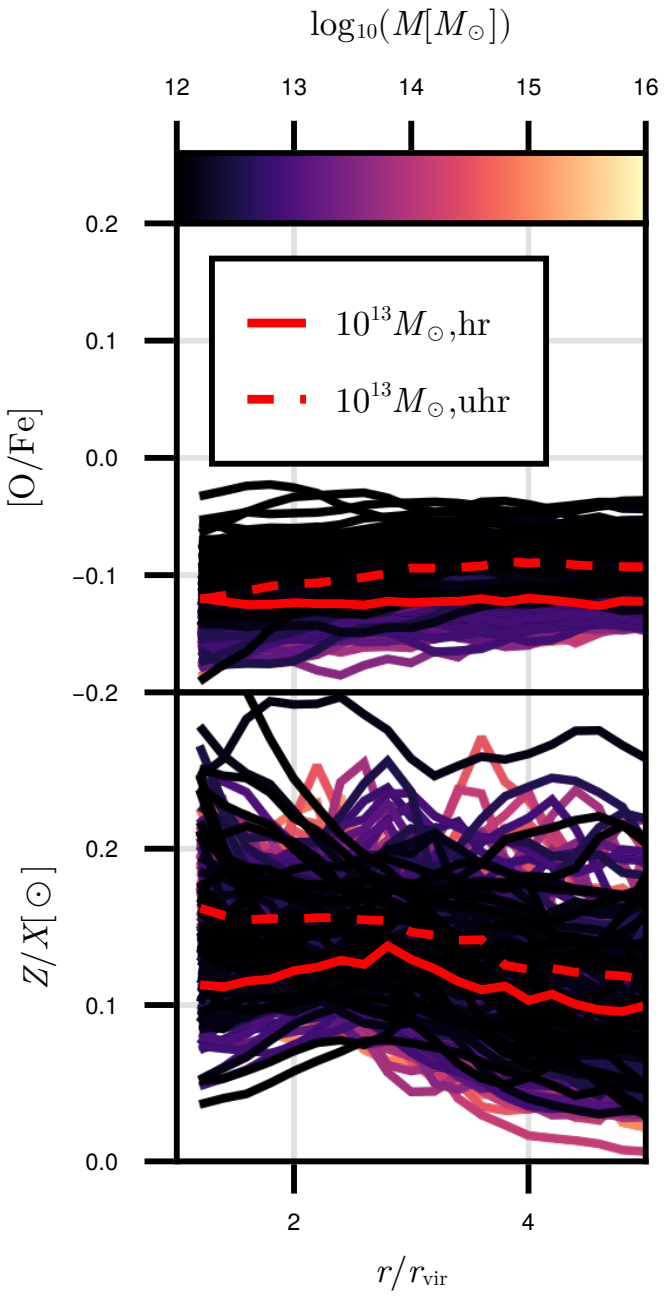


Figure 4.16: Stacked radial O/Fe (top) and total metallicity (bottom) profiles with the same mass colouring as in Fig. 4.8. All haloes from all bins are used.

4.6.2 Metallicity

Figure 4.15 shows the mean metallicity of the gas present in the outskirts of the sample split by flow direction. Compared to the clear mass scaling of the temperature curves, the metallicity inflow curves with respect to mass in Fig. 4.15 are relatively flat, indicating that the filaments and inflows in general are scale-independent in their chemical evolution. Notable is also a distinct lack of radial evolution, except for the fact that for the inner radial bins, there is a slight increase in metallicity for the massive clusters with decreasing radius. This effect is the strongest for the mass bin centred at $2 \times 10^{14} M_{\odot}$. Generally inflows are less metal-rich than outflows, as one would expect. The red outflowing curve has a similar shape to the inflow at small radii. It shows an overall stronger enrichment than the inflowing gas. This is consistent with the picture established in Section 4.4 for the individual cluster study: As gas falls onto massive clusters, it is pre-enriched by the evolving galaxies and groups infalling within the filaments and this evolution stops once the material encounters the shocks surface and is heated. The slight increase in inflowing metallicity with decreasing radius in the high-mass bins also fits into this picture since the gas evolves in metallicity as it falls closer to the central halo. This can also be seen in the tracks in Fig. 4.11 in combination with Fig. 4.12.

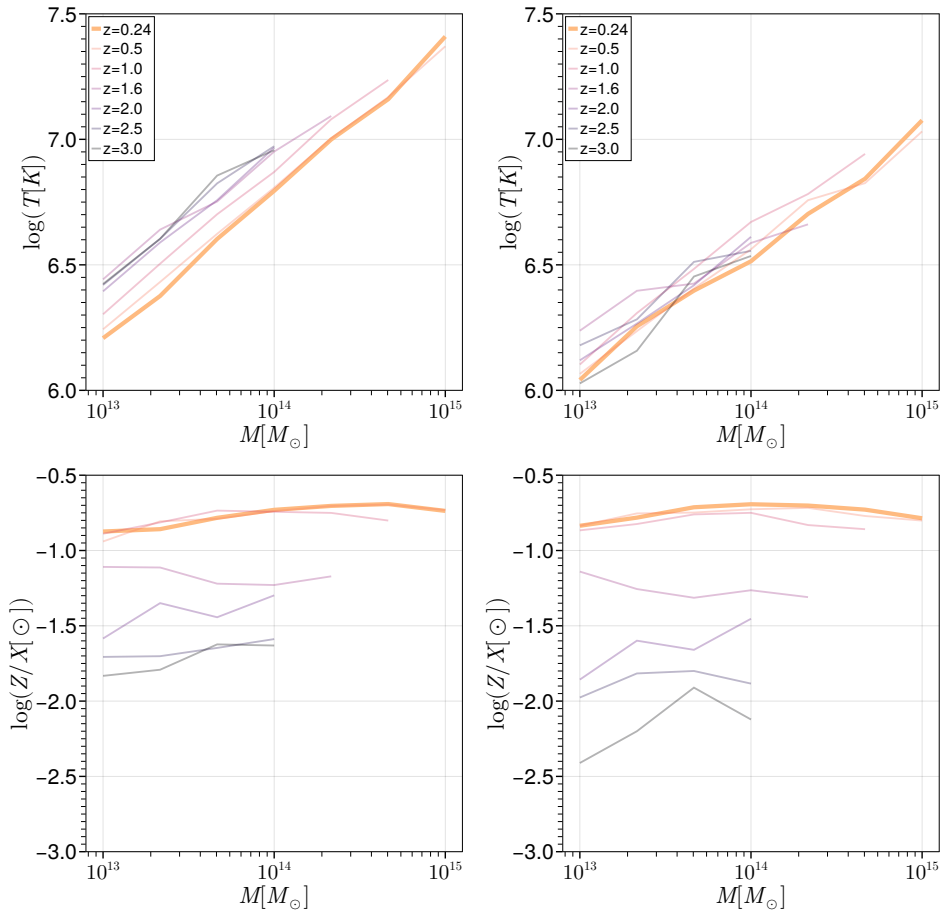


Figure 4.17: Redshift evolution of the temperature and metallicity at $1.2 r_{\rm vir}$ (left column) and $2.0 r_{\rm vir}$ (right column) as a function of mass. The bin masses are identical to the ones used in the previous section.

However, in contrast to the inflowing material, the outflows increase in metallicity going outwards from the central halo for the clusters (mass bins around $10^{14} M_{\odot}$). The increase in metallicity in the outflow for the highest mass bin is possibly a contamination effect of

massive neighbours of these clusters contributing to the outflow with their own accretion (dominating the mass averages due to the inflows being more dense overall). The metallicity curves in Fig. 4.15 show a stronger offset relative to the vertical scatter within the bins between outflowing and infalling material when compared to the temperature in Fig. 4.14. There additionally is, similarly to the temperature, a noticeable discontinuity in metallicity between the two simulations at the mass bin where they overlap at $10^{13} M_{\odot}$. Present in both components at small radii, this jump vanishes further out. While *Box2b/hr* and *Box4/uhr* differ in their global star formation and thus in their enrichment properties due to their different resolutions, the "floor" of enrichment is the same for both boxes in the relatively pristine and low density regime of the furthest halo outskirts. At around $0.1 Z_{\odot}$, most enriched gas particles have only been impacted by one to a few supernovae during their evolution independently of the resolution, explaining the agreement between the boxes at large radii. In the outflowing component there is a stronger residual resolution gap, consistent with the picture of the outflowing gas at large radii being the gas that is enriched and pushed out during the early formation of the central galaxy, where the resolution would indeed impact the efficiency of star formation and hence enrichment. The top panel of Fig. 4.16 shows the radial oxygen-to-iron ratio profiles for all haloes in the sample. The profiles are consistently flat across the entire mass range and are in agreement with previous numerical (Biffi et al., 2017, Vogelsberger et al., 2018, Angelinelli et al., 2022) and observational (Sakuma et al., 2011) studies on the inner regions of the ICM. There is however an apparent overall mass trend with higher mass haloes having lower oxygen to iron ratios at each radius. This trend is likely caused by the difference in resolution between *Box4/uhr* and *Box2b/hr* as the red median lines calculated with the $10^{13} M_{\odot}$ bin in both boxes indicate. Previous works have examined differences in the cosmological star formation rates and their histories between the resolution levels (e.g. Dolag et al., 2025) and these differences will plausibly also impact the chemical composition of the gas, especially the O/Fe ratio, which is directly sensitive to the timescales of star formation in the cosmological volume. The overall metallicity in the bottom panel of Fig. 4.16 demonstrates a global trend of similar consistency across the mass range. There is a slight negative metallicity gradient for all haloes evening out eventually as the chemical influence of the central halo vanishes at large radii. ($4 r_{\mathrm{vir}} < r < 5 r_{\mathrm{vir}}$). Overall these findings (flat O/Fe ratio, slightly negative radial metallicity gradient and increased temperature for the outflowing component) are consistent with the early enrichment and subsequently frozen-in chemical evolution in the outskirt gas found for cluster 20. To complete the picture from the individual cluster study, it is also necessary to consider the temporal evolution of the scaling relations from Fig. 4.14 and Fig. 4.15, which we discuss in the following section.

4.6.3 Redshift Evolution of Temperature and Metallicity

Figure 4.17 shows the evolution of the halo mass–gas temperature (upper panels) and halo mass–gas metallicity (lower panels) relation close to the virial surface and further in the outskirts. The temperature close to the virial surface decreases consistently across the mass range with time, keeping the mass scaling stable. This is still consistent with haloes and in consequence halo outskirts heating dynamically as they gain mass through mergers and accretion: As we consider equal-mass bins in time as opposed to tracing individual haloes, growing haloes will move from one bin to another in time and in consequence up the temperature mass relationship. The cooling trend in the temperature-mass relation rather reflect an overall cooling of the immediate surroundings of these objects as they evolve and accrete mass. In contrast, there is no clear time evolution of the mass-temperature scaling relationship at larger radii, which could plausibly be erased by the many factors that the temperature of the larger-scale environments of these objects depends on.

The metallicity evolution (lower panels) shows the picture of early enrichment and subsequent stagnation of the chemical evolution in the outskirt gas to be consistent across the mass range: At both sampled radii the normalisation of the metallicity-mass relation only significantly changes at $z > 1.0$. At later times the previously demonstrated flat mass-metallicity curve stabilises, showing little variation due to the enrichment in the outskirts having predominantly taken place at early times.

4.7 Conclusions

We have used the Magneticum suite of simulations to examine large-scale matter flows in the outskirts of haloes spanning a large range of masses and to study the mass scaling behaviour of these flows. This allowed us to determine how self-similar the accretion and outflow processes are across the entire range of masses. The main findings of this work are:

- While the individual spatial flow configurations are complex and vary strongly from halo to halo, the average inflows onto haloes in the simulation follow a mass scaling relation that is consistent with the semi-analytical model for a hierarchically accreting overdensity and that is stable in time. This is important because it implies that inputs for mass-accretion models that do not emphasise the exact configuration of the flow fields (e.g., the Bathtub model for the balance of mass accretion and star formation (Dekel et al., 2013)) can be kept relatively simple and consistent across scales.

- Considering the azimuthal symmetry of the inflow and outflow fields separately, inflows demonstrate a significantly less isotropic distribution when compared to outflows. This is consistent at all scales, though possibly the isotropy of outflows at small scales is overstated due to the feedback model used in the simulations not implementing kinetic feedback which might introduce additional anisotropy at these scales. These findings confirm the expectations of inflows being largely filamentary from coupling to the large scale cosmic web, where the tidal configuration aids the pre-collapse of these elongated structures. The consistency of this inflow anisotropy confirms this to also be true for smaller haloes, being fed by smaller sub-filaments given by the fractality of the cosmic web itself.

- The thermal effects break the self-similar mass scaling of the flow fields for the outflowing component. The stronger impact of AGN feedback on galaxy to group size haloes can be seen as a characteristic kink in the mass scaling relation as low-mass haloes show relatively stronger outflows at larger radii ($r > 3r_{\rm vir}$), extending previously found trends in simulations for clusters and groups in the mass scaling of the closure radius across an even larger mass range (Angelinelli et al., 2023).

- In the Magneticum simulations galaxy and group-mass objects have flat entropy profiles in the outskirts to larger radii as the gas is mainly heated by the feedback processes. In contrast, cluster-mass objects show entropy peaks that reach out to $\approx 2{-}3r_{\rm vir}$, consistent with expectations for MA-shocks (Zhang et al., 2020) in the outskirts of clusters that have undergone a massive merger recently. We report a decrease of entropy peak radius with mass for the objects that do have a significant entropy peak, consistent with previous work.

- The metals present in the outskirts of the example cluster we studied in detail are predominantly formed during gas infall and before the gas encounters the shock surface and thermalizes its kinetic energy, confirming the early enrichment scenario (Biffi

et al., 2018). Both the total metallicity and the O/Fe mass ratio as a proxy to enrichment history effectively stop evolving once the gas joins the hot expanding atmosphere in the cluster outskirts.

- The temperature in the cluster outskirts shows a consistent mass scaling behaviour of mass increasing with temperature with the outflows being consistently hotter than the cold inflowing gas due to shock heating and AGN feedback.

- The degree of enrichment of galaxy cluster and galaxy outskirts is very similar with no clear mass scaling behaviour. Overall the outflowing component demonstrates a higher degree of enrichment compared to the inflow, and the radial profiles are consistent with the ones found in previous work. We however report a peculiar increase of the metallicity of outflowing gas for cluster haloes in the intermediate to large radial range ($2 - 4r_{\rm vir}$).

In summary we find the inflows at the virial surface of haloes to be largely self-similar in their global properties. This indicates that the CGM and the ICM couple to the large scale environment in a similar manner when one considers the total inflow, which is dominated by the dense filamentary environment around haloes. This result verifies that in terms of the total inflow budget relatively simple accretion models (e.g. Dekel et al., 2009) provide enough accuracy.

Deviations from self-similarity arise in the relatively isotropic outflowing component. Here the different mechanisms of gas heating create significant discrepancies between galaxy cluster and galaxy outskirts. The large extent of the shock radius for galaxy mass halos especially significantly changes the infall structure for these objects, as the isotropic outflow component displaces isotropic inflows from the environment out to much larger radii. This can be expected to impact galaxy formation on much smaller scales, as previous studies showed that the connection of a galaxy to its environment can prolong its star formation activity (Galárraga-Espinosa et al., 2023). While the exact extent of the outflows is sensitive to the feedback implementation, we can expect the total balance of outflow energy to be relatively robust.

Similarly, the extended merger-driven accretion shocks we find in the outskirts of massive clusters can affect dynamical mass estimates of these structures, as it has been shown that whether a cluster outskirt region is inflowing or outflowing significantly impacts the dynamical state of the gas in that region (Lebeau et al., 2024a,c). In light of future detailed surveys of the gaseous outer regions of structures these differences between galaxy mass and cluster mass objects can help both improve the theoretical modelling of gas physics and interpret observational results.

Chapter 5

The Inflow Asphericity

We plan to submit this chapter to A&A as Seidel et al. 2026

Building on the previously demonstrated morphology of the inflow field, with relatively spherically symmetric outflows in terms of flow rate and anisotropic inflows dominated by filaments, in this chapter we will further elaborate how to quantify the flow field morphology. To this end we introduce the inflow asphericity based on the aspherical excess in the flow field measured in the previous chapter. Here, we only consider only the inflow field and demonstrate how the aspherical excess, measured in two variants, the linear and the logarithmic inflow asphericity can effectively trace both the inflow and the outflow morphology. We show this for an extensive test suite of mock inflow maps generated from simple assumptions about the environment haloes are connected to as well as for simulated haloes from the Magneticum Pathfinder simulations.

5.1 Introduction

Galaxies, groups, and clusters of galaxies evolve from the collapse of primordial perturbations in the cosmic density field. As these perturbations are never perfectly spherical, their gravitational collapse also happens non-spherically. The resulting tidal fields give rise to a number of dynamical and morphological phenomena such as galactic spins (Porciani et al., 2002, Neyrinck et al., 2020) and on larger scales the cosmic web with its elongated filaments and sheets (e.g. Bond et al., 1996a, Hidding et al., 2014).

Quantifying the morphology and topology of the cosmic web and its filaments has been a major goal of both theoretical (Sousbie, 2011, Kuchner et al., 2021) and observational (Hoang et al., 2023, Euclid Collaboration et al., 2025a) efforts since its first theoretical conception by Zel'dovich (1970). They connect the massive clusters and superclusters that sit at the nodes of the web and have been found to affect several internal properties of these structures (Gouin et al., 2021, Haggar et al., 2024).

From the perspective of galaxy formation especially its influence on smaller scales is a topic of major interest. First studies connecting galaxy properties to various parameters quantifying the position in the cosmic web show promising correlations between internal and external physics: Multiple studies, both observational (Alpaslan et al., 2016, Malavasi et al., 2017, Kraljic et al., 2018, Hoosain et al., 2024) and numerical (Bulichi et al., 2024, Hasan et al., 2024), found galaxies at the cores of filaments to be biased towards higher stellar masses while the expected star formation rate increases with increasing distance to the spine. This is also in agreement with theoretical expectations from excursion set theory (Musso et al., 2018), as in the vicinity of saddle points, accretion is expected to be influenced by the large-scale flows distorting the local velocity field.

A key issue with connecting the cosmological environment to galaxy evolution is that an unambiguous definition of cosmic structures is difficult to devise (Libeskind et al., 2018), due to the complex, multi-scalar nature of the web. In simulations, where one has access to the full density fields, this can be mitigated to a degree with multi-scalar structure identification algorithms like NEXUS and NEXUS+ (Cautun et al., 2013). This is however not feasible for observations, where the density environment of a galaxy can typically be constrained only on larger scales by its surrounding galaxy distribution (Alpaslan et al., 2016, Kraljic et al., 2018, Euclid Collaboration et al., 2025a, e.g.) and on small scales by trying to map the circumgalactic medium and cold gas components in the outskirts of a given galaxy. The intermediate scale gas distribution is currently only sparsely accessible to observations in field haloes, for example.

Additionally from modelling galaxy evolution on N-body simulations it became clear that the story of galactic gas accretion is more complex than the growth of dark matter haloes from purely cosmological accretion. Simulation models like the semi-analytic Millennium model (Croton et al., 2006) diverged at the low mass end of the stellar mass function at high-z and at the high-mass end at low-z (Bell et al., 2003, Li & White, 2009). This implicated galaxy scale outflows to play an important role as a regulation mechanism for accretion and thus also star formation. Direct evidence for these regulating gas flows has since been found observationally (Roberts-Borsani & Saintonge, 2019) and therefore most modern hydrodynamical cosmological simulations employ a combination of AGN and star-formation driven outflows from sub-grid modelling that are able to bring the galaxy stellar mass functions closer to the observations (Schaye et al., 2015a, Davé et al., 2019, Nelson et al., 2021, Schaye et al., 2023, 2026, Dolag et al., 2025). Nevertheless, these models come in many different flavours and the large-scale gas environment of galaxies has been shown to be sensitive to the specific implementation of the model or even parameter choices within a given model (Ayromlou et al., 2023). From a theoretical perspective, it is therefore a valuable exercise to consider the gas flow fields that shape these environments directly and study how the flows are connected to the internal galaxy evolution.

As the cosmic web evolves with time (Cautun et al., 2014) and galaxies evolve in terms of their stellar and gas content, the balance between inflow from the environment and outflows can be expected to change as well. A baseline equilibrium state is given by the so-called 'bathtub models', which directly relate the net gas inflow rate to the star-formation rate (Bouché et al., 2010, Davé et al., 2012, Lilly et al., 2013). Recent numerical analysis showed that, while galaxies generally follow these equilibrium relations at early times ($z > 2$), there is a transition towards late times with fewer galaxies following a simple relation between flow rate and star formation (Fortuné et al., 2025). This is also consistent with the finding that massive quenched galaxies accrete relatively isotropically at high-redshift until they quench and disrupt their environment significantly (Kimmig et al., 2025b). This disruption, in combination with a general hot halo build-up for massive galaxies can effectively cut them off from the cold gas inflows from the cosmic web (Dekel et al., 2009), which arise as anisotropies in the flow field around the galaxy. From numerical simulations (Remus et al., 2023) showed that such hot halos can already exist as early as $z = 4.2$ and a first observation of a hot x-ray halo was recently published (Bogdán et al., 2026).

The morphology of the flow field around a galaxy is therefore dependent on many complex processes from cosmic web evolution to stellar and AGN outflows. In this work we aim to quantify how (an)-isotropic the inflow field is for a given halo and to this end present and test a new parameter, the **inflow asphericity** (ζ) of a given simulated halo. This parameter is computed on an input inflow field measured at a certain boundary surface (e.g. a sphere with one virial radius) centred on the halo of interest.

In previous work we already demonstrated the flow fields on the outskirts of haloes to be vastly diverse from a morphological perspective, nevertheless exhibiting a clear trend of

inflows being more anisotropically distributed than the more spherically symmetric outflows (Seidel et al., 2025b). In that paper we employed a spherical harmonics decomposition of the flow field to measure how isotropic the flow field structure is, which gave rise to the inflow asphericity parameter. First exploratory studies employing this parameter started connecting the geometry of the inflow field to both the shapes (Valenzuela et al., 2024) and the star formation histories (Fortuné et al., 2025) of galaxies, making it a promising quantity to understand galaxy-environment connections better from a theoretical perspective. In this work we introduce this inflow asphericity parameter and explore and verify its behaviour in different idealized and simulated setups.

This chapter is structured as follows: In section 2, we introduce the basic methods we used to compute the asphericity parameter from a given flow field, as well as the simulations we employed to test this parameter. In section 3 we introduce idealized test cases to assess how the asphericity parameter corresponds to basic properties of the inflow field. In section 4 we demonstrate the spherical harmonics decomposition and the computation of the asphericity parameter using simulated maps from hydrodynamical simulations.

5.2 Introducing the Asphericity Parameter

The idea of the asphericity parameter is to quantify how spherically symmetrical the flow field around a given halo is, or ,conversely, how much large-scale variation there is in the inflow field. In the idealized case of perfectly smooth and purely spherical accretion the inflow will be the same in every direction from the perspective of an observer located within the halo. Deviations from this can have multiple sources: Filaments and infalling secondary haloes will create accretion hotspots, angular directions along which much more mass gets accreted compared to the average accretion rate. Throughout this work we will refer to this mode of accretion as the ”filamentary component”. Since major satellite mergers can be expected to generally align with the filamentary structure (e.g. Arora et al., 2025), this nomenclature is reasonable. Outflows on the other hand can, if they propagate out far enough, stop accretion entirely in the directions they are launched. Our goal is therefore to quantify these deviations from isotropic accretion as a measure of the evolution of the large scale structure a halo is connected to, as well as the internal processes of the halo such as star formation and AGN activity.

5.2.1 Spherical Harmonics Decomposition

In order to quantify the geometry of the inflow field we perform a spherical harmonics decomposition. Spherical harmonics decompositions are routinely employed in cosmology to study angular power spectra from the cosmic microwave background (e.g. Akrami et al., 2020) or galaxy distributions (Tessore et al., 2025). Analogous to a Fourier decomposition the general idea is to break a given function down into a sum of oscillating basis function with a well defined degree l, analogous to the frequency in the Fourier method, and an order m.

We decompose the inflow function $f(\theta, \phi)$ using a set of orthogonal spherical harmonics functions

$$f(\theta, \phi) = \sum_{l=0}^{l_{\max}} \sum_{m=-l}^{m=l} a_{l,m} Y_{l,m}(\theta, \phi). \tag{5.1}$$

From the coefficients $a_{l,m}$ one can compute the power spectrum $[C_l]$ via

$$C_l = \frac{1}{2l+1} \sum_{m=-l}^{l} |a_{l,m}|^2. \tag{5.2}$$

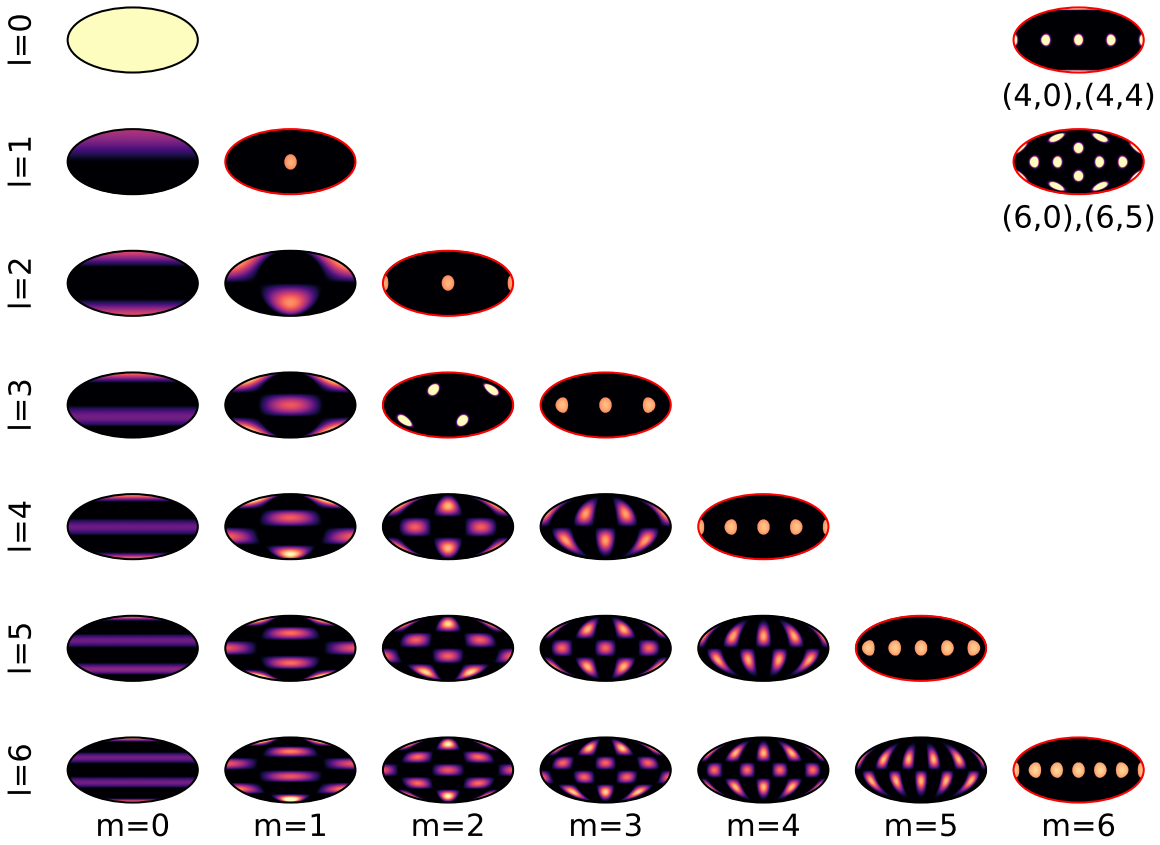


Figure 5.1: Spherical harmonics as surface maps. The row corresponds to the l-degree of the spherical harmonic, while the column indicates the order m (from 0 to 6). We show the planar test maps (see Section 5.3) at the positions of the sectoral harmonics with the corresponding l, m highlighted in red. We additionally show the platonic solid test maps (see Appendix A.4): The Tetrahedron configuration is shown at the position of the pure harmonic Y_{32} which has tetrahedral geometry. The two additional platonic solids which can be represented by linear combinations of spherical harmonics in the top right columns, with their corresponding (l, m) values given below.

The total power in each l-mode is given by $(2l + 1)C_l$. The decompositions in this work are computed using the *healpy* wrapper (Zonca et al., 2019) for healpix tessellated maps (Gorski et al., 2005).

Fig. 5.1 shows these spherical harmonics as mollweide projected surface maps. We deliberately normalize these maps in such a way that they are comparable to the test maps discussed in Section 5.3, namely instead of highlighting zones of positive and negative values, we focus on the positive regions here as they will be the proxies for our zones of inflow. Where there is a 1:1 correspondence between harmonics and synthetic test cases, we show the test maps at the appropriate position with a red frame. Additionally two of the polyhedral setups using the platonic solids (see Appendix A.4) can be obtained by appropriately combining two spherical harmonics. We therefore show the Octahedron and Icosahedron setup in the upper right of the figure, giving the harmonics they can be obtained from.

5.2.2 Asphericity

Techniques employing either projected or spherical harmonics decompositions have been used in the past to identify preferred directions of infall for satellite galaxies (Libeskind et al., 2011, Arora et al., 2025), to measure the degree of filamentary to isotropic accretion in isolated cluster simulations (Vallés-Pérez et al., 2020), and to study the correlation of the 2D-azimuthal symmetries in gas and DM to various halo properties (Gouin et al., 2022). In this work we calculate the aspherical excess on the sphere. This excess is given by the sum of all multipole moments higher than the monopole normalized to the monopole power, truncating the sum at the 9-th degree to ideally capture the large-scale anisotropic inflow modes:

$$\zeta = \frac{1}{C_0} \sum_{l=1}^{9} (2l + 1)C_l. \tag{5.3}$$

In principle the choice of cut-off is arbitrary, we arrive at $l = 9$ for the following reasons: For $l = 9$ a typical angular scale of fluctuations is $\pi/9$ or 20. At the virial radius of a massive galaxy cluster (assuming $r_{\rm vir} = 1$ Mpc) this corresponds to a physical scale of ≈ 0.35 Mpc, which can be expected to capture the physical width of simulated cosmological filaments at all redshifts (e.g. Yang et al., 2025). Additionally, using the combined power spectra of 2000 halos from the Magneticum simulations (see Section 5.4.1) we found that this harmonic degree marks a transition point between the large-scale power spectrum and the smaller scale features of a typical simulated inflow map (see Appendix A.2).

A more homogeneous field has less power in the non-isotropic angular modes, thus lowering ζ with a perfectly homogenous inflow field having a ζ of 0. For a more complex inflow field the exact value of ζ will depend on the spatial configuration (for example filament thickness and alignment), so to disentangle the exact structure the full spectrum of the spherical harmonics is necessary (see the discussion in Appendix A.5).

5.2.3 Logarithmic Versus Linear Asphericity

We introduce two complementary methods to compute the large-angle fluctuations in the flow field: From Fig. A.1 it can be seen that the computed inflow values around simulated haloes span a wide dynamical range. Therefore the purely linear maps will be dominated by the regions where the inflow is maximal. A way to reduce the dynamical range of a given inflow map is to instead analyse the spatial distribution in log space instead. As will be demonstrated in the following, computing the asphericity on the linear flow field, denoted $\zeta_{\rm lin}$ hereafter, is most sensitive to the dominant regions of inflow, where the flow is several orders of magnitude above the inflow averaged over the spherical surface. Consequently it serves to

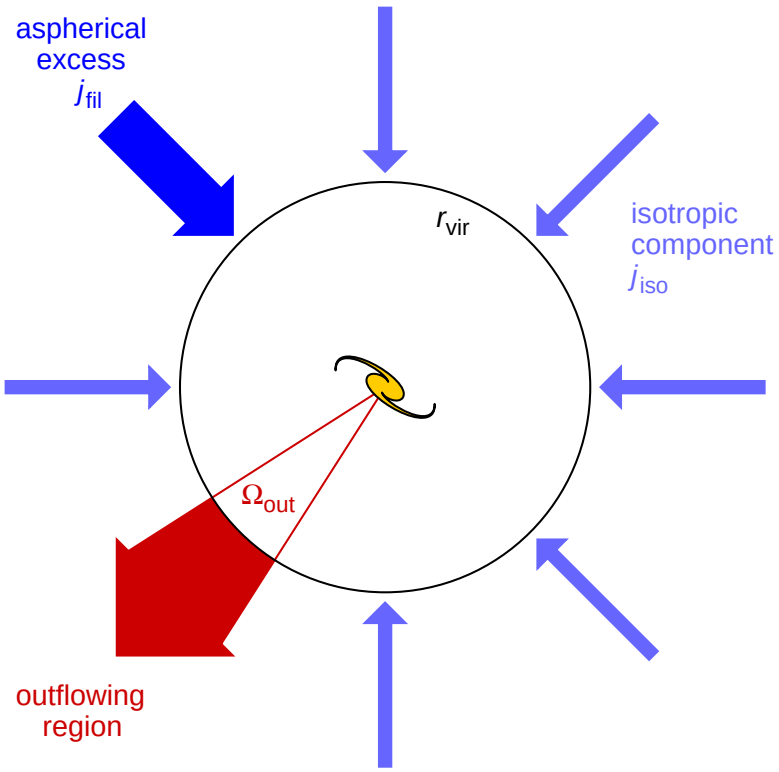


Figure 5.2: Schematic of the Toy Model Setup.

measure the amount of inflow through filaments and infalling galaxies, where densities are the highest. Computing the asphericity on the logged map on the other hand ($\zeta_{\log}$) is more sensitive to the overall covering fraction of the inflowing component on the virial surface. This makes this variant of the asphericity more sensitive to outflows driven by the feedback processes inside the halo, as will be demonstrated in thec

5.3 Idealized Test Cases

5.3.1 Test Setup

The inflow maps of simulated haloes are inherently complicated and a superposition of many components both in real and in spherical harmonics space. To better illustrate how the asphericity parameter works, we set up a set of idealized test cases. The basic idea of these test setups is to break the complex inflow maps down to three components:

- A filamentary component, represented by $N_{\rm fil}$ hotspots on the sphere of solid angle extent d and a total inflow power $j_{\rm fil}$
- An isotropic component with a base inflow level j_0
- Holes in the isotropic component (i.e. regions with zero value) representing regions of outflow, characterized by either a cone or a bi-cone with a total solid angle $\Omega_{\rm outflow}$. We parametrize this by the surface ratio $f_{\rm outflow}$, the fraction of the spherical surface covered by the outflow.

Fig. 5.2 visualizes these three components. We adapted a Gaussian profile for the intensity distribution within each filament (the cross-section corresponds to the full width at half

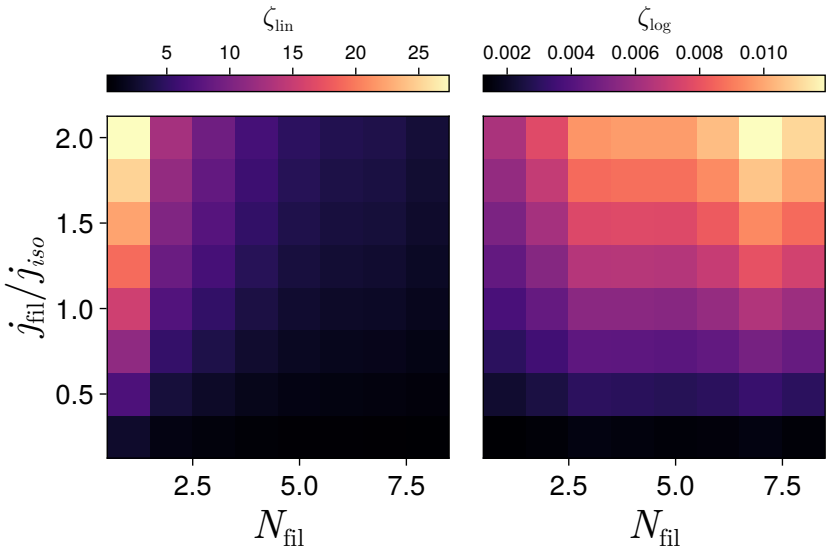


Figure 5.3: Linear (left panel) and logarithmic (right panel) asphericities of the toy model. f_{outflow} is kept constant at 0.0. We vary the total number of filaments and the relative strength of filamentary inflow along the x and y axis respectively.

maximum here). As the default FWHM we chose 0.2 rad, which corresponds to a physical filament width of $\approx 0.2 r_{\mathrm{vir}}$ assuming the flow field is measured at the virial radius. The goal of this idealized study is then to demonstrate how the asphericity behaves as a function of N_{fil}, j_{fil} and f_{outflow}. To this end we kept the total square integral in the filamentary component equal between different geometrical arrangements (i.e. we always assigned a total power $\int j_{\mathrm{fil}}^2$ to distribute over the N_{fil} filaments). The resulting maps can be found in Fig. A.3.

Fig. 5.3 demonstrates the behaviour of the two flavours of asphericity when the filamentary strength j_{fil} and number of filaments N_{fil} are co-varied. Each grid point represents the asphericity of a single synthetic map. The left panel shows the behaviour of the linear asphericity ζ_{lin}, while the right panel shows the logarithmic asphericity, ζ_{log}. As can be seen, the two parameters behave orthogonally to each other: The asphericity of the linear map is very sensitive to the number of filaments N_{fil}, with a strong peak at a dipole map with a single inflowing hotspot. Since the integral of the filamentary inflow is kept constant in each row in the figure, adding additional filaments lowers the overall asphericity. The logarithmic variation on the other hand is only weakly sensitive to the number of filaments and peaks at maps with a large number of inflow hotspots. This counter-intuitive positive scaling is a consequence of the aforementioned normalization, which is applied in linear space. Increasing the total inflow in the aspherical components expectedly increases both parameters, with the logarithmic variant exhibiting a stronger relative dependence.

Fig. 5.4 shows the impact of regions of zero inflow (i.e. outflowing regions) with the number of filaments N_{fil}. As in the previous figure, the left panel shows the linear asphericity and the right panel shows the logarithmic asphericity. While increasing the opening angle of the outflow cone doesn't drastically change the linear asphericity, the logarithmic asphericity is very sensitive to this due to the reduced dynamical range as can be seen by values being more than an order of magnitude larger than for the case without holes. This strong scaling is present for all filament configurations.

To study this behaviour of the logarithmic asphericity in greater detail we plot it against the covering fraction of the outflow in Figure 5.5 with the other model parameters kept

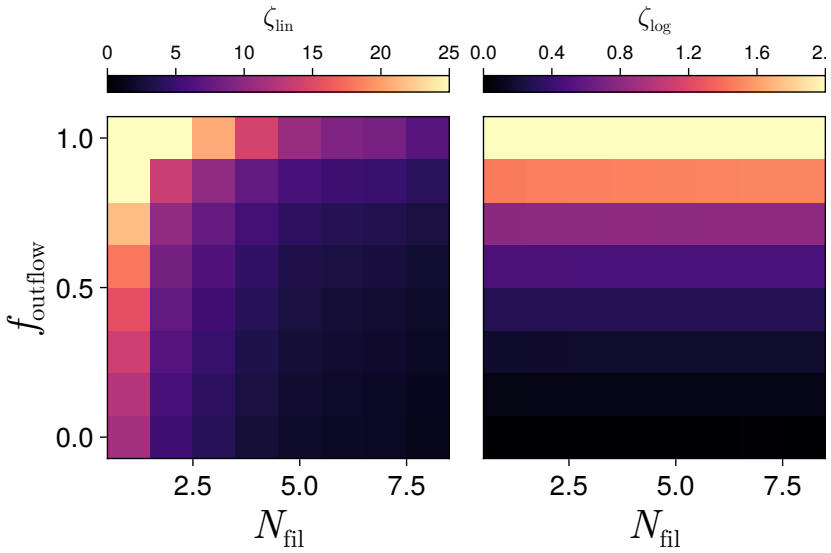


Figure 5.4: Linear (left panel) and logarithmic (right panel) asphericities of the toy model. $j_{\mathrm{fil}}/j_{\mathrm{iso}}$ is kept constant at 3.0. We vary the total number of filaments and the outflow covering fraction along the x and y axis respectively.

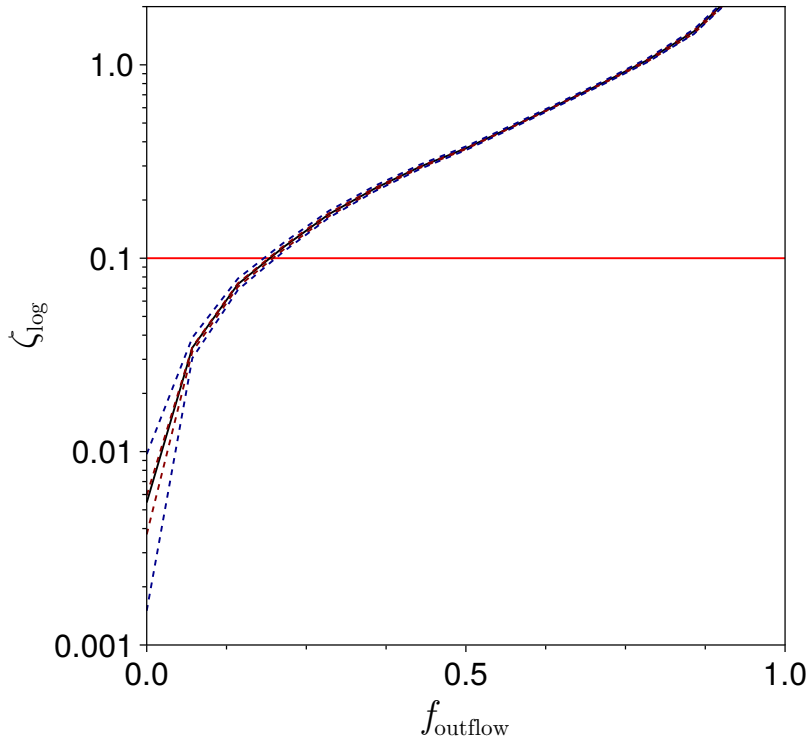


Figure 5.5: Direct dependence of the logarithmic asphericity on the outflow covering fraction. The red line marks typical values for galactic haloes in simulations. All other parameters of the model are kept constant ($j_{\mathrm{fil}}/j_{\mathrm{tot}} = 1$, $N_{\mathrm{fil}} = 4$). The dashed lines show the same functional dependence computed with the extremal model parameter values $N_{\mathrm{fil}} = 1, 8$ (dark red) and $j_{\mathrm{fil}}/j_{\mathrm{iso}} = 0.25, 2$ (dark red).

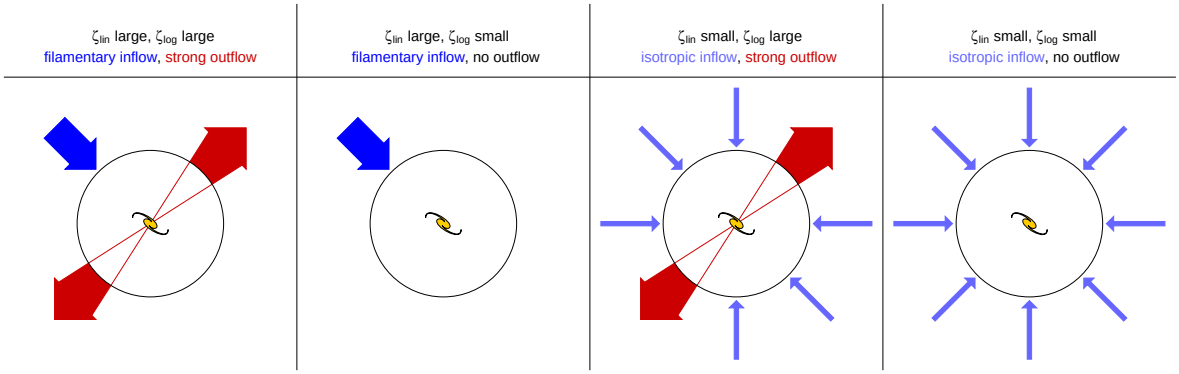


Figure 5.6: Schematic presentation of four limiting cases with high and low $\zeta_{\rm lin}$ and $\zeta_{\rm log}$ respectively.

constant. There is a very strong power-law scaling at low covering fraction, then a transition to a shallower slope around 10% covering fraction. In the intermediate regime the slope is almost constant with the asphericity reaching values typically found for galactic haloes in Magneticum (see companion paper Seidel+2026b) at around 20%. In the limit of a covering fraction of 1 the logarithmic asphericity converges into the regime of the linear values $\simeq$ 1, as the isotropic component is completely removed, leaving only filaments and outflow regions. As can be seen from the enveloping dashed lines, the shape of this dependency is largely independent of $N_{\rm fil}$ and $j_{\rm fil}/j_{\rm iso}$ indicating that indeed the logarithmic asphericity is largely driven by the covering fraction of the outflows. In summary Fig. 5.3 and Fig. 5.4 demonstrate that in combination $\zeta_{\rm lin}$ and $\zeta_{\rm log}$ trace both to what degree the inflow is dominated by concentrated high-inflow regions such as filaments, as well as the fraction of the halo boundary that is actively inflowing and conversely the coverage of the outflow region. The findings of this section are summarized in sketch form in Fig. 5.6: A high $\zeta_{\rm log}$ and $\zeta_{\rm lin}$ indicate a strongly anisotropic inflow focussed on few strongly inflowing filaments as well as an isotropic component that is strongly disrupted by outflows. A low $\zeta_{\rm log}$ in combination with a high $\zeta_{\rm lin}$ indicates a strongly focussed inflow with an unperturbed isotropic component. Conversely, if only $\zeta_{\rm log}$ is large, this is an indication of fairly isotropic inflow with multiple infall direction in combination with strong outflow components disrupting the weak isotropic component. The case with both parameters having low values represents the ideal case of a very isotropic and undisrupted inflow.

These properties make the asphericity parameters ideal analysis tools to study how haloes interact with their environment both in terms of cosmological accretion and feedback from star formation and AGN activity.

5.4 Tests on Simulated Flow Fields

For the simulation tests, we make use of the Magneticum Pathfinder simulations (Dolag et al., 2025) (see also Chapter 3). We compute the flow fields and asphericities for the 29 most massive galaxy clusters from *Box2b/hr*, classified according to their dynamical state by Kimmig et al. (2023). Additionally, we employ a statistical sample of halos above a stellar mass of $M_\star = 10^{8.5} M_\odot$ from *Box4/uhr*.

5.4.1 Reconstructing the Peculiar Mass Flow from Simulation Data

The flow through a surface given a continuous velocity field $\mathbf{v}(\mathbf{x})$ can be generally computed by either integrating its divergence over the enclosed volume or via the Gaussian theorem by

$$\int_V \nabla \cdot \mathbf{F}\, dv = \oint_{\partial V} \mathbf{F} \cdot \hat{n}\, da \tag{5.4}$$

. From a numerical perspective the latter method is the more sensible (integrating over a volume, scaling with r^3, vs. a surface, with r^2 scaling). The largest haloes in the sample reach several Mpc in virial radius or in other words scales where the expansion of the background cosmology becomes relevant, therefore we use *peculiar* velocities throughout this work. In SPH the gas discretisation is based on representative point particles that are smoothed over a volume of space with a density dependent kernel. To accurately model the gas flow given a set of gas "particles" it is therefore necessary to take into account the geometry and smoothing lengths of the kernels. This ensures that there are no holes in the density/velocity field due to the SPH particles' clustering leaving empty pixels, which in turn ensures that the holes in the inflow map actually correspond to real outflowing regions instead of holes in the density field at the surface. We use the program SMAC (Dolag et al., 2005b) to generate flow maps from the simulations. The procedure is identical to the one described by (Seidel et al., 2025b). To demonstrate this, we applied the formalism to two example haloes from the Magneticum simulations, namely Box2bhr. The halos are selected for their dynamical states, we deliberately chose one relaxed galaxy cluster and one dynamically active cluster following (Kimmig et al., 2023) (ID 5 and ID 20 respectively) at z=0.25. We used the SMAC method described in Section 5.4.1 to compute maps from the particle data of the simulation and measure the flow field at $1r_{\mathrm{vir}}$ for each halo. Figure 5.7 visualizes the obtained flow

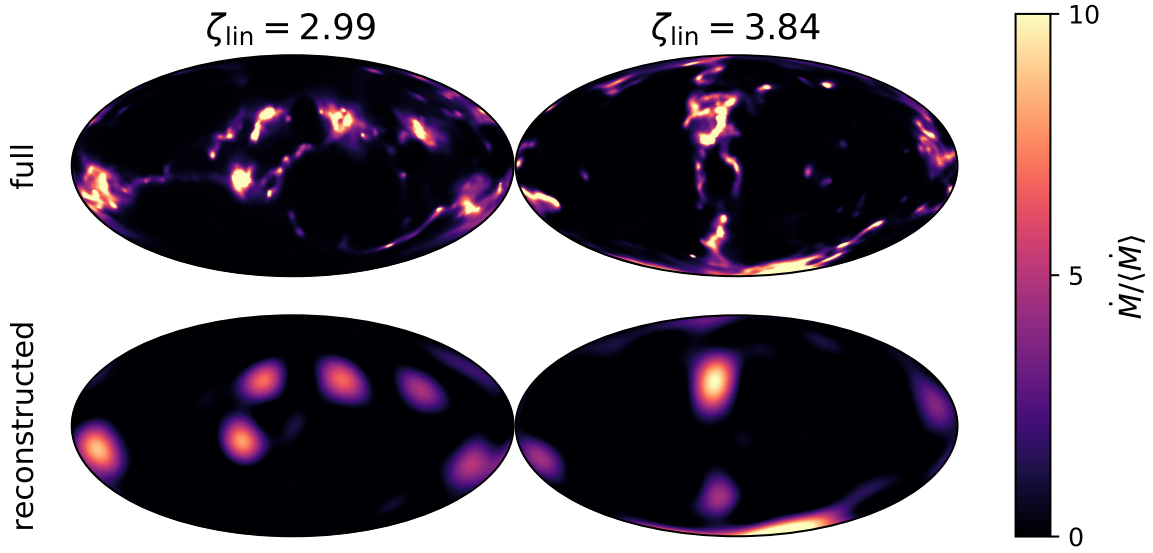


Figure 5.7: Visualization of the effect of the spherical harmonics decomposition using the inflow field of two simulated halos from Magneticum. The top row shows the full linear inflow field normalized by the mean inflow across the map. The dynamically active cluster ID 20 is shown in the left column, while the more relaxed ID 5 is shown in the right column. The bottom row shows the same map expressed only with spherical harmonics of order $l = 1$ to $l = 10$, filtering out the monopole and higher-order harmonics.

fields. It can be immediately seen from the linear inflow maps that while the toy model is a simplification, the decomposition into small circular high flow field zones is a reasonable

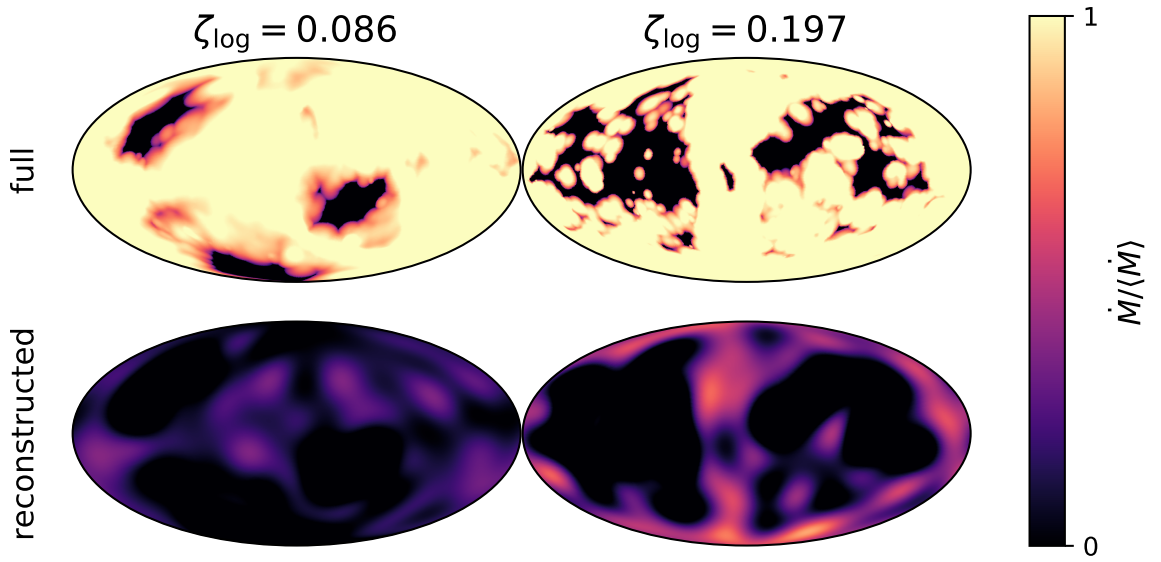


Figure 5.8: Same as Fig. 5.7 for the logarithmic flow field. The top row shows the full logarithmic inflow field normalized by the mean logarithmic inflow across the map. The bottom row shows the same map expressed only with spherical harmonics of order $l = 1$ to $l = 10$, filtering out the monopole and higher-order harmonics.

morphological approximation of the inflow these halos receive, as the linear flow field is dominated by around 2-6 hotspots on the spherical surface. As for the test cases the halo with a greater number of distributed filamentary hotspots has a lower linear asphericity compared to the one with fewer filaments. In the bottom row we show the maps obtained by first computing the spherical harmonics decomposition and then setting the coefficients of all a_{lm} with $l = 0$ and $l > 10$ to zero (essentially applying a bandpass filter). This demonstrates how the limits of the sum in Equation (5.3) filter out the large-wavelength fluctuations in the flow field. The individual hotspots become even more apparent in the reconstructed maps with the smaller scale fluctuations filtered out. The dynamical state appears to not be directly connected to the instantaneous accretion field at z=0.25 since the values for both the relaxed and unrelaxed halo are similar. The fact that the dynamically more active cluster (ID 20) accretes more isotropically is in general consistent with the positive correlation between connectivity and dynamical state (Gouin et al., 2021): As cluster 5 accretes through two major hotspots compared to the six inflow hotspots in cluster 20, its linear asphericity is higher because the flow varies on larger scales and is therefore less distributed over the virial surface (assuming a similar total inflow). For a complete picture of the connection between the dynamical state of galaxy clusters and their inflow asphericity, a temporal analysis is necessary (see also the contours in Fig. 5.9), since the instantaneous flow state at the virial scale encodes the future of mass accretion onto the cluster itself rather than the past. We leave this thorough analysis for future work.

Figure 5.8 shows the same decomposition for the logarithmic maps. Computing the logarithm of the flow field significantly decreases the dynamic range of inflow values, emphasizing the regions with zero inflow (where the outflows dominate). This can be seen in the dark regions in the full maps. The spherical harmonics decomposition also reflects this morphology as the lower row shows. The second halo also has a higher logarithmic asphericity value, as a larger fraction of the spherical surface is covered by these zero-inflow regions. These two example halos show that the behaviour of the two parameters in the test sample is indeed replicated in more complex flow fields. The spherical harmonics decomposition and the cut-off in $l-$ order effectively isolates the large scale fluctuations in the flow field

corresponding to filamentary regions and infalling haloes. Additionally the decomposition of the logged flow field measures the large-scale fluctuation between inflow and outflow. To

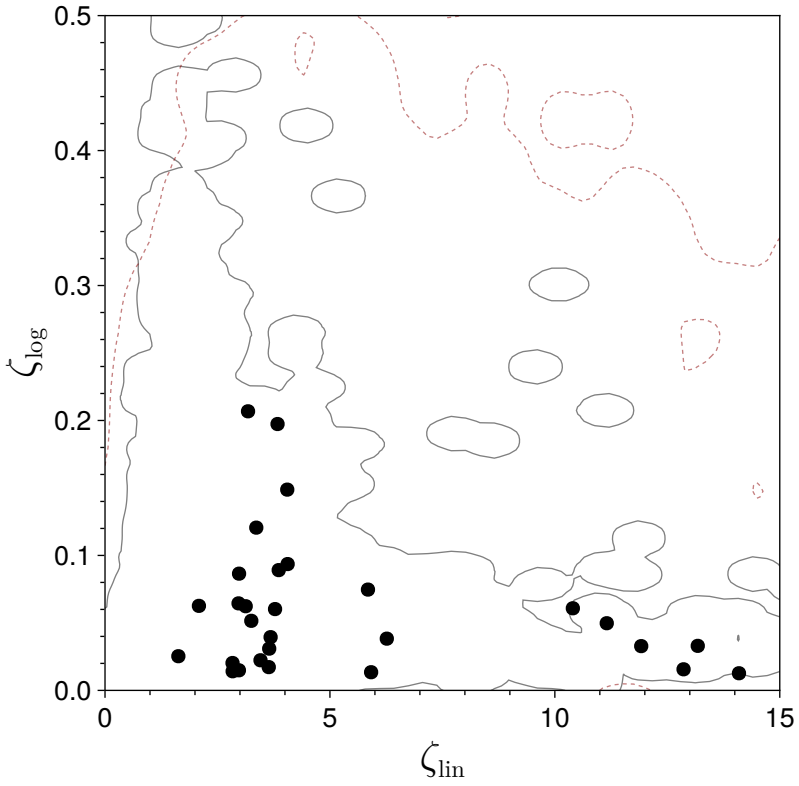


Figure 5.9: Distribution in the asphericity-space of the 29 most massive galaxy clusters in Box2b (black circles) at z=0.25. The contours show a larger sample from a higher resolution Box (Box4/uhr) at z=0.25 (black) and z=1.3 (dark red dashed).

put these two case studies into a wider context, we show the parameters for the 29 most massive galaxy clusters ζ_{lin} and $\zeta_{\log}$ plotted against each other in Fig. 5.9. As can be seen from the figure, at z=0 the clusters sit at relatively low logarithmic asphericities, while in the linear parameter two distinct groups can be seen. One set clusters at low to intermediate values while a second group can be found at rather high linear asphericities. Due to the low number of galaxy clusters and the limited resolution of Box2b, we also compare this to a more general halo sample from the smaller Box4uhr, where the higher resolution allows to compute the asphericities for a larger mass range. The black contours in Fig. 5.9 show that the cluster sample is generally in good agreement with the larger sample, matching the striking L-shape of the contour. Overall this shows that at the present time, halo inflows are either dominated by a highly focused filamentary component (second column in Fig. 5.6) or a strong outflowing component (third column). In contrast, the red contours show the parameter space to be much more evenly occupied at higher redshifts, where strong outflows and highly focussed inflows appear to coexist much more frequently. We will study this temporal evolution of the morphology of inflow fields in greater detail in the companion paper to this work by Seidel+2026b.

5.5 Summary and Conclusions

We introduced the inflow asphericity parameter, a new quantitative analysis tool for evaluating the inflow structure of haloes in numerical simulations. This tool is based on a spherical harmonics decomposition and measures how non-isotropic the inflow field around a given

object of interest is. Using a toy model setup to simulate the inflow across a spherical boundary, we showed how the multipole decomposition works and which features this method extracts. For this we varied a number of components of the toy model, corresponding to filaments, isotropic inflow and outflowing regions. There are two complementary approaches to analysing the flow maps: Performing the spherical harmonics decomposition on the linear field extracts the high-flow regions where mass flows are orders of magnitude above the average mass inflow. On the other hand, using the logged inflow field isotropizes the inflow maps significantly and the regions with zero inflow, where outflows dominate become more important.

In combination, these two parameters help distinguish galactic accretion in four distinct phases:

- Highly focussed, filamentary inflow in combination with a strong outflow
- Filamentary inflow with an unperturbed isotropic component, no outflow
- Isotropic inflow, disrupted by outflow
- Unperturbed isotropic inflow

These groups will help identify how a given halo is coupled to the environment in numerical simulations. To demonstrate this, we applied the extraction method to two simulated haloes from the MAGNETICUM simulations. We demonstrated how the features in these more complex flow fields were extracted by the formalism, and showed how it quantifies qualitatively visible differences in the flow fields of two distinct haloes from the simulations. By comparing the linear and logarithmic asphericities for an extended simulation sample, we furthermore demonstrated these two parameters to be uncorrelated, encoding different information about the flow field.

This makes the asphericity a powerful tool to analyse environmental coupling on the intermediate scale just outside of collapsed haloes. With its two variants this parameter is able to reliably trace both the inflow from the cosmic web as well as outflows from the halo interior. In the companion paper to this work, we will further analyse how these two quantities are connected to galaxy properties like star formation rate, gas fractions and metallicities. We will further test how sub-grid modelling influences the flow field geometry around galactic haloes specifically.

Chapter 6

Asphericity in Practice: Accretion at Cosmic Dawn and Beyond

The previous chapter introduced the asphericity parameter as a measure of the flow field isotropy at the bounding surface of a simulated halo. In this chapter we apply this formalism to a large number of simulated halos from *Box4/uhr* in order to explore the evolution of inflow morphologies and its connection to internal halo evolution. Fig. 6.1 shows the evolution of hot and cold gas in *Box4/uhr* on a global scale. It is apparent how the cold gas distribution with its complex filament structure is already established at high redshifts, while the hot atmospheres of halos establish as the halos collapse. At $z = 0$ a stable state appears to be reached with the complex filamentary structure found at higher redshifts simplified due to smaller sub-filaments merging and the hot atmospheres, which are relatively non-spherical at the time they are formed, stabilized into spherical shells around their central halos. From these qualitative insights into the gas morphologies combined with the results from the previous chapter, we expect the flow field morphology as quantified by the linear and logarithmic asphericities to undergo a global evolution as well. Because the logarithmic asphericity is more sensitive to the outflowing hot gas, we expect this parameter to be closely tied to the global evolution of the hot gas atmospheres of galactic haloes. This could be a key indicator of the overall regulation between galactic in- and outflows and as a consequence the star formation and kinematics of the central galaxy. In the following we therefore investigate the co-evolution of the flow field morphology and important signatures of the stellar and kinematic maturity of galaxies.

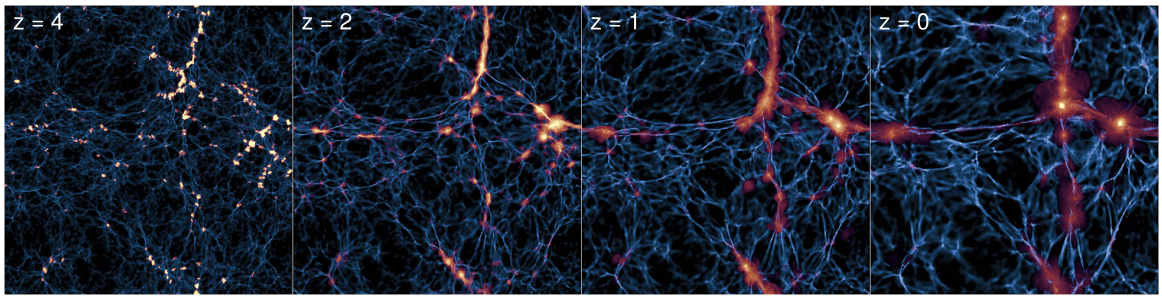


Figure 6.1: Distribution of hot gas (magma colormap) and cold gas (blue colors) density in *Box4/uhr* at four redshifts. In accordance with the visualizations by Dolag et al. (2025), cold gas is defined as all gas particles with a temperature $T \leq 10^4 K$, and additionally all particles actively undergoing star formation. All particles not belonging to the former group are defined as the hot gas component. The thickness of the slices is 1 cMpc at all redshifts.

6.1 The Global Evolution of the Flow Field Morphology

Following (Dolag et al., 2025), we apply a cut in stellar mass of $M_* > 5 \times 10^9 M_\odot$ in order to ensure that the galaxies within the selection haloes are resolved to a sufficient degree. Since this work is focused on the connection of galaxies to the cosmic web, we furthermore restrict the selection to field galaxies (i.e. galaxies that are the most massive subhaloes of their FOF group). In order to ensure sufficient resolution of the gas dynamics, we limit the discussion to the flow field at $1r_{\rm vir}$ here, as a direct measurement of the connection to the environment around a given halo. Because the stellar mass cut leads to reduced statistics for *Box4/uhr* at high redshifts, we additionally employ *Box3/uhr* as a reference for the high-z Universe.

Fig. 6.2 shows the global evolution of the inflow asphericity for both linear and logarithmic asphericity. Both parameters show a peaked evolution with the linear parameter peaking very early on at $z \approx 5$, while the logarithmic asphericity has its peak at around $z \approx 1$.

Linear Asphericity: Evolution The early peak in the linear asphericity is consistent with the early assembly of cold gas filaments around galaxies seen in Fig. 6.1. The linear asphericity declines monotonically after the initial spike upwards. This is consistent with filaments merging and overall trend of filaments increasing in width found in cosmological simulations (Galárraga-Espinosa et al., 2024). An increase in filament width decreases the linear asphericity (see Fig. A.5), due to the inflow being less focused on the virial surface. There is a plateau in this decrease around at an age of 4-5 Gyr, where the decrease stagnates. As this is correlated with the logarithmic asphericity reaching its peak, a possible explanation for this plateau is the interaction of the outflows with the filaments halting the overall growth of relative filament widths, as the atmosphere could effectively disrupt the lower density inflow regions at the outskirts of the filaments. Between *Box3/uhr* and *Box4/uhr*, there is mostly a difference in maximal linear asphericity achieved, while the temporal profile is consistent between the two boxes. As can be seen by the test run (dashed line) which is in agreement with the standard *Box4/uhr*, this amplitude difference can most likely be attributed to the larger box size.

Logarithmic Asphericity: Evolution The logarithmic asphericity increases with a significant delay to the evolution of the cosmic web, reflecting the observation that the hot atmospheres in Fig. 6.1 take time to build up against the cold gas filaments of the cosmic web. It peaks at an age of around 5 Gyr. After this peak the logarithmic asphericity decreases again at a shallower slope than the previous increase. This late time decrease can most likely be attributed to the equilibration seen in Fig. 6.1, the outflowing phase dilutes and spherically expands at late times, allowing for a more isotropic accretion. Additionally re-accretion of the ejected gas can contribute to this late-time decrease in asphericity. This process is known as the so-called halo fountain (Oppenheimer & Davé, 2008, Tumlinson et al., 2017). It should be noted that the median asphericities shown in this global picture only reflects the general evolution within the simulation volume, individual galaxies can evolve on drastically different timescales. Interestingly, there is a discrepancy between *Box4/uhr* and *Box3/uhr* in the logarithmic parameter: The larger Box experiences a much earlier and much steeper rise. Demonstrably in the test simulation, which employs a similarly improved black hole feedback coupling model, the logarithmic asphericity rises steeper than in the Magneticum simulation as well. There is however still a large discrepancy between this simulation and *Box3/uhr*. In part, this can be explained by the more realistic large-scale dynamics in *Box3/uhr*: As discussed in Section 3.8, the larger simulation of *Box3/uhr* captures the cosmic variance more accurately up to large scales, allowing for an earlier collapse of relatively massive nodes of the cosmic web. However, the exact implementation of the

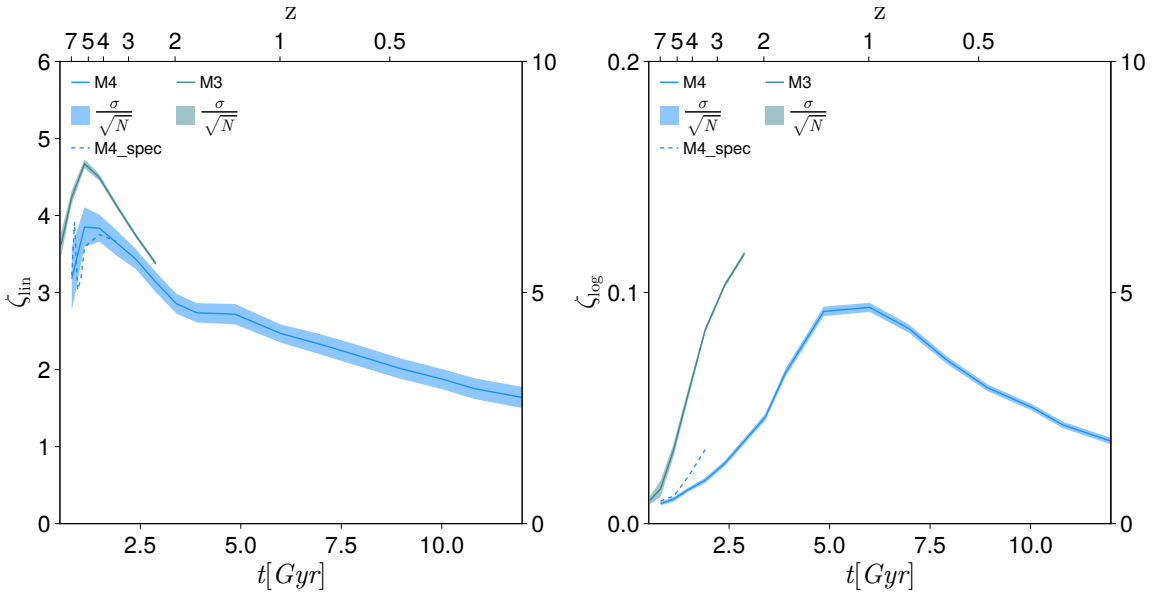


Figure 6.2: Time evolution of the linear (left column) and logarithmic (right column) as a median over all galaxies with $M_\star > 5 \times 10^9 M_\odot$. The curves are shown for both *Box3/uhr* (teal line and shades) and *Box4/uhr* (blue line and shades). For the first few snapshot a test run using *Box4/uhr* but with the improved BH treatment from *Box3/uhr* is shown using the dashed lines.

feedback model seems to be a factor in the asphericity evolution as well. We will discuss this point in more detail in Section 7.2.

6.2 Connecting Asphericity and Galaxy Properties

In the following we test the evolution of the logarithmic asphericity, $\zeta_{\rm log}$, for different subsamples of host galaxies. Fig. 6.3 shows the same evolution as in Fig. 6.2 but for galaxies split by halo mass, star formation activity and kinematic class (left to right). To distinguish between non-quenched and quenched galaxies, following (Kimmig et al., 2025a) we use the criterion by (Carnall et al., 2020). Specifically we compute

$$ssfr_{\rm cut} = \frac{0.2}{t_{\rm H}(z)} \tag{6.1}$$

at each redshift (where $t_{\rm H}$ is the Hubble time) and defined as active all galaxies with a specific star formation rate (sSFR) $\geq ssfr_{\rm cut}$ and as quenched all those below. To classify the galaxies into ETG, LTG and intermediates, we employ the **b-value** (Teklu et al., 2015):

$$\mathrm{b} = \log_{10}(j_\star[\mathrm{kpc} \times \mathrm{km/s}]) - 2/3 \log_{10}(M_\star[M_\odot]) + \log_{10}(\sqrt{z+1}) \tag{6.2}$$

with the additional $\sqrt{z+1}$ scaling factor included to account for the evolution in $j_\star$ (Obreschkow et al., 2015). Using this parameter we define

$$\text{type} \begin{cases} b \leq -4.73 \Rightarrow \text{ETG} \\ -4.35 > b > -4.73 \Rightarrow \text{intermediate} \\ b > -4.35 \Rightarrow \text{LTG} \end{cases}. \tag{6.3}$$

From Fig. 6.3, it is apparent that all three quantities impact the logarithmic asphericity: The

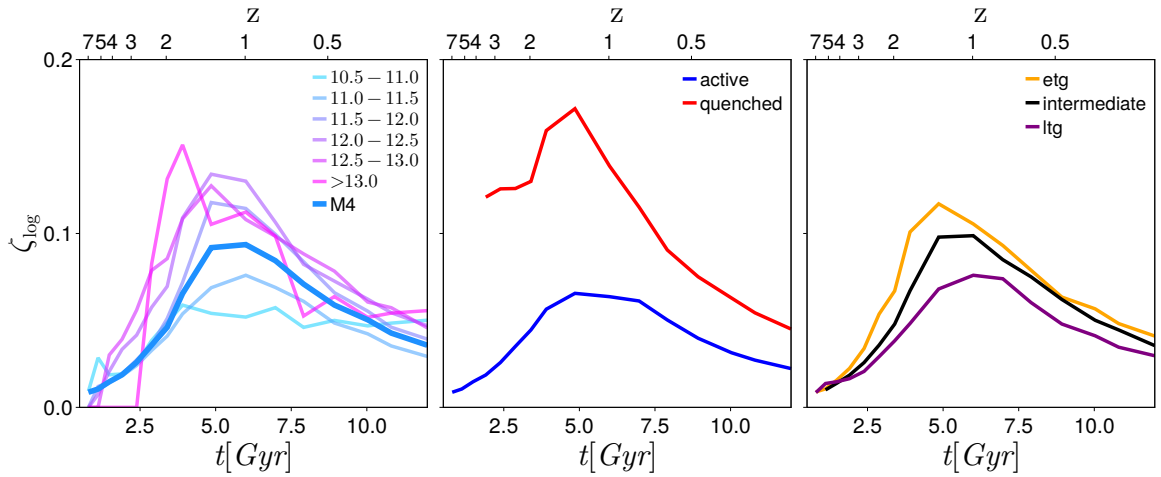


Figure 6.3: Comparison of the logarithmic asphericity distribution between active (blue) galaxy populations and quenched (red) galaxy populations. The medians of the populations at each time is indicated by the vertical lines. In congruence to Fig. 6.4, the distinction between the two classes is made using the criterion by Carnall et al. (2020).

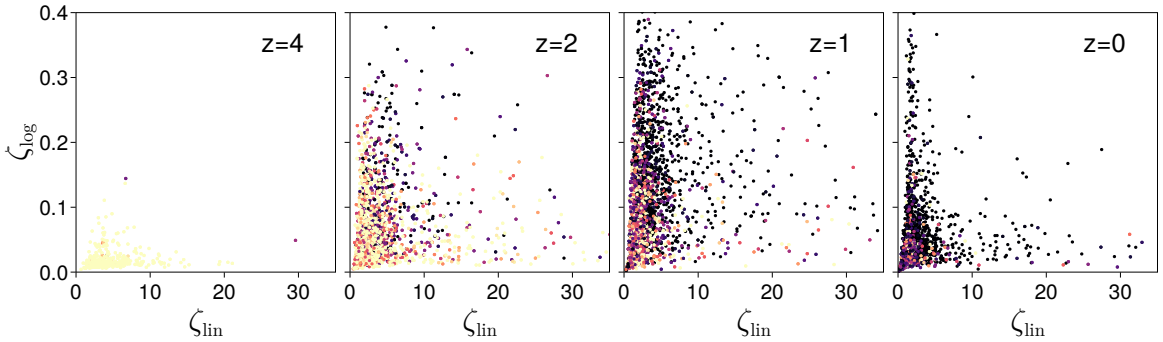


Figure 6.4: Time evolution of the Box4 galaxies in asphericity space. The color indicates the star formation rate relative to the specific star formation rate threshold given by Carnall et al. (2020). All galaxies below that threshold are colored in black.

left column shows that there is a mass dependence for the asphericity with more massive haloes generally peaking at earlier times and achieving higher values than their less massive counterparts. The middle column furthermore demonstrates a clear difference in inflow asphericities between star-forming and quenched galaxies at all times. While star-forming galaxies generally also undergo the increase-peak-decrease evolution, the overall peak is clearly driven by the galaxies that have already quenched their star formation. This is consistent with the picture of the logarithmic asphericity peak resulting from the disruption of the isotropic inflow component by feedback driven outflows: As a galaxy undergoes a star burst and/or a phase of heightened AGN activity, the hot gas outflow reaches the virial surface of the galactic halo when the star formation activity has already been quenched by the burst itself. Fig. 6.5 shows the evolution in asphericity space in general. At high-z the parameter space is limited to relatively low linear as well as logarithmic asphericities (despite the median for the linear asphericity being near its peak as evident in Fig. 6.3.) In general at later times higher values are possible due to the non-linear evolution of galactic environments. However the left panel in Fig. 5.6, with strong outflow coexisting with a very focused inflow is only occupied during the "peak of asphericity" phase around $z = 2$. Until $z = 0$ the upper right corner is significantly less populated again. The color of the points in Fig. 6.4 indicates the ratio of the specific star formation rate to the expected star formation rate using

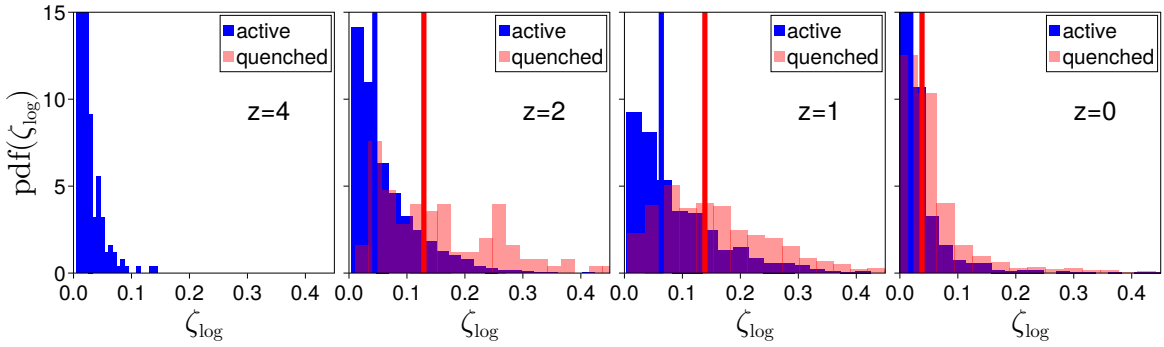


Figure 6.5: Comparison of the logarithmic asphericity distribution between active (blue) galaxy populations and quenched (red) galaxy populations. The medians of the populations at each time is indicated by the vertical lines. In congruence to Fig. 6.4, the distinction between the two classes is made using the criterion by Carnall et al. (2020).

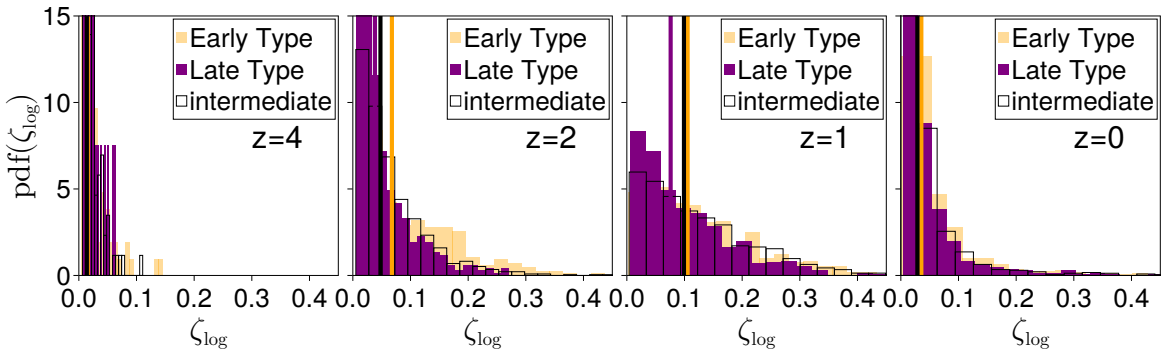


Figure 6.6: Comparison of the logarithmic asphericity distribution between active (blue) galaxy populations and quenched (red) galaxy populations. The medians of the populations at each time is indicated by the vertical lines. In congruence to Fig. 6.4, the distinction between the two classes is made using the criterion by Carnall et al. (2020).

Eq. (6.1). The trend of quenched galaxies (shown in black) settling at higher logarithmic asphericities can be observed here as well. [discuss maybe correlations]. To examine this in more detail we give specifically the PDF of the logarithmic asphericity for active and quenched galaxies in Fig. 6.5. Firstly, the overall evolution of the parameter is observed in the four redshift slices, demonstrated by the medians of both distributions (vertical lines) increasing from $z = 4$ to $z = 2$ and then decreasing towards $z = 0$. Interestingly, the PDF at $z = 2$, the peak of asphericity shows three distinct groups for the quenched population. There is a group that is fairly congruent with the active population from $\zeta_{\log} = 0.05$ to $\zeta_{\log} = 0.1$, albeit missing the peak close to zero. Then there is a second peak around the median (red vertical line). A third clustering of galaxies can be found at even higher asphericities, around $\zeta_{\log} = 0.25$. This multi-modality of the distribution could be connected to how long ago these galaxies quenched, and consequently how strong the hot outflows cutting the galaxy off from the environments still are at the time the PDF is measured. We will investigate the exact origin of these apparent sub-classes in quenched galaxies in future work. Fig. 6.6 shows a similar combination of PDFs, this time divided by dynamical type. The trend that ETG tend to have higher logarithmic asphericities is visible in the form of an excess in the PDF consistently through all redshifts. At $z = 2$ this excess is located at the same values as the median peak and the secondary peak in Fig. 6.5, even though the signal is by far not as clear as for the classification by star formation activity.

6.3 Conclusions

We have explored the behavior and evolution of the **inflow asphericity** parameters, ζ_{lin} and ζ_{log}, which quantify how strongly the inflow onto haloes from their environment varies on large angular scales. The linear asphericity, which is most sensitive to the high-inflow zones from feeding filaments and in-falling haloes peaks at high redshifts, around $z = 5$, where the filamentary structure in the baryonic component becomes prominent against the background. After this peak it declines monotonically. The logarithmic asphericity on the other hand peaks much later at $z \approx 1.5$ and exhibits a sharp increase until this point, as the hot atmospheres of haloes, that counteract the more diffuse inflowing component, build up. This evolution is largely consistent for different box sizes, however we find the logarithmic asphericity to be sensitive to the specific implementation of the subgrid physics, a point we will further explore in Section 7.2. Furthermore, exploring the connection of the logarithmic asphericity to mass, galaxy star formation activity and kinematical type as defined by the b-value, we find galaxies that reach a high degree of large-scale anisotropy in the logarithmic flow field to be predominantly high-mass, quenched and elliptical rather than disky. This corroborates the findings discussed in Chapter 3 and especially Section 3.8, which showed that the process of quenching leaves an imprint on the density environment of early quenching galaxies. The logarithmic asphericity, as a measure for how much of the surface of a halo is covered by in- and outflowing material offers a unique way to quantify that impact.

Chapter 7

Intermission: Further Testing of the Asphericity Parameter

7.1 Flow Resolution: Sensitivity to the Discretization

In Chapter 5 we demonstrated how holes in the inflow field, caused by outflowing material from the inner regions of the halo drives especially the logarithmic inflow asphericity (see particularly Section 5.3). This raises a rather technical question: The shape and extent of these outflowing regions is determined by the overlap of particles on the edge of inflowing regions and particles inside outflowing regions. Due to the adaptive nature of the smoothing scale in SPH (see Section 3.1), this means that the aforementioned particles at the transition between in and outflow will be particles with large smoothing lengths due to their low ambient densities. Fig. 7.1 illustrates this effect: Shown is the logarithmic inflow map for the same halo at two different resolutions. The white pixels are the regions where the outflow dominates. While both maps resemble each other in terms of the dominant inflow hot spots, it can clearly be seen that the additional smoothing in the lower resolution halo leads to a significant underestimation of the extent of the outflows. Consequently, one also would underestimate the logarithmic asphericity. This effect is also measureable on the global scale, using a large sample of halos: Fig. 7.2 shows the evolution of the asphericity in *Box2/hr* compared to *Box4/uhr*. While the linear asphericity is largely similar in terms of its median value between the two boxes, in the logarithmic asphericity the resolution lowers the obtained values drastically. While *Box2/hr* shows a peaked logarithmic asphericity with comparable timings to *Box4/uhr*, the dynamic range is much smaller with values only reaching to $\approx 20\%$

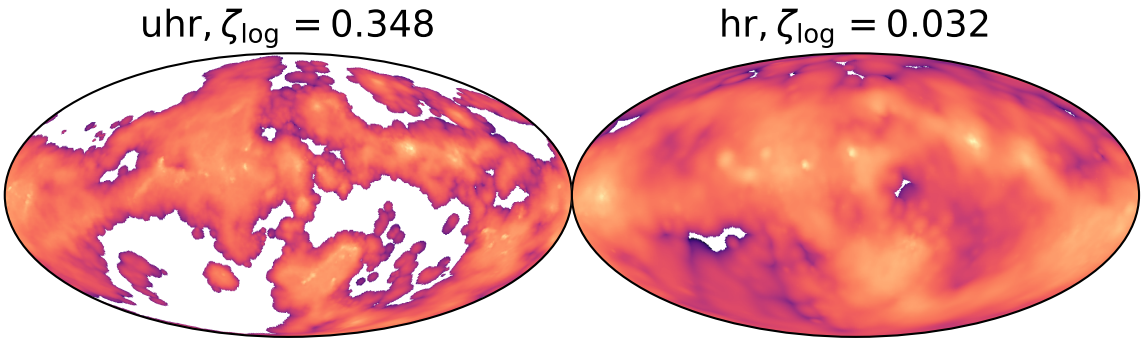


Figure 7.1: Logarithmic inflow map of the same MAGNETICUM halo (Box4) in two different mass resolutions. The logarithmic asphericities are given above.

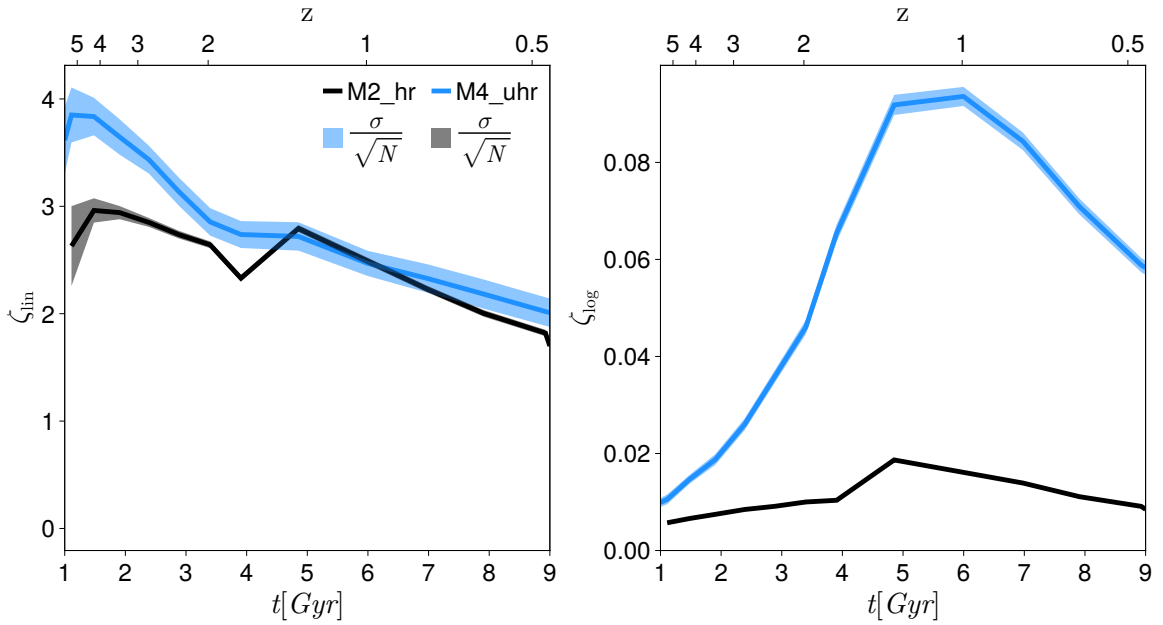


Figure 7.2: Asphericity evolution across time compared between *hr* and *uhr* resolution. Left panel shows the linear asphericity, while the right panel shows the logarithmic asphericity

of the values at *uhr* resolution. Clearly, the visual difference in Fig. 7.1 is present in the simulation volume as a whole. Therefore we focused on *Box4/uhr* in the previous chapter for its suitable resolution to capture the information in both parameters.

7.2 DAWN of Asphericities: Model Dependence of the Parameter

Since the logarithmic asphericity is sensitive to the outflows driven across the virial surface, one can reasonably assume this parameter to be sensitive to the parameters of the sub-grid model employed to describe the physical processes that drive outflows. In the following we systematically test the most important parameters of the Magneticum Pathfinder model using the verification and testing runs created for the MagneticumDAWN simulation suite. We group these runs into four categories according to the part of the sub-grid model they affect.

Stellar Feedback This group consists of runs altering the stellar feedback, either by enhancing the star formation rate through a lower density threshold for star formation or by increasing the wind velocity.

Black Hole Feedback This set aims to costrain the effects of black holes injecting the feedback energy more efficiently into the surrounding medium. Additionally we include a model with the feedback efficiency being dependent on the black hole spin parameter following Sala et al. (2024).

Black Hole Seeding Mass More massive black holes at high redshifts could also result in stronger outflows or faster growth of the outflow covering fraction. Therefore we include also two runs with modified seeding masses for the black holes. One adapts the redshift dependent seeding described by Kimmig (2026) where the seeding mass decreases with time

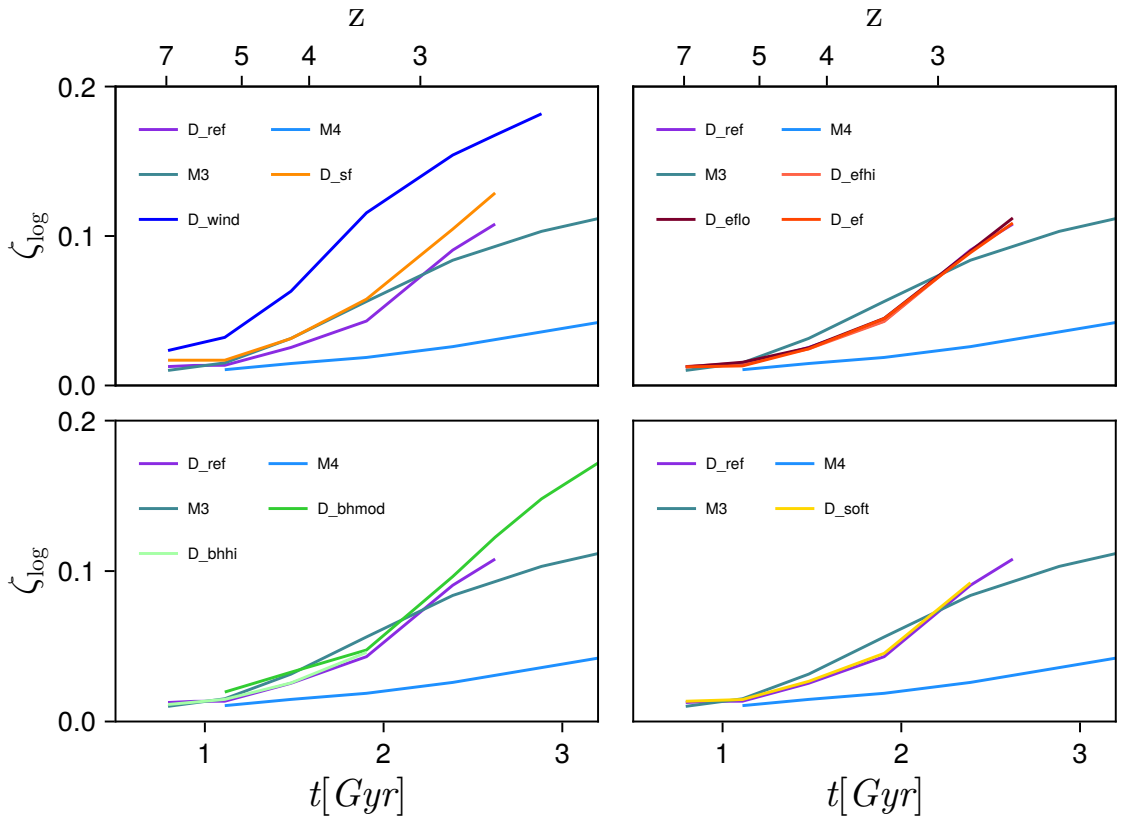


Figure 7.3: Logarithmic asphericity evolution at high redshifts for the different parameter tests. Panels show the different groups (*Clockwise, starting at the upper left panel*): Stellar Feedback, black hole feedback, black hole mass seeding, gravitational softening. Each panel additionally includes the fiducial DAWN test run (purple line) as well as *Box4/uhr* (metallic blue line) and *Box3/uhr* (dark green line) from MAGNETICUM PATHFINDER.

Run	Wind velocity	SF threshold	BH Growth	BH Seeding	Special
MAGNETICUM	350	0.5	100	fixed	–
Box4-AA	450	0.1	50	fixed	–
Box4-AI	450	0.05	50	fixed	–
Box4-AJ	550	0.1	50	fixed	–
Box4-AB	450	0.1	50	fixed	higher ϵ_f
Box4-AC	450	0.1	50	fixed	lower ϵ_f
Box4-AD	450	0.1	50	fixed	spin coupled ϵ_f
Box4-AH	450	0.1	50	K10	–
Box4-AF	450	0.1	50	fixed, 5e-5	–
Box4-AF	450	0.1	50	fixed	gas softening =1.4

Table 7.1: Adaptation of Table 2.3 from (Kimmig, 2026). We show only the runs used in this work, grouped into fiducial (colour here), stellar feedback (color here), black hole feedback (color here), black hole seeding (color here) and softening test (color here). Note that the MAGNETICUM PATHFINDER simulations were run with a much older version of the code and therefore also employed a larger gravitational softening length of 1.4kpc/h, while the fiducial value for the MAGNETICUMDAWN simulations was 0.75 kpc/h. Box4-AF therefore is the **high softening** test case for the newer runs.

in order to avoid quickly growing black holes at low redshifts. The second run seeds black holes at 10 times higher mass than the fiducial value (10^{-4} vs. $10^{-5} M_\odot/M_\star$ fiducial.)

Softening Test Additionally we measure the asphericity for a run re-implementing the higher gravitational softening length from MAGNETICUM PATHFINDER into the simulation as a sanity check. Table 7.1 lists these runs and their specific parameter combinations. For the full overview, we refer the reader to Kimmig (2026).

As the fiducial runs we use the MAGNETICUM PATHFINDER *uhr* simulations, as well as a baseline simulation from the test set: Fig. 7.3 shows the four groups in the redshift range where the runs had available snapshots. Strikingly, the only parameter variation to have any significant impact on the evolution of the logarithmic flow asphericity is the variation of the stellar feedback group. Especially the simulation with the higher wind velocity shows a strong increase compared to the fiducial run and the MAGNETICUM PATHFINDER simulations. There is a slight indication of this effect being especially strong at high redshifts $z > 3.5$ as the slope flattens out for the strong winds run, while for the fiducial run the slope increases at this point. Decreasing the star formation density threshold almost self similarly lifts the logarithmic asphericity to higher values, as stars form more easily in that simulation, and are consequently able to inject more feedback energy into the surrounding medium. A very interesting observation is that the evolution is extremely unaffected by all black hole properties except for possibly the redshift dependent seeding showing an enhanced asphericity later on. However, due to the relatively high final redshift of the reference run, how large the discrepancy grows until $z = 2$ is impossible to deduce. Expectedly, the gravitational softening length has no impact on the evolution of the logarithmic asphericity, as the softening mostly affects encounters in high-density regions. Therefore this runs serves as an additional verification run and shows the global logarithmic asphericity to be robust in different iterations of the same simulation.

7.3 Summary

In this chapter we have performed additional tests with regards to the two previously introduced parameters for the flow field morphology, the linear and logarithmic asphericity. We have shown that how well a numerical simulation can resolve the transition region between dense inflows and diffuse outflows profoundly affects the logarithmic parameter, which traces the surface fraction of the outflows. The linear asphericity is largely unaffected by this, because it traces the configuration of the dense inflow regions. Using a set of simulations with varied sub-grid model parameters, we have additionally shown the logarithmic asphericity to be strongly connected with the stellar winds resulting from the star formation activity within the central galaxy. This is consistent with the findings from the previous chapters, where we demonstrated the galaxies with the largest outflow covering fractions to be the ones already quenched, possibly driven by a preceding massive starburst such as the ones found for the massive quiescent galaxies investigated in Section 3.8 and Kimmig et al. (2025a). These findings further solidify that a galaxy's ability to drive out its gas via strong winds is a crucial part in especially high redshift quenching.

Chapter 8

Further Flowing

This chapter briefly summarizes published work where the inflow asphericity was tested against galaxy and halo properties. For each of these papers I provided data for the plots shown in the respective section and helped with interpreting the results.

8.1 Die Aspherically: Galaxy Classes and Asphericity.

This section has been partially published as Fortuné et al. 2025, A&A 704 A185, "Die Hard: The on-off cycle of galaxies on the star formation main sequence". I provided the asphericity data for Figure 12.

A galaxy's star formation activity can be classified beyond simply calling galaxies with star formation rates (SFRs) below a certain threshold value quenched. In the picture of an equilibrium between gas depletion from star formation and gas inflow from the environment, it is reasonable to postulate a certain equilibrium state (commonly referred to as the bath-tub model see for example Bouché et al. (2010), Lilly et al. (2013), Burkert (2017)). This theoretical equilibrium then gives rise to the so-called **Star Formation Main Sequence**, a scaling relation between the stellar mass of a galaxy and its star-formation rate. Galaxies in this equilibrium state, i.e. that fall onto this scaling relation can be assumed to continuously form stars. Fortuné et al. (2025) showed, using observationally calibrated star formation main sequences at various redshifts in combination with *Box4/uhr*, that galaxies that actually stay in this regulated state throughout their evolution are relatively rare. Tracing a sample of 1282 central galaxies throughout their evolution, the authors were able to identify five main groups of galaxies:

- **Main Sequence:** Galaxies that stay on the main sequence throughout their history. The Milky Way was widely assumed to fall into this category, however recent analytical calculations were able to show this to be implausible due to its current stellar mass (Kimmig, 2026, as well as Kimmig et al. 2026 to be submitted)

- **Quenched Early:** Galaxies that drop more than 0.5 dex below the main sequence before $z = 1$.

- **Quenched Late:** Galaxies that drop more than 0.5 dex below the main sequence after $z = 1$.

- **Quenched Late:** Galaxies that drop more than 0.5 dex below the main sequence after $z = 1$.

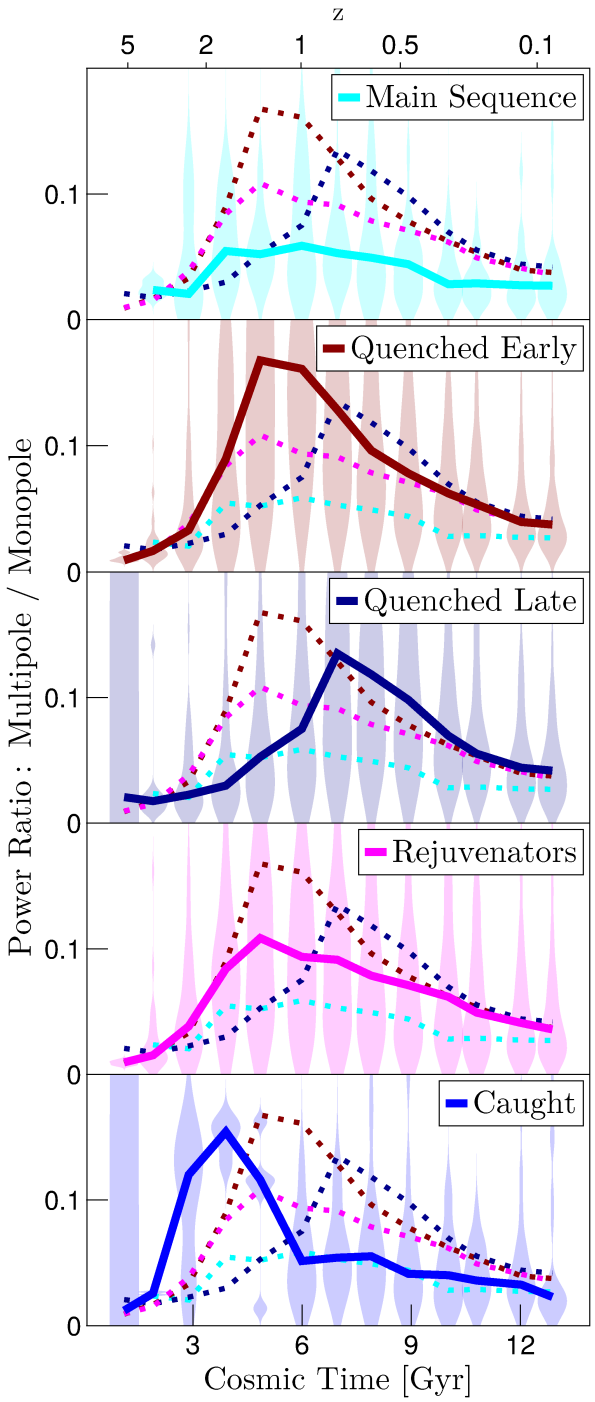


Figure 8.1: Figure 12 from Fortuné et al. (2025).

- **Rejuvenators:** Galaxies that are considered as quenched at some point during their history, but return to the main sequence later. These galaxies can also undergo multiple cycles of quenching and rejuvenation

- **Caught:** Galaxies that maintain a constant but sub-main sequence star formation rate which lie on the main sequence at low redshifts, because the main sequence itself shifts to lower values. Therefore these galaxies are 'caught' by the main sequence.

Fortuné et al. (2025) then analyse these galaxies for various properties such as their merger rates, kinematics and inflow rates compared to the steady state inflow rate. For the scope of this work however it is of interest, how the flow field morphology corresponds to these star formation history.

Fig. 8.1 shows the asphericity evolution for the five classes. In the top panel it can be seen, that main sequence galaxies experience a much less pronounced evolution throughout their histories. This is in stark contrast to all the other classes that drop below the star formation sequence at least once during their lifetime. Notably the early quenching and late quenching galaxies each undergo a strong peak, but offset in time corresponding to the delayed quenching of the latter group. Rejuvenating galaxies exhibit a much weaker peak at times comparable to the early quenching galaxies. A possible explanation is that these galaxies experience a starburst at similar times to the early quenching galaxies, but can later recover their star formation rates, due to the outflows not being as strong and consequently not stopping further accretion as efficiently as for the galaxies that stay quenched. The caught category presents an interesting case as well, due to an early peak in logarithmic asphericity following a steep drop and subsequent main sequence like evolution. This very early disruption of their infall structure apparently allows them to maintain a constant, albeit low star formation rate, which in turn is then compatible with late time main sequence star formation rate.

In summary, Fortuné et al. (2025) further corroborate the evidence that the star formation evolution of galaxies is strongly tied to how affected their gaseous environments are by feedback. This is manifested by the classes identified by the authors showing different evolution with regards to their logarithmic asphericity, with each group's quenching behaviour largely reflected in their gas flow field. In future work we will investigate this connection even further, utilizing the full statistical power of the DAWN flagship runs.

8.2 Shaped by the Flow: Galaxy Halo Shapes and Asphericity

This section has been partially published as Valenzuela et al. (inc. Seidel) 2024, A&A 690 A206, "Galaxy shapes in Magneticum - I. Connecting stellar and dark matter shapes to dynamical and morphological galaxy properties and the large-scale structure". I provided the asphericity data for Figure 14.

As we demonstrated in Chapter 5, the linear asphericity is most sensitive to how focussed the inflow is on the dominant inflow directions set by filaments and neighbouring structures. The tidal environment of haloes has long been known to affect their shape (Chen et al., 2016, López et al., 2025, e.g.). An interesting connected question is how strongly these tidal fields are also imprinted in the gas flow field. Valenzuela et al. (2024) investigated the stellar and dark matter shapes of haloes in *Box4/uhr* at $z = 0$ and how they are correlated and connected to the kinematics. To this end they quantified the shapes of the haloes in terms of three parameters:

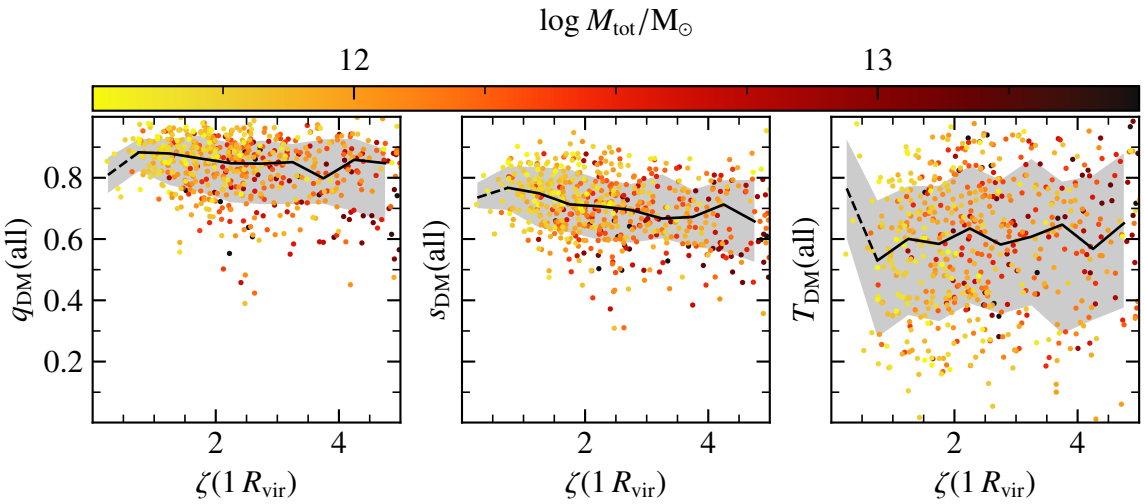


Figure 8.2: Figure 14 from Valenzuela et al. (2024).

- The ratio of the second largest to largest eigenvalues of the mass distribution tensor $q = \sqrt{\lambda_2/\lambda_1}$
- The ratio of the smallest to the largest eigenvalue $\sqrt{\lambda_3/\lambda_1}$, a measure for the sphericity of the halo, where s=1 indicates a perfectly spherical halo.
- The Triaxiality $T = \frac{1-q^2}{1-s^2}$, measuring whether a halo is oblate ($0 \leq T < 1/3$), triaxial ($1/3 \leq T < 2/3$, or prolate ($2/3 \leq T \leq 1$).

Fig. 8.2 shows these parameters computed for the full dark matter haloes at $z = 0$ plotted as a function of the linear asphericity. The triaxiality and q appear to be completely uncorrelated with $\zeta_{\rm lin}$. There is however a weak correlation with the sphericity s. The more the gas inflow of a halo is concentrated on a few dominant inflow zones, the less spherical the dark matter halo. The correlation is not a strong one, but given the fact that the halo shape at $z = 0$ represents the time integrated result of all infall epochs the halo underwent during its evolution, whereas the inflow asphericity measures the instantaneous gas inflow morphology only at $z = 0$, it is quite remarkable that there is a correlation at all.

In summary we have shown the linear asphericity to be connected to the dark matter halo shape at z=0. The more ellipsoidal the halo is at that time the higher the linear asphericity. In future work we will aim to connect the asphericity parameter also to more common structure components, like filaments and sheets, which are also connected to the shape of the dark matter haloes embedded within them.

8.3 Summary and Conclusions

In this brief overview we have highlighted further connections between the inflow asphericity parameter and galaxy properties. In agreement with Chapter 6, we showed that dividing the global evolution curve of the logarithmic asphericity according to the star-formation classes introduced by Fortuné et al. (2025) reveals the peak in the evolution to be driven by galaxies that quench at some point during their evolution. Galaxies that never leave the main sequence on the other hand do not disrupt their inflow field as strongly as the quenched group due to them never undergoing a quenching outflow period. This further highlights the importance of the gaseous environment of galaxies in their star formation evolution.

The linear asphericity could be demonstrated to be indeed connected to the gravitational environment of a galaxy: Galaxies with a strongly anisotropic linear inflow field, that is galaxies with dominant filamentary regions, tend to be more ellipsoidal than galaxies without a strong linear asphericity. This lends further support to the picture established in Chapter 5 and Chapter 6, that the linear flow field traces strongly the large-scale environment and the logarithmic asphericity the baryonic feedback interaction with the resulting flow field.

Part III

Flows in the Local Universe

Chapter 9

Going Local: From Cosmological Simulations to Constrained Simulations

> And now for something completely different.
>
> –John Cleese, *And Now for Something Completely Different* (TV Series)

This chapter is based on the introduction of the simulation techniques published in Seidel et al. 2025, A&A 702, A243, "Simulating the LOcal Web (SLOW) - IV. Not all that is close will merge in the end: Superclusters and their Lagrangian collapse regions". The version in this work includes several additions and updates.

One challenge when comparing cosmological simulations to observational data is that such comparisons can usually only be done in a statistical sense. The initial density field of a cosmological simulation resembles the observed Universe only in terms of the power spectrum $P(k)$ of density fluctuations, while the phases are entirely random and thus do not generally reproduce the exact same structures we observe in the real Universe. Testing the simulation models against real-world observations is complicated by this, especially for observations of physical processes that require a high spatial resolution, severely limiting the statistics due to limiting samples to nearby structures. One example for this is the observed low velocity dispersions from line broadening in local galaxy clusters (Aharonian et al., 2016, XRISM Collaboration et al., 2025, Zhang et al., 2026), which is in significant tension to simulation averages (Truong et al., 2024) (even though simulations can in principle reproduce the observed dispersions). For such a discrepancy, it is a priori unclear whether the deviation stems from an incompleteness of the hydrodynamical modelling (e.g. viscosity additionally suppressing turbulence) in the simulations, or if the observed local clusters are just in the tail of the population of clusters with similar general properties.

One approach to mitigating this problem is to attempt to construct the simulations in such a way, that simulated structures are as similar as possible in terms of their environment and formation history to actual observed structures. This can be achieved by subjecting the initial density field of the simulations to constraints, usually derived from observations of the large scale density or velocity fields in the Local Universe. Simulations of this kind are commonly referred to as **Constrained Simulations**.

9.1 Constrained Simulations

The goal of constrained simulations is to generate large-scale environments that are not only compatible with random Gaussian initial fluctuations but also match the locally observed structures such as galaxy clusters, groups, and the cosmic web in our neighbourhood. The idea of subjecting the Gaussian random fields for numerical simulations was already proposed by Bertschinger (1987). In the past decade, with the availability of better and better data from the Local Universe, this approach to cosmological simulations has gained significant traction with a number of different methods and constraints being used. The approaches can be roughly divided into two groups: Constrained simulations based on galaxy number density information and simulations with constraints based on galaxy peculiar velocity data. The Coruscant simulations are examples of the former approach (Dolag et al., 2005a). Additionally constrained simulations based on Bayesian forward modelling (Kitaura et al., 2012, Heß et al., 2013) such as the Sibelius simulations (Sawala et al., 2022) take galaxy density as an input, but add dynamical modelling. Using velocity data has the distinct advantage of implementing information about an underlying field that fluctuates on a larger scale than the density field, thus providing better large-scale constraints. Simulations using galaxy velocities to build constraints include the CLONES simulations (Sorce, 2018, Sorce et al., 2021), which the HESTIA suite (Libeskind et al., 2020) and the SLOW set of initial conditions and simulations (Dolag et al., 2023) are based on. Previous galaxy cluster and large-scale studies using constrained realizations obtained with these methods include, but are not limited to: analysis of the pressure profiles of a digital Virgo clone, accounting for projection effects (Lebeau et al., 2024c) and the variation in the splash-back radius of Virgo when estimated with different tracers (Lebeau et al., 2024a). Additionally, Malavasi et al. (2023) studied the connectivity of a simulated Coma cluster counterpart to the cosmic web and compared simulated properties to the observed Coma cluster. Large-scale studies with constrained simulations investigated the local galaxy distribution (McAlpine et al., 2022) and velocity waves in the local Hubble diagram as a diagnostic tool for cluster potentials and masses (Sorce et al., 2024) and aimed at constraining the local magnetic field (Dolag et al., 2005b). On larger scales yet, a possible impact of local clusters on CMB anomalies via the thermal and kinematic Sunyaev–Zeldovich effect was quantified by Jung et al. (2024).

9.2 The SLOW Simulation Suite

The following chapters in this work will be mainly based on the SLOW suite of constrained cosmological simulations (Dolag et al., 2023, Hernández-Martínez et al., 2024, Seidel et al., 2025b). We therefore describe the methods and basic principles of the construction of constrained simulations using this specific suite as an example.

9.2.1 Initial Conditions

The starting point of the constrained initial conditions is the Cosmicflows-2 catalogue of distance moduli and redshifts (Tully et al., 2013). From this, the peculiar radial velocities of the respective groups and galaxies can be inferred. Additionally, a grouping scheme is applied (Sorce & Tempel, 2017), which factors out the collapse motions of galaxies gravitationally bound to a specific group or cluster (finger-of-god-effect) and provides a more robust distance through averaging over group members. A number of additional bias correction procedures are subsequently applied to the raw data in order to maximize the accuracy and robustness of the reconstruction and handle the shot noise and intrinsic uncertainty from the Cosmicflows-2 data (Sorce, 2015, Sorce et al., 2017, Sorce & Tempel, 2018). From this

data, the cosmic displacement field ($\mathbf{s}(q)$ in Eq. (1.27)) is then inferred using a Wiener Filter technique (Zaroubi et al., 1995, 1999). Using this displacement field, the reverse Zeldovich approximation is then applied to the tracers to relocate them to their positions at $z_{\rm ini}$ (Doumler et al., 2013), this amounts to rewinding the quasi-linear evolution of the Universe, applying Eq. (1.27) with the displacements reversed. The initial radial velocities of the tracer galaxies are replaced by the 3D velocities inferred by the Wiener Filter in order to accurately factor in the uncertainties in the peculiar radial velocities (Sorce et al., 2014), which prevent the velocity field from being completely described by just the radial velocities (which would be the case for an ideally sampled linear velocity field). The final initial conditions are then obtained by applying the constrained realization algorithm introduced by Hoffman & Ribak (1991) to the reconstructed velocities. The method of obtaining the initial conditions is described in comprehensive detail by (Hoffman & Ribak, 1991, Hoffman, 2009, Sorce, 2015, Sorce et al., 2017, Sorce, 2018, Dolag et al., 2023).

A closely related alternative method to obtain the initial conditions from velocities is to obtain the initial density field by forward modelling, essentially running small PM N-Body simulations and updating the density field in a Bayesian way in order to reproduce the observed final velocities. This approach has the advantage of relaxing the assumptions of linearity in the formerly described method but suffers from biases of its own. One example of such a method is the Hamlet-PM code described by (Valade et al., 2026).

	$\epsilon_{\rm gas/DM}$ $[h^{-1}{\rm kpc}]$	ϵ_* $[h^{-1}{\rm kpc}]$	$m_{\rm DM}$ $[h^{-1}M_\odot]$	$m_{\rm gas}$ $[h^{-1}M_\odot]$	m_* $[h^{-1}M_\odot]$
768	11	3	2.0×10^{10}	3.8×10^{9}	9.5×10^{8}
1536*	5.4	1.5	2.5×10^{9}	4.7×10^{8}	1.2×10^{8}
3072	2.7	0.75	3.1×10^{8}	5.8×10^{7}	1.5×10^{7}
6144	0.75	0.35	3.8×10^{7}	7.1×10^{6}	1.8×10^{6}

Table 9.1: Resolution level conventions in the SLOW suite of simulations. The $\star$ symbol indicates the settings of the current full physics fiducial run SLOW – FP1536^3.

9.2.2 Simulation Runs

Starting from a set of low-resolution constrained white noise, the resolution was increased self-consistently by adding shorter wavelength density fluctuation to the matter power spectrum and finally generating initial particle positions from the upscaled velocity fields. This was done using the Ginnungagap software[1] (Pilipenko et al., 2025) . With the basis field being a 512^3 white noise field in a box of 500 Mpc/h side length (realization 8 from CLONES), SLOW covers a number of up- and down-scaled resolutions, which can be found in Table 9.1. The following work will focus on the SLOW volume currently combining the most complete subgrid physics (including feedback from active galactic nuclei, AGNs) with the highest resolution, termed the SLOW – FP1536^3 run. All simulations were performed using the smoothed-particle hydrodynamics (SPH) code OpenGadget3, which expands on the Tree-SPH code Gadget2 (Springel, 2005). The SLOW – FP1536^3 run employs a subgrid model largely identical to the Magneticum suite of simulations (Dolag et al., 2025) discussed in Chapter 3. All simulations in the SLOW suite assume a *Planck*-like cosmology(Ω_m=0.307 ; Ω_Λ=0.693 ; H_0=67.77 km s^{-1} Mpc^{-1} and σ_8=0.829, see Planck Collaboration et al., 2014).

[1] https://code.google.com/p/ginnungagap/

Name	Resolution	a_{final}	$N_{\text{snaps,future}}$
CLAIRVOYANT	768	1000	1
CLAIRVOYANT REDUX*	768	1100	27
CLAIRVOYANT HIRES	1536	1100	27

Table 9.2: CLAIRVOYANT runs. The $\star$ symbol indicates the run used by (Seidel et al., 2025a).

9.3 Looking Ahead: The CLAIRVOYANT Suite

In order to study the late-time dynamics of Local superclusters (see the following chapter), we additionally performed N-Body runs of the SLOW initial conditions that ran into the far future. This small suite of simulations is called the CLAIRVOYANT set. The first run was performed using the 768 initial conditions from SLOW and ran until a scale factor $a = 1000$. Subsequent simulations followed to improve spatial resolution and optimize the snapshot density. In order to test the convergence of the initial simulation these runs were also ran to an even higher scale factor. An overview of the N-Body forward runs is given by Table 9.2. All additional settings were identical to the SLOW setup for the respective resolutions (see Table 9.1). Using these forward runs in combination with the full-physics SLOW runs, we now turn towards the supercluster regions in the Local Universe.

Chapter 10

SLOW-ly Growing Giants: Superclusters in Constrained Simulations

This chapter is published as Seidel et al. 2025, A&A, 702, A243, "Simulating the LOcal Web (SLOW) - IV. Not all that is close will merge in the end: Superclusters and their Lagrangian collapse regions".

10.1 Introduction: Superclusters

Descriptions of the large-scale structure of the universe usually categorize components of the overarching structure, the cosmic web (Bond et al., 1996b, van de Weygaert & Bond, 2008), according to their collapse mode. Two dimensional collapsing structures are called sheets, linear collapsing structures are called filaments, and the intersection points of filaments, where the most massive clusters are located are called nodes.

Superclusters, as arrangements of galaxy clusters, fall somewhat outside of these three categories since their definition is elusive and encompasses a variety of different morphologies, masses and collapse modes. For example, these regions have been dynamically identified with their basins of attraction, regions within which all large-scale flow lines (disregarding the background evolution) converge to a single point (Tully et al., 2014). Subsequent work has shown this definition to cleanly partition the entire cosmological volume into discrete regions (Dupuy et al., 2019) and these regions then encompass matter organized into all three components of the cosmic web and even voids. Other work (Einasto et al., 2018, 2019) defines superclusters as regions enclosed by contours of enhanced density – or, correspondingly, luminosity – within the cosmic web itself partitioning nodes and sections of filaments according to their density contrast. Studies of the morphologies of the superclusters obtained with these methods yielded two main morphological groups of superclusters using Minkowski functionals: Spider superclusters formed around one central massive object fed by multiple filaments and filament superclusters where the mass is more evenly distributed along one massive filament giving rise to a more elongated geometry (Einasto et al., 2007b). Einasto et al. (2007b) additionally connected these types to the richness of the region, with filaments representing the richest superclusters, while spiders were found to be in general poorer. An even more restrictive definition is given by the "superstes" cluster, coined by Chon et al. (2015), comprised only of components that are actually gravitationally bound to each other. All of these definitions capture a different aspect of the largest matter arrangements in the universe and can thus yield radically different properties.

Supercluster regions are of considerable interest from a number of different perspectives: They host a large number of bridges and filaments connecting galaxy clusters in a pre-merging state making them prime targets for a number of thermal and non-thermal emis-

sion processes as well as the influence of different environments on galaxy evolution (e.g. Aghanim et al., 2024). Additionally these massive structures have been investigated in studies aimed at understanding large scale magnetic fields (e.g. Xu et al., 2006). Finally, as the largest coherent density perturbations in the universe, they decouple from the Hubble flow last and in fact only a few of these objects have been shown to be already actively collapsing (Pearson & Batuski, 2013, Pearson et al., 2014, Reisenegger et al., 2000). This relatively pristine state allows studies of the primordial configuration of matter density perturbations from a cosmological perspective.

The Local Universe in particular is host to numerous peculiarities that possibly can challenge the current canonical cosmological model but at the very least point towards the local volume as being an outlier in terms of large-scale structure. Examples for such features are the local sheet (Einasto & Miller, 1983, Böhringer et al., 2021) which is a 100 Mpc pancake in the Local Universe and contains, among other structures, the local supercluster (Peebles, 2023). The local superclusters specifically have gathered significant observational and observational interest recently: Odekon et al. (2022) investigated the correlation of the in-fall velocity field and the density field, as well as the connection of redshift dispersion and mass (Odekon et al., 2024) of simulated filaments similar to the Perseus-Pisces supercluster in order to constrain a characteristic in-fall velocity from the observational data. Böhringer et al. (2025) examined the galaxy populations around these massive structures, specifically the Perseus-Pisces supercluster, and identified a structure extending over 400 Mpc, which they dubbed Quipu. Further studies found significant local over- (Makarov & Karachentsev, 2011) or underdensities (Böhringer et al., 2020) depending on the tracer for the underlying matter distribution used and supercluster structures that strain predictions of the cosmological model for the most massive structures in the universe (Sheth & Diaferio, 2011) though there is ongoing debate whether these structures can actually be reconciled with standard expectations (Sawala et al., 2025). These features can play an important role in resolving or contextualizing current tensions between cosmological parameters obtained from local data and derived from the CMB (assuming the standard cosmological model) such as H_0 and σ_8.

In the following we will use the simulations introduced in Chapter 9 and introduce the prominent local supercluster regions that arise in the Local Universe model. Furthermore we will study the late time dynamics of these regions and compare their final masses to analytical predictions and the supercluster masses estimated from linking schemes at z=0.

10.2 Methods

10.2.1 Cross-identification of Structures

Starting from four catalogs of local supercluster members with galaxy cluster masses (Boehringer & Chon (2021), Boehringer et al. (2021), Merluzzi et al. (2015), and Monteiro-Oliveira et al. (2022)), B1, B2, M, and MO hereafter, respectively, we first found the counterparts for the most massive clusters in each region in the catalog by Hernández-Martínez et al. (2024) (the exception here being the Hercules supercluster, where we expand on the catalog of Hernández-Martínez et al. (2024) by identifying A2147, see Section 10.3.1). In a second step, we searched for the secondary members using the observed separation of the main and the secondary as a starting point. We first identified all companions for the simulated main cluster, i.e., halos within 50 Mpc/h with masses above $1 \times 10^{13} (M_{\rm vir})$. The search radius was chosen such that the maximal observed companion cluster distance $\max(r_{\rm obs}) = 38.77$ Mpc/h (UGC3355) was contained with a margin within the search region. The mass limit was chosen mainly due to mass resolution limitations. For each observed companion we then searched for a match among the simulated companion candidates using the observed relative

position of the main cluster and the observed companion. This relative position vector, added to the position of the simulated main halo, gives an "ideal" counterpart position with respect to the configuration of the region. The two main criteria for picking a companion match are the deviation from this ideal configuration given by the difference in distance from the main halo and the angular distance to the ideal position and the mass agreement of the companion. By using these criteria, we aim to ensure that the companion matches we identify are found in a spatial configuration that resembles the observed supercluster structure (in 3D) and mimic the mass distribution in the supercluster. Fig. B.7 gives a visual illustration of this process. In the rare cases where the aforementioned criteria yield two or more good candidates we select the objects best matching additional observed properties specifically M_{500} and $L_{X,500}$. Due to the uncertainties in the observed 3D positions, which are not taken into account in the cross-identification process this can be considered a conservative estimate of how well the regions are reproduced.

To give an idea of the morphology of the resulting structures we then created mock all-sky observations in X-ray luminosity (0.1-2.4 keV band) and Compton-y using the program SMAC (Dolag et al., 2005b). The observer position was chosen according to Dolag et al. (2023), so all regions are viewed in the same projection. This perspective does not necessarily reflect the selection criterion, which employs the 3D arrangement of the clusters. As an observational reference for the produced Compton-y morphologies we used a Compton-y all-sky map extracted from *Planck* data (Planck Collaboration et al., 2016d) using the MILCA algorithm (Hurier et al., 2013) and cleaned for regions with high CO emission according to Khatri (2016) to which the *Planck* bands used for Compton-y measurements are also sensitive. As an X-ray reference observation, we used the all-sky ROSAT data at 1.5 keV (R6+R7=0.76-2.04 keV) from the ROSAT All-Sky Survey (RASS) (Snowden et al., 1997). The map was smoothed with a Gaussian kernel (σ = 10 arcmin). For the regions with a smaller field of view (Shapley, Hercules, Coma), we employed a different smoothing kernel size (σ = 5.4 arcmin) and used only R7 (1.05-2.04 keV).

10.2.2 Quality Assessment of the Crossmatches

To verify that the cross-identified regions stem from the constraints on the large-scale matter distribution obtained from the Local Universe rather than the intrinsic statistical clustering properties of the simulation, we introduced an angular two-point significance criterion, expanding on the approach described by Hernández-Martínez et al. (2024). The basic idea is to obtain an "uncertainty volume" based on the deviation of the position of the simulated cluster from the observed position. Based on this volume, one can then estimate the probability of finding the observed structure randomly by sampling this volume many times in an unconstrained simulation. This is equivalent to performing a null hypothesis test with the supercluster regions obtained from an unconstrained simulation serving as the null hypothesis. To obtain good statistics for the relevant mass range, we use Box0 of the Magneticum suite of simulations. This simulation features a volume of 2688 $\mathrm{Mpc/h}^3$ with a $1.73 \times 10^{10} M_\odot$ dark matter mass resolution and 5575 halos with masses exceeding $10^{15} M_\odot$.

Fig. 10.1 visualizes how the probabilities were calculated for the pair case. First, the expected position of the less massive companion was calculated by obtaining r_{obs}, the relative distance vector of the observed counterpart, and adding this vector to the simulated position of the main halo. This expected position ($x_{2,exp}$) together with the position of the simulated companion ($M_{2,sim}$) and the main halo (M_1) spans a triangle with the opening angle Θ. The volume corresponding to the spherical volume used for the one-point case by Hernández-Martínez et al. (2024) is then the cone obtained by rotating this triangle around the bisector of Θ. This cone covers a solid angle of $d\Omega \approx \pi\Theta^2$ (for small Θ), which quantifies how close the simulated companion is to the expected position in the reference coordinate system of

the main halo. We estimated the probability of finding the companion within $d\Omega$ by sampling random cones centered on randomly selected massive clusters (we chose a threshold of $M_{\rm vir} > 10^{15} M_\odot$ to sample only the most massive regions which can be expected to have the highest occurrence of massive companions) in the reference simulation. We then counted the frequency of companions with a mass equal to or larger than the mass of the SLOW counterpart. In total we sampled 10^6 cones in 5575 main halo vicinities. We further required that the companions lie in the radial range $r_{\rm sim} - dr_{\rm sim,obs}/2 < r < r_{\rm sim} + dr_{\rm sim,obs}/2$ to sample the supercluster regions in a similar radial regime. The geometric significance is therefore given by

$$p_{\rm pair} = 1 - \frac{N_{\rm found}}{N_{\rm cones}}, \tag{10.1}$$

the inverse of the fraction of cones sampled that contain at least one companion of $M > M_{2,\rm sim}$. Because we leave the mass for the randomly sampled companions unbounded toward more massive objects and because we take the observed relative positions of the secondary clusters as ground truth, without accounting for the uncertainties these positions themselves carry, the methods introduced above provide a conservative estimate of how well the simulations reproduce these regions.[1]

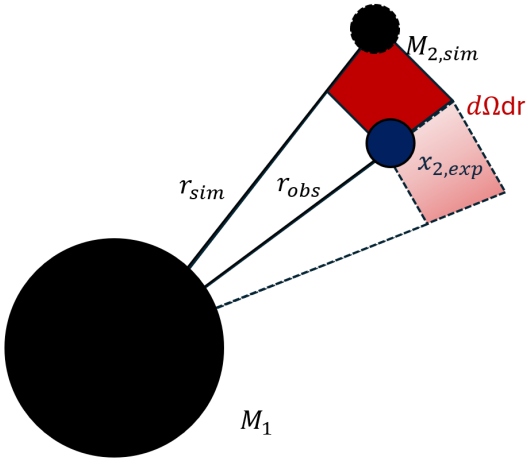


Figure 10.1: Schematic of how the two-point significances are estimated based on the radial (dr) and angular ($d\Omega$) separation of the simulated secondary cluster, M_2, to the expected position ($x_{2,\rm exp}$). The red color indicates the part of the cone that is used as a "significance volume" to compute the probability of obtaining the geometric arrangement randomly.

10.2.3 Simulating Ahead: The Clairvoyant N-body Forward Simulation Suite

To analyze to what degree the cross-identified supercluster regions are actually collapsing numerically, we performed forward simulations using a lower resolution (768^3) of the SLOW initial conditions set and let the dark matter particles (no gas particles were considered) evolve until a scale factor of $a = 1000$, equivalent to 119 Gyrs into the future or the equivalent cosmological redshift of z=-0.999 (it should be noted here that negative redshifts are not physically meaningful but serve as an illustrative temporal parameter), corresponding to roughly $8t_H$ with $t_H = 1/H_0$ and our assumed $h = 0.6777$. This specific time was chosen to

[1] This process can also be understood as defining a spatial metric $\mathcal{D}(r, dr, d\Omega)$. It is then possible to calculate for each cluster $\mathcal{D}_{\rm sim} = \mathcal{D}(r_{\rm obs}, dr_{\rm sim,obs}, d\Omega)$ and compute $p_{\rm pair}(\mathcal{D}_{\rm sim}, M_{\rm sim})$ as the fraction of companion clusters of a mass of at least $M_{\rm sim}$, where $\mathcal{D} > \mathcal{D}_{\rm sim}$ with regards to a randomly sampled observed position in the reference simulation.

ensure that the rapid expansion of the background due to dark energy domination has frozen in all large-scale evolution. As was already remarked upon by Nagamine & Loeb (2003), this causes the simulation itself to speed up at late times. We then ran the `Subfind` structure finder in an identical setup to the parent simulation on this evolved "final" state in order to identify final halos.

10.3 Results

Table 10.1: Reference set and cross-identified member clusters

Region	Reference	Observed members $M_{\rm vir} \geq 10^{14} M_{\odot}$ (all members)	Counterparts	Maximum Influence radius [Mpc/h] at z=0
Shapley	M	4(11)	6	15.95
Perseus-Pisces	B2	7(22)	8	9.90
Coma	B1	5(13)	4	13.93
Virgo	B1	1(5)	3	8.70
Centaurus	B1	2(10)	4	12.71
Hercules(core)	MO	2(4)	3	10.94

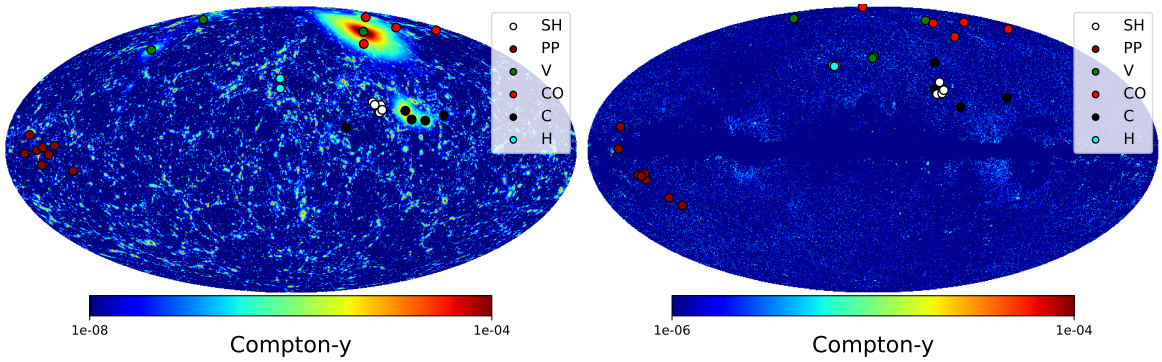


Figure 10.2: Simulated mock Compton-y map (projection from 5-350 Mpc) from SLOW (left) and observed Compton-y map (right) from Planck (Planck Collaboration et al., 2014). Similarly to (Dolag et al., 2023), the simulated map employs a larger dynamic range to highlight the imprints of the local clusters. SLOW cross-identified supercluster members compared to selected observationally obtained supercluster regions using the catalogs from Boehringer & Chon (2021), Boehringer et al. (2021), Proust et al. (2006), Monteiro-Oliveira et al. (2022). The different colors indicate the regions: C=Centaurus, CO=Coma, H=Hercules, PP=Perseus-Pisces, SH=Shapley, and V=Virgo (Local supercluster).

10.3.1 Superclusters in the SLOW Simulations

As the most massive and galaxy rich assemblages of matter, superclusters can be expected to be among the most well constrained regions in the SLOW simulations. Since the constraints are derived from the galaxy peculiar velocity field, their high galaxy density results in a well-sampled velocity field in these regions. We selected supercluster regions and member clusters from three observational supercluster catalogs and identified the corresponding regions in the SLOW simulations by utilizing the crossmatched most massive clusters in the simulation as described by Hernández-Martínez et al. (2024). We then identified the companion clusters and groups as outlined in the previous section. The general properties of the

six supercluster regions for which we find viable counterparts with the methods introduced above are shown in Table 10.1. As can be seen from the table, we are able to identify counterparts for most of the massive supercluster members in the observational catalogs. Fig. 10.2 shows the distribution of these regions on a simulated full-sky Compton-y map generated with SMAC (Dolag et al., 2005b) and centered on the SLOW optimal center from Dolag et al. (2023). The colored dots indicate each respective supercluster and show the simulated superclusters to reproduce the general spatial arrangement of the observed regions.

The crossmatched member clusters are listed in Table B.1 arranged by region and with their most important properties. To provide more details on each region and the exact arrangement of the member clusters, we show a four-panel figure for each supercluster - Fig. 10.3 for the Shapley supercluster and Fig. 10.5 for Perseus-Pisces. The remaining four regions can be found in Appendices B.2 to B.5. The four panel plots/Superclusters are structured as follows. The top row (panels A and B) compares a mock image from the simulation (A) and the respective X-ray observation (B). For an easier comparison of simulated and observed fluxes, both maps are normalized to the mean flux within R_{500c} of the simulated and the observed Coma cluster, respectively. To give a better idea of the underlying structure, panel A shows the gas density contours of the mock region in thin white (2D gas overdensity levels of $[1.25, 20] * \bar{\rho}_{\mathrm{image}}$) and thick white lines, respectively. The density was calculated using SMAC and a suitable projection depth to capture all of the member clusters, and smoothed with a Gaussian kernel ($\sigma = 4.5'$) to compute smoother contours. In the bottom row we show the predicted Lagrangian collapse volume of the supercluster calculated from the forward simulation described in Section 10.2.3 at different points in time. This Lagrangian volume is given by the Friends-of-Friends (FOF) group at the last snapshot (at z=-0.999). In the left panel (C) it is shown in the initial conditions with the individual member Lagrangian volumes overplotted. In the right panel (D) the Lagrangian volume is shown at z=0 in the context of the surrounding large-scale structure. Note that it is primarily the linear scale of the density, or rather the velocity field, that is constrained by the observational data for SLOW. Additionally resolution effects from the simulation itself can already impact halos in this mass regime even if they are induced in the correct place by the constraints. Therefore we do not expect the low-mass member clusters and groups ($M \approx 10^{13} M_{\odot}$) to be reproduced accurately and focus on the most massive member clusters for the cross identification.

The Shapley Supercluster Region

The Shapley supercluster as identified by Merluzzi et al. (2015) consists of four massive core members: A3558, A3556, A3562 and A3560. As can be seen in panels A and B of Fig. 10.3, we recover A3558 and A3560 (numbers 1 and 4 in the plots/Superclusters) in consistent positions in SLOW. Additionally, we find three more members of the outer supercluster, namely A3571, A1736 from Proust et al. (2006) and A3559 which is also identified by Merluzzi et al. (2015) but less massive. Shapley is one of the most massive supercluster structures observed to date (Zucca et al., 1993). This region, especially its central core has been the focus of many multiwavelength studies, investigating radio and X-ray evidence for sloshing at the center of A3560 (Venturi et al., 2013), nonthermal signatures of group-cluster interaction in the region between A3562 and A3558 (Venturi et al., 2022) as well as optical and spectroscopic analysis of substructures and filaments connecting the supercluster members (Merluzzi et al., 2015). A recent study performed a blind extraction of the full filamentary network from the galaxy distribution and connected the star formation activity of the galaxies in the region to the supercluster environment and its filamentary structure (Aghanim et al., 2024). The relatively large distance of the Shapley supercluster, with a redshift range of $z \in [0.04, 0.055]$ (Proust et al., 2006), puts it at the very edge of the SLOW region one could reasonably expect to be constrained. Evaluating the tracer galaxy positions

from Cosmicflows-2, we find only a single galaxy velocity within the collapse volume of the region (see also Fig. B.8). Nevertheless, this structure is recovered to striking detail. The characteristic large-scale arrangement can be clearly seen in Fig. 10.3, with the gas density contours indicating the central filamentary structure connecting A3558 (1) to A3560 (4) and A3571 (2) as found by Aghanim et al. (2024). Additionally, the structure connecting A3559 (6) and A1736 (3), which is also identified as a filament by Aghanim et al. (2024), can be seen in the underlying gas density. In addition to these morphological agreements, Fig. 10.4 shows the two-point significances discussed in Section 10.2.2 for four exemplary member clusters. The small separation angles ($\sqrt{\Omega_{sim}}$, (vertical red lines) for these members (in combination with their high masses) lead to a very low probability of random detection, quantitatively solidifying the agreement from the projection in Fig. 10.3.

A notable distinction from the observed supercluster is the stage of the merger in the core of the region: A3558 and A3562 have already merged at $z = 0$ in the simulation forming a double core that is already identified as a single halo and additionally undergoes another merger briefly before z=0 (likely responsible for the lack of a counterpart for A3556). These slight offsets in merging state/time occur quite often and most likely arise from the positional uncertainties that can significantly shift the in-fall history in collapsing systems. Additional uncertainty factors for these histories are introduced by the assumed background cosmology, the linking criterion of the halo finder, and possibly the exact numerical implementation of the simulation code.

A3532: Differences between one-point and two point results The distant member cluster A3532 illustrates how considering the relative positions of the member clusters - as opposed to the distance to their observed position - can impact the cross-identification of SLOW clusters with observed counterparts. The match identified by Hernández-Martínez et al. (2024) is selected because its mass in combination with the small distance to the observed position of A3532 gives it a high one-point significance. Relative to the Shapley SC core A3558, the previous counterpart is, however, in the wrong position, indicating another simulated cluster as a better counterpart based on the arrangement of the wider region. The previous match is found to be a better fit for A3559 with respect to the supercluster structure. Fig. 10.3 shows the situation. Cluster 6 is the previous match, now identified with A3559 and cluster 5 the new counterpart for A3532. The resulting two-point significances for the two matches can also be seen in Fig. B.6, quantitatively demonstrating the alternative match to be in a better position with respect to the supercluster environment. This is the only supercluster member also identified by Hernández-Martínez et al. (2024) where the supercluster environment indicates a different counterpart to the method used in that work, so a disagreement between the two methods appears to be a rare occurrence and can likely be attributed to the previously discussed sparsity of constraints in this particular region.

The Perseus-Pisces Supercluster Region

The Perseus-Pisces complex, as was identified by Boehringer & Chon (2021), is notable by its filamentary and branching morphology (Einasto et al., 1980) and comprises seven high-mass members; namely, A426, AWM7, CIZAJ0300.7+4427, 3C129, A262, NGC507, and UGC3355. We identified counterparts for all of these members (see the third section of Table B.1) and reproduced this filamentary appearance to a striking degree. This can be seen in the top row of Fig. 10.5: the V-like structure of the main branches of the filament given by A426 (1), AWM 7 (2), and UGC2562 (3) found in the observation is reproduced by the simulated region, as is indicated by the gas density contours connecting the two companions to A426.

The Coma Supercluster Region

The Coma supercluster or, as it is alternatively called, the Great Wall (Gott et al., 2005), has five massive member clusters identified by Boehringer & Chon (2021): A1656, A1367, A1185, MKW4, and NGC4325. We find counterparts for the first four of these clusters in the SLOW simulation. The main halo A1656 – the Coma cluster – is one of the most prominent and best-studied structures in the Local Universe. The properties of the crossmatched members are listed in Table B.1. The region spanning the triangle of the Coma cluster, MKW4, and A1185 constrains this supercluster region especially well, as can be seen from the red dots in Fig. 10.2 and in more detail in Fig. B.1 where a zoom-in view of the region is provided both in observations and in simulations, as well as the collapse structure of the supercluster and its large-scale (dark matter) environment.

The Local Supercluster Region

The Local supercluster is a typical spider-type supercluster (Einasto et al., 2007a), dominated by one central rich cluster (Virgo) which is also the only member of this region from the catalog by Boehringer & Chon (2021) above $10^{14} M_{\odot}$. We identify a match for this cluster as well as another less massive system, NGC5846, from the catalog in the SLOW simulations. Otherwise, the Virgo supercluster is composed of galaxies in a filamentary arrangement. This property is well reproduced by SLOW, as can be seen in the lower right figure of the four panel plot Fig. B.3 and in the three projections of Fig. B.7, with the dominant filament being the Virgo-Centaurus filament. Additionally, we identify a promising counterpart for one of the "traditional" local supercluster members; namely, the M94 group (sometimes referred to as CVn or CVn I group), which was omitted in the catalog by Boehringer & Chon (2021). The Local SC is the most tentative FOF association described by Boehringer & Chon (2021), requiring alleviation of the criteria the authors apply. Several of the smaller groups that the authors list as members of the structure fall below the luminosity limit applied to the other superclusters and additionally they list the giant ellipticals M86 and M87 as separate members, despite belonging to the Virgo cluster itself. The problem of the relatively low mass of the members identified by Boehringer & Chon (2021) is further aggravated in the simulations by the uncertainty of the center, i.e., the position of the observer in the model Universe (see Dolag et al. (2023)). Additionally, as an extremely close-by region the geometric distortions of a shift in center are expected to be the most severe for this supercluster. Correspondingly, the members of this region – defined by Boehringer & Chon (2021) – have only relatively weakly constrained counterparts in the simulation, or rather no counterparts at all are identified with our methods, as is the case for some of the observed clusters.

The Centaurus Supercluster Region

The Centaurus supercluster, as was identified by Boehringer & Chon (2021), hosts only two massive structures, A3526 and NGC5044. We find a counterpart for A3526 in the SLOW simulation and additionally identify matches for three of the less massive systems, NGC4936, AS0753, and A3574E. Whether the Hydra and Centaurus supercluster region is composed of one joint supercluster rather than two separate agglomerations is a matter of debate in the literature. Boehringer & Chon (2021) find these regions to be separate using their luminosity-weighted linking length. However, in the SLOW simulation, the distance of Hydra and Centaurus is reduced significantly ($r_{\mathrm{sim}} = 9.6$ Mpc) compared to the observed distance ($r_{\mathrm{obs}} = 30.9 \pm 6.0$ Mpc)[2]. As a result, the two clusters are gravitationally bound

[2]Relative distance and error are based on the positions and velocity uncertainty given by Tully (2015)

together with Hydra falling onto Centaurus. Thus the supercluster regions are merged into one, consequently also biasing the masses in the region toward higher masses. The closer proximity of the Hydra cluster compared to the observed Centaurus supercluster additionally changes the geometry of the region, complicating the identification of clear counterparts for the member clusters, especially NGC5044, the most massive secondary cluster in this region.

The Hercules Supercluster

Cross-identification of A2147 Because (Hernández-Martínez et al., 2024) do not find a counterpart for the main cluster of the Hercules supercluster structure, namely A2147, applying their search criteria, we start by trying to identify a counterpart with a slightly extended search radius. In their study on the Hercules supercluster core, Monteiro-Oliveira et al. (2022) give a total mass of $13.5^{+2.1}_{-1.7} \times 10^{14} M_{\odot}$, placing it well into the mass regime of the most massive halos in the simulation box. This means that a detection, even at a higher distance to the observed position, is likely to be reliable. We identify a candidate halo at $r_{\rm obs} = 53.54$ Mpc/h separation from the observed position. We computed the M_{500}-based significance as described by Hernández-Martínez et al. (2024) for this detected counterpart. The resulting probability is $p = 0.043$, indicating a detection probability of 95.7%, indicating that this halo is a viable counterpart (see also Fig. B.5).

The Hercules supercluster core itself is a concentrated structure ($r_{proj} \approx 9$ Mpc according to observations (Monteiro-Oliveira et al., 2022)) constituted by three main structures: A2147, A2151 (Hercules cluster), and A2152. Monteiro-Oliveira et al. (2022) additionally identified two massive sub-clumps not previously identified in the structure. In the SLOW simulation, A2147 as the central halo is fed by at least three filaments (see the contours in Fig. B.4) along which other massive groups and clusters such as A2151 and A2152 fall in. Both of these infalling structures have counterparts in the SLOW simulation. However, in the catalog by Boehringer et al. (2021) only the low-mass tail of the larger supercluster region lies within the survey volume, leading to relatively low-mass members ($10^{13} - 10^{14} M_{\odot}$) in their study. Due to their distance to the supercluster core and the low masses, we currently do not find reliable counterparts for these structures in SLOW.

10.3.2 The Future of Bound Structures

In the linear picture of structure formation, initial density fluctuations of small to intermediate wavelengths enter their collapse and virialization phase first, followed by the long wavelength modes. For this reason, galaxies and even clusters of galaxies form relatively early on in a phase of moderate background cosmology expansion. The biggest structures, however, namely superclusters, are only just forming today, making the cosmological context they evolve in a quite different one to the matter-dominated background Universe at $z = 0.5$ and higher. Their relatively young dynamical age at the present time makes superclusters hard to separate and it is unclear to which degree structures that appear connected in observations can actually start collapsing and form virialized structures. In Section 10.2.3 we introduced the additional forward propagated box of the SLOW initial conditions. Fig. 10.6 shows a slice through this `Clairvoyant` simulation at the present time and in the far future. It demonstrates the evolution of the cosmic web to be already almost progressed to its final morphological state at the present time. It should be noted here that this standstill occurs only in co-moving space, in real space the frozen structure is rapidly drifting apart.

There is little to no late time evolution in co-moving space at the largest scales, consistent with previous numerical experiments (e.g., Nagamine & Loeb, 2003, Busha et al., 2003, Hoffman et al., 2007, Araya-Melo et al., 2009). Collapsing overdensities separate into gravitational "islands" with all flows between those regions halted by the rapid expansion pulling

theses islands apart in real space. For similar reasons, while the voids continue to empty out after the present time, there is also a significant amount of matter that is left behind in the voids, never reaching the walls on its outflowing trajectory.

The suppression of structure formation is also reflected in the evolution of halo masses. Fig. 10.7 shows the halo mass in the Clairvoyant simulation and its evolution with cosmic time. While the halo mass function (hmf) evolves to some degree after $z = 0$, barely reaching objects with masses of $10^{16} M_{\odot}$, its evolution is severely slowed down. Additionally, it is precisely the largest structures that assemble after the present time, with a completely halted evolution at the group to small cluster mass end. This reflects the assembly of the supercluster structures that are dynamically still very young at the present time. Beyond 60 Gyr the evolution of large-scale structures is strongly suppressed in co-moving space, as can be seen by the last halo mass function lines completely overlapping at the high-mass end even though there is not one finite point in time when it is halted completely.

Fig. 10.8 shows the mass evolution of the halos associated with the superclusters introduced in the previous section in the `Clairvoyant` simulation. We furthermore show the evolution of the most massive halo in the simulation volume overall (black line) as a reference for the general structure evolution in the box. Generally, two classes of superclusters can be identified with respect to their mass growth history: those that have already assembled their mass fully at the present time (Perseus and Virgo); and superclusters that undergo significant mass accretion and major mergers in the future before freezing out.

The most prominent example of such late-growing superclusters is Shapley: this supercluster experiences two major mergers in the future, associated with the infalls of A3560 and A3571, respectively. A common peculiarity of these late-time mergers is that the virial mass of the halos actually decreases again after reaching a peak after the secondary cluster has fallen in. This peculiarity can also be understood with the late time merger of the Shapley supercluster with A3571 (the rightmost spike of the blue curve in Fig. 10.8). While A3571 reaches the cluster center against the expansion of the background and can thus be considered bound to the survivor cluster, a significant amount of its mass is lost again by the subsequent puffing up of the halo. This leads to particles being ejected to radii where they can rejoin the Hubble flow, keeping them from collapsing to the final virialized object and subsequently decreasing the mass within a virial radius of the halo again (although in total the mass increases).

The effect of post merger-relaxation has been studied by Lee et al. (2018), albeit at z=0. They find that significant post-merger mass losses are common, with low-mass halos being more strongly affected by this effect than high-mass halos. Interestingly at z=0 in their highest mass bin centered at $\log(M[M_{\odot}]) = 13.45$ they find a fraction of $\approx 5\%$ of halos that experience a mass-loss greater than 10% of the peak mass (i.e., the maximum mass the halo reaches in the merging process). In our (statistically not significant) sample, 50% of halos lose more than 10% of their peak mass, with Coma achieving the highest loss fraction of $\approx 16\%$ (see also Table 10.2). Considering the mass trend found by Lee et al. (2018) and the masses of the halo sample in this work, this is a strong indication that this mass-loss process is much more drastic in the late-time Universe, aided by the rapid expansion. Another distinction to the mass loss studied by Lee et al. (2018) is that for the late-time mergers the mass loss is generally not recovered through re-accretion of the lost material. This is illustrated by the trajectory of Hercules in Fig. 10.8: due to the final major merger happening early enough ($t \approx 18 Gyr$), the supercluster is able to recover nearly all of its peak mass after an initial post-merger mass loss. In contrast, the mass lost by the last major mergers, in for example Coma, is lost to the Hubble flow and never recovered.

The concept of "unbound" particles was previously discussed in the literature by, for example, Behroozi et al. (2013), though this study was limited to massive halos that do not undergo a major merger after z=0. Nevertheless the finding that simple energy considerations

are poor predictors of whether particles are actually bound to a given structure is in excellent agreement with the diversity of mass history trajectories and irregular collapse volumes we find in this study (see e.g., Fig. 10.3 and the more detailed discussion in Section 10.3.3).

Freeze-Out Time

To more accurately estimate the freeze-out time, the time at which structure formation is stopped completely, we considered the mass assembly histories of the most massive structures; namely, the most massive supercluster from the sample, the Shapley supercluster, and the halo with the largest final mass in the box overall (black line) shown in Fig. 10.9. Though the overall mass growth is already suppressed significantly after $\approx 2t_H$, there is still considerable growth in mass for both halos after this point, finally evening out at a freeze out time of $t \approx 50$ Gyr (the most massive halo in the simulation evens out its growth to a growth rate of less than 0.1% of its final mass ($M_{\mathrm{vir,fin}} = 5.5 \times 10^{15} M_{\odot}$) per Gyr at 52.85 Gyr). Additionally, Fig. 10.10 shows a histogram of the assembly fractions of the 10000 most massive halos in the final snapshot at five points in time in the future. This evolution solidifies the impression from Fig. 10.9 of there being a non-negligible fraction of halos still evolving in the far future. From the median at $3t_H$ it can be seen that the average massive halo still assembles approximately 4% of its final mass beyond that point. Interestingly, compared to the simulation run by Nagamine & Loeb (2003), which used a similar approach and found a freeze-out time of about 30 Gyr in the future (or $\approx t_0 + 2t_H$ with their parameters) this convergence time is further in the future the SLOW simulation seems to still assemble structures beyond this point in time. It should be noted, however, that this is quite hard to judge from the halo mass function alone, since Fig. 10.7 seems to be in good agreement with Figure 2 in (Nagamine & Loeb, 2003). We conclude from this that the observed late-time evolution in this does not necessarily contradict the previous result. Rather, it expands on what (Nagamine & Loeb, 2003) found for their simulations. Nagamine & Loeb (2003) used different cosmological parameters ($\Omega_0 = 0.3, \Omega_\Lambda = 0.7, h = 0.7, \sigma_8 = 0.9$) and a smaller simulation volume with vacuum boundary conditions. The assumed cosmology can impact the exact timing of the freeze-out: the slightly higher dark energy density and larger H_0 used by (Nagamine & Loeb, 2003) shift the freeze out closer to z=0 because the background expansion dominates against gravity at an earlier time. A sensitivity to the σ_8 used for the simulation is also likely as the strength of the clustering can additionally affect the exact collapse times.

Additionally the freeze-out time can be impacted by the boxsize as a larger box contains longer wavelength density perturbations compared to a smaller volume. As the superclusters, being the largest bound structures in the volume, are expected to sit at the peaks of these large-scale fluctuations, one would expect a constructive effect on the evolution of these regions in the slightly larger box of SLOW and thus a shortening of the freeze-out time. However without a dedicated experiment, the relative importance of these effects is difficult to assess. We leave this experiment for future work as it is beyond the scope of this first study on the SLOW superclusters.

Whether SLOW Predicts that the Milky Way Will Fall onto Virgo

At the present time, the Local Group has a measurable peculiar velocity with respect to the Hubble flow in the direction of the Local supercluster (e.g., Lynden-Bell et al., 1988). This raises the question of whether the Local Group itself might be bound to the Local supercluster. Previous numerical works, for example, tackled this question from both a numerical (Nagamine & Loeb, 2003) and an analytical (Chon et al., 2015) perspective. All current evidence points toward the Local Group receding away from the Local supercluster in the future due to cosmic expansion. We can verify this result in the SLOW simulation by us-

ing the collapse volume of the Local supercluster from the `Clairvoyant` simulation. Since there is no direct counterpart for the Local Group in SLOW, we use the box center as the first proxy for its position. This choice is reasonable, since the constraining data are by construction centered on our position in the Universe. A second plausible choice would be the SLOW-optimal center given by Dolag et al. (2023) as the Milky Way position taking into account the distortions that affect the positions of local galaxy clusters. Fig. 10.11 shows both of these proxies and their position relative to the collapse volume of the Local Supercluster. In agreement with previous works, the SLOW simulation predicts the Local Group to be unbound from its closest supercluster as the collapse volume of the Local Supercluster does not contain either choice for the Milky Way, or rather Local Group position. Chon et al. (2015) also compared the peculiar velocity of the Local Group toward the Virgo cluster of about 220 km/s with the velocity necessary for collapse, which they computed to be about 800 km/s at the position of the Local Group. Computing the center-of-mass dm velocity of a spherical region of 500 kpc/h around both our Local group position proxies, we measure a Virgo-centric inflow of 272 km/s for the SLOW optimal center and 316 km/s for the box center. [3]In agreement with the collapse volume, these velocities show that neither center is bound to the Virgo cluster. In addition the SLOW optimal center reproduces the observed Virgo-centric in-fall velocity quite well. Similarly to (Nagamine & Loeb, 2003), we also computed the total peculiar velocities at the SLOW optimal center. We find a total velocity of 625 km/s with respect to the Box rest frame, in great agreement with the observed CMB dipole of 620 ± 15 km/s (Planck Collaboration et al., 2020). This also indicates the collapse volumes computed in this work to generally agree with analytical expectations, which we shall explore further in the next subsection.

10.3.3 Collapse Regions

What constitutes a supercluster region from a physical perspective is an inherently ambiguous question. The definitions from previous works can be summarized into the following three criteria:

1. Density criteria, i.e., selecting a region enclosed by some density contour (e.g., Boehringer & Chon (2021), Boehringer et al. (2021)).

2. Dynamical criteria, i.e., selecting mass tracers converging onto a local attractor (e.g., Dupuy et al. (2019)).

3. Boundness criteria, i.e., selecting a region that will collapse onto a structure in the future respecting the background evolution of the cosmology (e.g., Araya-Melo et al. (2009), Dünner et al. (2006), Chon et al. (2015)).

There have been a number of theoretical and numerical approaches toward determining the collapsing or bound fraction of a given overdense region based on the evolution of a spherical overdensity with regards to a homogeneous background cosmology (Nagamine & Loeb, 2003, Busha et al., 2003, Dünner et al., 2006, Hoffman et al., 2007, Araya-Melo et al., 2009, Pearson & Batuski, 2013, Chon et al., 2015). These works all aimed at deriving a critical density (or mass given an observed radius) a region needs to be able to form a single structure in the future. The derivation by Busha et al. (2003) arrived at a critical density ratio of $\Omega_c = 5.56$ for a marginally collapsing shell at $a \to \infty$. In contrast, by relaxing the assumption of particles moving with the Hubble flow at the present time and working purely with spherical collapse theory Dünner et al. (2006) obtained a lower critical density ratio of

[3]To improve the sampling of the velocity field locally, these velocities are based on a higher resolution 3072^3 (non-hydro) run of the SLOW-Box

$\Omega_c = 2.36$, a value later confirmed by Chon et al. (2015) to be stable across different cosmologies. Chon et al. (2015) referred to those collapsing regions as superstes clusters (lat. survivor) because they are able to survive the accelerated expansion of the Universe at late times and in the future. These objects are systematically smaller and contain less mass than the supercluster regions obtained with criteria 1 and 2 and rather represent the dense cores of these associations, see (Chon et al., 2015) whereas especially the dynamically defined "basins of attraction" – i.e., the regions from which all large-scale flow lines converge on a single point – have been shown to partition a given cosmological volume completely (Dupuy et al., 2019).

In numerical simulations, criterion 3 is accessible by letting the gravitational part of the simulation propagate far into the future and keeping track of which parts of an associated region reach the center at $t_{\rm final}$. A first-order approach to this is simply evaluating the FOF groups in the final snapshot, as described in Section 10.3.1. This method associates every particle that comes within a linking length of a supercluster member particle with the selected supercluster. It will conservatively include every particle that reaches the supercluster center, which has some technical benefits for creating a new class of zoom-in initial conditions for galaxy cluster and supercluster simulations further discussed in a companion paper to this work (Seidel, Dolag and Sorce in prep.). For a direct comparison between the method used in this work and purely theoretical approaches, Chon et al. (2015) calculate the extent of the collapsing region (maximum radius to which the overdensity necessary for collapse is fulfilled) of the Shapley supercluster and the Local supercluster at z=0. Fig. 10.12 shows the comparison between this radius and the convex hull of all FOF particles from `Clairvoyant` for both structures. It can be seen that the total extent is in good agreement, with deviations arising mainly from the more adaptive shape of the Lagrangian region for the Shapley supercluster, while the collapse volume for Virgo is larger than estimated from the in-fall velocity structure by (Chon et al., 2015). A possible explanation for this is the slightly larger total mass in the Virgo counterpart in SLOW, but this is a small difference and the velocities in Section 10.3.2 showed the dynamics to be in good agreement between observed and simulated Virgo region (at the position of the Local Group), so this discrepancy needs to be explored in further detail in future work. Table 10.2 lists the final collapse masses of the

Table 10.2: Survivor halos of the local superclusters

Region	$N_{\rm m}$	$M_{\rm FoF}$	$M_{\rm vir}$	$M_{\rm est}$ (reference)	$\frac{M(z=0)}{M_{\rm fin}}$	$\frac{M_{\rm fin}}{M_{\rm peak}}$
Shapley	3	72.86	44.42	500.0[a]	0.42	0.86
Perseus-Pisces	2	18.09	12.13	249.0 (B2)	0.87	0.99
Coma	2	47.08	29.52	168.0 (B1)	0.64	0.84
Virgo	2	16.59	11.91	25.0 (B1)	0.84	0.98
Centaurus	2	34.56	21.59	56.0 (B1)	0.47	0.89
Hercules	3	38.13	24.05	21 ± 2 (MO)	0.64	0.99

[a](Proust et al., 2006)

Note: For each region we list number of accreted members and their masses at the final snapshot ($a = 1000$). All masses are given in units of $10^{14} M_\odot$.

introduced regions. It is apparent that conventional linking methods such as the ones used to link the superclusters in the catalogs B1,B2 and (Proust et al., 2006) systematically over predict the mass that is actually bound to these superclusters. This usually only contains the central most companion halos as can be seen in Table B.1. The exception from this in our sample is the Hercules supercluster, where the mass estimate from the observation is based

only on the innermost core members, which are gravitationally bound to the central halo due to their proximity at z=0 according to `Clairvoyant`. Notable is also that the two most massive regions in the local supercluster set have the lowest ratios of FOF mass to mass contained within the virial volume. This fact is related to the mass loss these halos experience when they undergo a massive merger, as discussed earlier. The lost particles stay within the FOF density contour but remain frozen outside of the virial surface due to the background expansion.

One of the predictions made by spherical collapse models such as the one of Dünner et al. (2006) is the critical density contrast of marginally collapsing regions at z=0: $\Omega_{\rm col} = \frac{\rho_{\rm col}}{\rho_{\rm crit}}$. Numerically we computed this ratio for the collapsing supercluster regions ($\Omega_{\rm SC}$) from the forward simulation via

$$\Omega_{\rm SC} = \frac{\rho_{\rm SC}}{\rho_{\rm crit}} = \frac{M_{\rm SC}}{\rho_{\rm crit} V_{\rm SC,z=0}}, \tag{10.2}$$

where $M_{\rm SC}$ is the mass of all particles in the previously defined collapse regions and $V_{\rm SC,z=0}$ is the volume occupied by them at z=0 estimated by computing their 3D convex hull. Fig. 10.13 shows how the present-time density contrast of these particle groups compares to the theoretical predictions from spherical collapse theory (Dünner et al., 2006). It is apparent that, while the theoretical prediction is a good estimate, the scatter of the numerically obtained densities of the collapse volumes is quite high. Because the spherical estimate from Dünner et al. (2006) considers only radial motions, there is a straightforward explanation for the clusters exhibiting a higher density ratio than predicted. These halos develop in different tidal environments and, due to these large-scale tidal fields, accrete angular momentum differently. Since angular momentum hinders the gravitational collapse, a higher density contrast is needed for the region to be bound. This argument is similar to the one used by Dünner et al. (2006) to explain the difference to the numerical experiments performed by Busha et al. (2003), which yielded a significantly higher critical density. As can be seen from Fig. 10.9 and from the masses in Table 10.2, even particles that make it into the final FOF group can actually end up and freeze (in co-moving space) outside the halo by virtue of the finite timescale of virialization. A prerequisite for this complication is a very late in-fall as demonstrated by the in-fall of A3571, as discussed before. An overall consequence of this is a more diffuse final dark matter halo, as is evident from the density contrasts in Fig. 10.13 for the Shapley and Coma supercluster regions.

10.4 Summary and Conclusions

We used the SLOW constrained simulations of the Local Universe to study nearby superclusters. By matching these structures and their member clusters pairwise to their observed counterparts, we are able to compare basic properties of these clusters, such as their masses, their relative positions, and their X-ray luminosities, to observations. By running an N-Body version of SLOW, the `Clairvoyant` suite, into the far future (z=-0.999), we are furthermore able to determine the final masses of these superclusters and discern which member clusters are actually bound to them. We furthermore compare these results to previous numerical and theoretical estimates. Our main conclusions are:

1. In total we cross-identified supercluster members in six observationally identified regions in the SLOW simulation with their observed counterparts. Most of the supercluster members with masses exceeding 10^{14} can be reliably recovered in the simulation, providing a number of viable targets for future studies and expanding on the existing catalog of cross-identified galaxy clusters in the SLOW simulation from Hernández-Martínez et al. (2024). Examples of such future targets include the Shapley supercluster core (A3558, A3571, A3560, and A3562), where the planned high-resolution

zoom-in simulations based on the collapse volumes introduced in this work can provide insightful comparisons and context for the rich multiwavelength observational data for this region.

2. We introduced a quantitative method of estimating how likely a given crossmatched galaxy cluster pair is a result of the constraints rather than random clustering from the simulation. According to this criterion, only a few of these members can be confused with random cluster pair arrangements, with the majority of (77% of secondaries) cross-identifications exceeding 80% significance. This shows that the SLOW simulation not only reproduces the massive clusters within supercluster regions with unprecedented accuracy, but additionally also mimics their 3D geometric arrangement by providing suitable structures close to the positions where one would expect them based on the observed 3D arrangement of the member clusters within the supercluster. This builds on previous works concerning the environments and collapse dynamics of local galaxy clusters (e.g., Sorce et al. (2024), Malavasi et al. (2023)) and will contribute to future studies of the detailed properties of the individual member clusters, such as their turbulent pressure support and nonthermal and thermal emission features, as the environments these members evolve in are well constrained.

3. The Clairvoyant forward N-Body integration of the SLOW initial conditions shows the local dominant galaxy clusters to have largely finished their evolution by $t = 33$ Gyr, with the less massive regions such as Perseus and Virgo effectively reaching their final gravitational state at $z = 0$.

4. A notable feature of the late-time evolution is the massive mergers some of these clusters undergo as late as $t = 2t_H$. In this process these structures undergo as much as a 16% loss of their peak mass. This is a significantly higher fraction of merger mass loss than previous work found for z=0 (Lee et al., 2018). At late times in the Λ-dominated Universe, these mass loss processes appear to be enhanced. Furthermore, for these very late-on mergers the peak mass is never reached again due to the particles freezing out in co-moving space (or accelerating away with the Hubble flow in real space).

5. In general the Clairvoyant volume completely stops its mass evolution approximately 40 Gyrs in the future when the most massive node in the simulation stops growing. Compared to previous results (Nagamine & Loeb, 2003, Hoffman et al., 2007), this shows that individual structures still significantly evolve at late times, even with structure formation being hindered by the rapid expansion. However, small changes in the assumed cosmology and numerical modeling can significantly impact the exact timing of these late-stage dynamics.

6. Determining the density ratios of the Lagrangian collapse regions of massive clusters at $z = 0$ shows good agreement with predictions from spherical collapse theory, with the scatter explained by the different accretion histories these objects undergo after the present epoch.

Building on these results, in future work we plan to study the supercluster regions introduced above in greater detail, additionally making use of zoomed-in initial conditions built on the Lagrangian collapse regions shown above (Seidel, Dolag, and Sorce in prep.). Furthermore we plan to identify supercluster regions in the SLOW simulations with a blind search in order to compare these superclusters with the set introduced in this work.

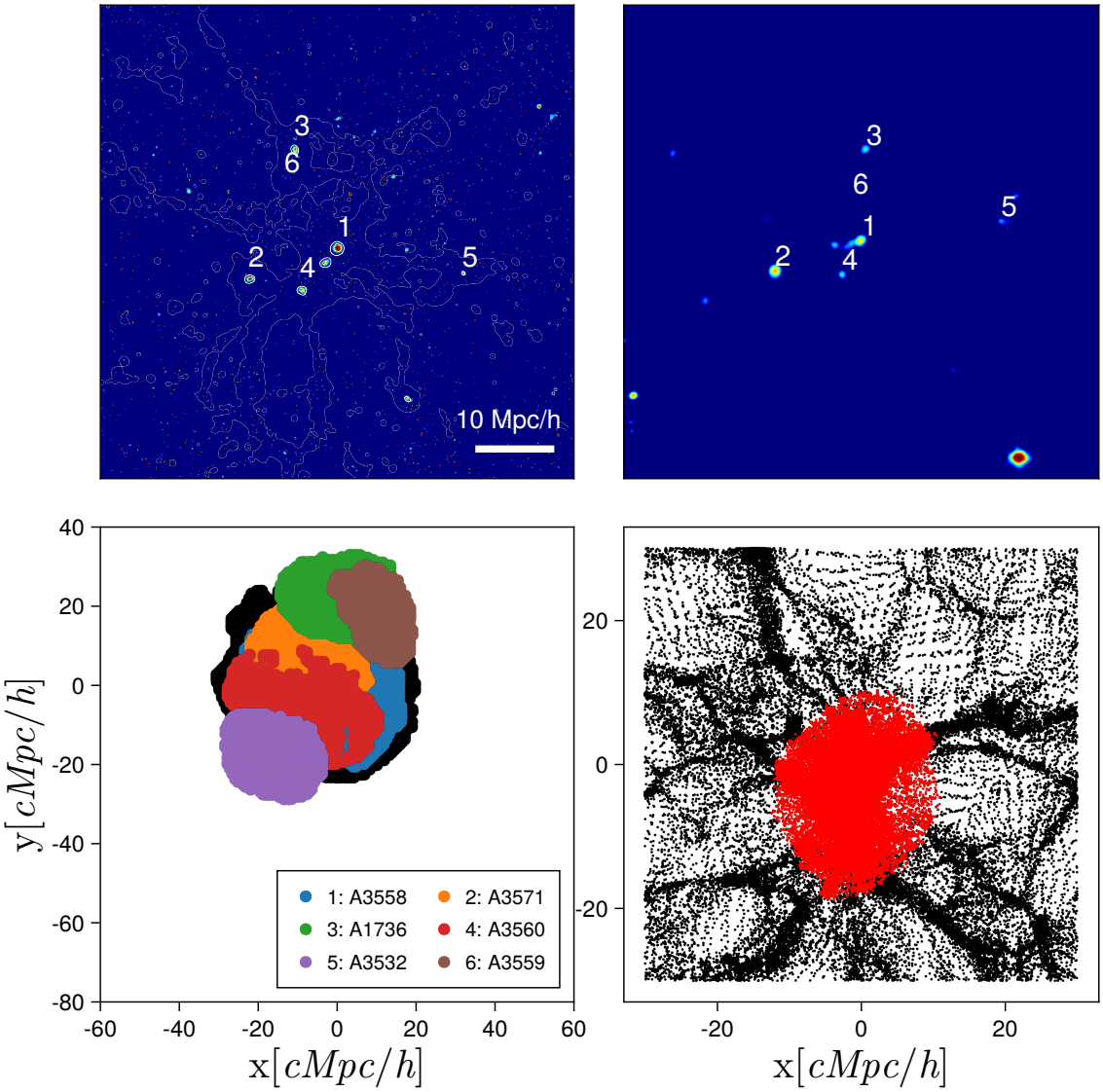


Figure 10.3: *Top left:* Shapley supercluster region in the SLOW simulation with the cross-identified counterparts: 1:A3558, 2:A3571, 3:A1736, 4: A3560, 5:A3532, and 6:A3559. The white bar indicates 10 Mpc at the distance of the main cluster in both the simulated and the observed image. The white contours show the 2D gas overdensity levels of $[1.25, 20] * \bar{\rho}_{\mathrm{image}}$. The gas density was computed in a spherical shell of 47 Mpc/h thickness centered on the main cluster. *Top right:* Same FOV as the one viewed by ROSAT. *Bottom left:* Supercluster core region (black) according to the Clairvoyant N-Body forward simulation in the initial conditions ($z = 120$) with the member clusters from Table B.1 overplotted as colored dots. *Bottom right:* Collapse region (red) and its environment at $z = 0$.

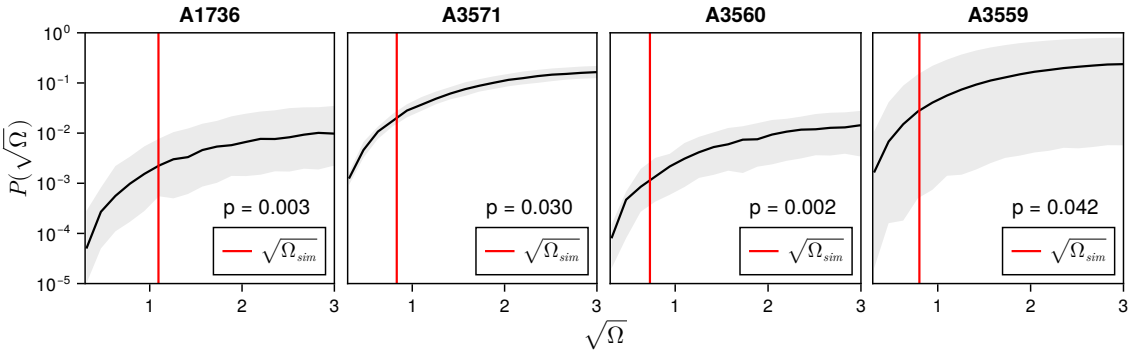


Figure 10.4: Two-point probabilities for the Shapley member clusters as a function of the opening angle $\sqrt{\Omega}$ of the cone spanned by the observed and simulated relative position of the secondary cluster to the main. The shaded gray regions reflect the mass uncertainty of the secondary halo. The vertical red line indicates the deviation angle measured in the SLOW simulation. The x value of the intersect of this line with the angular probability function gives the probability of finding the secondary within the deviation cone in a random simulation.

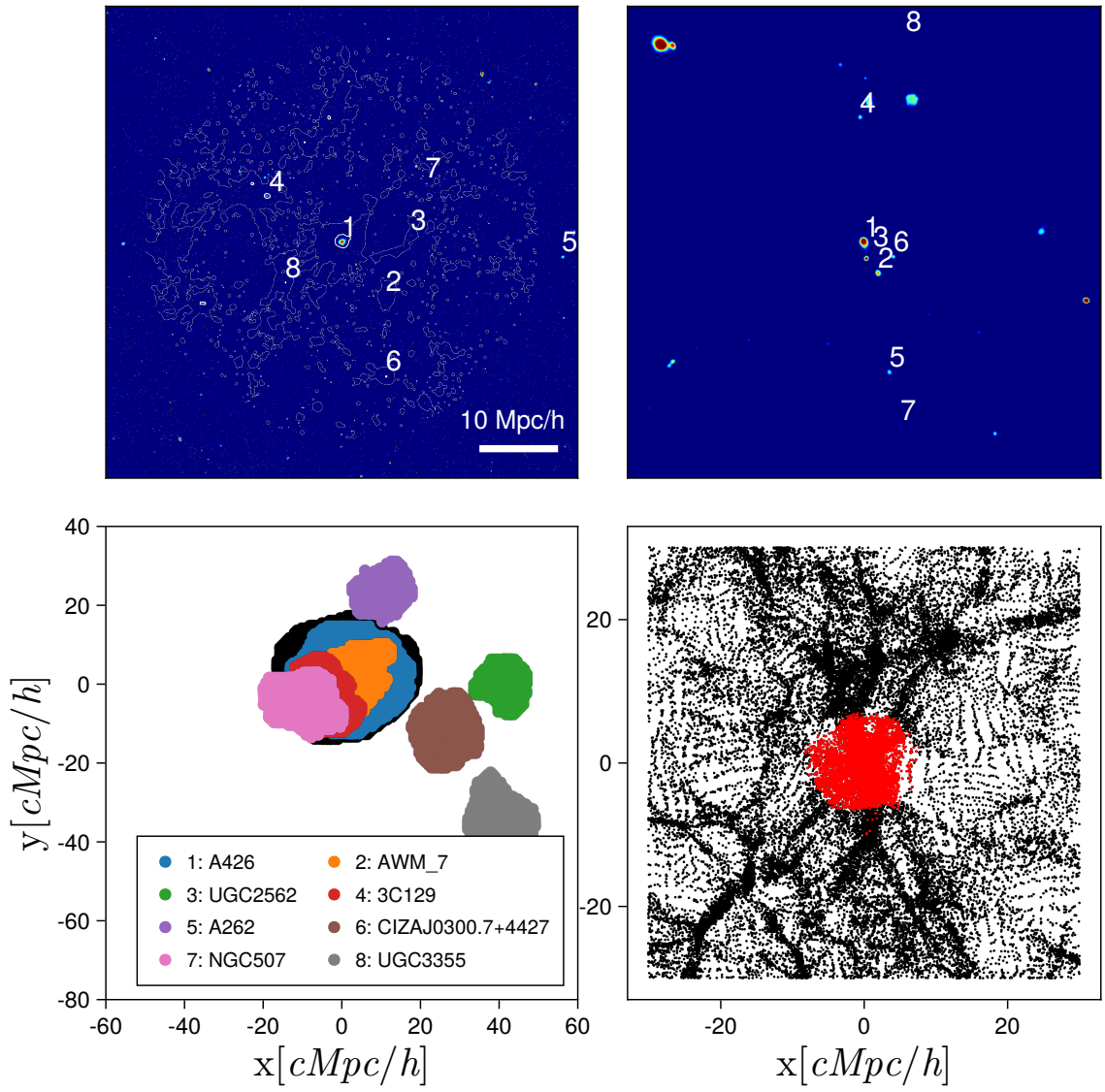


Figure 10.5: Perseus-Pisces supercluster region in the SLOW simulation with the cross-identified counterparts: 1: Perseus (A426), 2: AWM 7, 3: UGC2562, 4: 3C129, 5: A262, 6: CIZAJ0300.7+4427, 7: NGC507, 8: UGC3355. The white contours show the 2D gas overdensity levels of $[1.25, 20] * \bar{\rho}_{\rm image}$. The gas density was computed in a spherical shell of 54 Mpc/h thickness centered on the main cluster. *Top right:* Same region as viewed by ROSAT. *Bottom left:* Supercluster core region according to the Clairvoyant N-Body forward simulation in the initial conditions ($z = 120$).*Bottom right:* Collapse region (red) and its environment at $z = 0$.

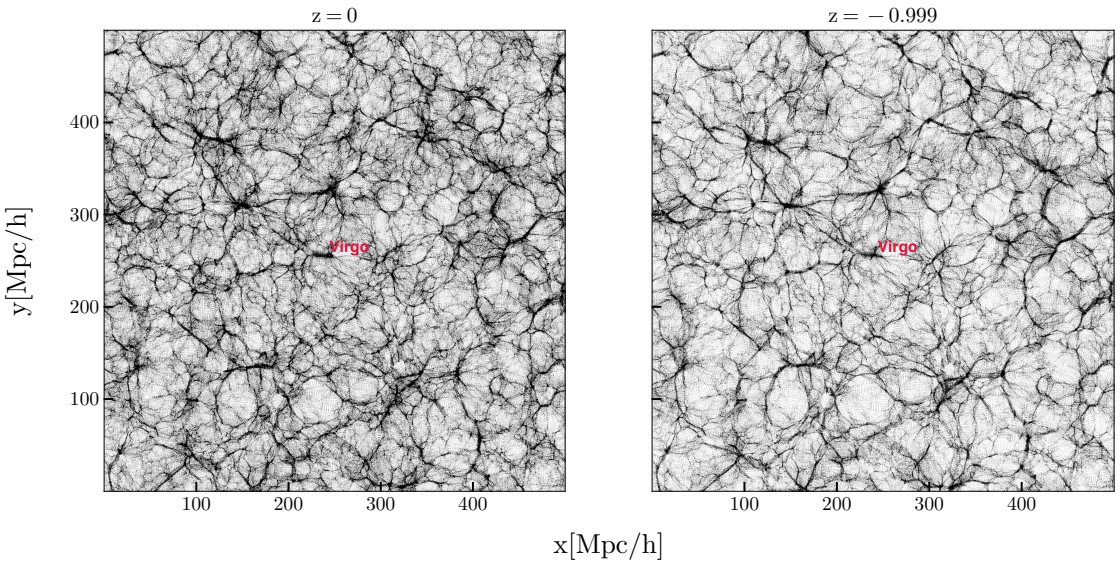


Figure 10.6: Cosmic web in the `Clairvoyant` simulation (dark matter component) within a slice of 10 Mpc/h at the present time (left) and in the far future (right). The position of the Virgo cluster as the nearest cluster to the observer position is marked in crimson.

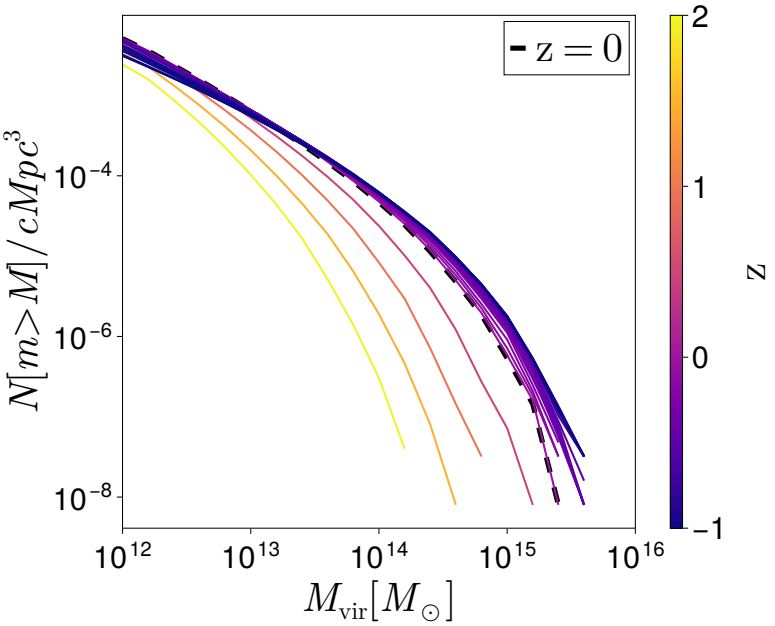


Figure 10.7: Evolution of the local halo mass function far into the future. Each line represents the hmf at the redshift indicated by the line color The present time hmf is the dashed purple line.

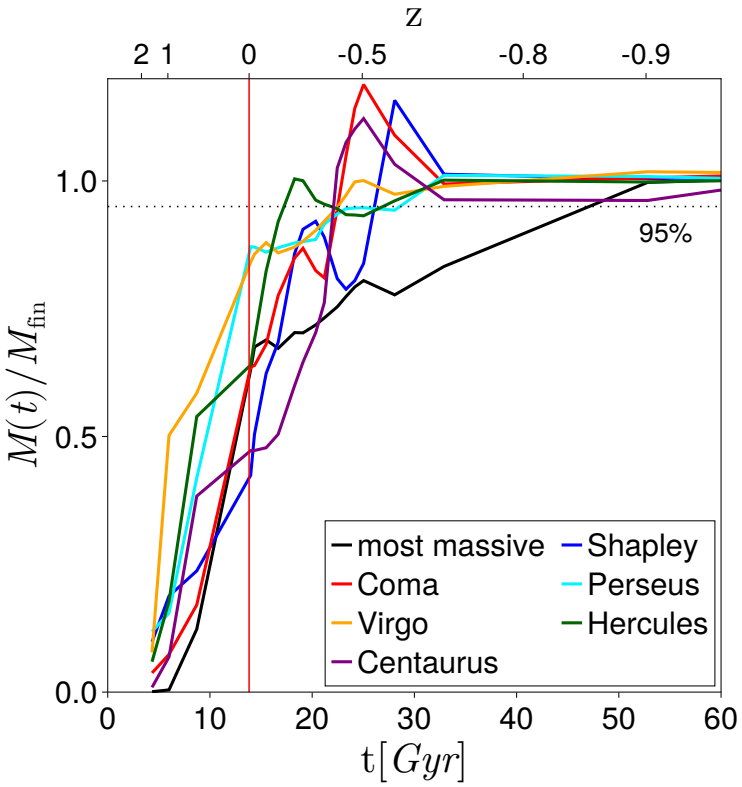


Figure 10.8: Late-time accretion histories for the six supercluster regions introduced in the previous section relative to their respective final halo masses.

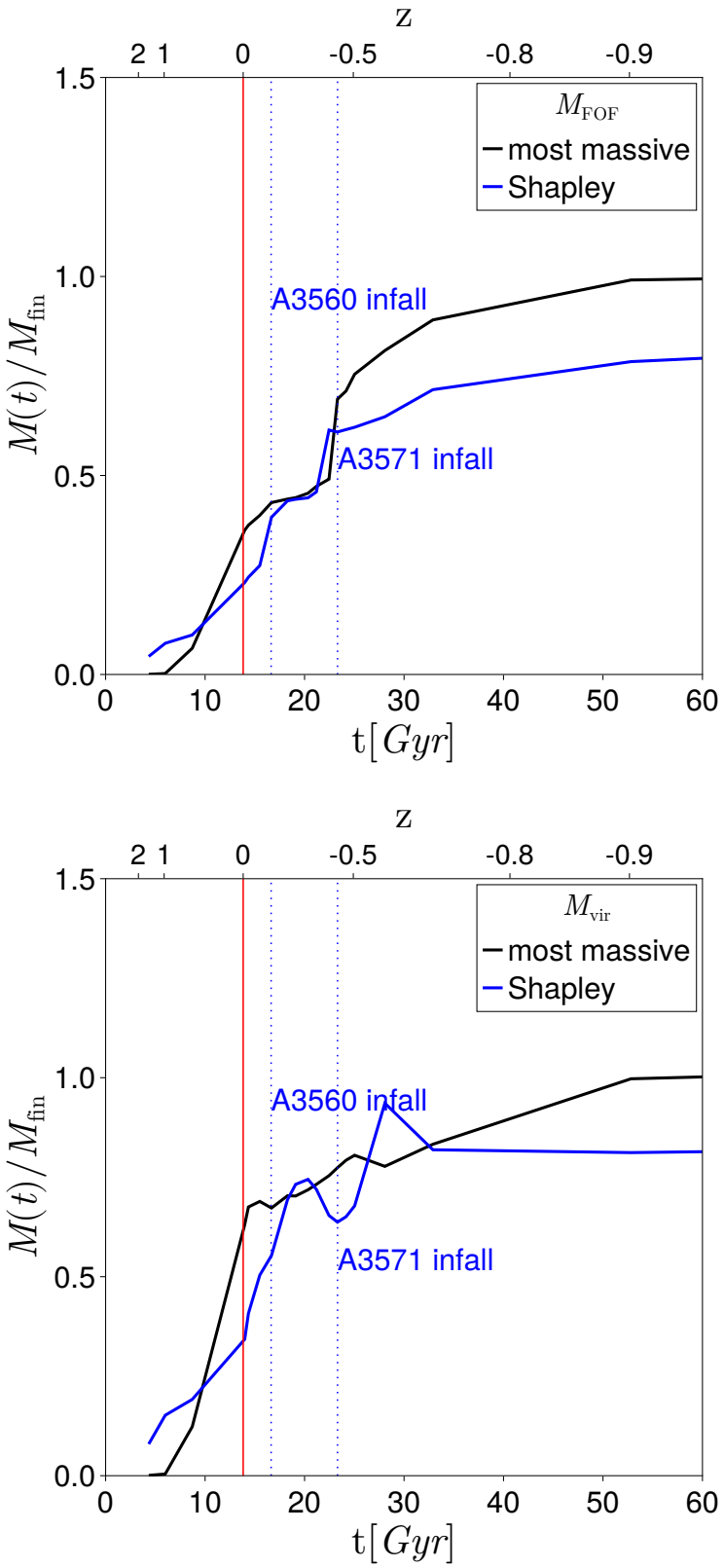


Figure 10.9: Mass assembly co-evolution of the most massive node and the Shapley supercluster in total FOF mass (left panel) and the mass constrained to $r_{\rm vir}$ (right panel). Both panels show the mass of each halo at a given time normalized to the final mass of the most massive halo in the simulation.

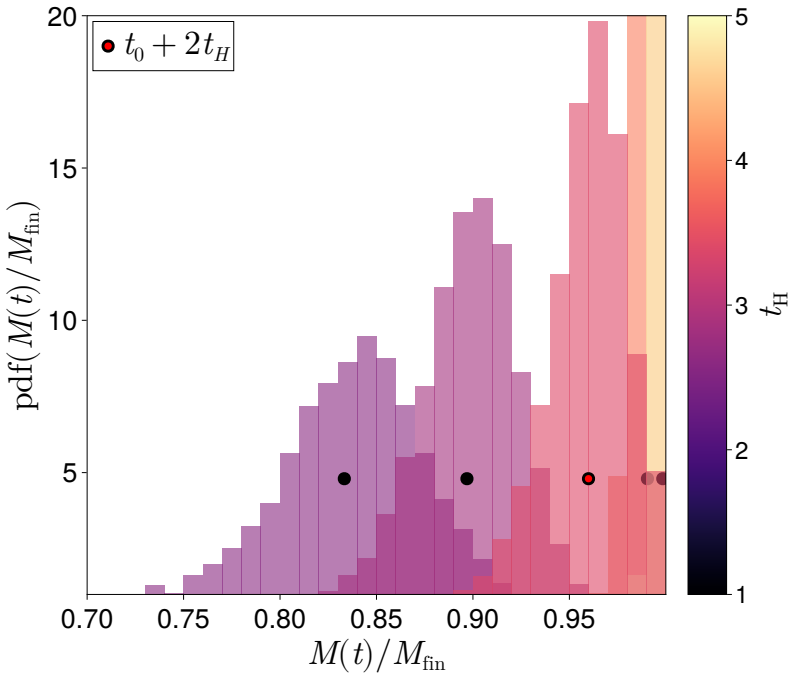


Figure 10.10: Probability density functions of assembly fractions at t=$t_0 + t_H, t_0 + 1.3t_H, t_0 + 2t_H, t_0 + 2.7t_H, t_0 + 4t_H$. The black dots show the median values of each distribution. The red dot marks the median value at $t = t_0 + 2t_H$.

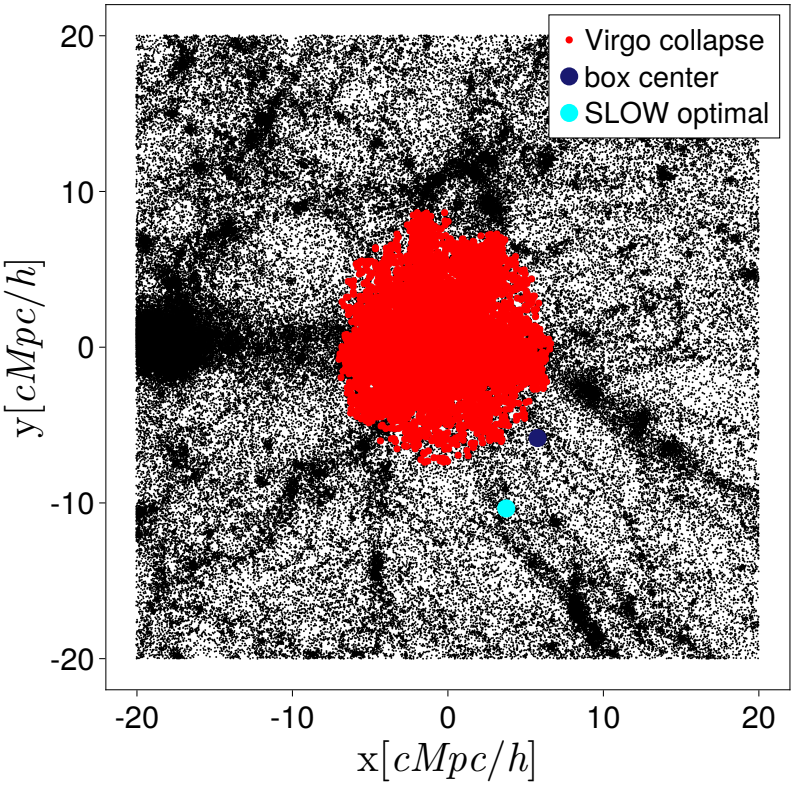


Figure 10.11: Collapse region of the Virgo cluster (red) and the relative position of the SLOW-Box center and the optimal center from Dolag et al. (2023) as proxies for the Milky Way position.

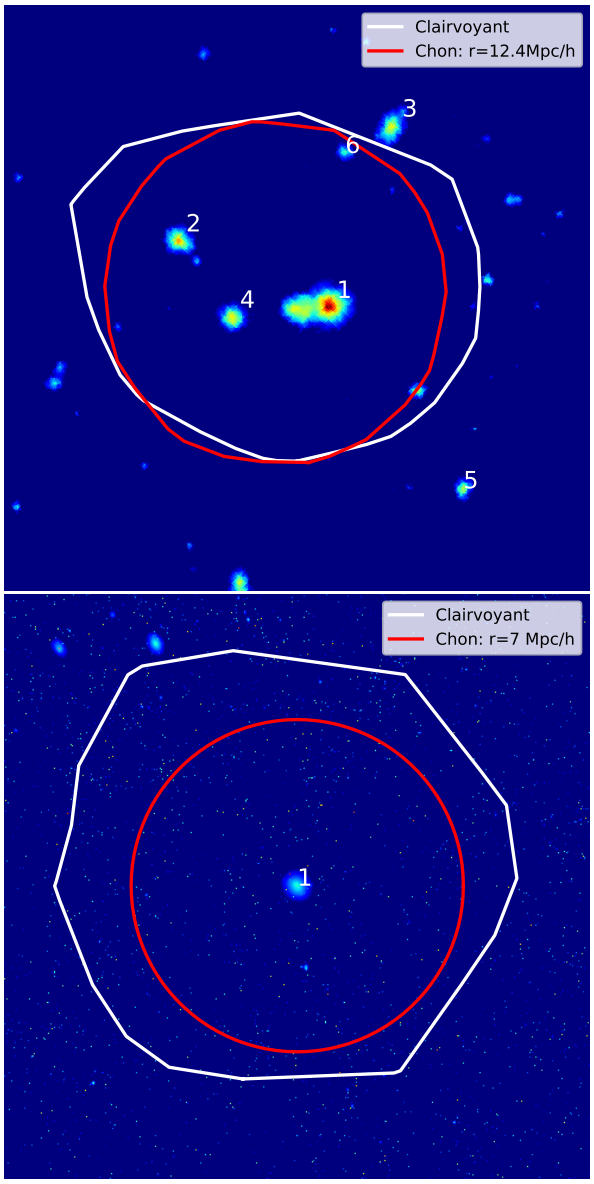


Figure 10.12: Mock observation of the thermal Sunyaev-Zeldovich signal indicating the shape of the Shapley (top) and Local (bottom) supercluster collapse regions at z=0 (white) vs. predicted extent of the superstes region (red) today given by the bound radius derived by Chon et al. (2015). The number labels are identical to Fig. 10.3 and Fig. B.3, respectively

.

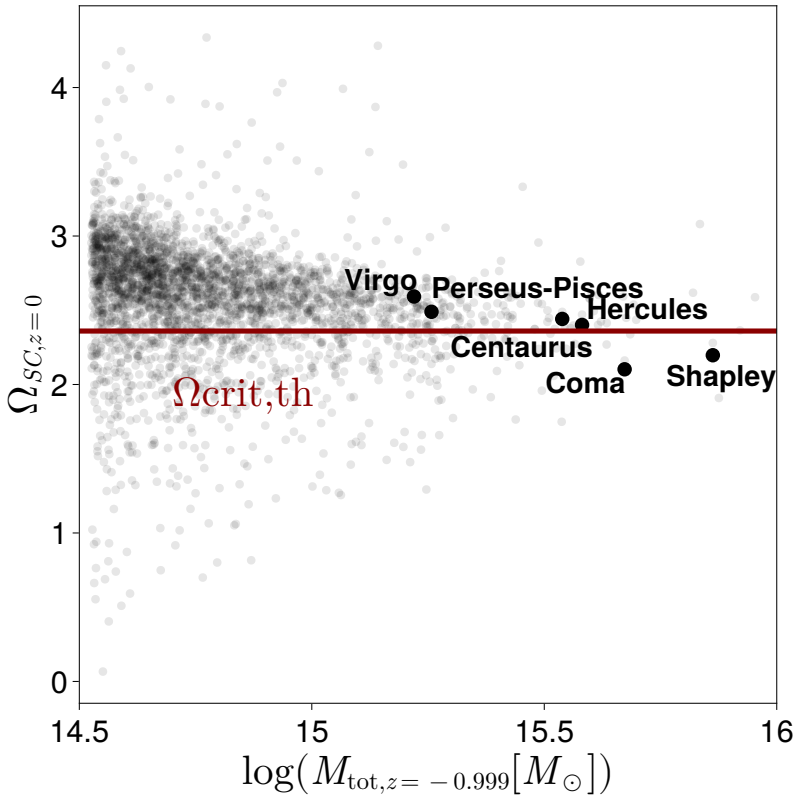


Figure 10.13: Density ratio at $z = 0$ of the final FOF groups of the supercluster regions identified in the `Clairvoyant` simulation compared to the critical collapse density contrast derived by Dünner et al. (2006) (horizontal red line). The 2000 most massive halos at z=-0.999, corresponding to the most massive superstes volumes, are shown additionally as transparent dots.

Chapter 11

Local Safari: Comparing Unique Structures between Simulations and Observations

This chapter briefly summarizes miscellaneous publications and further work with the SLOW simulation suite I was directly involved in.

Dolag et al. (2023), Hernández-Martínez et al. (2024) and Seidel et al. (2025a) showed the SLOW simulations to resemble the Local Universe in unprecedented fashion: Beyond properties of the density field on the linear scales, which is well constrained by a robust sampling of the velocity field, and the immediate vicinity of our position in the cosmos, the SLOW simulations, by virtue of the many years of work on the constraints (Hoffman & Ribak, 1991, Sorce, 2018), managed to also reproduce clusters at greater distances and match the groupings and geometrical arrangements of the real-world local clusters. On one hand, this provides a unique chance to correctly factor in local anomalies for cosmological studies as we will see in the following section.

On the other hand the advent of the modern era of X-Ray astronomy makes these advancements in constrained simulations even more opportune: All-sky surveys like the survey conducted with eROSITA (Merloni et al., 2012, Predehl et al., 2021) provide unique insights into the large scale structure and extended gas distribution around local clusters, allowing searches for the elusive WHIM components in filaments connecting clusters (Veronica et al., 2022, Dietl et al., 2024) and better statistical studies of their large-scale arrangements (Liu et al., 2024). At the same time, the unprecedented spectral resolution of XRISM and the Resolve spectrometer (XRISM Science Team, 2022) allows deeper insights into the thermal and turbulent structure of the ICM and connect it to their dynamical states as well as constrain the impact of AGN.

For those reason, a reference set of simulated galaxy clusters that **individually** match observed clusters in terms of their environment and accretion history has great potential for the task of furthering our understanding of how the ICM builds up and evolves from a multi-scalar perspective, because it essentially allows to effectively marginalize the environmental impact and study how different model properties affect the agreement between theory and observations.

This chapter will feature several projects focussing on objects of interest from the SLOW simulation. The first section is specifically impacted by the immediate neighbourhood of local clusters and the second and third section introduce the A3667 Bridge and the Fornax region. As an overview of the current state of the SLOW local neighbourhood of clusters, Fig. 11.1 provides an overview of all currently cross identified structures. The dominance of the Virgo cluster due to its proximity can clearly be seen from the figure. This will

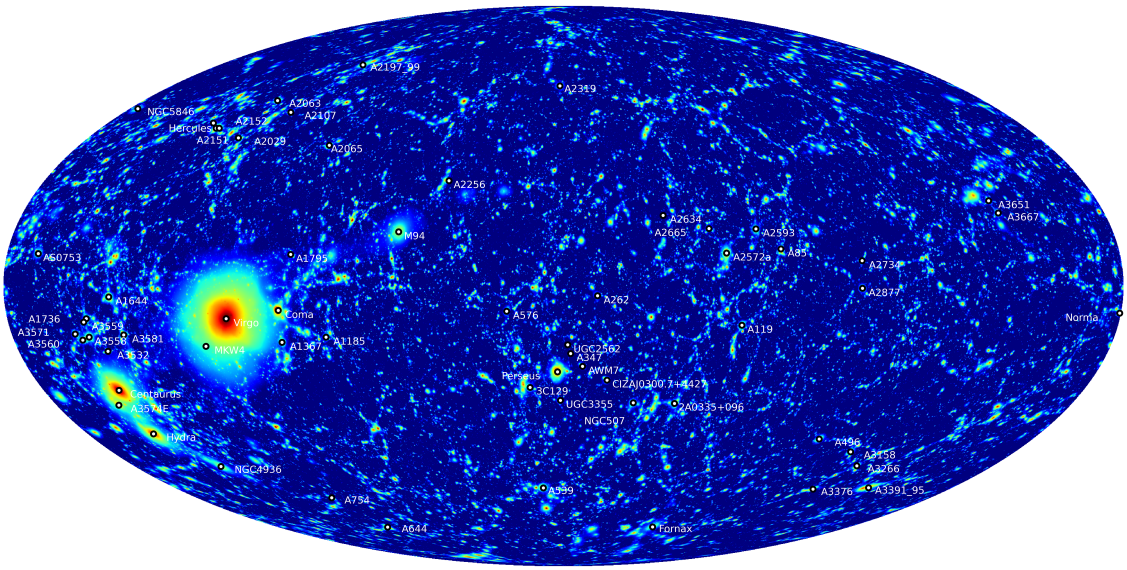


Figure 11.1: The combined SLOW Local Universe, merged from Dolag et al. (2023), Hernández-Martínez et al. (2024), Seidel et al. (2025a) with the updated counterpart from Dietl et al. (2024) (see Section 11.2). The underlying colour map is the mock Compton-y parameter, calculated with SMAC to a depth of 350 Mpc/h.

be an important point in the following section, where we constrain the effect these local anisotropies, especially the large-angular size ones like Virgo, have on the large-scale end of the CMB via the SZ effect (Sunyaev & Zeldovich, 1970).

11.1 Local Imprints on the CMB

The contents of this section are published as Jung et al. (incl. Seidel) 2024, A&A 692 A180, "Revisiting the CMB large-scale anomalies: The impact of the Sunyaev-Zeldovich signal from the Local Universe". I contributed the simulated tSZ and kSZ maps from SLOW and Magneticum Pathfinder.

In Part I, the homogeneity and isotropy of the universe were introduced as foundational principles of modern cosmology. As was specifically discussed in Section 1.2, the CMB as seen by modern instruments such as Planck (Planck Collaboration et al., 2016b), largely confirms this hypothesis. However several anomalies were found in the signal, many of which had been already measured in the WMAP or even the COBE missions to later be confirmed by Planck (for a review, see Schwarz et al., 2016). They are called anomalies, because they violate either the isotropy assumption or are incompatible with a pure Gaussian random field. The most prominent examples are: The **cold spot**, a very large region of reduced CMB temperature incompatible with standard assumptions of gaussianity (e.g. Cruz et al., 2005, Vielva, 2010), the **lack of correlation** at scales $\theta > 60$ (e.g. Hinshaw et al., 1996, Copi et al., 2015), the **quadrupole-octopole alignment** (e.g. de Oliveira-Costa et al., 2004), a peculiar alignment of the so-called vector harmonics indicating a violation of isotropy, and the **hemispherical asymmetry** (e.g Eriksen et al., 2004, Kester et al., 2023) an inconsistency between the power spectra of hemispheres divided by an axis orthogonal to the ecliptic plane.

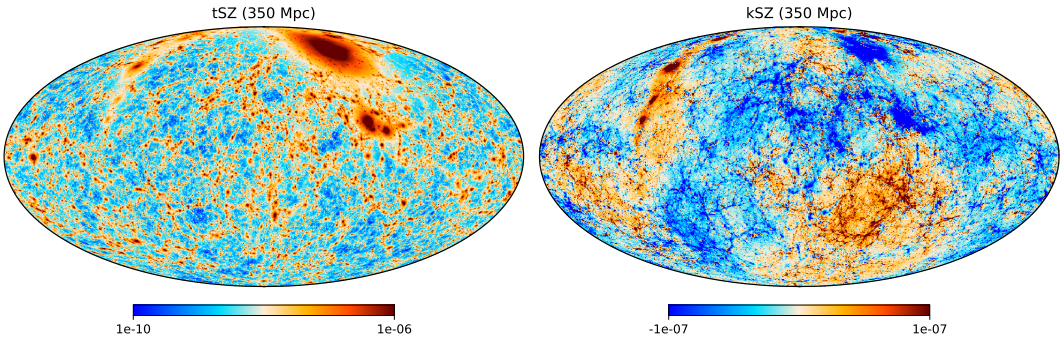


Figure 11.2: Local tSZ and kSZ maps generated with SMAC (Dolag et al., 2005b) from the SLOW observer position following (Dolag et al., 2023).

These signatures could point to new physics violating the very foundations of Λ-CDM cosmology and many exotic models have been proposed in the past to explain them (e.g. Byrnes & Tarrant, 2015, Jazayeri et al., 2017, Agullo et al., 2021). There is however a possible alternative explanation: Very Local anisotropies can be expected to introduce spectral distortions on the CMB via the thermal and kinematic Sunyaev-Zeldovich effects described by Sunyaev & Zeldovich (1970) (see also Eq. (2.8) and Eq. (2.9)). Using the SLOW simulations, Jung et al. (2024), therefore set out to constrain the effect the Local Universe could potentially have on these anomalies. Fig. 11.2 shows the Sunyaev-Zeldovich distortions created by the Local Universe via tSZ (left image) and kSZ (right image). Both maps, but especially the tSZ map, can be seen to be dominated by a few massive structures. Especially the Virgo cluster near the pole is extremely prominent due to its proximity and resulting large angular size. In fact Jung et al. (2024) showed the Virgo cluster to be the dominant factor in the large-scale tSZ power spectrum and produced a tension between both theoretical tSZ power spectra and even a statistical set of 27 synthetic observers on a grid throughout *Box2* from Magneticum Pathfinder as well as the SLOW volume. This is further evidence, that the local volume is somewhat of an outlier in terms of nearby structures, as was discussed in Section 9.1.

The idea was then to combine these locally obtained tSZ maps with a set of statistically generated CMB maps compatible with the Planck power spectrum, in order to assess whether the local distortions could account for the aforementioned anomalies in the actual Planck CMB (for technical details on the synthetic CMB realizations, we refer the reader to Jung et al., 2024). The analysis was limited to the tSZ because at the frequency of the synthetic CMBs, 143 GHz, the tSZ is by far the dominant effect (due to the functional form of the $g(\nu)$ factor in Eq. (2.8)).

For three anomalies, Jung et al. (2024) then calculate estimators for each synthetic CMB map. The quadrupole-octopole alignment is quantified by S_{QO} which is the sum of the three octopole vectors projected onto the quadrupole direction. The hemispherical asymmetry is quantified via A_d, which essentially measures the difference in variance of the pixel values in disjunct patches of the sky. The lack of large-scale correlation is quantified with $S_{1/2}$, which is the square integral of the angular two-point correlation function from angles $60 < \theta$ $S_{1/2} = \int_{-1}^{1/2} C(\theta)^2 d(cos\theta)$. For the exact details of how these estimators are computed, we refer the reader to Jung et al. (2024). Each statistic is first computed for the pure CMB maps and compared to the value in the actual Planck CMB. Jung et al. (2024) find a high significance for each of the anomalies: The Planck quadrupole-octopole alignment larger than 541 out of 600 simulated CMBs from the SEVEM set and larger than 91 out of 100 Commander simulations. With similar significance the authors find an excess variance in the supergalactic southern hemisphere, with the asymmetry of Planck in the 97th and 99th

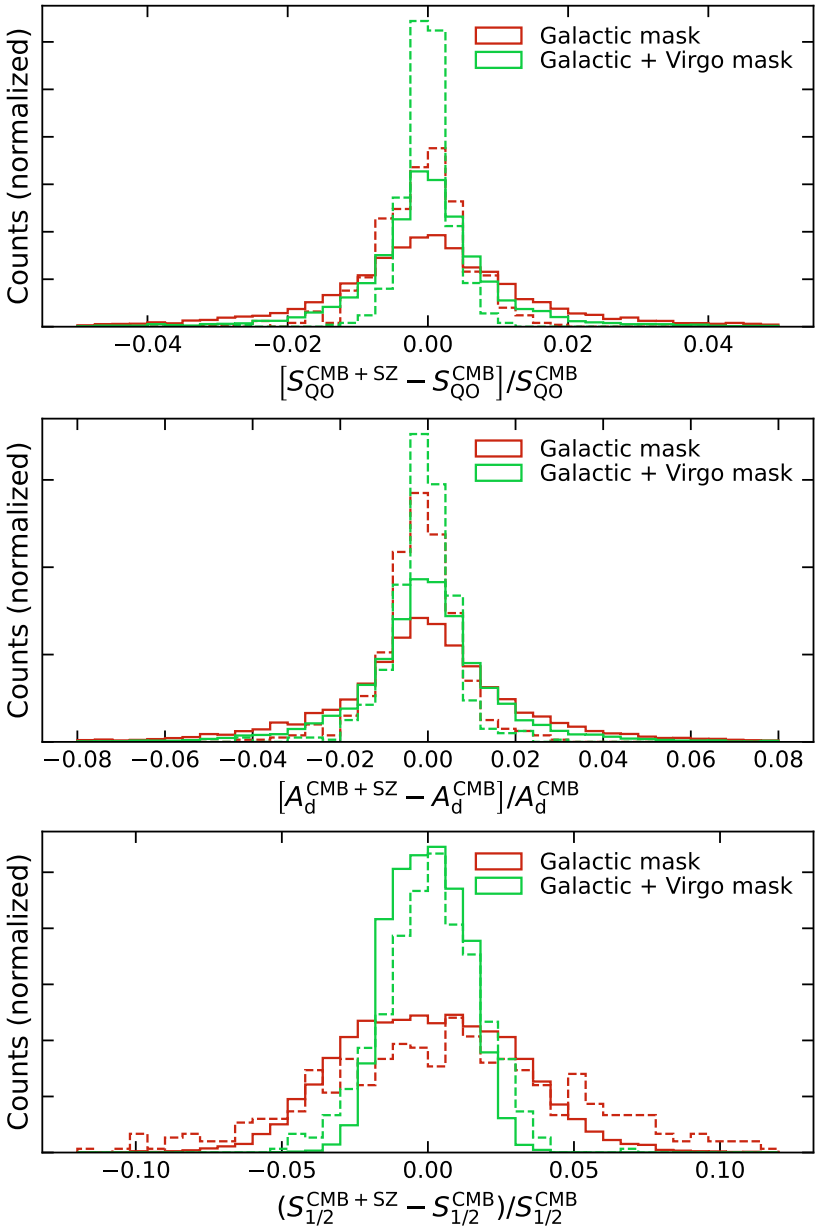


Figure 11.3

percentile for the two simulation sets respectively. Finally the lack of correlation of the Planck CMB is found to be completely incompatible with the synthetic sets.

From this calibration of the synthetically generated CMB maps under the assumptions of gaussianity and isotropy, the authors then apply the SLOW tSZ spectral distortions to assess the impact of the local LSS. Fig. 11.3 shows the effect the local tSZ has on the quadrupole-octopole alignment, the hemispherical asymmetry and the lack of correlation from top to bottom. Due to the dominance of the Virgo cluster in the tSZ power spectrum each set is additionally shown with the cluster masked. It can be immediately seen for all three anomalies, that the impact of the local tSZ on the overall anomalies is a few percent at best. The strongest effect (indicated by the widest distribution) is found for the lack of correlation on large scales, but even there the discrepancy is much larger between the statistically generated CMBs and the observed Planck CMB. $S_{1/2,Planck}$ is less than half the value of the lowest simulated CMB value (Jung et al., 2024), making even the most generous Local tSZ deviation from the lowest panel in Fig. 11.3 of about 10 percent not nearly sufficient to cover the gap to the real CMB.

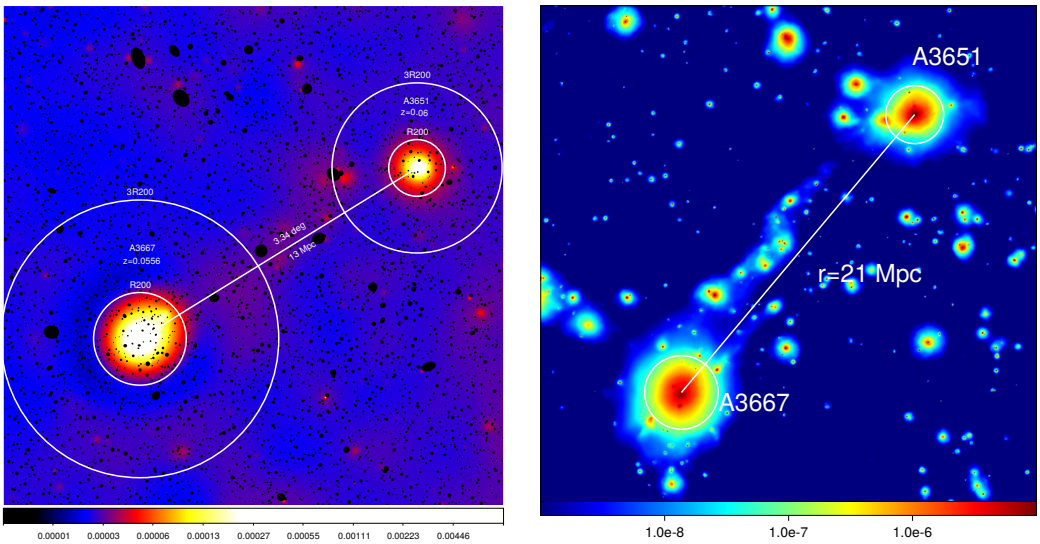


Figure 11.4: The A3667-A3651 system in X-Ray surface brightness. *Left panel:* Wavelet-filtered eROSITA image (Figure 2 from Dietl et al. (2024)) The white circles indicate r_{200} and $3r_{200}$ for each cluster respectively. *Right panel:* The same region in SLOW simulated X-Ray surface brightness produced with SMAC in the 0.1-2.4 keV band. The white circles indicate r_{200} for each cluster. Adapted form of Figure 9 from Dietl et al. (2024).

In summary using the spectral distortions from the local LSS in SLOW, Jung et al. (2024) were able to convincingly demonstrate that this effect can not be the origin of the most famous anomalies in the CMB.

11.2 A3667-A3651 Bridge

The contents of this section are published as Dietl et al. (incl. Seidel) 2024, A&A 691 A286, "Discovery of a > 13 Mpc long X-ray filament between two galaxy clusters beyond three times their virial radii". I contributed the mock X-Ray maps and the electron density profile of the SLOW filament.

The A3667-A3651 pair of galaxy clusters is a well-known system (Arp & Russell, 2001). Especially A3667 exhibits a number of interesting features indicating that the cluster is in an active state and possibly also underwent mergers in the past. The most prominent features are an extended Radio Relic (Rottgering et al., 1997) and a prominent cold front in the central region of the cluster (Ichinohe et al., 2017).

Dietl et al. (2024) used this pair to try and identify extended emission in the region between the two galaxy clusters. Filamentary regions between galaxy clusters are present promising candidates to detect the ever-elusive WHIM, ionized gas at $10^5 - 10^7 K$ representing the pre-heated gas accreting onto filaments. Due to its low density, direct observation is challenging, even with modern X-Ray or Microwave instruments (Yao et al., 2012, Churazov et al., 2023), even though it could constitute as much as one third of the entire baryon budget of the universe and could help relieve the so called "missing baryon" problem (e.g. Persic & Salucci, 1992).

In order to increase the detection probability, usually either stacking of multiple systems is employed (e.g. Zhang et al., 2024a, Isopi et al., 2025) or campaigns focus on systems that are already strongly interacting and only connected by short filaments (< 10Mpc) (e.g. Bonjean et al., 2018), where the gas is already being compressed by the two merging clusters. The eROSITA survey has allowed unprecedented strides in the detection of the diffuse

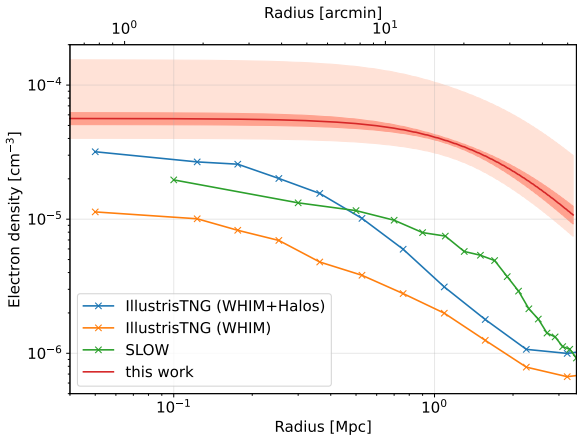


Figure 11.5: Electron density profiles for the observed A3667 filament compared to the SLOW cylinder and a statistical sample from IllustrisTNG (Galárraga-Espinosa et al., 2021). Figure 12 from Dietl et al. (2024).

material in the outskirts of cluster systems, for example the filamentary structure enveloping the merging pair A3395 and A3391 (Reiprich et al., 2021). The novelty of the study by Dietl et al. (2024) is then the detection of extended emission in the soft X-Ray band along a structure > 10 Mpc **connecting** two separated clusters, A3667 and A3651. This marks the first detection of this kind of structure.

The left panel of Fig. 11.4 shows this extended structure imaged in the 0.3–2.0 keV band of eROSITA. The projected separation of the two clusters was determined to be 13 Mpc, with an estimated 3D filament length of 25-31 Mpc based on the redshift difference between the two clusters and assuming them to be moving towards each other, compressing the filament.

In the right panel the corresponding region is shown in the SLOW simulation in a mock image created with SMAC (Dolag et al., 2005b) in the 0.1-2.4 keV band. The mass ratio and individual clusters are in good agreement, as can be seen from Table 12.2 ($(M_1/M_2)_{\rm sim} = 2.1$, $(M_1/M_2)_{\rm obs} = 1.8$). Strikingly, the constrained simulation reproduces the morphology of the cluster pair as well. The elongated emission found in the observations can also be seen, with a similarly curved and off-axis structure relative to the connecting line between the two clusters. The separation between the simulated clusters is slightly below the assumed separation from the observed data at 21 Mpc. This agreement provided a unique opportunity: It was possible for the first time to directly compare a filamentary density profile one-to-one between an observed and a simulated filament. Since the observational electron densities were measured along the connecting line between the two clusters, we chose a similarly simple approach for measuring the density profile from the simulation: A central spine was selected from the peak of the integrated density along the connecting line between the cluster pair, and subsequently the density was calculated from the total gas within cylindrical shells of increasing radius. Fig. 11.5 shows the obtained density profiles with an additional comparison to a sample of filaments obtained from a conventional cosmological simulation. The simulated filaments consistenty underestimate the gas density compared to the values obtained by Dietl et al. (2024). The profile for the SLOW filaments lies closer overall to the total gas density in Ilustris TNG than the density profile purely for WHIM, which makes sense, because we applied no halo masking to the SLOW filament. But even the higher densities obtained this way is unable to reach the observed densities. Nevertheless shape of the SLOW profile, with its extended shoulder at larger radii matches the observed density profile closer than the statistical filaments, which exhibit a steeper slope in the outskirts. This is ultimately an effect of the measurement along a straight line, rather than following the exact density ridge of the filament, leading to denser parts of the structure contributing at larger radii. The similarity of

the simulated and observed slope at 1-2 Mpc distance from the centre corroborates the visual impression from Section 11.2 that the two structures have similar curvature. Summarizing, we have confirmed the discovery of an extended and elongated filament-like gas structure discovered in the eROSITA all-sky survey to be also present in the SLOW simulation, matching in terms of the overall size of the system and with regards to the cluster masses, as well as the general morphology of the system. We cannot confirm however the unusually high gas densities inferred from the observational data for the simulated filament. Overall the SLOW filament is similar to simulated filaments from non-constrained simulations in terms of total gas mass in the region, despite closely resembling the observed filament. This discrepancy could be due to systematics in the observational data or the scaling between X-Ray luminosity and electron density. Another possible explanation is the contribution from unresolved collapsed haloes elevating the observed emission (the authors find a corresponding central overdensity of $\delta_c = 200$, an overdensity corresponding to the inner few Mpc of a massive galaxy cluster). The resolution of the SLOW simulation might not accurately reproduce the physical processes determining the gas budget of these smaller haloes, causing them to accrete onto the filament with most of their gas already heated and stripped or expelled. We will explore this possibility in the future, using the zoom-in re-simulations described in the next chapter and possibly also different simulation models. This will further help elucidate the dynamics of the baryonic component and especially the WHIM in these dynamically highy active systems.

11.3 Fornax

The contents of this section are published as Reiprich et al. (incl. Seidel) 2025, A&A 703 A9, "The SRG/eROSITA all-sky survey – View of the Fornax galaxy cluster". I contributed the mock X-Ray, stellar, and gas density maps as well as additional information about the infall state of the simulated system.

Another class of viable targets are nearby clusters, where the large angular size allows high-resolution studies of the gas density and allows to follow the gas to much lower densities in general, ideal for WHIM searches. The two largest galaxy clusters in terms of angular size are the Virgo cluster and the much less massive Fornax cluster, both of which were part of the eROSITA program (McCall et al., 2024, Reiprich et al., 2025).

The Fornax galaxy cluster has been the target of many observational campaigns in the past. X-Ray studies with XMM-Newton and Chandra have revealed an active history in the centre, with one of the two giant elliptical galaxies falling in and triggering sloshing motions as well as cold fronts (Su et al., 2017b,a). A population of faint dwarfs and UDGs was discovered by Muñoz et al. (2015) and studies with infalling galaxies allowed a study of the impact of the infall direction on the survival of cold disks (Ding et al., 2023). Additionally, not just the past of the system, but also its future appears to be turbulent, with the infalling Fornax A group (Drinkwater et al., 2001) nearby and the whole system embedded in a complex filamentary superstructure (Raj et al., 2024). The Fornax A group also allows unique studies of the pre-processing of gas within a group that is itself infalling into another cluster, especially with its rich neutral hydrogen structure as seen by MeerKAT (Kleiner et al., 2021).

Fig. 11.6 shows the Fornax region as viewed by eROSITA with the most important large-scale morphological features highlighted. There is a bridge of gas in the direction of the Fornax A group as well as multiple finger-like protrusions and X-Ray surface brightness excesses to the north- and southwest. The galaxy density contours (obtained from NED) reveal differences to the gas component: In several directions, but most strikingly at the position of Fornax A, the galaxy density peaks are significantly offset from the peaks of X-Ray

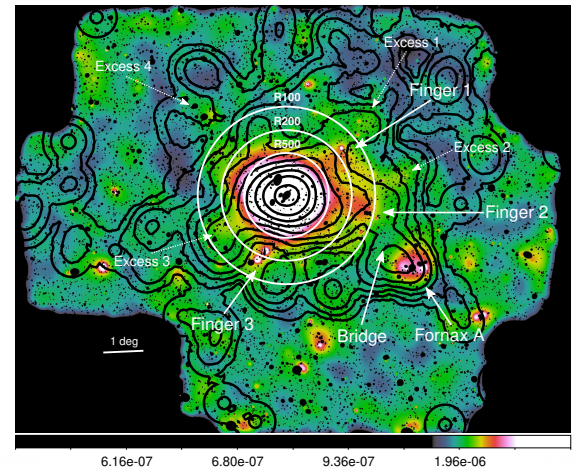


Figure 11.6: Wavelet-filtered eROSITA image in the energy band 0.2– 2.3 keV. Overlaid are galaxy density contours obtained from the NED catalogue (black contours). Characteristic X-Ray emission features as well as the scale radii for the main cluster are highlighted in white. Figure 10 from Reiprich et al. (2025).

surface brightness. This could potentially reflect intra-group gas sloshing motions or even ram-pressure from the outer cluster gas acting only on the collisional component of the infalling group. Furthermore the galaxy density contours exhibit a clear east-west elongation. Fig. 11.7 shows the same region in the SLOW 1536/agn run. As in the previous section the mock X-Ray image was created with the program SMAC (Dolag et al., 2005b) and the same eROSITA-like energy band of 0.1-2.4 keV was applied. From the black contours indicating the gas density as well as the X-Ray surface brightness it is immediately clear, that the bridge to Fornax A is also present in the simulation. Additionally, the south-western finger can also be seen extending into this bridge structure (lower right). The north-western finger has a similar surface brightness hot-spot, however in the SLOW simulation this is a projected structure, which is far outside the actual Fornax region, as can also be seen by the contours which are computed in a 25 Mpc thick slice around the cluster. However there is also some extension in the north-western direction indicated by a slight bending in the contours toward the right top direction, which corresponds to excess 1 and potentially Finger 1 in Fig. 11.6. Overall, the perturbed X-Ray morphology and the dominant infalling structures are exceptionally well reproduced in the simulation. Furthermore, considering the white contours, which indicate the stellar component, a similar offset between gas and stars seems to exist at the position of the Fornax A counterpart. Similarly, the observed east-west elongation is visible in the simulated stellar component, matching the observed galaxy density. The time resolution of the SLOW simulation snapshots unfortunately is insufficient to confirm the intra-group sloshing hypothesis for the offset of the stellar component around Fornax A. Nonetheless, the simulation predicts this subgroup to be on first in-fall, in agreement with the common understanding of this system's history and because it is well outside of the clusters r_{200}, ram pressure stripping seems unlikely. In future work, we plan to study this systems dynamics at greater spatial and temporal resolution in order to constrain its dynamics more precisely.

To summarize, the Fornax A counterpart in the SLOW simulation appears to be an excellent match in terms of large-scale morphology and gas distribution, reproducing many of the interesting X-Ray low surface brightness features identified by eROSITA. This makes this region a promising candidate for future studies of gas stripping and connections between large-scale structures and dynamical features in the ICM. The high-resolution re-simulations we will discuss in the following chapters are especially promising for this endeavour, since

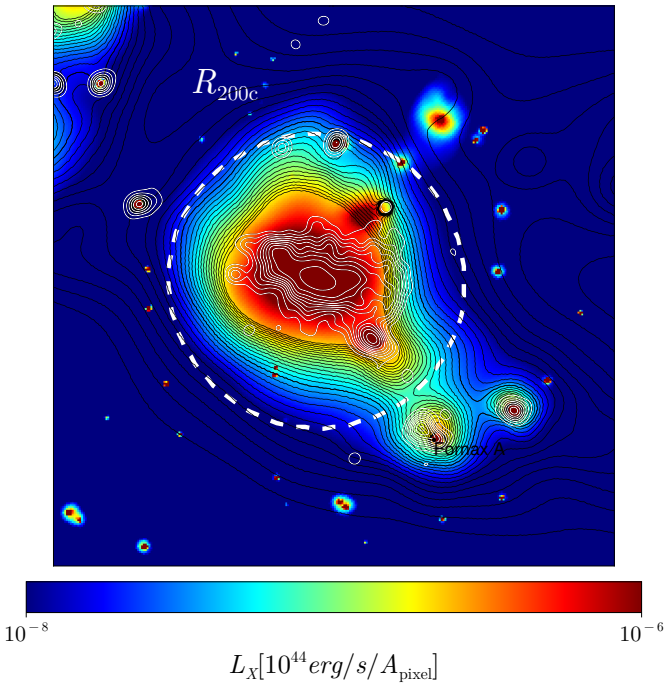


Figure 11.7: The Fornax cluster viewed in SLOW simulated X-Ray surface brightness produced with SMAC in the 0.1-2.4 keV band. The white dashed circle indicates r_{200}. Black contours show the gas density within a 25 Mpc thick slice centered on the Fornax cluster position. The contour levels are in the interval $[0.8, 6.0] \times \rho(r_{200})$. The white contours indicate the stellar density in the same slice. Figure 16 from Reiprich et al. (2025).

they allow to follow the dynamics in much greater detail than the cluster-centric SLOW parent simulation.

11.4 Conclusions

During the course of this section, we have further demonstrated the potential of constrained simulations of the Local Universe. We have used a realistic SZ-effect foreground to rule out local biases being responsible for long-standing cosmological conundrums stemming from anomalies in the CMB. Furthermore we have demonstrated how the realistic large-scale structure built from the constraints reproduces local structures exceptionally well in terms of their large-scale gas distribution. To this end, we compared two special systems, the extended bridge between A3667 and A3651, and the nearby Fornax cluster to their real-world counterparts as observed by eROSITA. We found the counterparts for both regions to be in very good morphological agreement with observations, while there were some interesting discrepancies especially with regards to the overall density of the observed versus the simulated filament. Understanding these discrepancies in the baryonic component in a system that is well reproduced in terms of the large-scale dynamics provides a unique opportunity to deepen our understanding of the assembly and evolution of such filamentary systems, and possibly even aid in further detections of the warm-hot gas phase in the Local Universe.

In the following chapter we will introduce a zoom-in follow-up project based on the constrained environments of the SLOW simulations. The significantly improved resolution of these zoom-in simulations will allow us to model and study the gas distribution and dynamics in more detail than the base SLOW simulation suite.

Chapter 12

Level Up: Re-Building the Local Universe in High Definition

We plan to submit this chapter to A&A as Seidel et al. 2026

12.1 Introduction

One of the biggest challenges in studying the Universe is the multi-scalar nature of physical processes in nature. In astrophysics, dynamics on Megaparsec to Gigaparsec scales can be non-trivially connected to processes on Parsec to Kiloparsec scales. Large cosmological numerical simulations including hydrodynamics are especially suited to study structures and processes on large and small scales simultaneously. There is, however a computational trade-off that needs to be considered: Ideally one wants to simulate a large enough region to capture the largest actively collapsing density perturbations - or there is a risk of large structures being affected by boundary effects or simply not forming at all (e.g. Bagla & Ray, 2005). On the other hand, the spatial resolution needs to be high enough to allow to follow hydrodynamics and even higher, when galaxy formation physics has to be followed (Steinmetz & White, 1997), or the turbulent dynamo process in the ICM has to be resolved within a magneto-hydrodynamical framework. (Steinwandel et al., 2024). This has become ever more important in the age of large-scale galaxy surveys like Euclid and LSST, which can probe galaxies down to stellar masses as low as $10^8 M_\odot$ (Euclid Collaboration et al., 2025b, Ivezić et al., 2019). For this reason current cosmological simulations have to skirt the boundary of modern high performance computing.

One solution for this are so called zoom-in techniques (e.g. Frenk et al., 1996, Tormen et al., 1997, Dolag et al., 1999, 2004, Jenkins, 2010, Bonafede et al., 2011, Hahn & Abel, 2011) that are widely applied to particle-based simulations as well as hydrodynamical grid codes. Here, the resolution of the simulation is increased in a specific Lagrangian volume of interest, with the rest of the pseudo-particles simulated at a lower resolution to save computational cost. A major challenge of this approach is to choose the Lagrangian region in such a way that low-resolution and high-resolution particles mix as little as possible for the duration of the simulation. This mixing can introduce spurious energy transfers due to particles of different masses interacting. This is especially an issue in the high-resolution region, where high-mass boundary particles would not only interact with high-resolution dark matter particles but additionally the collisional baryonic particles and stellar particles, which have even smaller masses in most numerical simulations (in our Magneticum-like approach this is simply the dark matter mass multiplied by the cosmological baryon fraction).

Because of this, a major issue of modern multi-mass zoom-in simulations is contamination - the intrusion of high-mass low-resolution boundary particles deep into the high-

	BS1996	E1998	Hutt	B2006	Dianoga	The300	C-EAGLE	Rom-C	TNG-C	PICO	SLOW-C
$N_{\rm cluster}$	10	10	8	3	27	324	30	1	325	25	45
$M_{\rm 200c,max}$ $[10^{15}h^{-1}M_\odot]$	2.4	1.8	2.3	1.3	3.2	2.6	2.5	0.2	2.5	~ 2.5	1.5
$L_{\rm parent}$ $[h^{-1}{\rm cMpc}]$	150	180	479	192	1000	1000	2169	34	680	1000	500
$R_{\rm clean}$ $[R_{\rm vir}]$	0.1-2.6	4-8	3.7-8.1		5.0-6.0	0.1-7	-	-	0.15-5.0	1.1-4.8	≈ 10
$m_{\rm DM}$ $[h^{-1}M_\odot]$	3.2×10^{11}	1.8×10^{10}	2×10^{9}	4.8×10^{8}	3.3×10^{6}	1.5×10^{9}	6.6×10^{6}	2.3×10^{5}	4.1×10^{7}	4.0×10^{7}	3.9×10^{7}

Table 12.1: Overview of the characteristic of different zoomed cluster simulations campaigns. From left to right BS1996 (Bartelmann & Steinmetz, 1996), Eke11998 (Eke et al., 1998), Hutt (Dolag et al., 2004), B2006 (Borgani et al., 2006), Dianoga (Bonafede et al., 2011), The300 (Cui et al., 2018), C-EAGLE (Barnes et al., 2017), Romulus-C (Tremmel et al., 2018), TNG-Cluster (Nelson et al., 2024), PICO (Tevlin et al., 2025) and SLOW-Cluster (this work). Listed are the number of clusters in the set, the size of the parent box, the size of the cleaned region, e.g. the (typical) distance from the center to the clusters to the nearest boundary particles at $z = 0$ and the mass of the dark matter mass particles at the highest resolution available for the set.

resolution region. (Oñorbe et al., 2014) demonstrated that while the effect of contamination on purely gravitational dark matter dynamics weak in terms of general halo properties, even a small amount of boundary particles can alter sensitive baryonic properties. They showed the gas density profiles and baryon fractions to be significantly altered in haloes with contamination versus the uncontaminated case, with an overall effect of a decreased baryonic density in the contaminated halos. The authors furthermore showed that the high-mass intruders can add as sink particle for the gas creating additional unphysical substructures. As the aim of zoom-in simulations is precisely to resolve the small scale gas dynamics in greater detail than pure cosmological simulations, it is therefore critical to keep the contamination as low as possible.

This chapter is structured as follows: In section 2 we describe historical and current zoom-in simulations as a direct reference. In section 3 we introduce our method in detail. In section 4 we compare the results from our simulations to the previously described reference simulations. Section 5 provides a summary and final discussion of our findings.

12.2 A Brief History of Cluster Zoom-In Simulations

From the very beginnings of galaxy cluster simulations it became clear that, in order to model the ICM physics with enough detail to predict observational properties of clusters, it is necessary to boost the resolution of cosmological volume simulations in the regions where those clusters form. The first such cluster zoom-in initial conditions were created by running a low resolution parent box to $z = 0$, identifying over-densities corresponding to massive clusters, tracing them back to the initial conditions and resampling cubic regions around this volume with higher resolution particles. Table 12.1 lists a selection of sets for different zoom-in cluster initial conditions together with their properties. The first sets of this kind were employed to, for example, study the impact of sub-structures on the strong lensing signal (Bartelmann et al., 1995) and predictions of the evolution of X-ray scaling relations for clusters (Eke et al., 1998). These sets typically contained ten clusters with masses of $\approx 10^{15}h^{-1}M_\odot$ extracted from parent simulations with sizes of $\approx$ 300Mpc. Those where also used to study the evolution of magnetic fields (Dolag et al., 1999) as well as to address biases for different mass estimates for galaxy clusters (Bartelmann & Steinmetz, 1996, Dolag & Schindler, 2000).

With the introduction of ZIC (Tormen et al., 1997) a significant advance was made, as here the region which was replaced with high resolution particles could be described by a

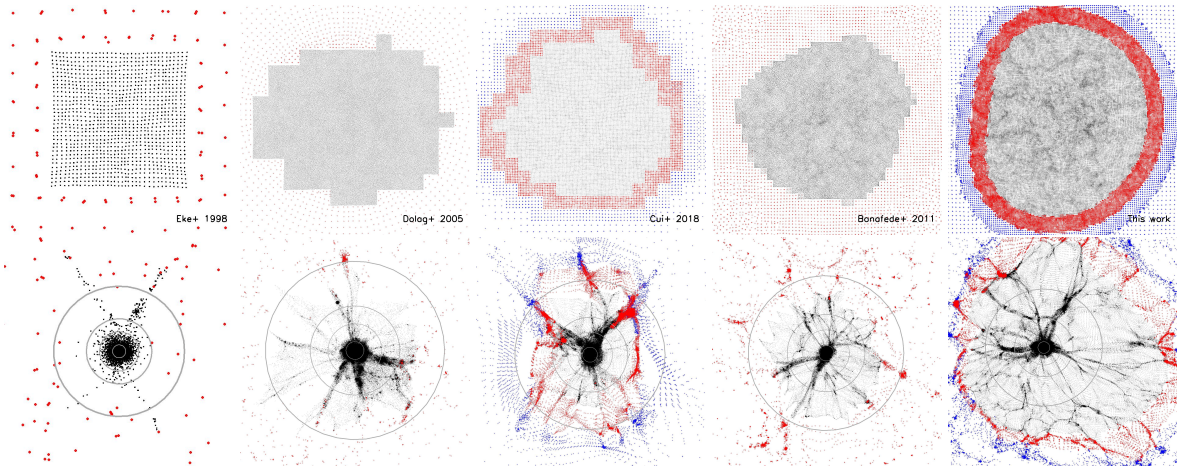


Figure 12.1: Thin slice of one cMpc/h through a galaxy clusters from the different simulation sets, showing a 70 cMpc/h region. Shown are for different cluster ICs the high resolution particles (black) and the different layers of boundary particles (red and blue). Top row shows the initial state, bottom row shows the evolved systems at z=0. From left to right: on cluster from Eke1998 (Eke et al., 1998), Hutt (Dolag et al., 2004), Nifty (e.g. The 300) (Cui et al., 2018), Dianoga (Bonafede et al., 2011) and SLOW cluster set (this work). The gray circles mark 1,3,5 and 10 times the virial radius.

cubic lattice, based on 16^3, 32^3 or 64^3 cells which allowed to extract high-resolution volumes of arbitrary shapes. It also introduced a iterative procedure, where low resolution zoom-in simulations were used to refine that region to have the final cluster free of contaminating boundary particles while minimizing the required volume. Another advantage of ZIC is that it allows to place an arbitrary number of high resolution particles within the zoom-in region and the tool therefore does not depend on an underlying mesh where spatial resolution can be only increased by factors of two. This was originally used to extract a small set of massive clusters with masses of $10^{15}h^{-1}M_{\odot}$ (Hutt, Dolag et al., 2004) from a $479h^{-1}$Mpc box (Yoshida et al., 2001) as well as creating three extremely high resolution clusters (B2006, Borgani et al., 2006) from a $192h^{-1}$Mpc, full hydrodynamical simulation (Borgani et al., 2004). Later the same technique was applied to a $1h^{-1}Gpc$ box to extract the Dianoga set of 24 massive (e.g. $M > 10^{15}h^{-1}M_{\odot}$), Coma like clusters (Bonafede et al., 2011). These sets of initial conditions were especially created to have a large boundary particle free region enclosing them, e.g. $R_{\rm clean} > 3.5R_{\rm vir}$ (Hutt) and $R_{\rm clean} > 5R_{\rm vir}$ (Dianoga). Among many other studies, they have been used to study the thermodynamics of the ICM (Fabjan et al., 2011), the role of AGN feedback for galaxy clusters (Planelles et al., 2014), the chemical enrichment of the ICM (Biffi et al., 2017) and intra-cluster light properties (Dolag et al., 2010). Recently, the resolution of these initial conditions have been further increased and reached levels of 10^9 particles within individual clusters, allowing to fully resolve the turbulent dynamo within the ICM (Steinwandel et al., 2024).

The three-hundred (The300) project (Cui et al., 2018) consists of 324 galaxy clusters extracted from a $1h^{-1}$Gpc parent box using MUSIC (Hahn & Abel, 2011). Also here, arbitrary volumes can be defined, but spatial resolution can be only increased by factors of two and there was no iteration to optimize for contaminating boundary particles used when creating the initial conditions. Therefore, as listed in table 12.1, there are clusters where boundary particles are present within the virial radius. The set was originally simulated employing a number of different models such as Gadget-X (Springel, 2005, Beck et al., 2016), Gadget-music (Sembolini et al., 2013) and a selection of semi-analytical models for galaxy formation. Recently, this was extended to include a GIZMO-SIMBA (Cui et al., 2022) variant. Studies carried out with this suite include, but are not limited to exploring the connection between the

dynamical state and the morphology of these clusters (De Luca et al., 2021), filament detection studies (Kuchner et al., 2021, Cornwell et al., 2023) and environment-galaxy connection studies (Wang et al., 2018).

An even larger parent box of $2169h^{-1}$Mpc in size is used in the C-EAGLE project (Barnes et al., 2017). This set consist of 30 zoom in galaxy clusters in the mass range from $10^{14} - 10^{15.4} M_{\odot}$, that include as well the Hydrangea (Bahé et al., 2017) set of clusters simulated specifically to study galaxy formation. Simulations were run with the EAGLE model (Schaye et al., 2015b) with a modified P-Gadget3 from (Springel, 2005). The simulations were used to study the infall of gas onto galaxy clusters through filaments (Vurm et al., 2023), the galaxy mass functions in those regions (Negri et al., 2022) as well as the disruption of infalling satellite galaxies (Bahé et al., 2019).

To push the resolution to much higher level, the Romulus-C project (Tremmel et al., 2018) features a low mass galaxy cluster with $2 \times 10^{14} h^{-1} M_{\odot}$. It is selected from a $34h^{-1}$Mpc parent box from the Romulus cosmological simulations (Tremmel et al., 2017) and run with an identical setup in terms of hydrodynamics and sub-grid modeling. The project, due to its high mass-resolution, focused mainly on member galaxies and specifically dwarf galaxies, investigating environmental quenching and thermal AGN feedback effects (Tremmel et al., 2017) as well the formation of ultra-diffuse galaxies in cluster environments (Tremmel et al., 2020).

The TNG-Cluster project (Nelson et al., 2024) pushed for a large set of clusters with higher resolution than the The300 set. It is suite of 325 galaxy clusters selected from a $680h^{-1}$Mpc parent box and therefore has a similar mass range than previous projects and was ran with the TNG Model (Weinberger et al., 2017, Pillepich et al., 2018) using the Arepo code (Springel, 2010). Similar to the The300 project, there was no iterative approach when selecting the initial volumes. Here, even more of the clusters suffer from boundary particles within the virial radius (see discussion in Nelson et al., 2024). It features an improved resolution compared to The300. Science results include a possible connection of ICM velocities to halo and galactic properties (Ayromlou et al., 2024), a prediction for X-ray velocity dispersion measurements from Perseus (Truong et al., 2024), cool-core and non-cool core fractions of these clusters (Lehle et al., 2024) as well a study on the hot CGM of cluster satellites and how it can be retained by its host and observed in the X-ray band (Rohr et al., 2024).

The PICO cluster project (Berlok et al. in prep., Tevlin et al., 2025) is a recent zoom-in campaign for clusters using the Arepo/TNG Model. It is based on an increased parent box which has a size of $1h^{-1}$Gpc and the zoom-in regions are increased so that there a no boundary particles within the virial radius of the clusters at $z = 0$. It contains 25 clusters performed with the Arepo-2 code and the TNG galaxy formation model. Its focus lies on studies of plasma physical processes in the ICM, such as anisotropic viscosity and conduction and cosmic rays. The simulations have been used so far to demonstrate an accelerated magnetic field amplification via dynamo processes through including galaxy formation physics, especially at higher redshifts. (Tevlin et al., 2025).

To allow a more compact overview of these different campaigns for cluster zoom-in simulations, we list some general properties of the aforementioned studies in table 12.1. Among the properties we list the size of the parent box, the mass of the galaxy clusters and the typical size of the region free from boundary particles. In addition, figure 12.1 shows a slice through the initial condition as well as the same slice in the $z = 0$ cluster for the subset of these studies where we could access these data. All figures are to the same scale to better visualize the differences in the high-resolution volume extraction methods and the degree and spatial distribution of contamination by low-resolution particles. We also include an example from the cluster initial conditions of this work for comparison.

As mentioned, the studies mentioned above typically select the high resolution region

by finding particles within a certain distance or in the Friends-of-Friends (FOF) group of the central structure at z=0. Some are using iterative approaches to improve the size of the volume, which subsequently remains uncontaminated. However, they al. commonly start from a sphere with an arbitrary radius around the cluster at $z = 0$ to trace back the volume for the high resolution region within the initial conditions. In this work we propose an extension to this procedure in order to capture the dynamics of the region more accurately: We run an N-body only version of the parent simulation to the far future in order to reliably predict which particles interact with the central structures during the simulation time. This method allows us to create initial conditions with far more stable high-resolution regions than the traditional methods provide even with a generous safety margin. As a test set for this method we employ the highest resolution version of the SLOW (Simulating the Local Web) simulation, which bases on the realization number 8 of CLONES (Sorce, 2018). We construct a set of constrained initial conditions for which we extract the Lagrangian collapse regions of local cluster and supercluster analogues with our method.

12.3 Methods: SLOW Cluster ICs

The methods introduced in this section for obtaining zoom-in ICs are in principle applicable to any particle based simulation box. In this work we demonstrate the basic principles of the IC extraction using the realization 8 of CLONES (Sorce, 2018), the so called SLOW constrained simulation (Dolag et al., 2023). These simulations reproduce the local large scale density field with all its peculiarities (Dolag et al., 2023) and have the additional advantage that the zoom-in regions obtained this way contain the simulated analogues of some of the most well studied clusters in the local Universe (see Table 12.2) and their specific environments. For a discussion of general properties of these local clusters and supercluster regions see Hernández-Martínez et al. (2024), Seidel et al. (2025a).

12.3.1 Clairvoyant - The Parent Simulation

The parent simulation for the initial conditions generation is a pure N-Body version of the SLOW simulation at various resolution levels, including versions with 768^3, 1536^3 and 3072^3 resolution elements. For tracing the structures we used the initial conditions with 3072^3 particles in a $500\,h^{-1}Mpc$ side length box, giving a mass resolution of $m_{dm} = 3.1\times10^8 h^{-1}M_\odot$. The method of obtaining the initial conditions for the parent box is described in detail in previous works (Sorce, 2018, Dolag et al., 2023), thus we limit the discussion here to a brief overview: From the Cosmicflows-2 catalogue of distances and peculiar velocities (Tully et al., 2013) which suffers from shot noise and intrinsic uncertainty, the local velocity field is reconstructed using a Wiener Filter technique of variance minimization (Zaroubi et al., 1995, 1999). There are a number of sophisticated bias correction procedures that are applied both to the raw data and the reconstructed field, to maximize the efficacy of the reconstruction, for details refer to: Sorce (2015), Sorce et al. (2017), Sorce & Tempel (2018), Sorce (2018).

We performed a standard gravity-only run using these constrained ICs. Instead of using $z = 0$ as the reference point for the zoom-in region extraction, as is done usually, we let the simulation propagate past this point to a scale factor of $a = 1000$. The N-Body forward run is performed using OpenGadget3 (OpenGadget3 collaboration in prep., refer to Groth et al., 2023, and references therein), based on Gadget2 (Springel, 2005). It incorporates several updates including an optimized tree-walk and an improved domain decomposition (Ragagnin et al., 2016). We apply the Subfind algorithm (Springel et al., 2001, Dolag et al., 2009) on the fly to all simulation outputs to obtain the Friends-of-Friends (FOF) particle groups. All simulations we ran adopt a background cosmology according to Planck Collaboration

et al. (2016c) with $H_0 = 67.77\,\mathrm{km\,s^{-1}\,Mpc^{-1}}$, $\Omega_\mathrm{m} = 0.307115$, $\Omega_\Lambda = 0.692885$, and $\Omega_\mathrm{b} = 0.0480217$.

12.3.2 Cluster target selection

Using constrained SLOW simulations, we can focus the generation of initial conditions on a number of identified analogues of local galaxy clusters (Hernández-Martínez et al., 2024) as well as their large-scale arrangements, the local superclusters (Seidel et al., 2025a). This provides a unique opportunity to study these well-observed regions in greater detail than previously possible. We therefore prioritized the selection to firstly cover the supercluster regions introduced by (Seidel et al., 2025a) as the first target volumes for the test set. This set contains the Coma and Virgo superclusters, the Perseus-Pisces supercluster, the Shapley supercluster and the Hercules supercluster. In addition, we added regions of high interest, including the A3667-A3651 region, where an elongated X-ray filament was discovered recently (Dietl et al., 2024), as well as the A2199/97 region which is another well-known cluster pair (e.g. Rines et al., 2001). Additional clusters were added to the set based on the XRISM target selection (XRISM Science Team, 2022) for PV, A01 and A02, with the long-term goal to provide high-resolution counterparts of these clusters for one-to-one ICM velocity structure comparisons (Groth et al., 2026). A large number of these clusters also overlap with the ACCEPT databases (Cavagnolo et al., 2008, 2009, Baldi, 2014) providing exquisite X-ray coverage and also have a large overlap with clusters where deep optical images allow investigations of the intra cluster light (ICL) properties (Kluge et al., 2025). Therefore our first set consists of 20 regions containing 30 of the coss-matched galaxy clusters. The details of this regions and the associated clusters are listed in table Table 12.2. We have also identified 20 more regions for which we will create the zoom-in initial conditions in the future.

12.3.3 Constructing the High-Resolution Volume

The common approach for defining a region of interest to re-simulate with higher resolution is to select the halo of interest at z=0 and define all particles in the simulation within a virial radius or multiples of the virial radius as the target Lagrangian region. These particles can then be traced back to the initial condition of the box and there define the high-resolution volume, where subsequently the resolution is enhanced with one of the methods described below. The size one sets for the initial selection of the Lagrangian region aims to ensure that flows between the low-resolution volume and the high-resolution volume are minimized and at the same time keep the volume as small as feasible to reduce computational cost. To optimize this selection process, we propose an alternative approach for this pre-selection of the Lagrangian volume. This method is both shape-free already in the pre-selection process (as opposed to the spherical radii being used traditionally) and additionally incorporates dynamical information from a forward propagated auxiliary run of the parent box to ensure that the boundary surface of the high resolution region deforms as little as possible during the re-simulation.

By letting the gravitational part of the parent SLOW simulation propagate into the far future ($a = 1000$, as described in Paper I), we are able to extract a finally collapsed halo for a given structure by running the SUBFIND algorithm on the final snapshot output instead of the state of the simulation at z=0. Contained within this ”final halo” are all dark matter particles that are gravitationally bound to the region. To further ensure boundary stability we incorporate the local particle velocities to extend this Lagrangian volume adaptively. The bounding surfaces are computed using a HealPIX tesselation (Gorski et al., 2005) of a sphere centered on the target halo. Since nearby, but non-merging massive structures can impact the

stability of such a boundary significantly through tidal interactions, we hierarchically merge adjacent Lagrangian Volumes of galaxy clusters with the volume of interest.

The complete process to compute the Lagrangian volume is then as follows

1. Extract FOF group from the snapshot at $a = 1000$
2. Create a Healpix tessellated distance map of these particles, where each angular pixel is mapped to the largest FOF particle distance within the angular bin
3. Starting at this distance for each pixel, compute the radial velocity
4. For each pixel with a negative (inward) radial velocity, compute the radial velocity profile and set as the new pixel value the distance at which the radial velocity crosses zero.
5. Repeat this process for close by massive structures
6. Find all particles that lie within any of the resulting bounding surfaces

Tracing the set of particles obtained with this method back to the initial conditions of the forward run, we obtain the final selection volume by once again putting the particles on a HealPIX distance map and setting the maximal radial distance within each pixel as the boundary radius in the corresponding angular bin. To obtain a smoother boundary we additionally upscale this map to a higher resolution and smooth over it with an angular gaussian kernel.

12.3.4 Multimass Layering

There are several methods to combine volumes of different resolution into one simulation. The approach we use in this work is comparable to the multimass approach employed by the ZIC code (Tormen et al., 1997): We start by creating several instances of the parent box in different resolution levels using the GINNUNGAGAP[1] code (Pilipenko et al., 2025). Particles within the high-resolution selection volume are extracted from the highest resolution box. We then add several boundary layers (depending on the target resolution) by upscaling the selection volume self-similarly several times and selecting the particles between the boundary surfaces from initial conditions of decreasing resolution. An example of such a region and its enclosing can be seen in figure 12.2. The current highest resolution grid we are using is the 6144^3 realization of the box. Additionally we keep the 3072^3, 1536^3, 768^3 and 384^3 realizations as low resolution version of the full box for boundary selection and lower resolution test zoom-ins. This allows for a combination of five layers of decreasing resolution ($6144^3 - 384^3$) for the highest resolution zoom-ins and, correspondingly, four layers for the second highest ($3072^2 - 384^3$). We thus call these the L5 and L4 sets respectively with the L5 being the ”gold standard” set.

This layering dampens possible spurious effects from very high-mass and low-mass particles interacting. We ensure mass conservation by checking first if a given particle of the low resolution grid lies within the applied boundary and obtaining its children from the high resolution grid if this is the case. The fact that particles can be obtained self-consistently from the different full-box resolution grids is a major advantage of pre-computing the box in all applied resolutions beforehand instead of increasing the resolution exclusively in the designated volume. In the future, we plan to extend the current range to even higher resolutions for the zoom-in regions as well as lower resolution versions based on the 3072^3 resolution for testing. Both operations are feasible within the GINNUNGAGAP framework.

[1] https://github.com/ginnungagapgroup/ginnungagap

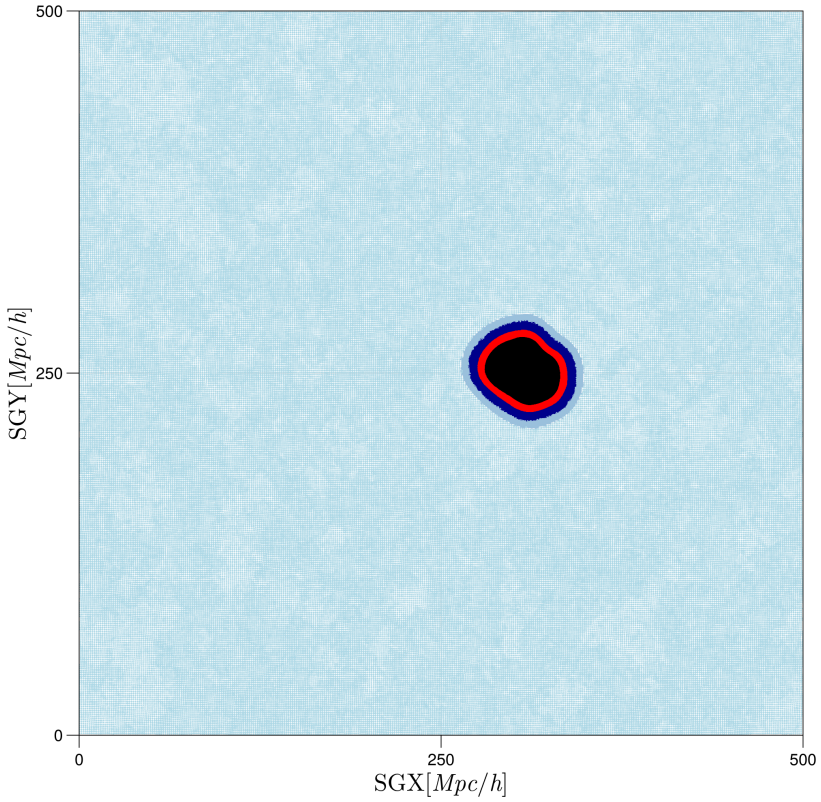


Figure 12.2: Layered initial conditions from the SLOW Perseus counterpart with five resolution levels. Each color represents a different mass resolution, resolution decreases with increasing radius.

12.4 Results

We ran the dm-only version of the initial conditions generated with the method introduced above. The resulting structures at $z = 0$ can be seen in Figure C.1 for 30 local galaxy clusters found within the Lagrangian region set. As can be seen from the figure some of these regions contain multiple local cluster analogues because they are actively merging supercluster regions at $z = 0$ (for further details see Seidel et al. (2025a)). As can already be gathered from the gray circles in Fig. C.1 as well as the boundary distances shown in the lower left panels, the initial conditions provide an unprecedented level of cleanliness, with boundary particles at least $\sim 6r_{\rm vir}$, in some cases even far beyond $\sim 10r_{\rm vir}$, removed from any of the clusters of interest.

12.4.1 Cleanliness

Figure 12.1 visualizes the evolution of zoom-in initial conditions including the SLOW cluster set. As can be seen from the top row of the figure, the high resolution and boundary regions of the SLOW cluster initial conditions are comparable in size their historical predecessors. In the bottom row, showing the final state at z=0, however it becomes apparent that the adaptive nature of the SLOW cluster set, taking into account the whole collapsing region around the central structure, helps the boundary to be much more stable across time. In the final snapshot there is no boundary particle (shown in red) within 10 virial radii of the cluster of interest, a clean region extent that none of the comparison initial conditions can reproduce. For a more quantitative comparison between previous simulations and our initial conditions, we show the minimum encounter distance distribution for various comparison sets and all the 30 SLOW cluster from our 20 selected volumes in Figure 12.3. The lowest

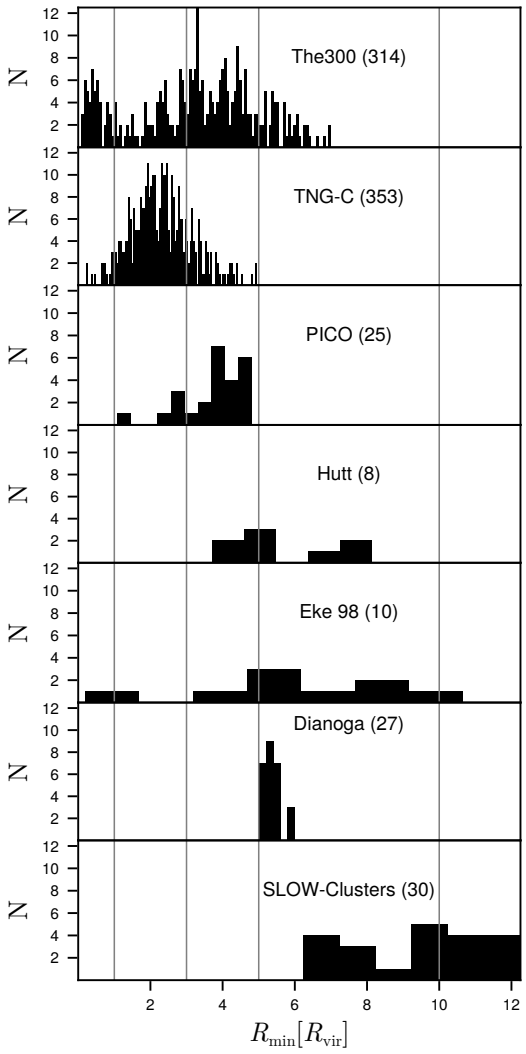


Figure 12.3: Distribution of the minimum encounter distance for the different IC sets. Gray lines mark 1,3,5 and 10 R_{vir} as also indicated as circles in figure 12.1.

SLOW encounter distances are comparable to or exceed most of the other simulation suites' highest encounter distances. This shows that the SLOW cluster IC achieve unprecedented cleanliness, which will allow a much larger region to be studied from a hydrodynamical perspective and ensures that the central cluster or clusters are absolutely free of spurious effects caused by low resolution dark matter particles. This additionally allows to properly study the immediate environment of the cluster, including the filaments which are connecting the cluster to the cosmic web.

12.4.2 Mixing Layer

Figure 12.4 shows the co-evolution of the minimal encounter distance for low-resolution particles and the maximal encounter distance for high-resolution particles for one of the SLOW clusters and two clusters from other IC sets for comparison. Effectively these two curves give the evolution of the mixing layer, where high-resolution particles and low-resolution particles co-exist. The evolution of the SLOW cluster shows the mixing layer to be relatively stable for this set: Both the minimal boundary distance and the mixing layer stay almost constant from $a = 0$ to $a = 1$ for the SLOW cluster cluster. For the Dianoga set, where the target size of the clean regions was set to $\approx 5r_{\rm vir}$, the depth of the mixing layer is only slightly

increasing. Nevertheless the clean region is significantly shrinking as the initial cutout is still within the in-fall region of the final structure. In addition, we added the reported behavior of the initial and final size of the sphere of boundary particles (Nelson et al., 2024) as well as its distribution for all TNG-Clusters as colored histogram at z=0. The reason why the contamination in the TNG-Clusters is significant higher than in the Dianoga clusters, despite starting from similarly sized Lagrangian Volumes is the fact that the creation of the Dianoga cluster used several iterations to obtain a optimized description of the shape of the region in the initial conditions.

Because the regions from the SLOW IC set can be highly aspherical we additionally show the angular distribution of mixing layer thickness for the 20 simulation volumes, centering on the most massive cluster in Figure 12.5. This statistic is computed by putting the high-resolution particles and the boundary particles on a healpix map (NSIDE=16) and then subtracting the minimal boundary particle distance from the center from the maximal high-resolution particle distance. For comparability we added the distances D to the global minimal boundary particle distance $r_{\rm min}$ for each cluster, so the actual maximal high-resolution particle distances are not reflected by this statistic. From the figure we see that for all of the clusters, the mixing layer is small compared with the overall size of the clean region. Some of the clusters additionally exhibit a separation region, where there are no high resolution particles overlapping the boundaries (shown by the tails of the histograms that lie to the left of the minimal boundary distance).

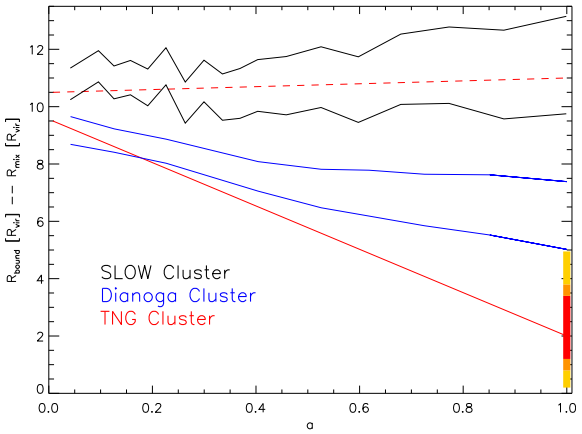


Figure 12.4: Evolution of the boundary layer for the SLOW cluster (black), Dianoga cluster (blue) and TNG Cluster (red), always expressed in units of the virial radius of the cluster. The lower line indicates the minimum distance of a boundary particle to the cluster center. For the SLOW/Dianoga cluster a typical cluster is shown, while for the TNG clusters the median value is shown and the histogram at a=1 (e.g. z=0) shows the distribution, where the yellow region shows 10% of the cluster population, the orange 20% and the red the remaining 70%. The upper lines show the maximum distance of high resolution particles, so together with the lower line they mark the mixing layer between boundary and high resolution particles, where physical processes can be significantly influenced by this mixing.

12.5 Conclusions

We introduced a novel method for constructing zoom-in initial conditions achieving high-resolution regions that are free of contamination from low-resolution particles to an unprecedented degree. To evaluate this method, we constructed a suite of regions encompassing prominent galaxy clusters from the SLOW suite of constrained simulations. In total we

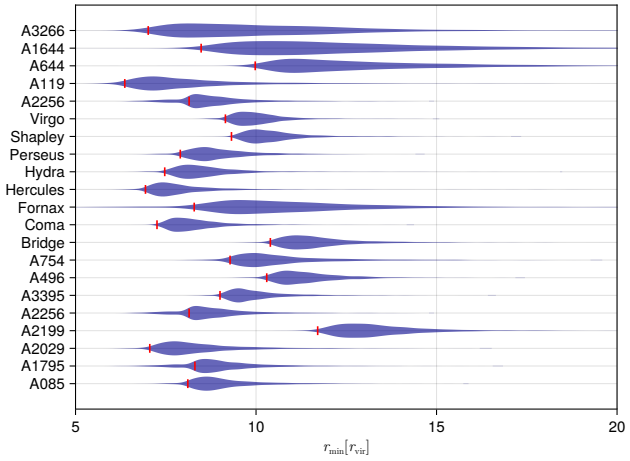


Figure 12.5: Minimal boundary distances for the individual regions from the SLOW cluster set (red vertical lines) at z=0. The dark blue violins additionally show the histogram of mixing layer thickness $D + r_{\rm min}$ across an NSIDE=16 healpix map centered on the main cluster. Values $< r_{\rm min}$ therefore indicate a negative thickness, i.e. the high resolution particles and the low resolution particles are separated at z=0.

evolved 20 such regions, containg 30, cross identified clusters, utilizing two resolution levels until z=0 to evaluate for their cleanliness. We find the following:

1. The boundaries, which are composed of layers of particles of decreasing resolution (and conversely increasing mass) are extremely stable across time, showing very little deformation and crucially shrinking

2. All 30 clusters are free of any boundary particles to within at least 6 $r_{\rm vir}$, half of them have clean volumes even beyond $\approx 9 r_{\rm vir}$. This significantly improves on previous zoom-in initial condition suites.

3. There is a certain degree of high-resolution particles diffusing outwards, however these so-called mixing layers are small compared to the size of the pristine volume ($\approx 10\%$)

Due to these properties, our method is ideally suited for carrying out high-fidelity hydrodynamical simulations including the large scale cluster environment and the filaments which connect the clusters to the cosmic web. In future work we will introduce a set of fully hydrodynamical simulations of the set presented in this paper. This will be the first large set of such re-simulations built on constrained counterparts of real local Universe clusters. With the mass resolution achieved, we will also for the first time be able to study galaxy formation in these realistic large scale environments. Due to the large uncontaminated volume encompassing these clusters, this additionally makes it possible to study the large scale environmental effects of galaxy clusters and their surrounding filaments on galaxy formation in great detail. These advantages make these simulations invaluable for interpreting the results from ongoing observational campaigns. We plan to generate detailed X-Ray mock observations and spectra in order to provide theoretical predictions and comparisons for the ICM dynamics and morphology as observed by Chandra, XMM and XRISM, as well as through the eROSITA all-sky survey for these local clusters. As the large-scale environment of our clusters is well-constrained, we will also be able to carry out novel galaxy population studies in the future, expanding on the work which has been already done on the Coma and Virgo cluster.

Name	$N_{\rm gal}$	M_{500c}^{Sim}	M_{500c}^{Obs}	X_{SG}	Y_{SG}	Z_{SG}
Virgo	305	6.5	4.8	-3.6	10.4	-1.6
Perseus	447					
A426	–	5.1	–	59.2	2.2	-24.6
AWM7	–	0.5	–	60.1	-6.7	-23.2
Bridge	4					
A3667	–	4.4	5.8	-156.8	-111.3	66.7
A3651	–	2.1	3.2	xxx	xxx	xxx
A2029	4	6.0	6.8	-92.6	142.4	141.4
A1795	0	1.8	4.5	6.3	201.7	28.2
Clstr pair	43					
A2199	–	3.0	2.1	-13.0	48.8	97.1
A2197	–					
Hydra	1859					
A1060	–	2.6	–	-21.2	9.9	-19.4
A3526	–	6.2	1.3	-22.7	11.3	-13.2
A754	1	1.9	6.7	-34.3	78.5	-144.3
A085	3	6.6	6.1	50.8	-143.1	25.9
A3395	49	7.0	3.0	-53.3	-43.2	-101.7
Shapley	22					
A3558	–	9.3	4.4	-141.0	66.1	-37.2
A3571	–	4.0	4.7	-142.4	54.1	-33.9
A3560	–	3.2	–	-145.5	60.6	-39.7
A1736	–	3.3	–	-137.5	65.6	-22.6
A3559	–	1.6	–	-131.1	32.9	-59.9
A496	2	4.2	4.3	-13.3	-94.5	-83.5
Hercules	30					
A2147	–	2.8	2.5	-77.42	77.33	100.6
A2151	–	1.2	1.4	-77.4	69.1	100.6
A2152	–	0.4	0.6	-76.5	79.8	101.6
Coma	972					
A1656	–	9.5	5.3	-2.9	82.3	-9.1
A1367	–	1.1	1.8	-2.9	71.4	-18.7
Fornax	32	0.4	—	4.5	-6.6	-21.5
A2256	3	1.7	6.2	115.9	96.3	79.4
A119	191	5.8	3.4	73.6	-117.3	-24.9
A644	2	5.0	5.1	-26.5	70.6	-204.2
A1644	491	4.4	3.7	-97.3	64.9	-5.7
A3266	9	8.6	6.6	-60.0	-93.2	-128.1

Table 12.2: Set of galaxy clusters in the IC set. We list general properties like masses and position taken from the parent box. Additionally, $N_{\rm gal}$ indicates the number of galaxy velocities from (Tully et al., 2013) within the convex hull of the Lagrangian region, giving a measure of how well constrained the density field for the zoom-in simulation is.

Chapter 13

Graduating from the LowerDecks: Combining High-Resolution Zoom-In Simulations of the Local Universe with State-of-the-Art Observational Data

The method for creating pristine initial conditions described in the previous section made it possible to create a large set of high-resolution zoom-in simulations containing digital clones of some of the most well-studied galaxy clusters in the Local Universe. The high mass resolution of the L5 runs provides the opportunity to study these systems in unprecedented detail, expanding on the project outlined in Chapter 11. The simulations were performed with an updated version of the Magneticum Pathfinder version of OpenGadget3 (Groth et al., 2023), similar to the code version employed for the MagneticumDAWN runs. The main changes to the simulation model are an updated version of the dynamical friction module for black holes (Damiano et al., 2024) as well as a spin evolution model coupled to the feedback efficiency of black holes (Sala et al., 2024). Fig. 13.1 gives an overview of all galaxy clusters in the thus far completed full-physics simulation runs. As can be seen by the frame colours, which indicate overlap with the XRISM targets in the PV phase and the two General Observation phases (AO1, AO2) respectively (XRISM Science Team, 2022). Many regions, such as the Shapley supercluster members (A3558, A3571) or the A3667-A3651 region and the Fornax cluster discussed in Chapter 11 can be seen to be quite active with respect to their large-scale environment and exhibit strongly distorted stellar densities and X-Ray contours due to interaction. In order to assess how these environments affect the turbulent structure of the ICM, the stellar component, the general galaxy population and the neutral gas reservoir, in this chapter we will highlight exploratory studies performed with the current Local zoom-in set.

Name/Res	dm/gas	agn
Season 1		
Virgo/L4(a)	v0	–
Virgo/L5(a)	v0	v0
Coma/A1656/L4	v1	–
Coma/A1656/L5	v1	v1
Perseus/A426/L4	v2	–
Perseus/A426/L5	v2	v2
Fornax/L4	v3	–

continued on next page

Name/Res	dm/gas	agn
Fornax/L5	v4	v4
A2029/L4	v4	–
A2029/L5	v4	v1
Bridge/A3667/L4	v2	–
Bridge/A3667/L5	v2	v0
Shapley/A3558/L4	v1	–
Shapley/A3558/L5	v1	v0
A1795/L4	v1	–
A1795/L5	v1	v1
A2199/L4	v3	–
A2199/L5	v3	v3
Hydra I/L4 (A1060)	v1	–
Hydra I/L5	v1	v2
A085/L4	v1	–
A085/L5	v1	v0
A496/L4	v3	–
A496/L5	v3	v3
Hercules/L4	v1	–
Hercules/L5	v1	v1
A3395/91/L4	v1	–
A3395/91/L5	v1	v1
A2256/L4	v2	–
A2256/L5	v2	v2
Season 2		
A754/L4	v4	–
A754/L5	v4	v4
A119/L4	v1	–
A119/L5	v1	v1
A644/L4	v1	–
A644/L5	v1	v1
A1644/L4	v1	–
A1644/L5	v1	v1
A2319/L4	v1	–
A2319/L5	v1	v1
A3158/L4	v1	–
A3158/L5	v1	v1
A3266/L4	v1	–
A3266/L5	v1	v1

Table 13.1: Overview of all LowerDecks regions with a completed full physics (agn) run to date. For initial conditions that were iterated once or several times adding neighbouring structures as described in Chapter 12, we denote this fact with the version (vx). v0 indicates the first verification ICs, which in some cases already could be used for full-physics simulations.

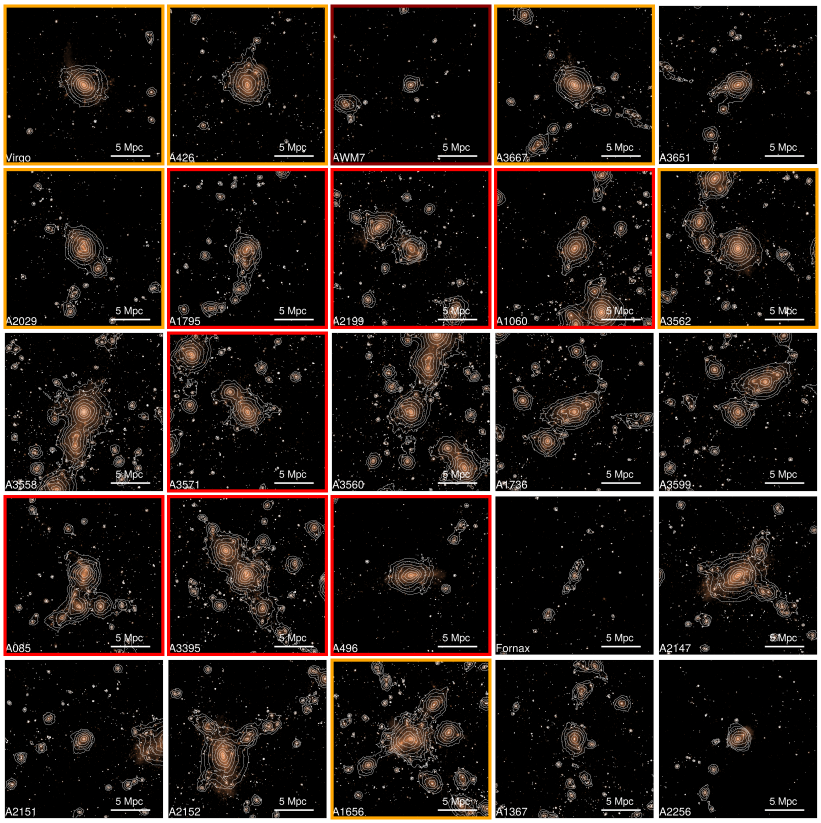


Figure 13.1: Zoom-in suite of the simulated local clusters in LowerDecks. Stellar surface density and X-ray surface brightness (contours). XRISM PV targets are marked in orange, XRIMS AO1 targets in red and AO2 targets in a darker red.

13.1 Turbulent pressure fractions

The content of this section has been published as Groth et al. (inc. Seidel) 2025, ApJ 100 75, "Turbulence in Simulated Local Cluster Analogs: One-to-one Comparisons between SLOW and XRISM/Hitomi". I contributed the initial conditions for the simulations.

An important physical process in the evolution of the ICM is the so-called turbulent cascade (e.g. Vazza et al., 2012, Mohapatra et al., 2020) where energy is transferred from large-scale gas motions like bulk flows and shocks with spatial dimensions of order 1 Mpc down to kpc scales and beyond, depending on the viscosity of the ICM, where it is dissipated into thermal energy. These motions can effectively act like an extra pressure component beyond the pure thermal pressure of the gas. Because galaxy cluster mass estimates for cosmology are usually built on assumptions of hydrostatic equilibrium, this non-thermal pressure is a very important bias to constrain (Wicker et al., 2022, Ettori & Eckert, 2022). Projection effects complicate this bias estimation additionally as was recently shown using a Virgo clone simulation (Lebeau et al., 2024b).

Interestingly, recent observational efforts to constrain the amplitude of this turbulent component by measuring velocity dispersions from the broadening of X-Ray lines in the ICM have yielded surprising results: They found consistently lower velocity dispersions for Perseus (Aharonian et al., 2016, Hitomi Collaboration et al., 2018) and similarly for Coma (XRISM Collaboration et al., 2025) and Centaurus (Audard et al., 2025) than previously expected from numerical simulations (Truong et al., 2024, Groth et al., 2025). The inferred turbulent pressure fractions were consequentially equally low at around 4%. Using the SPH-only runs for Virgo, Coma, and Perseus from the LowerDecks set (see Table 13.1), Groth et al. (2026) set out to establish the first one-to one comparisons of the turbulent pressure

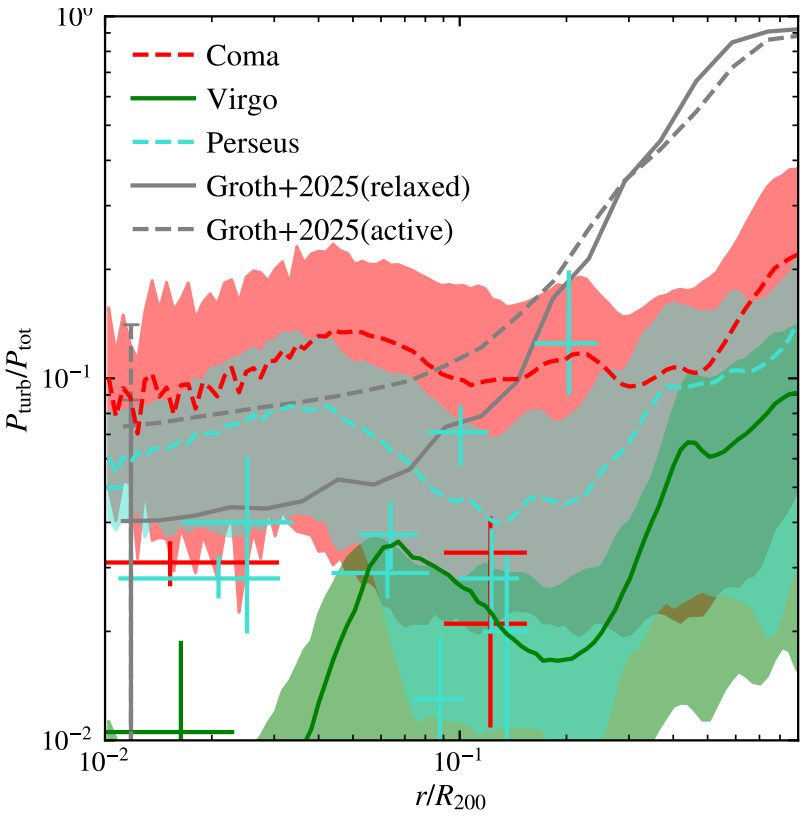


Figure 13.2: Radial turbulent pressure profiles for Coma (red), Virgo (green) and Perseus (cyan) at redshift z = 0. Active clusters are plotted with a dashed line, while relaxed clusters are indicated by a solid line. Observed turbulent pressure fractions by Hitomi (cyan) and XRISM (red) are overplotted with their uncertainties where available. In addition, mean values for relaxed (solid black) and active (dashed black) clusters by Groth et al. (2025), including the central 1-σ scatter as an error bar. Figure 3 from Groth et al. (2026).

fraction in the ICM with observations.

Fig. 13.2 shows the resulting turbulent pressure profiles compared to the Hitomi data for Perseus and the two Coma pointings from XRISM as well as a statistical sample from Groth et al. (2025), split into dynamically active and relaxed clusters. The Perseus simulation reproduces the dynamics observed by Hitomi excellently. Virgo, as the most relaxed cluster shows the lowest pressure fractions out of the set, highlighting the importance of the dynamical state in determining the ICM turbulence. Even Coma, which is classified by the authors as the most dynamically active cluster among the three and one of the most dynamically active galaxy clusters in general, demonstrates a turbulent pressure fraction consistent with the dynamically active comparison set mean in the inner region. While the XRISM observations for Coma are below the simulated profile consistently, they are in agreement within the error bars of the simulated runs. Especially the outer regions, where the simulated turbulent fraction is much higher than the observations and even exceeds the statistical sample might be sensitive to timing differences in the simulations: There is some indication for the Coma cluster in the SLOW simulation to be slightly underdeveloped with respect to the real system (see e.g. Fig. 13.3 where especially the inner region is less massive than observations generally infer). This could be related to spatial shifts of the overdensity modes that merge to form the final cluster caused by uncertainty in the constraints. Future analysis will consider this region in an advanced state (i.e. a simulation ran a few 100 Myr into the future) to determine whether the timing can account for the difference between observations and constrained simulations.

In summary, Groth et al. (2026) have shown, that accurate one-to-one comparisons for the turbulent pressure fraction in local galaxy clusters can help relieve the tension between observations and simulations significantly. Furthermore having the full 3D information and formation histories for these clusters can help disentangle selection effects in observations and perhaps even motivate future pointings in order to better understand the connection between environment and small scale effects in the ICM (such as for example the impact of connecting filaments or the turbulence driven by the AGN). Furthermore the timing differences with respect to the merging state of the constrained clusters and the resulting differences in the turbulence structure of the ICM provide valuable information to the constrained simulations pipeline and could help improve the constraints even further in the future.

13.2 ICL+BCG: A Dynamical Tracer

*The content of this section is planned to be submitted as part of Kimmig et al. (inc. Seidel) 2026, "Intra-cluster light as a dynamical clock for galaxy clusters: Insights from the SLOW/*LowerDecks *simulated local cluster equivalents". I contributed the initial conditions for the simulations.*

As massive galaxy clusters evolve, so does their stellar component. Accreted galaxies are eventually destroyed by tidal forces and added to either the central BCG or the ICL component of the cluster. (Kimmig et al., 2025a) showed that as this process happens on similar timescales for different galaxy clusters, the fraction of the stellar mass in a given cluster that is found in the ICL and BCG components, i.e. not associated with a bound substructure like a galaxy is directly related to the clusters dynamical age: The earlier the cluster forms, the more time it had to dissolve the relatively massive substructures from its primary assembly, and consequently the higher the ICL+BCG stellar mass compared to the total stellar mass.

Fig. 13.3 shows the mass assembly history for the 25 most well-studied clusters from the LowerDecks set. What was seen before in the turbulent pressure fractions for Coma, Virgo and Perseus in Fig. 13.2 is directly confirmed here: Coma is by far the most dynamically

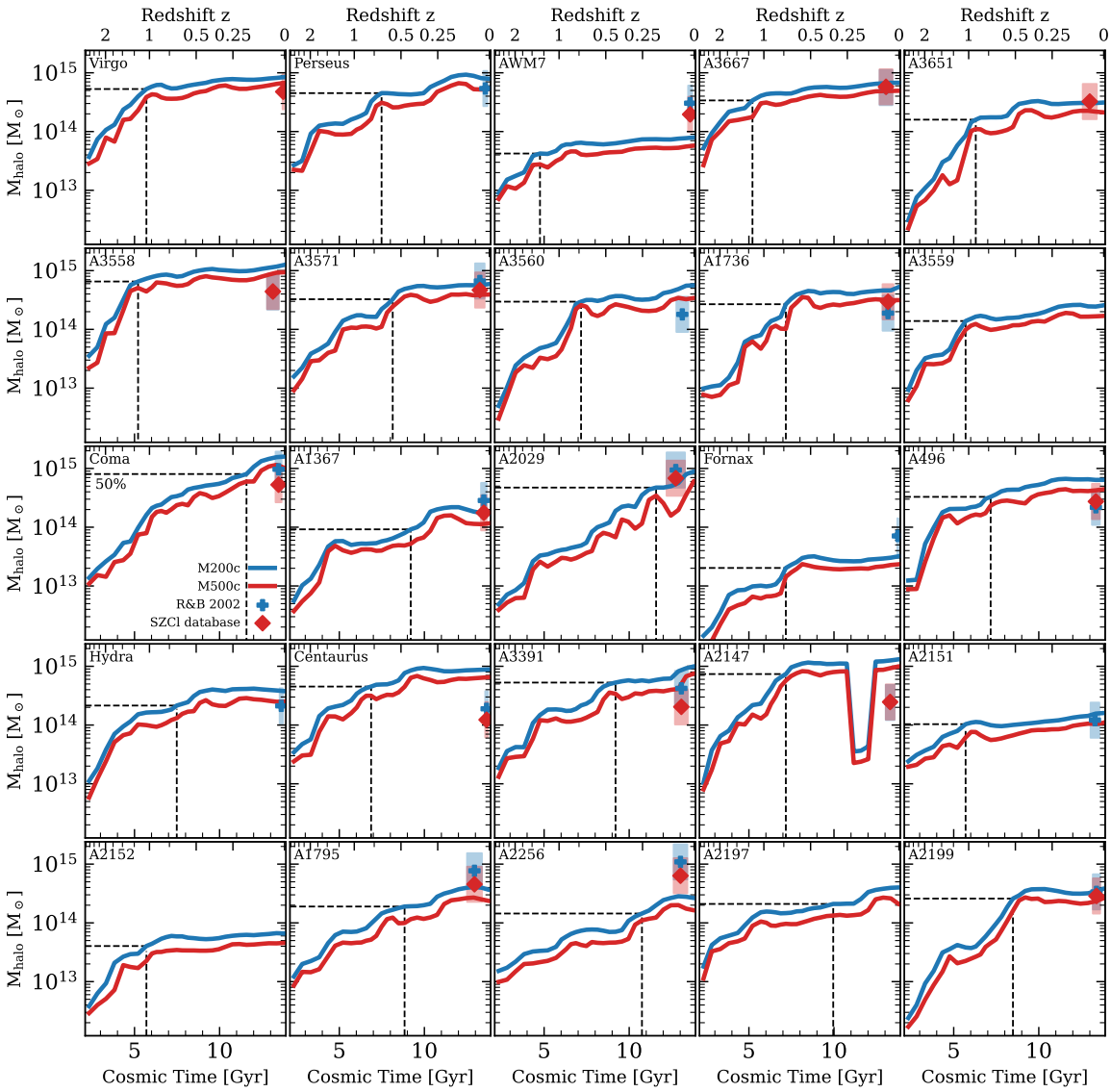


Figure 13.3: Mass assembly histories of the LowerDecks clusters. Shown are the evolution of the M_{500} and the M_{200} respectively, additionally X-Ray Masses by Reiprich & Böhringer (2002) (blue pluses) as well as SZ Masses from the publicly available SZ cluster database [1]are given as estimates of the current cluster mass where available. The dashed lines indicate the mass (horizontal line) and the redshift (vertical line) at which the cluster reaches half of its present-day mass. Figure taken directly from Kimmig et al. 2026 in prep.

active clusters out of the three clusters, and in fact the cluster has one of the lowest formation redshifts out of the set of 25 shown in Fig. 13.4. On the other hand, the Virgo cluster is among the earliest assembled clusters in the set and can therefore be considered to be dynamically relaxed. Interestingly for the supercluster regions and pairs, it can be seen that the most massive clusters in the regions are forming quite early and are therefore dynamically relaxed at z=0. Notable examples for this are the Shapley supercluster region, where A3558 is the earliest formed cluster out of the set and despite a very close by merging substructure that can be seen in Fig. 13.1, which is even already part of the FOF group, as was discussed in Chapter 10, this cluster is still very spherical and relaxed (as indicated by the circular X-Ray contours in Fig. 13.1). Similarly for the A3667-A3651 regions, as well as for the Hercules

[1]`http://szcluster-db.ias.u-psud.fr/sitools/client-user/SZCLUSTER_DATABASE/project-index.html`

supercluster (with A2147 being the main cluster of that region), the most massive structures are very early formed and dynamically relaxed, because the massive mergers that finally assemble the supercluster core into a single region lie mostly in the future as was shown by the CLAIRVOYANT future MAH for these structures (see Fig. 10.8). A notable intermediate case is the Perseus cluster with a relatively early assembly combined with a recent re-ignition of merging activity. This could be the reason of the somewhat contradictory observational evidence for this cluster being a cool-core cluster, whilst at the same time showing signs of at least intermediate recent activity (e.g. van Weeren et al., 2024, Zhang et al., 2026). Fig. 13.4 shows the ICL+BCG fraction as a dynamical tracer compared to two other indicators: The gas center shift shown in the middle panel is caused by the collisionless stars behaving differently to the gas component, causing a shift between the gas centre of mass and the actual position of the BCG. As the cluster relaxes, this shift decreases in amplitude, causing the negative correlation that can be seen in Fig. 13.4. Another dynamical tracer closely related to the ICL+BCG fraction is the total mass present in substructures, which is also negatively correlated to the formation redshift and can be understood as the flip side of the increasing ICL+BCG fraction with increasing formation redshift, as the more substructures dissolve dynamically in the cluster environment, the more their stellar components will contribute to the ICL and the BCG. Overall, Fig. 13.4 shows the LOWERDECKS clusters to be in good agreement with previous work, indicating that the formation redshifts of nearby clusters can be well-constrained from observations of the ICL with instruments like *Euclid* (Kluge et al., 2025).

In this section, we showed the mass assembly history of the LOWERDECKS sample of local galaxy clusters, and shown the stellar component in these clusters to be a reliable tracer for their formation time. Directly related to the stellar properties of the ICL and BCG is the galaxy population of a cluster, which we will examine in the next section specifically for the Coma cluster.

13.3 The Galaxy Population of the Coma Cluster

The content of this section has been submitted to ApJ as part of Zöller et al. (inc. Seidel) 2026, "Galaxy Luminosity Function of the Coma Cluster from Deep u'-g'-r' Wendelstein Imaging Data". I contributed the simulated luminosity functions.

Another advantage of a 1:1 cluster reference set is that it is now possible to compare directly galaxy populations in specific regions with reduced selection biases compared to conventional fields. A powerful tool of quantifying galaxy populations numerically are so-called galaxy luminosity functions (GLF), which are closely related to the stellar mass functions discussed in Chapter 3. Similarly to stellar mass functions, these GLFs can be described by a Schechter function (Schechter, 1976), which is built on the basic assumptions of halo masses from Press & Schechter (1974), but critically allows for a so-called faint-end slope α to describe the increase towards less luminous galaxies. This faint end is sensitive to many physical processes: Early predictions from dm-only numerical simulations and their overprediction of smaller satellites to what was found in e.g. the Milky Way (Klypin et al., 1999) lead to the so-called "Missing Satellite Problem", which were later shown to be alleviated by introducing baryonic physics, which in the low-mass regime can severely impact the survivability of dm haloes as well as affect the efficiency at which gas is converted to stars (e.g. Brooks et al., 2013). This means however that, from a numerical perspective the behaviour of the GLF at the faint end is very sensitive to the feedback model choice and configuration. Additionally even alternative cosmological models, such as warm dark matter, could impact this faint end slope (Bullock & Boylan-Kolchin, 2017).

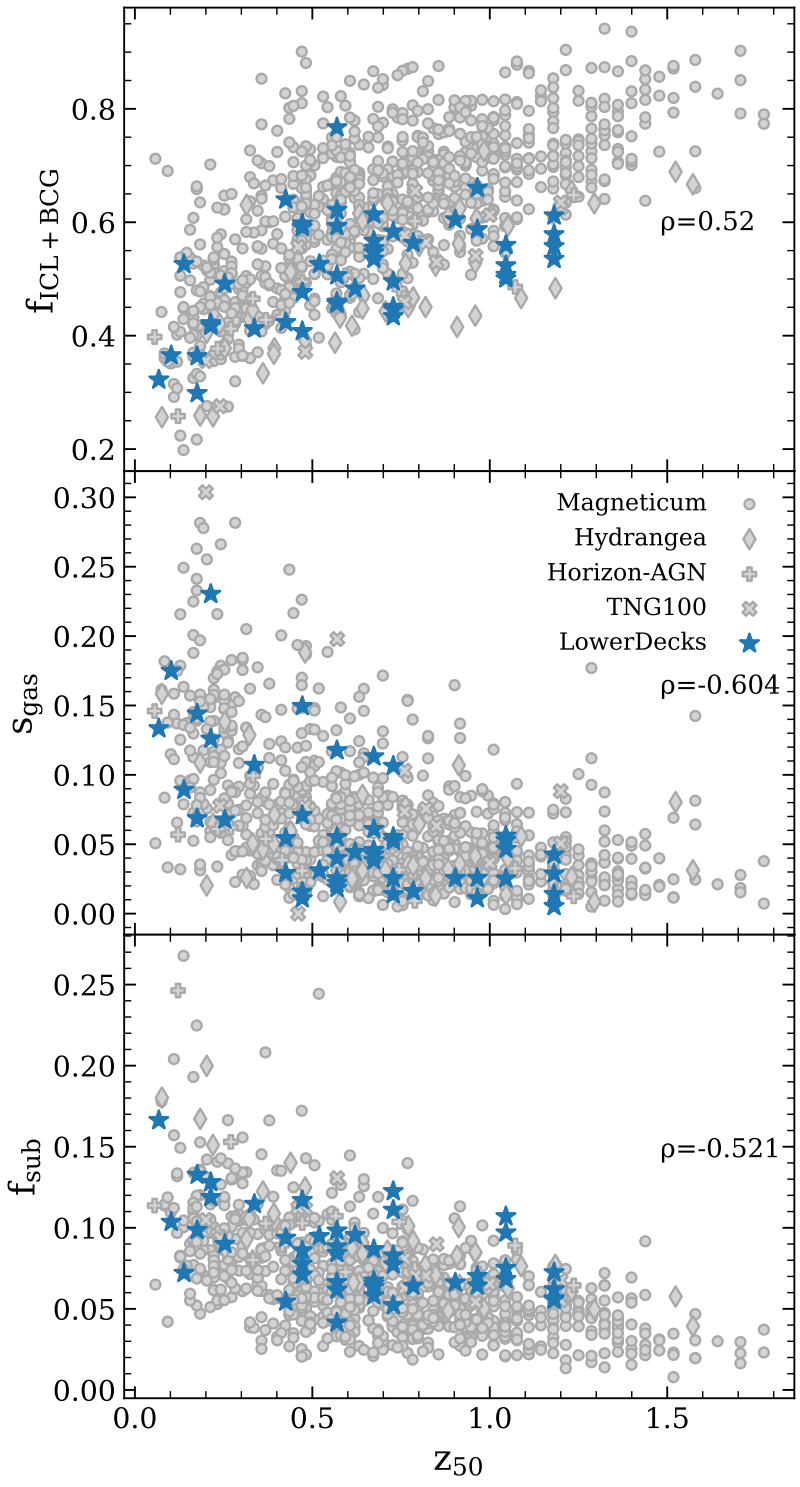


Figure 13.4: Correlation of the ICL+BCG fraction (top panel), the offset of the gas COM from the BCG position (middle panel), and the fraction of mass present in substructures (bottom panel) with the formation redshift z_{50}. The ρ give the Pearson correlations for the LowerDecks sample. Other numerical simulations are shown in grey (data from Kimmig et al. (2025a)).

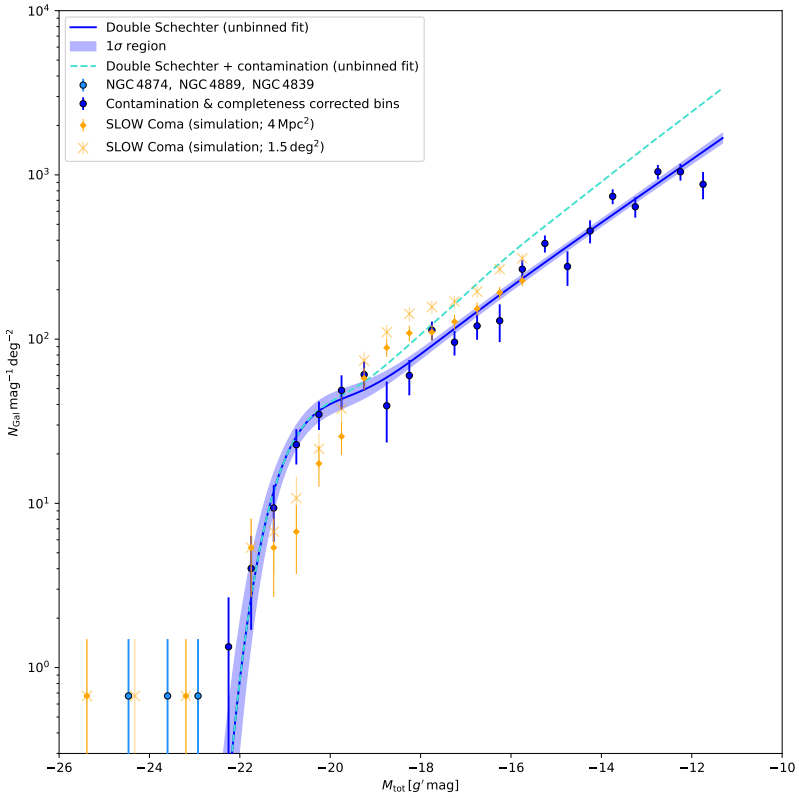


Figure 13.5: Coma G-Band luminosity function of the Coma cluster compared between the Wendelstein Wide Field Imager (fit lines + blue symbols) and the LowerDecks counterpart (yellow and orange symbols). Figure from Zöller et al. (2025).

Therefore it is important to separate as many possible impact factors as possible and understand how each effect impacts the GLF separately. One of the approaches to do this is to directly compare the GLF extracted from a nearby galaxy cluster, where one can resolve individual galaxies and expect good completeness for the faint end, to a simulated cluster with environmental properties and formation history as similar as possible to the observed cluster. Zöller et al. (2025) extracted the g-Band luminosity function of the Coma Cluster in a 1.5 square degree FOV using the Wendelstein Wide-Field Imager (Kosyra et al., 2014) at the 2.1 m Fraunhofer telescope at the Wendelstein in the Bavarian alps (Hopp et al., 2014). Fig. 13.5 shows the Double-Schechter fits as well as the individual data points from the observational data compared to the LowerDecks Coma counterpart. The different observer distances are reflected in the yellow and orange points: The authors assume a distance of 93.85 Mpc (from their measured luminosity distance), while the SLOW counterpart is 122 Mpc from the SLOW optimal observer following (Dolag et al., 2023). Correcting for this discrepancy, by selecting the simulated galaxies in a real-space (orange diamonds) rather than angular FOV (yellow crosses) brings the observed and simulated data at the faint end closer together.

There are other discrepancies to be found however: The intermediate-magnitude rise of the simulated GLF (mag $= -22$ – mag $= -18$) is significantly suppressed with respect to the observed galaxies. This in turn is compensated with an excess number of galaxies at ≈ -19.8, while the faint end is in excellent agreement, when using the corrected FOV. The overall shape of the simulated GLF makes a double-Schechter fit unviable, but the faint end slope was determined to be $\alpha = -1.37 \pm 0.04$, slightly shallower than the observed ($\alpha_2 = -1.539^{+0.024}_{-0.024}$ from the double-Schechter fit). A possible interpretation of the "bump" behaviour of the simulated GLF is the relatively aggressive AGN feedback of the fiducial run

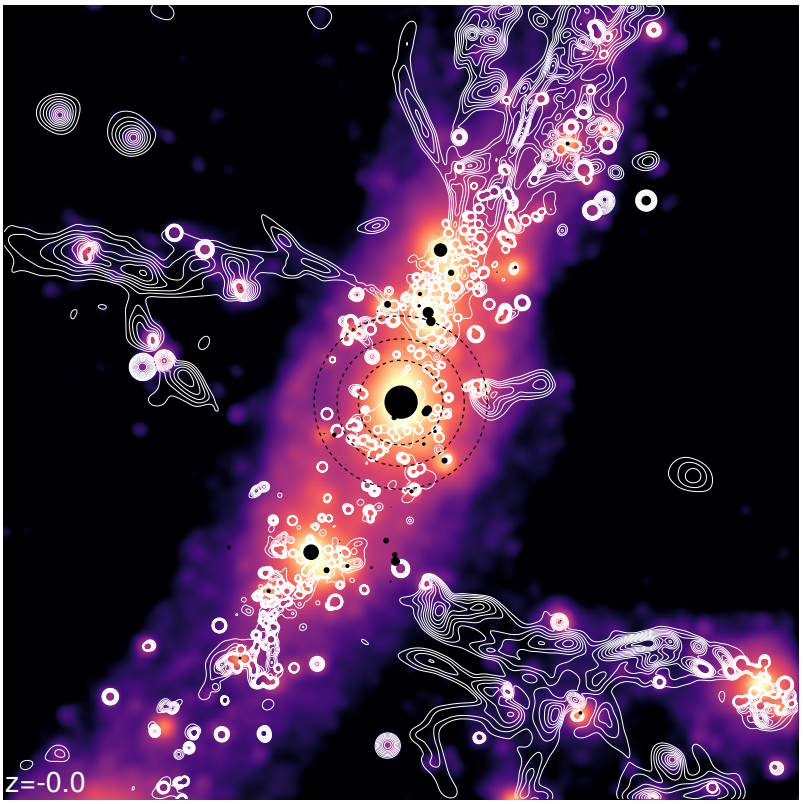


Figure 13.6: View of the Fornax region in LowerDecks. The colour map indicates the smoothed dark matter density field. The dashed circles indicate r_{500c}, r_{200c} and $r_{\rm vir}$ from inside to outside. Galaxies are indicated as black dots with the size of the dots scaled by $\sqrt{M_\star}$. The white contours indicate the HI density. The outer contours mark a column density of $N_{HI} = 6 \times 10^{12}/\mathrm{cm}^2$ with densities increasing by a factor of 1.5 for each contour.

used for this analysis. This could truncate galaxies growing into the mag = −21 range early, when the AGN feedback triggers and thus accumulate them at overall lower luminosities where the bump is found. However precisely determining the origin of this discrepancy will require the additional modified physics run (e.g. using the DAWN model). The faint-end slope poses another challenge with the shallower slope potentially being a result of the resolution given that the chosen magnitude cut-off at -15.5 corresponds to a stellar mass of $\approx 10^9 M_\odot$, which is roughly 400 stellar particles per galaxy at the 6144 resolution (see Section 9.1). Additionally this region in the GLF can be expected to be significantly impacted by the stellar winds, which are the main regulating mechanisms at these lower stellar masses.

In summary, we have created a one-to-one comparison between the Coma GLF obtained from an optical observation and its LowerDecks simulated counterpart. We find the luminosity functions to be in good agreement generally with some discrepancies in the faint end slope of the GLF and a peculiar depression and following excess at intermediate luminosities. In future work, we will explore how different sub-grid models, as well as further improved mass resolution impacts these results, helping to understand which physical processes shape the galaxy populations of individual clusters.

13.4 Cold Gas in the Fornax Region

Before galaxies fall into a galaxy cluster to form the galaxy population investigated in the previous section, they are believed to undergo pre-processing. Processes described by this term are environmental mechanisms, such as tidal or ram-pressure stripping, that transform

the galaxies gas content and may even quench it entirely before it ever enters the cluster atmosphere. This can happen in groups (Bianconi et al., 2018, Bahé et al., 2019) and potentially even upon infall onto filaments (Stephenson et al., 2024).

Neutral atomic hydrogen (HI) gas, as the dominant component of the ISM and a key indicator for the gas reservoir fuelling a galaxy's star formation is an ideal tracer for these pre-processing mechanisms. Its morphology has been shown to trace well both gravitational (de Blok et al., 2018, Kleiner et al., 2019) and hydrodynamical (Cowie & McKee, 1977, Chung et al., 2007, Jaffé et al., 2015) stripping processes.

One of the most promising laboratories for studying the HI component in a number of different environments is the Fornax cluster. Due to its proximity, as previously discussed, observations are able to map this regions with great spatial resolution. A HST survey utilizing the COS spectrograph is currently ongoing using quasar sight lines to map out the HI absorption across the entire region (Burchett et al., 2023). On the emission side, the MeerKAT Fornax survey is targetting the region in the 21cm band. Previous observations with this instrument were focussed primarily on the Fornax A group (Serra et al., 2019, Kleiner et al., 2021) which is a promising region to study group preprocessing in an active infalling group environment.

While constrained simulations can not yet be expected to exactly reproduce the dynamics and configuration of such an infalling group due to these processes being highly non-linear, assessing how the large-scale gravitational and gaseous environment translates into stripping dynamics in these regions can be a valuable method to understand and contextualize the observed HI morphologies. Kleiner et al. (2021) discovered multiple galaxies exhibiting signs of stripping through their HI distortions as well as independent HI systems, the authors hypothesized to be the result of a stripped infalling galaxy.

To provide a first numerical reference in this section we will explore the cold gas morphology of the LowerDecks Fornax and Fornax A counterparts in order to determine how it matches observational results and if this information may be used to inform the ongoing surveys searching for the HI in the cluster and its surroundings.

13.4.1 Methods: Post-Processing the HI Content

The modified Magneticum Pathfinder model employed in the zoom-in simulation run does not itself trace the ionization balance of the gas particles and as such no direct output exists for molecular, neutral and ionized hydrogen fractions. However this can be directly inferred using the density, temperature and metallicity information from the simulation. We implemented an approach to calculate the HI content particle-wise based on the work of Villaescusa-Navarro et al. (2016) and Ködel (2018) into our SPH density interpolation routine, which interpolates the HI masses of particles using a cubic-spline kernel. Star-forming particles allow for a temperature-independent treatment, since the model from (Springel & Hernquist, 2003) traces the fraction of gas in neutral cold clouds.

In general, the neutral fraction of hydrogen can be estimated assuming ionization equilibrium, optically thin gas allowing recombination radiation to escape freely, and a fixed UV background (Rahmati et al., 2013). The authors provide a fitting function for the photoionization rate from radiative transfer simulations:

$$\frac{\Gamma_{\text{phot}}}{\Gamma_{\text{UVB}}} = (1-f)[1+(n_H/n_0)^{\beta}]^{\alpha_1} + f[1+n_H/n_0]^{\alpha_2}, \tag{13.1}$$

where the values of the fitting parameters are provided for different redshifts and we input the UV background Γ_{UVB} from (Haardt & Madau, 2001), which is the fiducial UV background in the Magneticum Pathfinder model. The photoionization equilibrium is then written as

$$\eta(\Gamma_{\text{phot}} + \Gamma_{\text{col}}) = \alpha(1-\eta)^2 n_H, \tag{13.2}$$

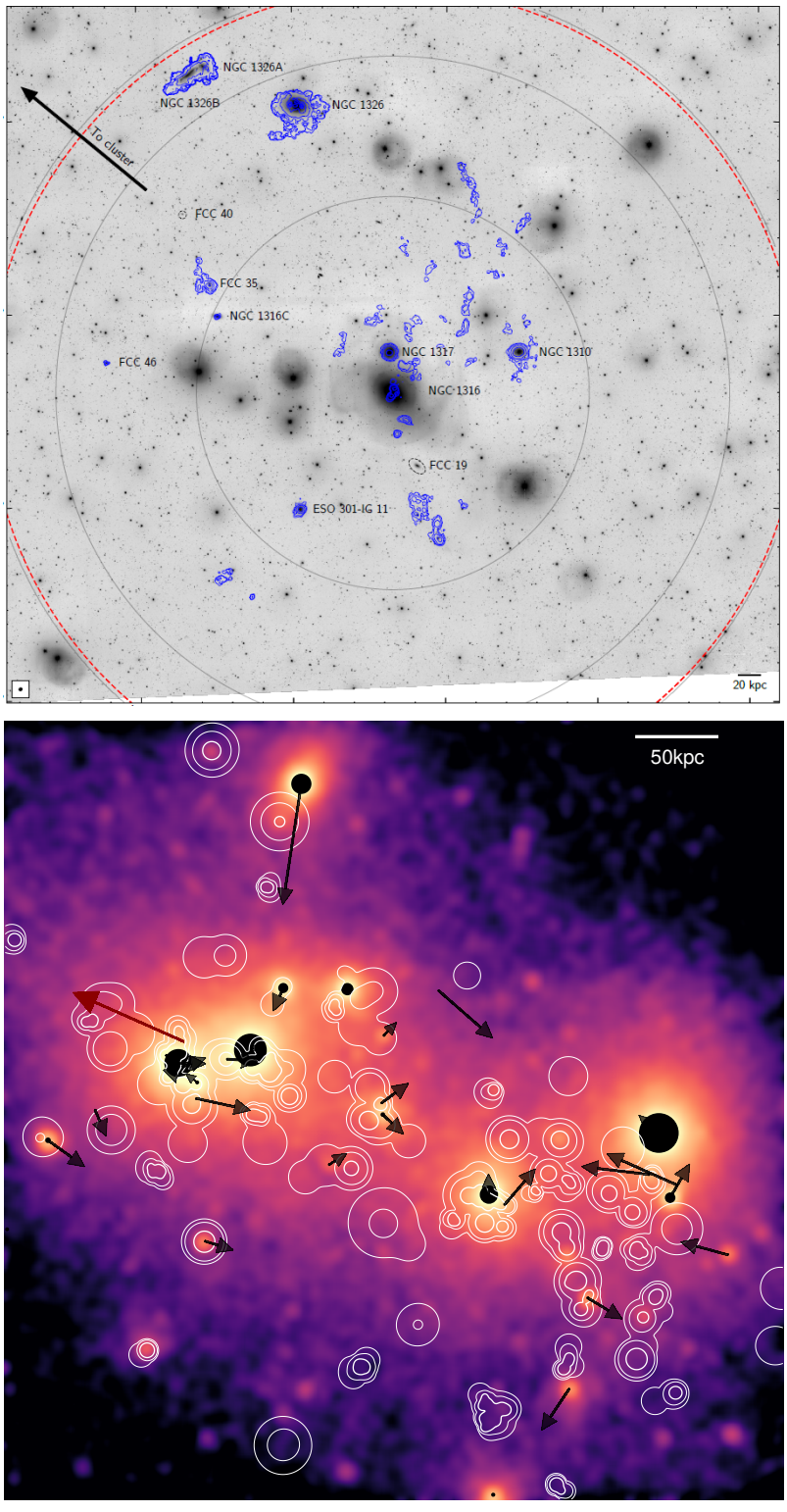


Figure 13.7: *Top Panel:* MeerKAT contours overplotted over an optical *gri* image (Iodice et al., 2016). The outermost contour represents a column density of $N_{HI} = 6 \times 10^{19}/\mathrm{cm}^2$, column densities increase by a factor of 3^n for the n-th contour. Figure directly taken from Kleiner et al. (2021). *Bottom Panel:* Same as Fig. 13.6, but zoomed-in on the Fornax A region. The red arrow indicates the position of Fornax. For the Galaxies, we additionally show the velocities relative to their common centre of mass. The inner contours mark a column density of $N_{HI} = 6 \times 10^{19}/\mathrm{cm}^2$, while the outer contours outline $N_{HI} = 6 \times 10^{17}/\mathrm{cm}^2$ and $N_{HI} = 6 \times 10^{15}/\mathrm{cm}^2$.

where η is the ratio of HI to total hydrogen number densities n_{HI}/n_H, and α and $\Gamma_{\rm col}$ are the recombination and the collisional ionization rates respectively. Both of these rates are computed by Rahmati et al. (2013) using fitting functions and depend only on the temperature of the gas particle. Using this equilibrium equation and computing the hydrogen number density and mass n_H, m_H from the density, total mass and metallicity of the gas particle, we can then calculate the neutral hydrogen mass of the particle by solving for η.

For star-forming particles, the cold gas fraction $f_{\rm cold}$ is readily available from the simulation data. Here, we employ the model developed by Krumholz et al. (2008, 2009), McKee & Krumholz (2010) describing a spherical cloud of molecular hydrogen shielded by a layer of neutral hydrogen with a sharp transition between the two species. For the incident radiation field, as well as for the properties of shielding dust, we assume the approximations introduced by (Villaescusa-Navarro et al., 2016), which effectively renders the fraction of molecular hydrogen, f_{H_2}, a pure function of the metallicity Z and the surface density $\Sigma = \rho \times r_{\rm SPH}$ of the gas particle. The HI mass of a star-forming particle is then obtained by subtracting the obtained molecular hydrogen mass from the cold hydrogen mass (assuming the cold gas component is completely neutral, which is one of the assumptions in the star formation model) $M_{\rm H,cold} = f_{\rm cold} \times (m_{\rm gas} - m_{\rm gas,\geq He})$, where $m_{\rm gas,\geq He}$ is the sum of all non-hydrogen elements in the gas particle and can be obtained from the metallicity output of the simulation. The underlying assumption of the model is that HI exists in a two-phase equilibrium between a warm and a cold neutral atomic hydrogen phase. Consequently this assumption breaks down in regimes, where either one of the phases is disfavoured by the pressure environment of the gas. In the high-pressure environment of nuclear star-bursts only the cold component is stable, while in the diffuse medium in the outer disks of galaxies one would expect only the warm component to be stable (Krumholz et al., 2009). Since we apply this model only for star forming particles and only at $z = 0$, long after the main peak of SFR in the following work, this effect can be neglected. However it can be a limitation of this methodology at earlier times.

13.4.2 The HI Distribution in the Fornax Region

Fig. 13.6 shows the large-scale HI distribution in the Fornax region obtained with this method (white contours). Interestingly, beyond the significant HI assembling along the main filamentary structure, which also includes the Fornax A region at the top right of the outer boundaries of the Fornax cluster, there are multiple HI systems in the lower density regions orthogonal to the central filament. These systems, such as the double lobe structure to the right of the virial boundary and the extended finger like structure to the left of the cluster could be interesting accreting targets for studying the deformation and overall HI content of infalling structures. In future work we will assess the agreement of the filamentary structure to the observed cosmic web structure as determined by e.g. Raj et al. (2024) and provide HI mass functions divided by sub-regions in order to assist the observational efforts to understand the stripping and pre-processing dynamics in the region.

For Fornax A specifically, Fig. 13.7 shows the MeerKAT HI detections with the blue contours. Below, we show the same region in the LowerDecks Fornax zoom-in with white contours indicating the HI column density. In the simulated image the inner contours are configured in such a way that they match the column density of the outer blue contours at $N_{HI} = 1.2 \times 10^{19}/cm^2$ in the MeerKAT image. The outer contours of the simulated image show the further extent of the HI systems going beyond what can currently be observed by MeerKAT. Even though the group is not virialized in the simulation and lacks the clear group centre with the NGC1316-NGC1317 pair, there are interesting parallels in the HI morphologies between the simulated and observed systems. Similarly to the MeerKAT image, the simulated Fornax A group contains a number of ”free” HI clouds not associated with a

galaxy or dm overdensity, some of which can reach quite large spatial extents. Active stripping can be seen in the offsets between galaxies and their HI components in the opposite direction to their motion within the group, for example the galaxy on the left edge of the image, where the HI centre is clearly lagging behind the galaxy. Finally, even though the simulated HI contours are generally more spherical, many of them also show clear distortions and extended bridge-like features connecting individual clouds. All of these features show a dynamically active system with infalling galaxies that are actively being stripped of their HI content in a comparable fashion to the observed systems. In future work, we plan to follow the infalling galaxies in the Fornax A group individually and trace their HI accretion and stripping through time. This data will be a valuable reference to the data the MeerKAT Fornax survey will yield in the future.

In this section we have introduced a method to calculate the HI distribution from numerical simulations. We have explored the HI morphology for the LowerDecks Fornax cluster counterpart. First comparisons with the MeerKAT survey map of the HI distribution in the infalling Fornax A group demonstrate this simulation suite to be a potentially valuable reference point for future HI observations in the Local Universe.

13.5 Conclusions

Throughout this chapter we have introduced the LowerDecks set of constrained zoom-in simulations of local galaxy clusters and superclusters. Summarizing the first scientific results obtained from these simulations, we have shown this simulation project to be a promising reference for exploring the physics of local structures on multiple scales. For the ICM, we have shown the local counterparts of Coma and Perseus to more closely reproduce the low turbulent pressure fractions observed with XRISM than simulation averages predict, pointing to these clusters possibly being outliers in their mass range. For the stellar component, we demonstrated that nevertheless the local clusters lie on expected scaling relations between their formation redshift and the fraction of stars in the ICL+BCG component, making constraints on the formation time of the real world clusters also a possible validation method for the constrained simulations. Furthermore we found the galaxy population of the Coma cluster to be generally well reproduced by the LowerDecks simulation, with present discrepancies allowing for further development of the sub-grid physics that regulate the star-formation in these cluster galaxies. Finally, we presented a proof-of-concept study on the neutral gas distribution in the Fornax region, comparing the simulated HI contours in the Fornax A group to current MeerKAT observations. We find in general a good agreement in the morphology of the fragmented and deformed HI clouds, even though the group is in a dynamically different state to the real system. Future observations constraining the large-scale distribution in this region will enable us to study the infall and stripping dynamics in a realistic digital clone environment of a group infalling into a cluster and elucidate the pre-processing happening in such groups.

All of these preliminary results highlight the potential of high-resolution digital clones of galaxy clusters in the Local Universe. By widening the scope of physical processes resolved in the simulations, they make it possible to fully leverage the constrained environments obtained from the local large-scale structure and additionally feed back even more data into the constrained simulations pipeline in order to improve the reconstructions even further.

Part IV

Conclusion

Chapter 14

Confluence: Summary and Conclusions

This work has aimed to elucidate the connection between large-scale structure and the evolution of bound structures like galaxies and clusters of galaxies. The main paradigm this connection was studied under was the gravitational and hydrodynamical flow of matter. As the main analysis tool we have used hydrodynamical cosmological simulations, which can model these flows in their full non-linear richness and also accurately factor in baryonic effects like stellar and black hole feedback on small scales.

14.1 In and out of the Box: Accretion and Outflows

In the first part of this work we focussed on the MAGNETICUM PATHFINDER simulation suite (Dolag et al., 2025), a state-of-the art hydrodynamical simulation. We demonstrated how structures form over time in that simulation and, comparing with observation of the baryonic structure, discussed the successes and shortcomings in replicating observed galaxy and cluster populations. Specific attention was given to the high-redshift Universe, where numerical simulations often fall short in replicating the massive quiescent galaxies observed by the current JWST mission. We demonstrated that a simulation combining a large enough volume to allow for massive overdensities to form early with a high resolution can in fact replicate the observed quenched fraction (Kimmig et al., 2025b, Remus & Kimmig, 2025). By analysing the sample of galaxies with respect to their gravitational environment, we showed that these early quiescents, which undergo a rapid quenching starburst, tend to form in slightly underdense regions with a shell of very low density usually surrounding them. This is then also reflected in the gas inflows, which, while initially visible in all directions around the galaxy get disrupted quite easily by the inset of feedback-driven outflows, demonstrating the importance of the large-scale environment around these galaxies and especially the flow field. We addressed the following key questions:

14.1.1 How Self-Similar Are In- and Outflows?

To understand the balance of in- and outflow and how this balance evolves in greater detail, we developed a halo-centric method for numerically computing the gas flow across a spherical boundary surface (Seidel et al., 2025b). We showed that the gas flows onto collapsed haloes have a complex morphology in terms of flow rate across the surface, but nonetheless follow the simple mass scaling law predicted by linear theory on average. The complex morphology is mainly driven by the highly anisotropic inflows, which generally are focussed onto a few dense high-flow regions where the filaments intersect the virial surface of the halo. The outflowing component, on the other hand is more isotropic and break the self-similarity, with lower mass halos driving significantly stronger outflows relative to their halo

masses compared to group- and cluster mass haloes. Consequently, these lower-mass haloes are able to relatively extend their heated diffuse gas to larger radii, resulting in a flat entropy profile, while higher mass haloes show a clear accretion shock from 1-3 $r_{\rm vir}$ where the maximum radius is consistent with merger accelerated accretion shocks. We also showed the outflows to be more metal rich than the inflows in general, as the gas mixes with metal rich gas from the central structure. Nonetheless, most of the enriched gas found in the outflows at $z = 0$ was found to have been enriched upon infall indicating a possible pre-processing scenario.

14.1.2 How Can the Morphology of the Accretion Field Be Quantified?

Building on the anisotropy of the inflowing component, we introduced the **inflow asphericity** parameter (Seidel et al. 2026, submitted), which is built on a CMB-like spherical harmonics transform of the inflow field across the virial surface. We tested the behaviour of this parameter extensively with simplified model inflow maps built on simple assumptions of a combination a decomposable field with a filamentary (i.e. concentrated) and an isotropic inflow component, as well as spherically symmetric outflows disrupting the isotropic inflow. Using this, we could demonstrate that using the linear flow field, one reliably constrains on how many hot spots the inflow is distributed and how concentrated these hot spots are. Computing the spherical harmonics decomposition on the logarithm of the flow field however, provided a direct measurement of how effectively outflows can displace the inflows on the halo boundary.

14.1.3 How Is the Evolution of the Flow Field Connected to Galaxy Properties?

Following up on this, we therefore analysed the evolution of the inflow asphericity through time using a population of simulated halos from the Magneticum Pathfinder suite. Both linear and logarithmic asphericities exhibit a peaked evolution, with the linear parameter peaking early indicating the early formation of the cosmic web structure. We also demonstrated the imprint of this structure in the flow field at $z = 0$, where there is a correlation between the linear asphericity and the halo ellipticity (Valenzuela et al., 2024), as the dark matter halo is shaped by the same tidal field that generates the inflows.

The build-up of the feedback-driven outflows on the other hand, causes the logarithmic asphericity to increase at a slower rate and as a consequence peak significantly later. Both the linear and the logarithmic asphericity decrease monotonically with time, most likely due to filament evolution and galactic fountain processes, which create a diffuse and isotropic re-accretion. Connecting the parameter to the star-formation rate of the individual galaxies showed the logarithmic asphericity to be connected to quenched galaxies at early times ($z = 2$) due to these galaxies having effectively removed their gas reservoir which is additionally stopping additional inflow. This is also consistent with the fact that the peak of asphericity an individual galaxy reaches is correlated with its complete star formation history: Galaxies that quench at least once during their lifetime drive significantly stronger outflows after quenching resulting in a more anisotropic inflow field. In contrast galaxies that continuously form stars never reach a comparable peak in their flow field anisotropy. This connection is also visible in the kinematics, where early-time galaxies reach slightly higher peak asphericities than rotation dominated systems.

14.2 SLOW Flow: The Local Universe

In the second part of this work we focussed on constrained simulations of the Local Universe. Specifically we used the SLOW simulation suite (Dolag et al., 2023), which is built from a reconstructed local velocity field using observed galaxy velocities (Sorce, 2018). These simulations combine a realistic linear density field on large scales, forming accurate counterparts for many of the local galaxy clusters (Hernández-Martínez et al., 2024), with the non-linear galaxy formation and hydrodynamics of a conventional cosmological simulation. Using these simulations, we aimed to answer the following questions:

14.2.1 Can Peculiar Local Structures Explain Observed CMB Anomalies?

Observations of the CMB show a couple of anomalies that seemingly violate basic assumptions about the isotropy of the Universe. From this the question arises, whether these anomalies can be explained by the ICM of the Local galaxy clusters distorting the background radiation. Using SZ-effect maps from the SLOW simulation in combination with statistically generated synthetic CMB maps, we showed (Jung et al., 2024) that this is not the case.

14.2.2 How Well Are Local Superclusters Reproduced by SLOW?

Because the velocity field gives relatively large-scale constraints on the density field (recall Eq. (1.23)), it is not guaranteed that a supercluster-like overdensity constrained by the data will necessarily form clusters at the position in the region where the real-world clusters are located. Non-linear effects and even hydrodynamics could significantly impact the masses and relative positions of such supercluster member clusters. To test how well this works in the SLOW simulations, we developed a quantitative criterion that evaluates how closely the relative arrangement of supercluster members matches their real-world counterparts (Seidel et al., 2025a). We then applied this criterion to six known supercluster arrangements from Local Universe catalogues (Boehringer & Chon, 2021, Boehringer et al., 2021, Monteiro-Oliveira et al., 2022). This showed the SLOW superclusters to reproduce the real-world alignments very well. Replicating these cluster-cluster arrangements is a key part of the potential that simulations like SLOW hold for advancing our understanding of the physics of the ICM. It allowed us to undertake one-to-one comparisons to observations with regards to the large-scale gas distribution in cluster-cluster filaments (Dietl et al., 2024) and the actively merging Fornax cluster (Reiprich et al., 2025). In both cases we could provide dynamical context to the observed structures and our data further emphasized a striking difference between simulated filament density profiles and observed ones. This also lead us to the question of how these structures move with respect to each other, and how bound supercluster in general really are:

14.2.3 How Bound Are Local Superclusters?

Using an N-Body version of the SLOW simulation, the CLAIRVOYANT runs (Seidel et al., 2025a), we simulated the gravitational evolution of the Local Universe beyond the present day. After approximately 40 Gyrs, structure formation has sufficiently been slowed down by the background expansion to allow for the computation of final collapsed halos, which will accrete no more mass. We showed that even though supercluster regions do not collapse spherically, the density contrast of their bound region at the present day is surprisingly well predicted by spherical collapse models (Dünner et al., 2006). However this bound core only

makes up a small fraction of the entire supercluster region due to the gravitational collapse freezing out at late times. Only some of the local clusters, like Coma, undergo massive mergers in their future, while the more relaxed structures like Virgo and Perseus do not accrete massive secondary clusters. Finally, we could show that the SLOW simulation provides additional evidence that the structure of the Local Universe implies our Milky Way not to be bound to the nearest cluster Virgo. We will forever be free after all! The bound volumes of the supercluster regions provided us with a key ingredient for taking Local Universe models a step further:

14.2.4 How Can We Construct Stable and Clean Initial Conditions for Cluster Zoom-Ins?

Because the collapse volumes resulting from the Clairvoyant simulation represent the final set of particles that will ever accrete onto a given halo, we could use these Lagrangian volumes, to pre-select regions in the initial conditions of the simulation which will deform only marginally and contain the target halo. From this principle, we created a set of 20 zoom-in regions, where the mass resolution can be locally enhanced. The collapse volumes ensure that there is minimal mixing between particles of different mass resolution, avoiding spurious energy transfers between such particles. Simulating these initial condition until $z = 0$ we showed that there are indeed minimal flows around the boundaries of these regions, ensuring that the central galaxy clusters are uncontaminated by low-resolution particles at least to $6 \times r_{\rm vir}$. This allowed us to perform high-resolution re-simulations of 30 local galaxy clusters that retain the information from the constrained large-scale structure. These simulations, the LowerDecks suite, will be a valuable tool for future high-resolution observations of the Local Universe

14.3 Future Flows: Outlook

In showing the first one-to-one comparisons between the LowerDecks clusters and observations, Chapter 13 provides a glimpse at the future. We demonstrated how the constrained counterparts for local clusters like Coma, Virgo and Perseus can be used to model and understand the turbulent structure of the ICM in greater detail (Groth et al., 2026). Constraining environmental impacts like filamentary inflows or merger configurations, will help to complement future observations of the ICM dynamics, like XRISM, which are limited by their small spatial footprint but offer high spectral resolution. Since the large-scale turbulence is driven by inflows and accretion, the spherical inflows framework presented in Chapter 4 and Chapter 5 can further help understand the observed dispersions. Applying this, we will be able to link bulk flow systems in the ICM and other dynamical features like cold fronts and shocks directly to the large-scale flow field from a theoretical perspective. Understanding the turbulent structure of the ICM and filaments is important for constraining the amplification of magnetic fields via the turbulent dynamo (e.g. Vazza et al., 2014), for which we plan future magnetohydrodynamical simulations of local clusters and filaments.

Furthermore, as we showed, the stellar component of these local clusters provides valuable information about their dynamical states (see Kimmig et al. (2025a) and Kimmig et al. 2026 in prep.). This connection can be a valuable tool in combination with high resolution studies of the ICL in local clusters, such as EUCLID (Kluge et al., 2025). Discrepancies in the global ICL+BCG fractions between observations and simulations should be relatively model independent and can help quantify small timing differences between the real clusters and their digital clones. Utilizing this information, it will then be possible to further improve the simulation data for ICM dynamics by taking these timing differences into account. In a

second step, this information and the spatial distribution of such offsets will help improve the next generation of these constrained simulations even further.

The mass resolution of the LowerDecks suite makes it possible to also study the galaxy populations of the Local Universe. While we do not expect individual galaxies to be constrained by the observational data, the galaxy populations of local clusters can further elucidate their structure and dynamical states. In comparisons to observations, such as the first one-to-one comparison for the Coma cluster we introduced (Zöller et al., 2025), these constrained clusters can drastically lower the impact of selection effects from simulations and make it possible study what current hydrodynamical models may lack to accurately describe the real Universe.

Since the simulation volumes are rather large, they usually also contain not only the cluster regions, but additionally large filaments and voids. This will inform future studies on the distribution of HI gas and the WHIM phase in these special environments. To further highlight this point, we presented a preliminary view of the neutral gas distribution in the Fornax region, where the ongoing MeerKAT Fornax survey will provide valuable insights into the accretion and stripping of this gas phase in the highly active region. We pointed out interesting regions with extended HI filaments in the LowerDecks simulation, as well as some indication for pre-processing in the infalling Fornax A group, which is in agreement with MeerKAT results (Kleiner et al., 2021). In the future we plan to connect these two datasets together with Lyman-alpha tomography observations of the same region (Burchett et al., 2023), to provide a full picture of the cold gas dynamics in the Fornax region. This will also shed light on the effectiveness of group and filament pre-processing. Here, the large-scale velocity field, combined with the non-linear motion of galaxies, can provide valuable information about the infall dynamics of the observed HI systems.

To summarize, in light of exciting new observations across the electromagnetic spectrum, the tools and data presented and analysed in this work will hopefully provide the foundation of many more theoretical and observational studies. By understanding especially potential local biases stemming from our place in the Universe better, we will be able to learn a lot more about how this marvellous place really works.

Appendix A

Asphericities

A.1 Calibrating the absolute values for normalization

In order to configure the numeric values of the test maps in a realistic manner instead of setting arbitrary values, we used the simulations as calibration for these test maps. To that end, we computed a cumulative log histogram from the pixels of the inflow maps of 100 randomly chosen haloes. We then normalized the inflow values with the halo masses to account for the mass-inflow relationship (see Seidel et al., 2025b).

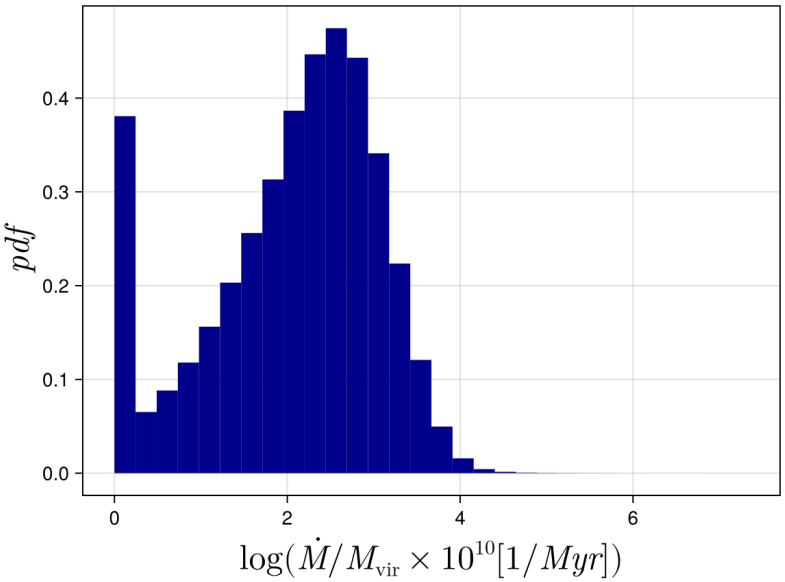


Figure A.1: Stacked histogram of inflow pixels for 100 halos at z=0.

A.2 Truncation of the sum

To motivate the choice of cut-off degree ($l = 9$) for the computation of the asphericity parameter, Fig. A.2 shows the combined spectrum for 2000 simulated halos from MAGNETICUM at z=0. The curve shows a characteristic dip at this specific wave number transitioning to a high-frequency rise at higher angular frequencies.

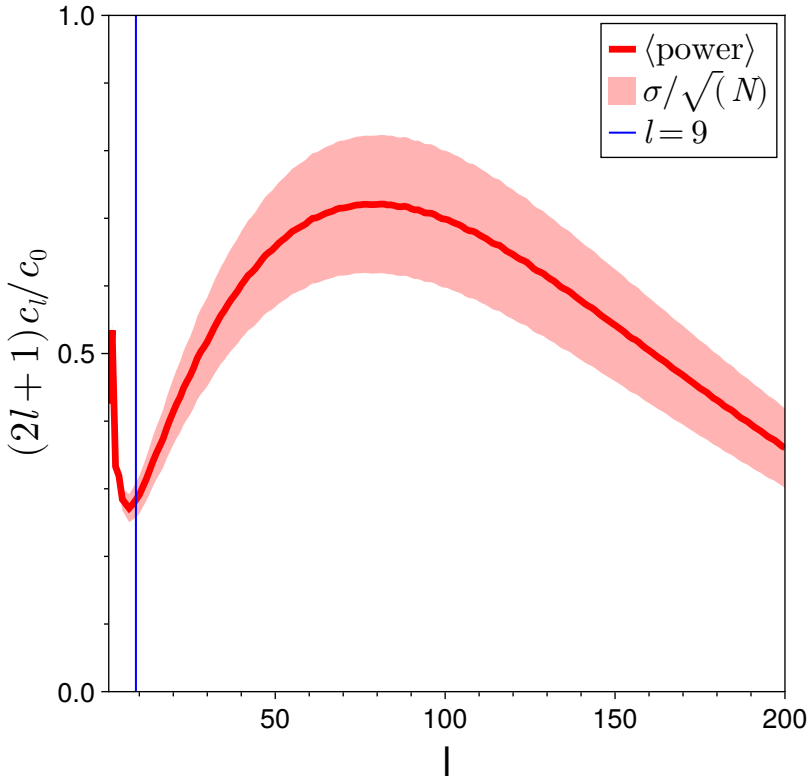


Figure A.2: Mean power spectrum of 2000 halos from Box4. The shaded area shows the standard error of the curve, while the blue vertical line marks the low-pass cut-off point for the large-scale part of the spectrum chosen throughout this work.

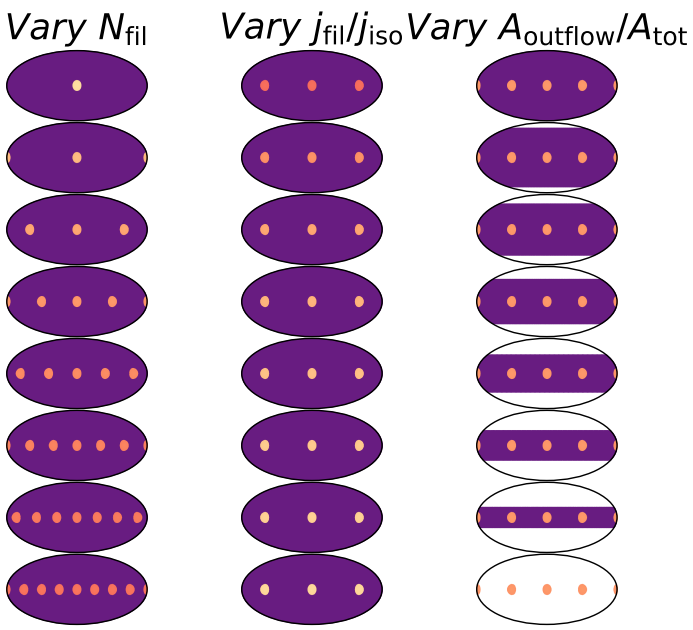


Figure A.3: Visualization of the three parameter variations for the toy model grids in Fig. 5.3 and Fig. 5.4.

A.3 Variation of the parameters

A.4 Special Cases

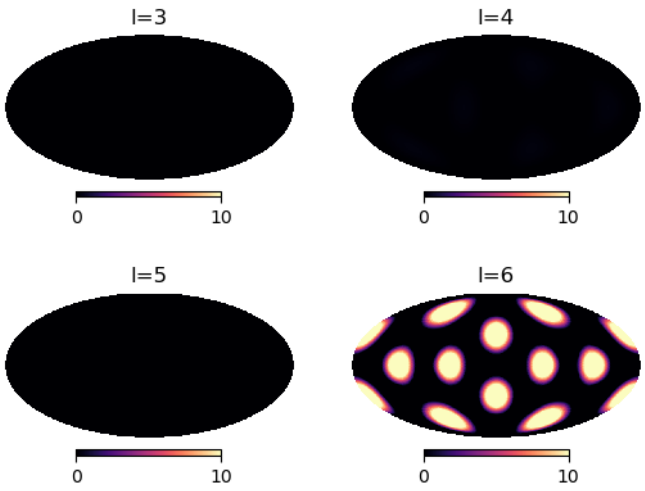


Figure A.4: Reconstruction of the Icosahedron setup with the spherical harmonics from $l = 3$ to $l = 6$.

The tests in Section 5.3 are setup with the simplest geometry: A planar configuration with all filaments in one plane. In terms of the spherical harmonics, this corresponds to the terms with $|m| = l$, the so-called sectoral harmonics. We additionally tested the behaviour of the asphericity using more complex geometries, making use of the full 3D information encoded in the flow maps.

Polyhedral configuration The simple planar setup corresponds to only a small subset of the spherical harmonics functions. In order to test more complex configurations we additionally constructed a set of symmetrical configurations derived from the five so-called platonic solids. These regular polyhedra are relatively simple to construct and provide a more general test case for infall geometry configurations. Following the procedure from the previous section we set up circular regions with a Gaussian profile at each vertex of each platonic solid. This provided five additional maps with 4,6,8,12 and 20 regions for the Tetrahedron, Octahedron, Cube, Icosahedron and Dodecahedron respectively. For the platonic solid setups, the simple correspondence between number of inflow regions and l degree with maximum power breaks down because modes with $l \neq m$ play a role for these symmetries. As a specific example, the Icosahedron configuration with 12 vertices can be completely represented by a linear combination of the m modes with degree $l = 6$ (see Fig. A.4). This makes these setups an ideal test case for the behaviour of the asphericity parameters in more complex geometries.

A.4.1 Impact of the configuration on the asphericity parameter

To ensure that the asphericity parameter is not affected by any specific geometry or choice of filament width, we test the simple relationship between filament number and asphericity for a number of different configurations. Additionally the possible impact of resolution is

studied, since the spatial smoothing lengths can significantly impact the spherical harmonics decomposition.

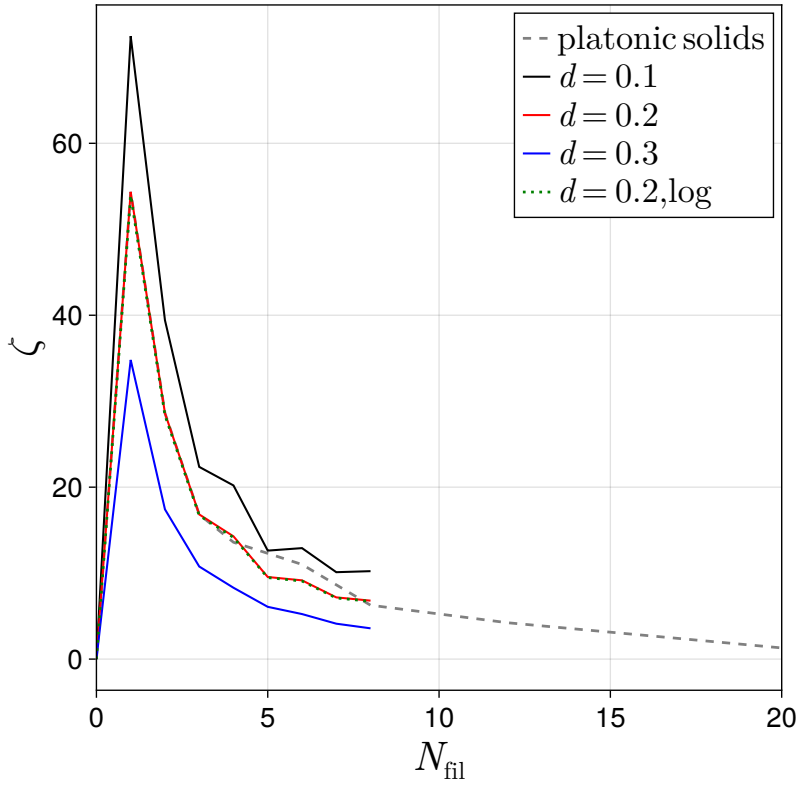


Figure A.5: Dependence of the linear asphericity on the Number and thickness of inflow hotspots in the test setup. The coloured curves from black to blue show the asphericity with increasing hotspot width. j_{fil}/j_{iso} is kept constant at 6/8 and $f_{\mathrm{out}} = 1.0$. The grey curve shows the same asphericity continued by the platonic solid setups (see previous section). Additionally the green dotted line shows the logarithmic asphericity, which is identical to the linear asphericity at $f_{\mathrm{out}} = 1.0$

A.5 Spherical harmonics and filament connectivity

From the value of the asphericity parameters itself, it cannot be conclusively derived how many filaments are feeding a specific system. This raises the question of whether this can be inferred from the full spectrum of a_{lm}. A first order approximation is to use the l mode where the power spectrum of a given map is maximal. Fig. A.6 shows that (blue line) this works for the planar test maps (up to order 7, where the individual spots essentially form a single band, leading to a dipole -like power spectrum). For the platonic solid setups, this simple approach is no longer valid because morphologically these configurations are much more similar to tesseral harmonics with zones at multiple latitudes and longitudes. For tesseral spherical harmonics with $0 < m < l$, the $2m$ meridian zero lines and the $l - m$ parallel isolatitude zero lines (Whittaker & Watson, 2021, e.g.) separate the spherical surface into $2m(l - m + 1)$ zones, half of which correspond to a peak in the flow field. Therefore an estimate of the number of peaks in a given map can be obtained from the l, m of the maximal $|a_{lm}|$ of the decomposition.

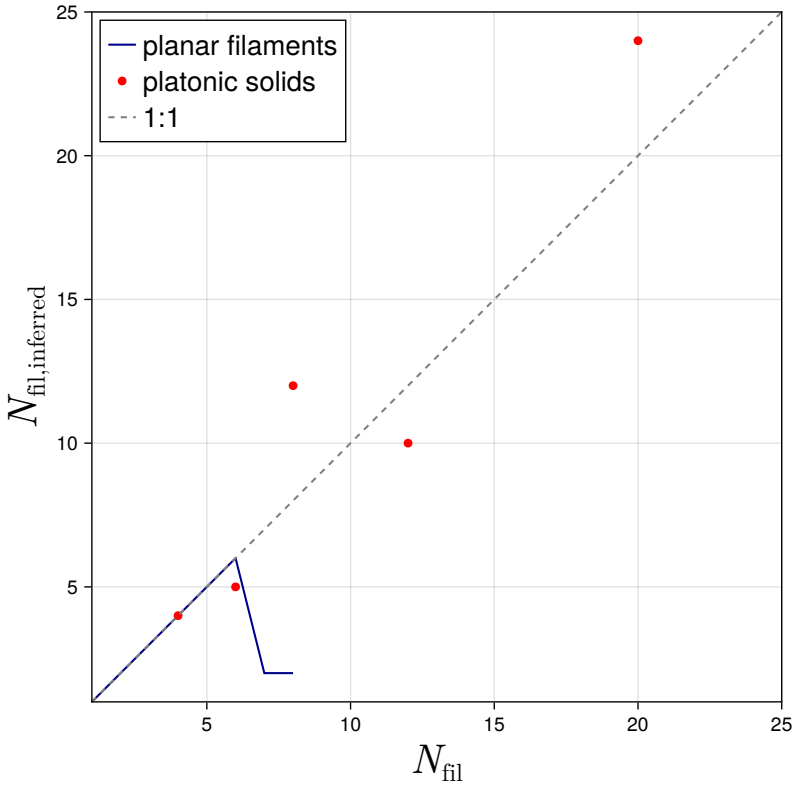


Figure A.6: Power spectra of the whole suite of idealized test cases with 1-8 hotspots.

A.6 Orthogonality of the Spherical Harmonics

Since the spherical harmonics decomposition we perform in this work is computed numerically, it is worthwhile to check how well this approximation holds for the inflow maps from the simulations but even more so the synthetic test map set. A good measure for the convergence of the numerical decomposition is the total power conservation: The spherical harmonics decomposition, similarly to i.e. a Fourier decomposition should obey a Parseval identity:

$$\int f^2 dA \stackrel{!}{=} \sum (2l+1)c_l, \tag{A.1}$$

namely the total power of the function is expected to be conserved in the power spectrum of the decomposition. Effectively this is a measure for the orthonormality of the numerically computed harmonics. Additionally, since the numerical decomposition is computed up to a truncation order l_{max}, which is usually set to 2-3 NSIDE, the power conservation also depends on the completeness of the orthonormal basis. Fig. A.7 shows this scaling for four different map types, two obtained from simulated maps, one synthetic map from Section 5.4.1 and a reference map created by realizing a randomized power spectrum of spherical harmonics. As expected, all maps exhibit a ”safe” region, where the Parseval identity holds well, which contains the truncation order employed throughout this work. After exceeding around 5 NSIDE, the decomposition breaks down as the frequency of the spherical harmonics approaches the sampling frequency of the healpix maps. More interestingly, at the low frequency end, both the simulated inflow maps as well as the synthetic maps show a much faster completeness, reaching identity at much smaller l_{max} than a map with a randomized power spectrum would. Since the synthetic maps scale almost identically to the simulated maps, they can be expected to be a faithful representation of the flow fields, validating the tests performed throughout this work.

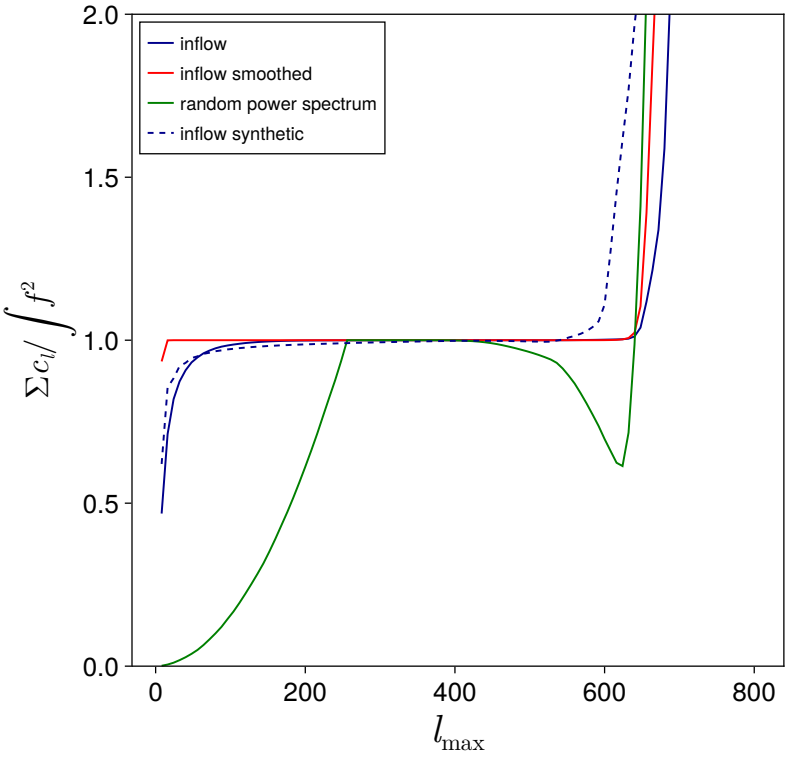


Figure A.7: Scaling of the Parseval Identity for spherical harmonics with the truncation l-mode of the decomposition. Shown is the scaling behaviour for a simulated inflow field (blue), a smoothed simulated field (red), a test map generated from spherical harmonics with randomized coefficients (green) and an example synthetic inflow map from Section 4.2. The pixel resolution of all maps is kept at NSIDE=128.

Appendix B

Superclusters

B.1 Local supercluster members

We present the full list of local supercluster members for reference in Table B.1. The bound members (indicated by the blue shading) make up $\approx 50\%$ of the visually identified members, though this varies from region to region. For Hercules, for example, the whole region is bound to A2147, indicating a very evolved supercluster region. Perseus, on the other hand only has one additional bound substructure. This shows the diversity of the dynamical states these supercluster regions are in at $z = 0$ in the SLOW simulation. Additionally the geometry of most of the cluster arrangements matches the observed structure of the regions quite well, as indicated by the low residual probabilities p. The large-scale constraints of the simulation appear to induce the non-linear collapse of the clusters at the right positions within the supercluster density perturbations.

Cluster/ Group	SG_{sim}			SG_{obs}			M_{200}		L_X		M_{vir}		M_{500}		p
	X	Y	Z	X	Y	Z	Sim	Obs	Sim	Obs	Sim	Obs	Sim	Obs	
Shapley A3558	-141.91	66.10	-37.17	-130.29	78.70	-3.64	13.07	-	13.25	17.4†	17.38	37.10	9.32	4.41 ±0.273	-
A3571	-142.64	54.10	-33.88	-109.39	58.57	4.39	5.93	-	5.45	21.2† ±0.3	7.09	8.76	4.04	4.67 ± 0.21	0.030
A3560	-145.74	60.55	-39.70	-130.96	73.42	-2.58	5.55	-	4.23	4.17† ±0.17	6.88	3.40$^{\flat}$	3.21	-	0.002
A1736	-137.66	65.92	-22.87	-117.47	83.34	-0.73	4.74	-	3.65	8.51† ±0.87	6.68	18.20	3.28	1.63 +0.46 -0.52	0.003
A3559	-134.88	61.53	-24.59	-121.23	78.36	-0.93	2.30	-	0.79	-	3.14	0.2$^{\flat}$	1.57	-	0.04
A3532 (+A3530)	-158.49	89.78	-55.89	-141.76	101.20	-27.98	4.22	-	2.04	0.08† ±0.17	5.28	8.9 ± 4.4	2.68	-	0.000
Perseus A426	59.22	2.13	-24.58	49.94	-10.73	-12.98	8.07	13.66	5.81	37.88	10.63	16.3	5.10	-	-
AWM 7	60.08	-6.71	-23.32	49.90	-13.20	-9.41	0.73	3.72	0.08	4.64	0.90	4.8	0.53	-	0.127
UGC 2562	101.39	-2.36	-27.86	85.97	-19.41	-19.40	0.80	0.45	0.81	0.15	1.15	1.81	0.42	-	0.019
CIZAJ 0300.7 +4427	81.61	-21.57	-39.01	85.13	-17.63	-14.87	1.66	3.70	0.86	4.65	2.09	8.4	1.15	-	0.008
3C129	55.55	11.33	-28.56	56.90	2.82	-24.05	1.82	3.41	0.80	4.07	2.29	7.80‡	0.86	-	0.097
A262	64.51	-12.44	-2.90	42.41	-19.81	-1.60	1.21	2.26	0.75	2.06	1.38	2.82	0.93	-	0.215
NGC507	49.14	-22.50	-32.42	40.34	-23.03	2.24	1.72	1.20	0.35	0.73	2.04	1.10‡	1.27	-	0.194
UGC 3355	95.07	1.84	-55.58	69.62	18.69	-28.81	1.58	1.18	0.47	0.73	2.04	3.32	1.10	-	0.32
Coma A1656	-2.93	82.27	-9.14	0.48	72.79	10.59	15.17	8.53	14.71	17.79	18.60	15.9	9.50	5.29 ± 0.20	-
A1367	-2.89	71.35	-18.73	-2.94	68.62	-12.68	1.67	2.55	0.58	2.53	2.18	5.4	1.08	1.76 ± 0.14	0.106
A1185	24.59	112.10	-27.24	16.31	99.93	-25.16	3.35	1.22	2.49	0.78	4.37	11.8	2.01	1.27 ± 0.19	0.012
MKW4	-27.22	51.95	-16.53	-22.11	57.35	-12.78	0.80	1.32	0.86	0.88	0.90	0.618	0.57	-	0.19
Virgo	-3.60	10.36	-1.64	-3.37	14.71	-0.66	8.3	1.64	7.13	0.88	9.8	6.3 ± 0.9	6.49	4.76 ± 0.55	-
M94 group	5.46	7.51	2.34	1.24	5.08	0.87	0.45	-	0.14		0.52	0.03	0.36	-	0.036
NGC 5846	-20.25	1.19	22.86	-9.16	13.29	10.08	0.13	0.36	0.08	0.05	0.46	0.84	0.23	0.14*	0.152
Centaurus /A3526	-22.82	11.21	-13.26	-34.25	14.93	-7.56	8.58	3.27	10.05	3.76	10.07	10.8	6.17	1.23 ± 0.11	-
NGC 4936	-15.97	11.66	-23.04	-28.37	18.76	-3.56	0.91	0.44	0.33	0.15	1.18	0.23§	0.63	-	0.288
AS0753	-42.15	7.50	6.38	-37.60	18.51	3.53	0.82	0.52	0.65	0.20	1.01	1.65	0.56	-	0.356
A3574E	-35.04	14.30	-23.29	-43.45	25.86	3.00	2.27	0.60	1.12	0.25	2.78	1.93	1.64	0.32*	0.049
Hercules A2147	-77.42	77.33	100.57	-26.06	71.85	86.49	13.02	13.5 +2.1 -1.7	14.44	7.49† ± 0.40	15.3	53.1	9.82	2.51*	0.049
A2151	-77.40	69.12	100.58	-22.47	71.88	87.34	1.65	2.88 +0.31 -0.27	0.80	2.33† ±0.07	1.90	2.88	1.21	1.38*	0.136
A2152	-76.53	79.80	101.63	-27.38	78.01	96.31	0.61	0.74 +0.13 -0.10	0.70	0.64*	0.81	0.72	0.43	0.6*	0.202

Table B.1: Supercluster members and their properties compared to observations. All masses are in units of $10^{14} M_{\odot}$ and X-ray Luminosities are given in units of $10^{43} erg/s/h^2$, measured in the 0.1 to 2.4 keV band if not specified otherwise. The base catalog for these properties are B,B1,M and MO. Where data was incomplete we used (Piffaretti et al., 2011) (*) and (Ikebe et al., 2002) (†) to supplement information. The dynamical masses are obtained from Tully (2015) with supplementary data from Pinzke et al. (2011) (‡), Mendel et al. (2008) (◊), Makarov & Karachentsev (2011) (§), M (♭) and MO (Hercules supercluster). Each subsection of the table lists the most massive or main member first. The blue shading in the names column indicates whether the member is bound to the supercluster core according to the method described by Section 10.3.3. The probabilities (p) in the last column represent the probability that a given supercluster member is identified purely by chance as introduced in Section 10.2.2. The main halos of the regions do not have an associated probability with this method. We refer to Hernández-Martínez et al. (2024) for the significance of these matches. The probability for A2147, the only main halo in this work not identified by Hernández-Martínez et al. (2024) is computed according to the method outlined in that study, see also Section 10.3.1. This is indicated by the violet color.

B.2 The Coma supercluster region

Fig. B.1 shows the very well reproduced Coma region, with Virgo in the foreground.

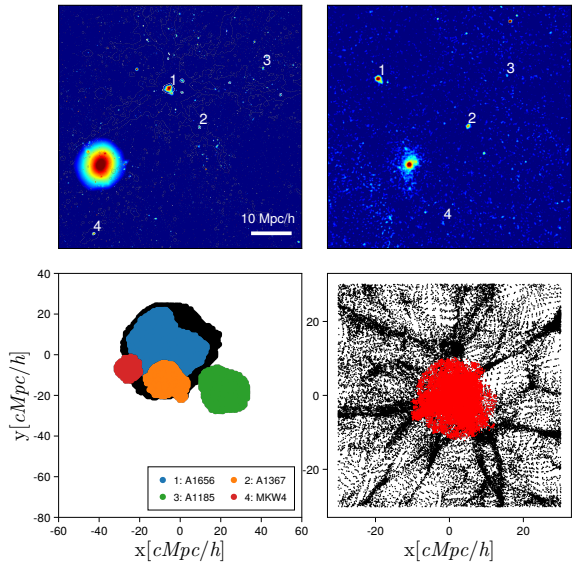


Figure B.1: The Coma supercluster region in the SLOW simulation compared to ROSAT. The gas density for the contours was computed in a spherical shell of 34 Mpc/h thickness centered on the main cluster.

B.3 The Centaurus supercluster region

Fig. B.2 shows the Centaurus region with the Hydra counterpart that does not belong to the supercluster set according to the observations.

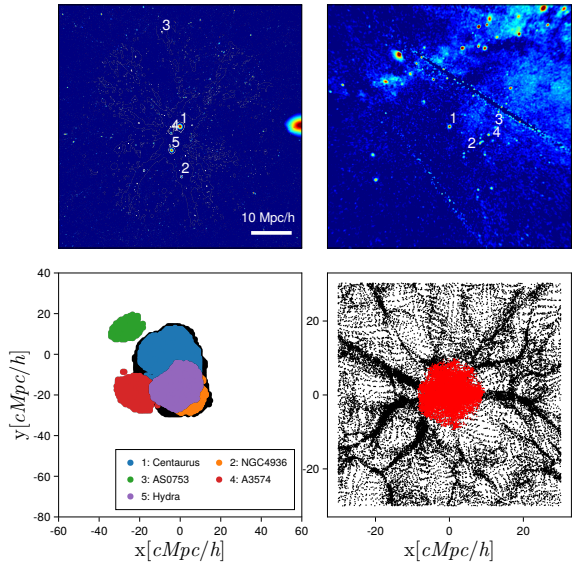


Figure B.2: The Centaurus supercluster region in the SLOW simulation compared to ROSAT. The gas density for the contours was computed in a spherical shell of 20 Mpc/h thickness centered on the main cluster.

B.4 The Local Supercluster

In Fig. B.3 the Virgo supercluster can be seen with a filament connecting Virgo to the M94 group.

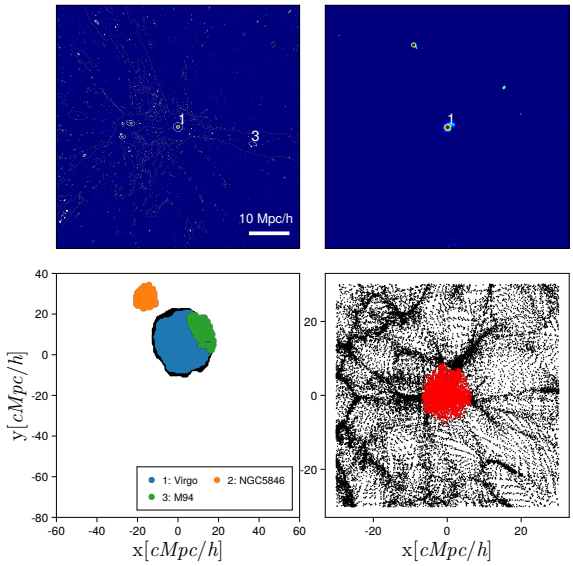


Figure B.3: The Local supercluster region in the SLOW simulation compared to ROSAT. The gas density for the contours was computed in a spherical shell of 27 Mpc/h thickness centered on the main cluster.

B.5 The Hercules Supercluster Region

Fig. B.4 shows A2147 with the two nearby clusters A2151 and A2152, where the gas density contours show the Hercules cluster A2151 to be isolated from the central structure while A2152 is directly connected to it, in agreement with Monteiro-Oliveira et al. (2022). Nevertheless both companion clusters are bound to A2147.

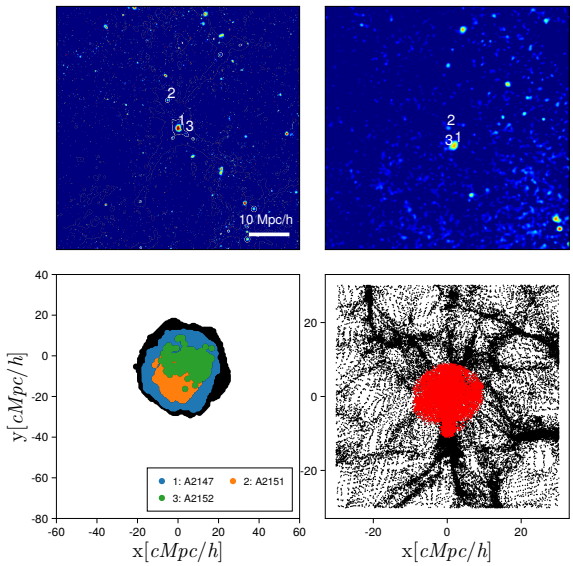


Figure B.4: The Hercules supercluster region in the SLOW simulation compared to ROSAT. The gas density for the contours was computed in a spherical shell of 14 Mpc/h thickness centered on the main cluster.

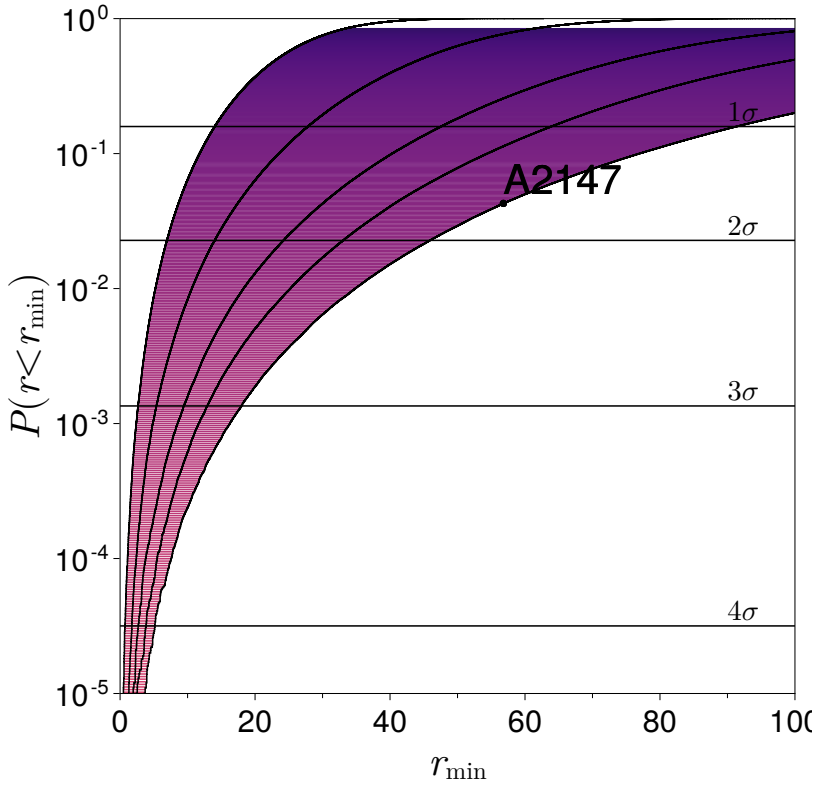


Figure B.5: Match probability of A2147, following Hernández-Martínez et al. (2024)

B.6 A2147

Because A2147, the most massive halo of the Hercules supercluster, does not have a counterpart defined by Hernández-Martínez et al. (2024), we evaluate the match we identify in this work with the method used in that work. The resulting probability cited in Table 10.1 is visualized in Fig. B.5.

B.7 Comparison of geometric significance and one-point significance

Fig. B.6 shows the how the two point significance introduced above changes between the two candidates for A3532. The better relative position of the counterpart in this work gives it a higher significance from the supercluster structure.

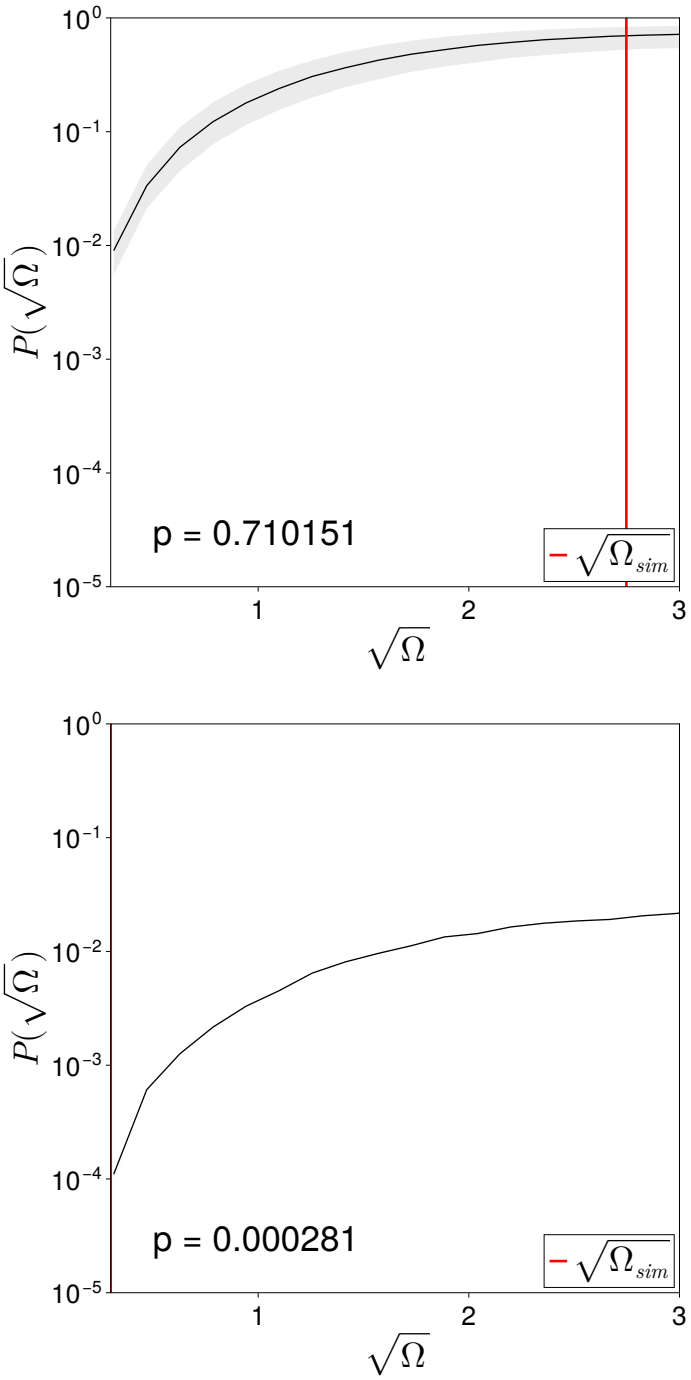


Figure B.6: Two-point probabilities of the match for A3532 as identified by Hernández-Martínez et al. (2024) (left panel) with the one-point approach and in this work taking the supercluster arrangement into account (right panel).

B.8 Selecting from the local halo distribution.

Starting from the main clusters of supercluster regions, which are often well reproduced in their simulation due to their mass and richness, we use the structure of supercluster regions to identify the more unconstrained secondaries. To this end we first take the observed positions of the main and the secondary to match in super-galactic coordinates and calculate r_{obs}, as it is also used in the two-point significance approach described in Section 10.2.2. This gives an indication for the rough relative position of the desired halo, based on which we then select halo candidates and pick the best matches in terms of mass, angular separation and radial separation with regards to the observed relative position. A visualization of this process is shown in Fig. B.7.

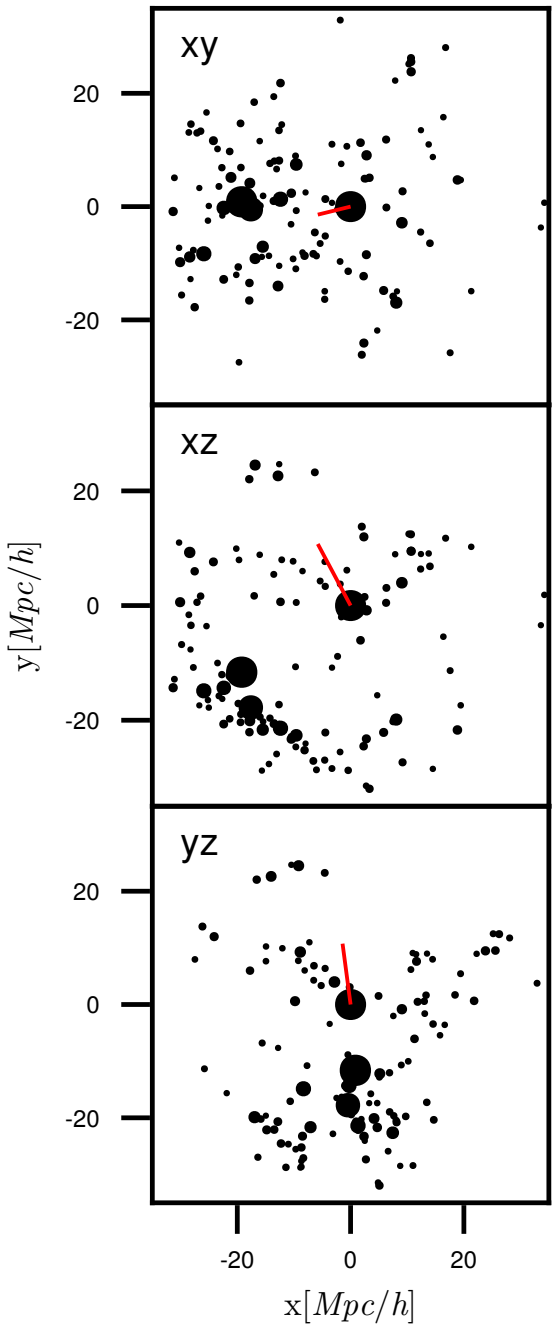


Figure B.7: SLOW halos in the vicinity of the Virgo (center) counterpart in three different projections. The point sizes are scaled with the square root of the virial masses. The red line indicates the vector separating the observed counterpart of the secondary halo to be matched (here NGC5846) and the observed primary (the Virgo cluster).

B.9 Constraint tracer distribution

The SLOW simulation uses galaxy velocities from Cosmicflows-2 to build the constraints. Therefore the degree to which the simulation volume can be considered as ”constrained” depends on the density of observed galaxies, as well as the accuracy of the distance measurement. To demonstrate the limitation (and how the simulation can reproduce structures even where the constraints are already sparse), we bin the number density of Cosmicflows-2

galaxies across our simulation volume and additionally weight these counts with the relative velocity error. Fig. B.8 shows this distribution in the SGX, SGY projection and demonstrates the Shapley supercluster (red contour) to be located in an area with already very low galaxy counts. The good agreement with observations in morphology and member cluster arrangement is therefore likely an indirect result of the velocity field being well-sampled along a filament connecting this structure to the more central regions where the constraint density is much higher.

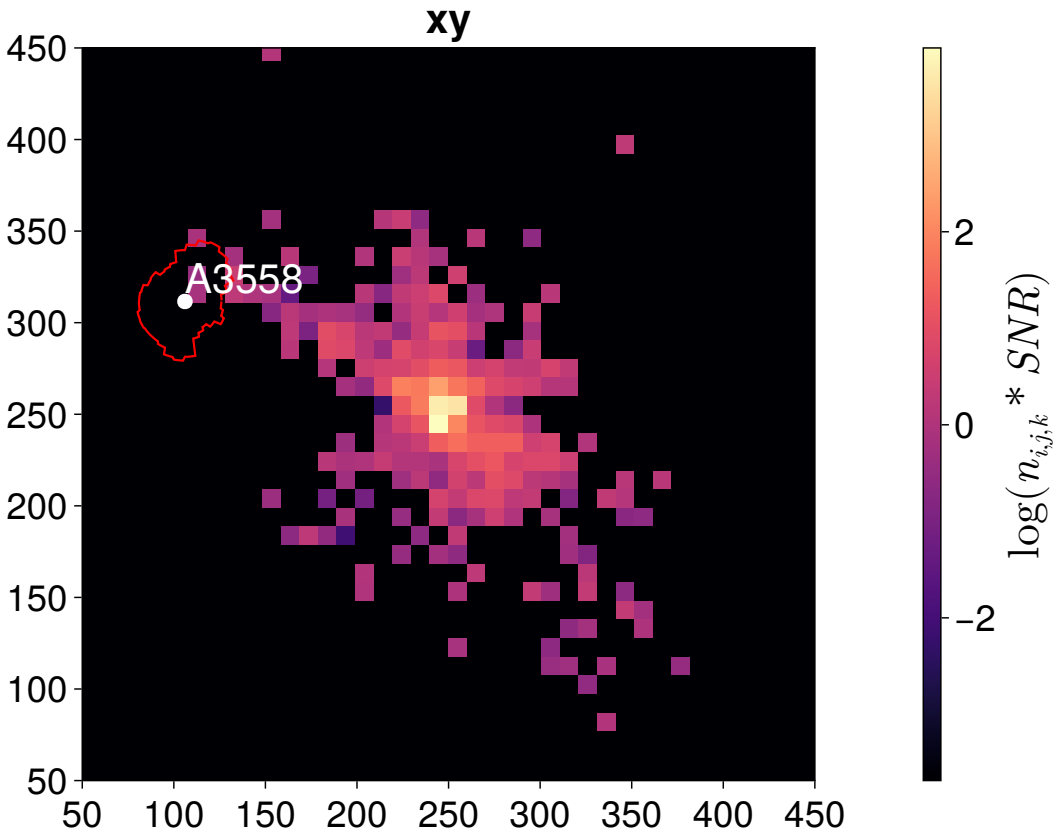


Figure B.8: Weighted counts of galaxy tracers using the signal to noise ratio (velocity amplitude:velocity error) computed from the Cosmicflows-2 database. The red contour shows the region of influence of the Shapley supercluster along with the position of A3558 in white.

Appendix C

Zoom-in Initial Conditions

C.1 The SLOW cluster zoom-IC suite

As mentioned in the main chapter the full SLOW cluster set contains 30 local galaxy clusters in 20 regions. We show the full sample at the final snapshot in Fig. C.1. Consistent with previous figures, the regions can be highly aspherical, nevertheless they remain free of boundary particles out to large distances from the central structure. For the regions containing multiple clusters (e.g. the Shapley supercluster region) it is apparent that, while the overall region is centred on the dominant structure, the secondary clusters stay similarly uncontaminated as they belong to the same basin of influence and can thus be cleanly isolated from the surrounding box.

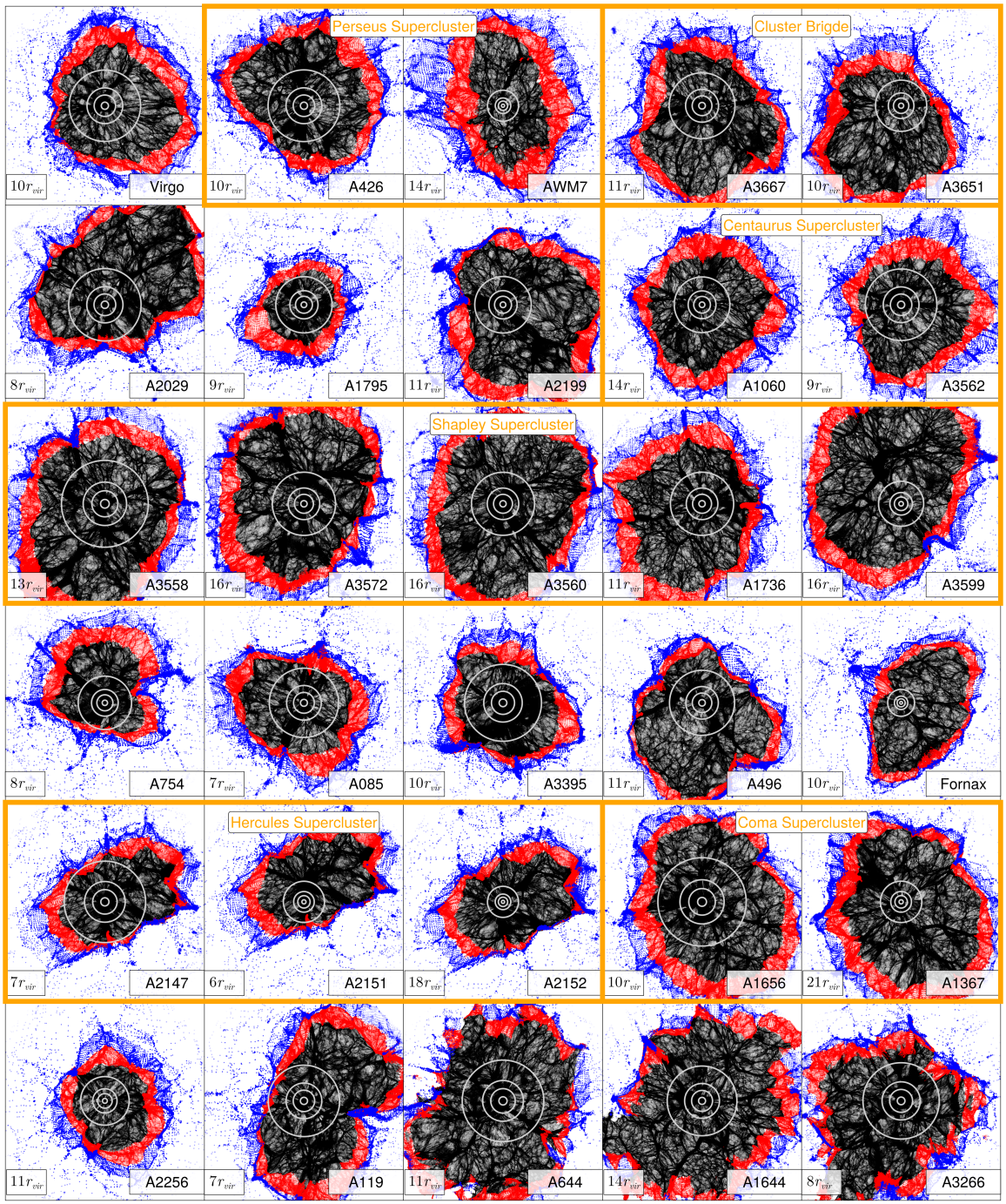


Figure C.1: Thin slice of one cMpc/h through the different galaxy clusters belonging to the first set of the SLOW Cluster selection. Shown is a 100 cMpc/h region with the high-resolution particles scattered in black, the first boundary in red and subsequent outer boundaries in blue with opacity decreasing with increasing distance from the central cluster. The supercluster regions containing multiple clusters are indicated with the orange frames. The gray circles indicate 1,3,5 and 10 times the virial radius of the respective cluster.

References

Abell G. O.: *Evidence Regarding Second-Order Clustering of Galaxies and Interactions between Clusters of Galaxies.* The Astronomical Journal **66**, 607 (1961)

Aghanim N., Tuominen T., Bonjean V., Gouin C., Bonnaire T., & Einasto M.: *Dissecting a Miniature Universe: A Multi-Wavelength View of Galaxy Quenching in the Shapley Supercluster.* A&A **689**, A332 (2024)

Agullo I., Kranas D., & Sreenath V.: *Anomalies in the CMB from a cosmic bounce.* Gen. Rel. Grav. **53**, 17 (2021)

Aharonian F., Akamatsu H., Akimoto F., Allen S. W., Anabuki N., Angelini L., Arnaud K., Audard M., Awaki H., Axelsson M., et al.: *The Quiescent Intracluster Medium in the Core of the Perseus Cluster.* Nature **535**, 117 (2016)

Ahumada R., Allende Prieto C., Almeida A., Anders F., Anderson S. F., Andrews B. H., Anguiano B., Arcodia R., Armengaud E., Aubert M., et al.: *The 16th Data Release of the Sloan Digital Sky Surveys: First Release from the APOGEE-2 Southern Survey and Full Release of eBOSS Spectra.* The Astrophysical Journal Supplement Series **249**, 3 (2020)

Akrami Y., Ashdown M., Aumont J., Baccigalupi C., Ballardini M., Banday A. J., Barreiro R. B., Bartolo N., Basak S., Benabed K., et al.: *Planck 2018 Results - VII. Isotropy and Statistics of the CMB.* Astronomy & Astrophysics **641**, A7 (2020)

Alpaslan M., Grootes M., Marcum P. M., Popescu C., Tuffs R., Bland-Hawthorn J., Brough S., Brown M. J. I., Davies L. J. M., Driver S. P., et al.: *Galaxy And Mass Assembly (GAMA): Stellar Mass Growth of Spiral Galaxies in the Cosmic Web.* Monthly Notices of the Royal Astronomical Society **457**, 2287 (2016)

Andreon S.: *The Stellar Mass Fraction and Baryon Content of Galaxy Clusters and Groups: Stellar Mass Fraction and Baryon Content.* MNRAS **407**, 263 (2010)

Angelinelli M., Ettori S., Dolag K., Vazza F., & Ragagnin A.: *Mapping 'out-of-the-box' the properties of the baryons in massive halos.* A&A **663**, L6 (2022)

Angelinelli M., Ettori S., Dolag K., Vazza F., & Ragagnin A.: *Redshift evolution of the baryon and gas fraction in simulated groups and clusters of galaxies.* A&A **675**, A188 (2023)

Araya-Melo P. A., Reisenegger A., Meza A., van de Weygaert R., Dünner R., & Quintana H.: *Future Evolution of Bound Superclusters in an Accelerating Universe.* MNRAS **399**, 97 (2009)

Arora A., Garavito-Camargo N., Sanderson R. E., Weinberg M. D., Petersen M. S., Varela-Lavin S., Gómez F. A., Johnston K. V., Laporte C. F. P., Shipp N., et al.: *Shaping the Milky Way: The Interplay of Mergers and Cosmic Filaments.* The Astrophysical Journal **988**, 190 (2025)

Arp H. & Russell D.: *A Possible Relationship between Quasars and Clusters ofGalaxies.* The Astrophysical Journal **549**, 802 (2001)

Audard M., Awaki H., Ballhausen R., Bamba A., Behar E., Boissay-Malaquin R., Brenneman L., Brown G. V., Corrales L., Costantini E., et al.: *The Bulk Motion of Gas in the Core of the Centaurus Galaxy Cluster.* Nature **638**, 365 (2025)

Ayromlou M., Nelson D., & Pillepich A.: *Feedback Reshapes the Baryon Distribution within Haloes, in Halo Outskirts, and beyond: The Closure Radius from Dwarfs to Massive Clusters.* Monthly Notices of the Royal Astronomical Society **524**, 5391 (2023)

Ayromlou M., Nelson D., Pillepich A., Rohr E., Truong N., Li Y., Simionescu A., Lehle K., & Lee W.: *An Atlas of Gas Motions in the TNG-Cluster Simulation: From Cluster Cores to the Outskirts.* A&A **690**, A20 (2024)

Baes M., Verstappen J., De Looze I., Fritz J., Saftly W., Vidal Pérez E., Stalevski M., & Valcke S.: *Efficient Three-dimensional NLTE Dust Radiative Transfer with SKIRT.* ApJS **196**, 22 (2011)

Bagla J. S. & Ray S.: *Performance Characteristics of TreePM Codes.* New Astronomy **8**, 665 (2003)

Bagla J. S. & Ray S.: *Comments on the Size of the Simulation Box in Cosmological N-body Simulations.* Mon Not R Astron Soc **358**, 1076 (2005)

Bahé Y. M., Barnes D. J., Dalla Vecchia C., Kay S. T., White S. D. M., McCarthy I. G., Schaye J., Bower R. G., Crain R. A., Theuns T., et al.: *The Hydrangea Simulations: Galaxy Formation in and around Massive Clusters.* **470**, 4186 (2017)

Bahé Y. M., Schaye J., Barnes D. J., Dalla Vecchia C., Kay S. T., Bower R. G., Hoekstra H., McGee S. L., & Theuns T.: *Disruption of Satellite Galaxies in Simulated Groups and Clusters: The Roles of Accretion Time, Baryons, and Pre-Processing.* Monthly Notices of the Royal Astronomical Society **485**, 2287 (2019)

Baldi A.: *The ACCEPT2 Database of Galaxy Clusters: Early Results on Global Properties and Morphology.* In: *15 Years of Science with Chandra.* P8 (2014)

Barnes D. J., Kay S. T., Bahé Y. M., Dalla Vecchia C., McCarthy I. G., Schaye J., Bower R. G., Jenkins A., Thomas P. A., Schaller M., et al.: *The Cluster-EAGLE Project: Global Properties of Simulated Clusters with Resolved Galaxies.* **471**, 1088 (2017)

Barnes J. & Hut P.: *A Hierarchical O(N Log N) Force-Calculation Algorithm.* Nature **324**, 446 (1986)

Bartelmann M., Steinmetz M., & Weiss A.: *Arc statistics with realistic cluster potentials. II. Influence of cluster asymmetry and substructure.* A&A **297**, 1 (1995)

Bartelmann M. & Steinmetz M.: *A Comparison of X-ray and Strong Lensing Properties of Simulated X-ray Clusters.* MNRAS **283**, 431 (1996)

Beck A. M., Murante G., Arth A., Remus R.-S., Teklu A. F., Donnert J. M. F., Planelles S., Beck M. C., Förster P., Imgrund M., et al.: *An Improved SPH Scheme for Cosmological Simulations.* MNRAS **455**, 2110 (2016)

Behroozi P. S., Loeb A., & Wechsler R. H.: *Unbound Particles in Dark Matter Halos.* J. Cosmology Astropart. Phys. **2013**, 019 (2013)

Bell E. F., McIntosh D. H., Katz N., & Weinberg M. D.: *The Optical and Near-Infrared Properties of Galaxies. I.Luminosity and Stellar Mass Functions.* The Astrophysical Journal Supplement Series **149**, 289 (2003)

Bennett C. L., Halpern M., Hinshaw G., Jarosik N., Kogut A., Limon M., Meyer S. S., Page L., Spergel D. N., Tucker G. S., et al.: *First-Year Wilkinson Microwave Anisotropy Probe (WMAP) Observations: Preliminary Maps and Basic Results.* **148**, 1 (2003)

Berta S., Lutz D., Santini P., Wuyts S., Rosario D., Brisbin D., Cooray A., Franceschini A., Gruppioni C., Hatziminaoglou E., et al.: *Panchromatic Spectral Energy Distributions of Herschel Sources.* Astronomy & Astrophysics **551**, A100 (2013)

Bertschinger E.: *Path Integral Methods for Primordial Density Perturbations: Sampling of Constrained Gaussian Random Fields.* The Astrophysical Journal **323**, L103 (1987)

Bianconi M., Smith G. P., Haines C. P., McGee S. L., Finoguenov A., & Egami E.: *LoCuSS: Pre-Processing in Galaxy Groups Falling into Massive Galaxy Clusters at z = 0.2.* Monthly Notices of the Royal Astronomical Society **473**, L79 (2018)

Biffi V., Planelles S., Borgani S., Fabjan D., Rasia E., Murante G., Tornatore L., Dolag K., Granato G. L., Gaspari M., & Beck A. M.: *The history of chemical enrichment in the intracluster medium from cosmological simulations.* MNRAS **468**, 531 (2017)

Biffi V., Planelles S., Borgani S., Rasia E., Murante G., Fabjan D., & Gaspari M.: *The Origin of ICM Enrichment in the Outskirts of Present-Day Galaxy Clusters from Cosmological Hydrodynamical Simulations.* MNRAS **476**, 2689 (2018)

Birnboim Y. & Dekel A.: *Virial Shocks in Galactic Haloes?* MNRAS **345**, 349 (2003)

Bocquet S., Saro A., Dolag K., & Mohr J. J.: *Halo Mass Function: Baryon Impact, Fitting Formulae, and Implications for Cluster Cosmology.* **456**, 2361 (2016)

Boehringer H. & Chon G.: *The Cosmic Large-Scale Structure in X-rays (CLASSIX) Cluster Survey IV: Superclusters in the Local Universe at z <= 0.03.* Astronomy & Astrophysics **656**, A144 (2021)

Boehringer H., Chon G., & Truemper J.: *The Cosmic Large-Scale Structure in X-rays (CLASSIX) Cluster Survey III: The Perseus-Pisces Supercluster and the Southern Great Wall as Traced by X-ray Luminous Galaxy Clusters.* Astronomy & Astrophysics **651**, A16 (2021)

Bogdán Á., Khabibullin I., Kovács O. E., Schellenberger G., ZuHone J., Burchett J. N., Dolag K., Churazov E., Forman W. R., Jones C., et al.: *Circumgalactic Medium on the Largest Scales: Detecting X-Ray Absorption Lines with Large-area Microcalorimeters.* ApJ **953**, 42 (2023)

Bogdán Á., Schellenberger G., Li Q., & Conselice C. J.: *An X-ray-emitting Protocluster at z ≈ 5.7 Reveals Rapid Structure Growth.* Nature **649**, 1134 (2026)

Böhringer H., Chon G., & Collins C. A.: *Observational Evidence for a Local Underdensity in the Universe and Its Effect on the Measurement of the Hubble Constant.* A&A **633**, A19 (2020)

Böhringer H., Chon G., & Trümper J.: *The Cosmic Large-Scale Structure in X-rays (CLASSIX) Cluster Survey - II. Unveiling a Pancake Structure with a 100 Mpc Radius in the Local Universe.* A&A **651**, A15 (2021)

Böhringer H., Chon G., Trümper J., Kraan-Korteweg R. C., & Schartel N.: *Unveiling the largest structures in the nearby Universe: Discovery of the Quipu superstructure.* A&A **695**, A59 (2025)

Bonafede A., Dolag K., Stasyszyn F., Murante G., & Borgani S.: *A Non-Ideal Magnetohydrodynamic Gadget: Simulating Massive Galaxy Clusters.* Monthly Notices of the Royal Astronomical Society **418**, 2234 (2011)

Bond J. R., Szalay A. S., & Turner M. S.: *Formation of Galaxies in a Gravitino-Dominated Universe.* Physical Review Letters **48**, 1636 (1982)

Bond J. R., Cole S., Efstathiou G., & Kaiser N.: *Excursion Set Mass Functions for Hierarchical Gaussian Fluctuations.* ApJ **379**, 440 (1991)

Bond J. R., Kofman L., & Pogosyan D.: *How Filaments of Galaxies Are Woven into the Cosmic Web.* Nature **380**, 603 (1996a)

Bond J. R., Kofman L., & Pogosyan D.: *How Filaments of Galaxies Are Woven into the Cosmic Web.* Nature **380**, 603 (1996b)

Bondi H. & Hoyle F.: *On the Mechanism of Accretion by Stars.* Monthly Notices of the Royal Astronomical Society **104**, 273 (1944)

Bondi H.: *On Spherically Symmetrical Accretion.* Monthly Notices of the Royal Astronomical Society **112**, 195 (1952)

Bonjean V., Aghanim N., Salomé P., Douspis M., & Beelen A.: *Gas and Galaxies in Filaments between Clusters of Galaxies. The Study of A399-A401.* Astronomy and Astrophysics **609**, A49 (2018)

Borgani S., Murante G., Springel V., Diaferio A., Dolag K., Moscardini L., Tormen G., Tornatore L., & Tozzi P.: *X-ray properties of galaxy clusters and groups from a cosmological hydrodynamical simulation.* MNRAS **348**, 1078 (2004)

Borgani S., Dolag K., Murante G., Cheng L.-M., Springel V., Diaferio A., Moscardini L., Tormen G., Tornatore L., & Tozzi P.: *Hot and cooled baryons in smoothed particle hydrodynamic simulations of galaxy clusters: physics and numerics.* MNRAS **367**, 1641 (2006)

Bouché N., Dekel A., Genzel R., Genel S., Cresci G., Förster Schreiber N. M., Shapiro K. L., Davies R. I., & Tacconi L.: *THE IMPACT OF COLD GAS ACCRETION ABOVE A MASS FLOOR ON GALAXY SCALING RELATIONS.* The Astrophysical Journal **718**, 1001 (2010)

Bournaud F., Jog C. J., & Combes F.: *Multiple Minor Mergers: Formation of Elliptical Galaxies and Constraints for the Growth of Spiral Disks.* Astronomy & Astrophysics **476**, 1179 (2007)

Brooks A. M., Governato F., Quinn T., Brook C. B., & Wadsley J.: *THE ROLE OF COLD FLOWS IN THE ASSEMBLY OF GALAXY DISKS.* The Astrophysical Journal **694**, 396 (2009)

Brooks A. M., Kuhlen M., Zolotov A., & Hooper D.: *A BARYONIC SOLUTION TO THE MISSING SATELLITES PROBLEM.* The Astrophysical Journal **765**, 22 (2013)

Bryan G. L. & Norman M. L.: *Statistical Properties of X-Ray Clusters: Analytic and Numerical Comparisons.* The Astrophysical Journal **495**, 80 (1998)

Buchert T.: *Lagrangian Perturbation Theory - A Key-Model for Large-Scale Structure.* Astronomy and Astrophysics **267**, L51 (1993a)

Buchert T.: *Higher-Order Lagrangian Perturbation Theory.* arXiv preprint, 10.48550/arXiv.astro-ph/9403023 (1993b)

Bulichi T.-E., Davé R., & Kraljic K.: *How Galaxy Properties Vary with Filament Proximity in the SIMBA Simulations.* Monthly Notices of the Royal Astronomical Society **529**, 2595 (2024)

Bullock J. S. & Boylan-Kolchin M.: *Small-Scale Challenges to the ΛCDM Paradigm.* Annual Review of Astronomy and Astrophysics **55**, 343 (2017)

Bundy K., Ellis R. S., & Conselice C. J.: *The Mass Assembly Histories of Galaxies of Various Morphologies in the GOODS Fields.* The Astrophysical Journal **625**, 621 (2005)

Burchett J. N., Chaturvedi A., Holguin Luna P., Maddox N., Nagai D., Putman M. E., Serra P., Tonnesen S., Tripp T. M., & Wang Q. D.: *A Comprehensive Survey of Diffuse Gas in the Fornax Cluster.* HST Proposal, 17478 (2023)

Burkert A.: *A Bathtub Model for the Star-Forming Interstellar Medium.* arXiv pre-print 10.48550/arXiv.1709.02112 **88** (2017)

Busha M. T., Adams F. C., Wechsler R. H., & Evrard A. E.: *Future Evolution of Cosmic Structure in an Accelerating Universe.* ApJ **596**, 713 (2003)

Butterworth S.: *On the Theory of Filter Amplifiers.* Experimental Wireless & the Wireless Engineer **7**, 536 (1930)

Byrnes C. T. & Tarrant E. R. M.: *Scale-dependent non-Gaussianity and the CMB Power Asymmetry.* JCAP **07**, 007 (2015)

Carnall A. C., Walker S., McLure R. J., Dunlop J. S., McLeod D. J., Cullen F., Wild V., Amorin R., Bolzonella M., Castellano M., et al.: *Timing the Earliest Quenching Events with a Robust Sample of Massive Quiescent Galaxies at $2 < z < 5$.* Monthly Notices of the Royal Astronomical Society **496**, 695 (2020)

Carnall A. C., McLeod D. J., McLure R. J., Dunlop J. S., Begley R., Cullen F., Donnan C. T., Hamadouche M. L., Jewell S. M., Jones E. W., et al.: *A Surprising Abundance of Massive Quiescent Galaxies at $3 < z < 5$ in the First Data from JWST CEERS.* Monthly Notices of the Royal Astronomical Society **520**, 3974 (2023)

Carroll S. M., Press W. H., & Turner E. L.: *The Cosmological Constant.* A&A Rev. **30**, 499 (1992)

Castignani G., Vulcani B., Finn R. A., Combes F., Jablonka P., Rudnick G., Zaritsky D., Whalen K., Conger K., Lucia G. D., et al.: *Virgo Filaments. II. Catalog and First Results on the Effect of Filaments on Galaxy Properties.* ApJS **259**, 43 (2022)

Cautun M., van de Weygaert R., & Jones B. J. T.: *NEXUS: Tracing the Cosmic Web Connection.* Monthly Notices of the Royal Astronomical Society **429**, 1286 (2013)

Cautun M., van de Weygaert R., Jones B. J. T., & Frenk C. S.: *Evolution of the Cosmic Web.* Monthly Notices of the Royal Astronomical Society **441**, 2923 (2014)

Cautun M., Benítez-Llambay A., Deason A. J., Frenk C. S., Fattahi A., Gómez F. A., Grand R. J. J., Oman K. A., Navarro J. F., & Simpson C. M.: *The Milky Way Total Mass Profile as Inferred from Gaia DR2.* Monthly Notices of the Royal Astronomical Society **494**, 4291 (2020)

Cavagnolo K. W., Donahue M., Voit G. M., & Sun M.: *An Entropy Threshold for Strong Hα and Radio Emission in the Cores of Galaxy Clusters.* The Astrophysical Journal **683**, L107 (2008)

Cavagnolo K. W., Donahue M., Voit G. M., & Sun M.: *Intracluster Medium Entropy Profiles for a Chandra Archival Sample of Galaxy Clusters.* The Astrophysical Journal Supplement Series **182**, 12 (2009)

Cavaliere A. & Fusco-Femiano R.: *X-Rays from Hot Plasma in Clusters of Galaxies.* Astronomy and Astrophysics **49**, 137 (1976)

Cavaliere A. & Lapi A.: *Probing the Evolution of Galaxy Clusters with the SZ Effect.* A&A **571**, A84 (2014)

Chabrier G.: *Galactic Stellar and Substellar Initial Mass Function.* Publications of the Astronomical Society of the Pacific **115**, 763 (2003)

Chen S., Wang H., Mo H. J., & Shi J.: *ALIGNMENTS OF DARK MATTER HALOS WITH LARGE-SCALE TIDAL FIELDS: MASS AND REDSHIFT DEPENDENCE.* The Astrophysical Journal **825**, 49 (2016)

Chon G., Boehringer H., & Zaroubi S.: *On the Definition of Superclusters.* Astronomy & Astrophysics **575**, L14 (2015)

Chung A., van Gorkom J. H., Kenney J. D. P., & Vollmer B.: *Virgo Galaxies with Long One-sided H I Tails.* The Astrophysical Journal **659**, L115 (2007)

Churazov E., Forman W., Jones C., & Böhringer H.: *XMM-Newton Observations of the Perseus Cluster. I. The Temperature and Surface Brightness Structure.* The Astrophysical Journal **590**, 225 (2003)

Churazov E., Khabibullin I. I., Dolag K., Lyskova N., & Sunyaev R. A.: *Prospects of Detecting Soft X-ray Emission from Typical WHIM Filaments around Massive Clusters and the Coma Cluster Soft Excess.* MNRAS **523**, 1209 (2023)

Churazov E., Khabibullin I. I., Lyskova N., Sunyaev R. A., & Dolag K.: *Perseus Cluster in Its X-ray Entirety with SRG/eROSITA - Merger and Radio-Uroboroses.* Astronomy & Astrophysics **707**, A381 (2026)

Chworowsky K., Finkelstein S. L., Spilker J. S., Leung G. C. K., Bagley M. B., Casey C. M., Gronwall C., Jogee S., Larson R. L., Papovich C., et al.: *ALMA 1.1 Mm Observations of a Conservative Sample of High-redshift Massive Quiescent Galaxies in SHELA.* The Astrophysical Journal **951**, 49 (2023)

Clemens M. S., Bressan A., Nikolic B., & Rampazzo R.: *The History of Star Formation and Mass Assembly in Early-Type Galaxies.* Monthly Notices of the Royal Astronomical Society **392**, L35 (2009)

Copi C. J., Huterer D., Schwarz D. J., & Starkman G. D.: *Lack of large-angle TT correlations persists in WMAP and Planck.* MNRAS **451**, 2978 (2015)

Cornwell D. J., Aragón-Salamanca A., Kuchner U., Gray M. E., Pearce F. R., & Knebe A.: *The Probability of Identifying the Cosmic Web Environment of Galaxies around Clusters Motivated by the Weave Wide Field Cluster Survey.* Monthly Notices of the Royal Astronomical Society **524**, 2148 (2023)

Courtois H. M., Pomarède D., Tully R. B., Hoffman Y., & Courtois D.: *COSMOGRAPHY OF THE LOCAL UNIVERSE.* The Astronomical Journal **146**, 69 (2013)

Cowie L. L. & McKee C. F.: *The Evaporation of Spherical Clouds in a Hot Gas. I. Classical and Saturated Mass Loss Rates.* The Astrophysical Journal **211**, 135 (1977)

Croton D. J., Springel V., White S. D. M., De Lucia G., Frenk C. S., Gao L., Jenkins A., Kauffmann G., Navarro J. F., & Yoshida N.: *The Many Lives of Active Galactic Nuclei: Cooling Flows, Black Holes and the Luminosities and Colours of Galaxies.* Monthly Notices of the Royal Astronomical Society **365**, 11 (2006)

Cruz M., Martínez-González E., Vielva P., & Cayón L.: *Detection of a non-Gaussian spot in WMAP.* MNRAS **356**, 29 (2005)

Cui W., Knebe A., Yepes G., Pearce F., Power C., Dave R., Arth A., Borgani S., Dolag K., Elahi P., et al.: *The Three Hundred Project: A Large Catalogue of Theoretically Modelled Galaxy Clusters for Cosmological and Astrophysical Applications.* Monthly Notices of the Royal Astronomical Society **480**, 2898 (2018)

Cui W., Dave R., Knebe A., Rasia E., Gray M., Pearce F., Power C., Yepes G., Anbajagane D., Ceverino D., et al.: *THE THREE HUNDRED project: The GIZMO-SIMBA run.* MNRAS **514**, 977 (2022)

Damiano A., Valentini M., Borgani S., Tornatore L., Murante G., Ragagnin A., Ragone-Figueroa C., & Dolag K.: *Dynamical Friction and the Evolution of Black Holes in Cosmological Simulations: A New Implementation in OpenGadget3.* Astronomy & Astrophysics **692**, A81 (2024)

Davé R., Finlator K., & Oppenheimer B. D.: *An Analytic Model for the Evolution of the Stellar, Gas and Metal Content of Galaxies.* Monthly Notices of the Royal Astronomical Society **421**, 98 (2012)

Davé R., Anglés-Alcázar D., Narayanan D., Li Q., Rafieferantsoa M. H., & Appleby S.: *Simba: Cosmological Simulations with Black Hole Growth and Feedback.* Monthly Notices of the Royal Astronomical Society **486**, 2827 (2019)

Davis S. W. & Laor A.: *The Radiative Efficiency of Accretion Flows in Individual Active Galactic Nuclei.* The Astrophysical Journal **728**, 98 (2011)

de Blok W. J. G., Walter F., Ferguson A. M. N., Bernard E. J., van der Hulst J. M., Neeleman M., Leroy A. K., Ott J., Zschaechner L. K., Zwaan M. A., et al.: *A High-resolution Mosaic of the Neutral Hydrogen in the M81 Triplet.* The Astrophysical Journal **865**, 26 (2018)

De Luca F., De Petris M., Yepes G., Cui W., Knebe A., & Rasia E.: *The Three Hundred Project: Dynamical State of Galaxy Clusters and Morphology from Multiwavelength Synthetic Maps.* Monthly Notices of the Royal Astronomical Society **504**, 5383 (2021)

de Oliveira-Costa A., Tegmark M., Zaldarriaga M., & Hamilton A.: *Significance of the Largest Scale CMB Fluctuations in WMAP.* Physical Review D **69**, 063516 (2004)

de Plaa J., Werner N., Bleeker J. A. M., Vink J., Kaastra J. S., & Méndez M.: *Constraining Supernova Models Using the Hot Gas in Clusters of Galaxies.* A&A **465**, 345 (2007)

de Sitter W.: *On the Relativity of Inertia. Remarks Concerning Einstein's Latest Hypothesis.* Koninklijke Nederlandse Akademie van Wetenschappen Proceedings Series B Physical Sciences **19**, 1217 (1917)

Dehnen W. & Aly H.: *Improving Convergence in Smoothed Particle Hydrodynamics Simulations without Pairing Instability.* Monthly Notices of the Royal Astronomical Society **425**, 1068 (2012)

Dekel A. & Birnboim Y.: *Galaxy Bimodality Due to Cold Flows and Shock Heating.* MNRAS **368**, 2 (2006)

Dekel A., Birnboim Y., Engel G., Freundlich J., Goerdt T., Mumcuoglu M., Neistein E., Pichon C., Teyssier R., & Zinger E.: *Cold Streams in Early Massive Hot Haloes as the Main Mode of Galaxy Formation.* Nature **457**, 451 (2009)

Dekel A., Zolotov A., Tweed D., Cacciato M., Ceverino D., & Primack J. R.: *Toy Models for Galaxy Formation versus Simulations.* MNRAS **435**, 999 (2013)

DESI Collaboration, Karim M. A., Adame A. G., Aguado D., Aguilar J., Ahlen S., Alam S., Aldering G., Alexander D. M., Alfarsy R., et al.: *Data Release 1 of the Dark Energy Spectroscopic Instrument.* arXiv preprint, 10.48550/arXiv.2503.14745 (2026)

Dietl J., Pacaud F., Reiprich T. H., Veronica A., Migkas K., Spinelli C., Dolag K., & Seidel B.: *Discovery of a > 13 Mpc Long X-ray Filament between Two Galaxy Clusters beyond Three Times Their Virial Radii.* A&A **691**, A286 (2024)

Ding Y., Zhu L., van de Ven G., Coccato L., Corsini E. M., Costantin L., Fahrion K., Falcón-Barroso J., Gadotti D. A., Iodice E., et al.: *The Fornax3D Project: Environmental Effects on the Assembly of Dynamically Cold Disks in Fornax Cluster Galaxies.* arXiv preprint, 10.48550/arXiv.2301.05532 (2023)

Dolag K., Bartelmann M., & Lesch H.: *SPH simulations of magnetic fields in galaxy clusters.* A&A **348**, 351 (1999)

Dolag K. & Schindler S.: *The effect of magnetic fields on the mass determination of clusters of galaxies.* A&A **364**, 491 (2000)

Dolag K., Bartelmann M., Perrotta F., Baccigalupi C., Moscardini L., Meneghetti M., & Tormen G.: *Numerical study of halo concentrations in dark-energy cosmologies.* A&A **416**, 853 (2004)

Dolag K., Jubelgas M., Springel V., Borgani S., & Rasia E.: *Thermal Conduction in Simulated Galaxy Clusters.* ApJ **606**, L97 (2004)

Dolag K., Grasso D., Springel V., & Tkachev I.: *Constrained Simulations of the Magnetic Field in the Local Universe and the Propagation of Ultrahigh Energy Cosmic Rays.* J. Cosmology Astropart. Phys. **2005**, 009 (2005a)

Dolag K., Hansen F. K., Roncarelli M., & Moscardini L.: *The Imprints of Local Superclusters on the Sunyaev-Zel'dovich Signals and Their Detectability with Planck.* Monthly Notices of the Royal Astronomical Society **363**, 29 (2005b)

Dolag K., Vazza F., Brunetti G., & Tormen G.: *Turbulent Gas Motions in Galaxy Cluster Simulations: The Role of Smoothed Particle Hydrodynamics Viscosity.* MNRAS **364**, 753 (2005c)

Dolag K., Reinecke M., Gheller C., & Imboden S.: *Splotch: Visualizing Cosmological Simulations.* New Journal of Physics **10**, 125006 (2008)

Dolag K., Borgani S., Murante G., & Springel V.: *Substructures in Hydrodynamical Cluster Simulations.* Monthly Notices of the Royal Astronomical Society **399**, 497 (2009)

Dolag K., Murante G., & Borgani S.: *Dynamical Difference between the cD Galaxy and the Diffuse, Stellar Component in Simulated Galaxy Clusters.* **405**, 1544 (2010)

Dolag K., Mevius E., & Remus R.-S.: *Distribution and Evolution of Metals in the Magneticum Simulations.* Galaxies **5**, 35 (2017)

Dolag K., Sorce J. G., Pilipenko S., Hernández-Martínez E., Valentini M., Gottlöber S., Aghanim N., & Khabibullin I.: *Simulating the LOcal Web (SLOW) - I. Anomalies in the Local Density Field.* Astronomy & Astrophysics **677**, A169 (2023)

Dolag K., Remus R.-S., Valenzuela L. M., Kimmig L. C., Seidel B., Fortune S., Stoiber J., Ivleva A., Hoffmann T., Biffi V., et al.: *Encyclopedia Magneticum: Scaling Relations from Cosmic Dawn to Present Day.* arXiv preprint, 10.48550/arXiv.2504.01061 (2025)

Doumler T., Hoffman Y., Courtois H., & Gottlöber S.: *Reconstructing Cosmological Initial Conditions from Galaxy Peculiar Velocities – I. Reverse Zeldovich Approximation.* MNRAS **430**, 888 (2013)

Drinkwater M. J., Gregg M. D., & Colless M.: *Substructure and Dynamics of the Fornax Cluster.* The Astrophysical Journal **548**, L139 (2001)

Duffy L. D. & van Bibber K.: *Axions as Dark Matter Particles.* New Journal of Physics **11**, 105008 (2009)

Duncan K., Conselice C. J., Mortlock A., Hartley W. G., Guo Y., Ferguson H. C., Davé R., Lu Y., Ownsworth J., Ashby M. L. N., et al.: *The Mass Evolution of the First Galaxies: Stellar Mass Functions and Star Formation Rates at $4 < z < 7$ in the CANDELS GOODS-South Field.* Monthly Notices of the Royal Astronomical Society **444**, 2960 (2014)

Dünner R., Araya P. A., Meza A., & Reisenegger A.: *The Limits of Bound Structures in the Accelerating Universe.* Monthly Notices of the Royal Astronomical Society **366**, 803 (2006)

Dupuy A., Courtois H. M., Dupont F., Denis F., Graziani R., Copin Y., Pomarède D., Libeskind N., Carlesi E., Tully B., & Guinet D.: *Partitioning the Universe into Gravitational Basins Using the Cosmic Velocity Field.* Monthly Notices of the Royal Astronomical Society: Letters **489**, L1 (2019)

Ebert R.: *Über Die Verdichtung von H I-Gebieten. Mit 5 Textabbildungen.* Zeitschrift fur Astrophysik **37**, 217 (1955)

Einasto J., Joeveer M., & Saar E.: *Structure of Superclusters and Supercluster Formation.* MNRAS **193**, 353 (1980)

Einasto J. & Miller R. H.: *Neighboring Superclusters and Their Environs.* 405 (1983)

Einasto J., Einasto M., Saar E., Tago E., Liivamägi L. J., Jõeveer M., Suhhonenko I., Hütsi G., Jaaniste J., Heinämäki P., et al.: *Superclusters of Galaxies from the 2dF Redshift Survey - II. Comparison with Simulations.* A&A **462**, 397 (2007a)

Einasto J., Suhhonenko I., Liivamägi L. J., & Einasto M.: *Extended Percolation Analysis of the Cosmic Web.* Astronomy & Astrophysics **616**, A141 (2018)

Einasto J., Suhhonenko I., Liivamägi L. J., & Einasto M.: *Evolution of Superclusters in the Cosmic Web.* Astronomy & Astrophysics **623**, A97 (2019)

Einasto M., Saar E., Liivamägi L. J., Einasto J., Tago E., Martínez V. J., Starck J.-L., Müller V., Heinämäki P., Nurmi P., et al.: *The Richest Superclusters - I. Morphology.* A&A **476**, 697 (2007b)

Einstein A.: *Die Grundlage Der Allgemeinen Relativitätstheorie.* Annalen der Physik **354**, 769 (1916)

Einstein A.: *Kosmologische Betrachtungen Zur Allgemeinen Relativitätstheorie.* Sitzungsberichte der Königlich Preussischen Akademie der Wissenschaften, 142 (1917)

Eke V. R., Cole S., & Frenk C. S.: *Cluster Evolution as a Diagnostic for Ω.* Monthly Notices of the Royal Astronomical Society **282**, 263 (1996)

Eke V. R., Navarro J. F., & Frenk C. S.: *The Evolution of X-Ray Clusters in a Low-Density Universe.* ApJ **503**, 569 (1998)

Eriksen H. K., Hansen F. K., Banday A. J., Gorski K. M., & Lilje P. B.: *Asymmetries in the Cosmic Microwave Background anisotropy field.* Astrophys. J. **605**, 14 (2004)

Ettori S.: *β-Model and Cooling Flows in X-ray Clusters of Galaxies.* Monthly Notices of the Royal Astronomical Society **318**, 1041 (2000)

Ettori S. & Eckert D.: *Tracing the Non-Thermal Pressure and Hydrostatic Bias in Galaxy Clusters.* Astronomy & Astrophysics **657**, L1 (2022)

Euclid Collaboration, Laigle C., Gouin C., Sarron F., Quilley L., Pichon C., Kraljic K., Durret F., Chisari N. E., Kuchner U., et al.: *Euclid Quick Data Release (Q1). Galaxy Shapes and Alignments in the Cosmic Web.* arXiv preprint, 10.48550/arXiv.2503.15333 (2025a)

Euclid Collaboration, Zalesky L., Weaver J. R., McPartland C. J. R., Murphree G., Valdes I., Jespersen C. K., Taamoli S., Chartab N., Allen N., et al.: *Euclid Preparation: TBD. Cosmic Dawn Survey: Evolution of the Galaxy Stellar Mass Function across 0.2.* arXiv preprint, 10.48550/arXiv.2504.17867 (2025b)

Fabian A. C.: *Cooling Flows in Clusters of Galaxies.* Annual Review of Astronomy and Astrophysics **32**, 277 (1994)

Fabjan D., Borgani S., Tornatore L., Saro A., Murante G., & Dolag K.: *Simulating the Effect of Active Galactic Nuclei Feedback on the Metal Enrichment of Galaxy Clusters.* MNRAS **401**, 1670 (2010)

Fabjan D., Borgani S., Rasia E., Bonafede A., Dolag K., Murante G., & Tornatore L.: *X-ray mass proxies from hydrodynamic simulations of galaxy clusters - I.* MNRAS **416**, 801 (2011)

Ferland G. J., Korista K. T., Verner D. A., Ferguson J. W., Kingdon J. B., & Verner E. M.: *CLOUDY 90: Numerical Simulation of Plasmas and Their Spectra.* Publications of the Astronomical Society of the Pacific **110**, 761 (1998)

Fixsen D. J.: *The Temperature of the Cosmic Microwave Background.* **707**, 916 (2009)

Fortuné S., Remus R.-S., Kimmig L. C., Burkert A., & Dolag K.: *Die Hard: The on-off Cycle of Galaxies on the Star Formation Main Sequence.* Astronomy & Astrophysics **704**, A185 (2025)

Frenk C. S., Evrard A. E., White S. D. M., & Summers F. J.: *Galaxy Dynamics in Clusters.* ApJ **472**, 460 (1996)

Friedmann A.: *Über Die Krümmung Des Raumes.* Zeitschrift fur Physik **10**, 377 (1922)

Friedmann A.: *Über die Möglichkeit einer Welt mit konstanter negativer Krümmung des Raumes.* Zeitschrift für Physik **21**, 326 (1924)

Gaite J.: *The Fractal Geometry of the Cosmic Web and Its Formation.* Advances in Astronomy **2019**, e6587138 (2019)

Galárraga-Espinosa D., Aghanim N., Langer M., & Tanimura H.: *Properties of Gas Phases around Cosmic Filaments at* z = *0 in the IllustrisTNG Simulation.* Astronomy & Astrophysics **649**, A117 (2021)

Galárraga-Espinosa D., Garaldi E., & Kauffmann G.: *Flows around Galaxies - I. The Dependence of Galaxy Connectivity on Cosmic Environments and Effects on the Star Formation Rate.* A&A **671**, A160 (2023)

Galárraga-Espinosa D., Cadiou C., Gouin C., White S. D. M., Springel V., Pakmor R., Hadzhiyska B., Bose S., Ferlito F., Hernquist L., et al.: *Evolution of Cosmic Filaments in the MTNG Simulation.* Astronomy & Astrophysics **684**, A63 (2024)

Gatkine P., Veilleux S., & Cucchiara A.: *The CGM–GRB Study. I. Uncovering the Circumgalactic Medium around GRB Hosts at Redshifts 2–6.* ApJ **884**, 66 (2019)

Gatuzz E., Mohapatra R., Federrath C., Sanders J. S., Liu A., Walker S. A., & Pinto C.: *Measuring the Hot ICM Velocity Structure Function Using XMM–Newton Observations.* MNRAS **524**, 2945 (2023)

González-García A. C. & Balcells M.: *Elliptical Galaxies from Mergers of Discs.* Monthly Notices of the Royal Astronomical Society **357**, 753 (2005)

Gorski K. M., Hivon E., Banday A. J., Wandelt B. D., Hansen F. K., Reinecke M., & Bartelmann M.: *HEALPix: A Framework for High-Resolution Discretization and Fast Analysis of Data Distributed on the Sphere.* ApJ **622**, 759 (2005)

Gott R. J. I., Jurić M., Schlegel D., Hoyle F., Vogeley M., Tegmark M., Bahcall N., & Brinkmann J.: *A Map of the Universe.* ApJ **624**, 463 (2005)

Gouin C., Bonnaire T., & Aghanim N.: *Shape and Connectivity of Groups and Clusters: Effect of the Dynamical State and Accretion History.* Astronomy & Astrophysics **651**, A56 (2021)

Gouin C., Gallo S., & Aghanim N.: *Gas Distribution from Clusters to Filaments in IllustrisTNG.* A&A **664**, A198 (2022)

Gould K. M. L., Brammer G., Valentino F., Whitaker K. E., Weaver John. R., Lagos C. d. P., Rizzo F., Franco M., Hsieh B.-C., Ilbert O., et al.: *COSMOS2020: Exploring the Dawn of Quenching for Massive Galaxies at 3 < z < 5 with a New Color-selection Method.* The Astronomical Journal **165** (2023)

Groth F., Steinwandel U. P., Valentini M., & Dolag K.: *The Cosmological Simulation Code OpenGadget3 – Implementation of Meshless Finite Mass.* MNRAS **526**, 616 (2023)

Groth F., Valentini M., Steinwandel U. P., Vallés-Pérez D., & Dolag K.: *Turbulent Pressure Support in Galaxy Clusters - Impact of the Hydrodynamical Solver.* Astronomy & Astrophysics **693**, A263 (2025)

Groth F., Valentini M., Seidel B. A., Vladutescu-Zopp S., Biffi V., Dolag K., & Sorce J. G.: *Turbulence in Simulated Local Cluster Analogs: One-to-one Comparisons between SLOW and XRISM/Hitomi.* The Astrophysical Journal **1000**, 75 (2026)

Gunn J. E. & Gott J. R., III: *On the Infall of Matter into Clusters of Galaxies and Some Effects on Their Evolution.* **176**, 1 (1972)

Gunn J. E.: *Massive Galactic Halos. I. Formation and Evolution.* The Astrophysical Journal **218**, 592 (1977)

Guth A. H.: *Inflationary Universe: A Possible Solution to the Horizon and Flatness Problems.* Physical Review D **23**, 347 (1981)

Haardt F. & Madau P.: *Modelling the UV/X-ray Cosmic Background with CUBA.* arXiv preprint, 10.48550/arXiv.astro-ph/0106018 (2001)

Haehnelt M. G. & Tegmark M.: *Using the Kinematic Sunyaev-Zeldovich Effect to Determine the Peculiar Velocities of Clusters of Galaxies.* Monthly Notices of the Royal Astronomical Society **279**, 545 (1996)

Haggar R., De Luca F., De Petris M., Sazonova E., Taylor J. E., Knebe A., Gray M. E., Pearce F. R., Contreras-Santos A., Cui W., et al.: *Reconsidering the Dynamical States of Galaxy Clusters Using PCA and UMAP.* Monthly Notices of the Royal Astronomical Society **532**, 1031 (2024)

Hahn O. & Abel T.: *Multi-scale initial conditions for cosmological simulations: Multi-scale initial conditions.* Monthly Notices of the Royal Astronomical Society **415**, 2101–212 (2011)

Harrison E. R.: *Fluctuations at the Threshold of Classical Cosmology.* Physical Review D **1**, 2726 (1970)

Hasan F., Burchett J. N., Hellinger D., Elek O., Nagai D., Faber S. M., Primack J. R., Koo D. C., Mandelker N., & Woo J.: *Filaments of the Slime Mold Cosmic Web and How They Affect Galaxy Evolution.* The Astrophysical Journal **970**, 177 (2024)

Hernández-Martínez E., Dolag K., Seidel B., Sorce J. G., Aghanim N., Pilipenko S., Gottlöber S., Lebeau T., & Valentini M.: *Simulating the LOcal Web (SLOW) - II. Properties of Local Galaxy Clusters.* Astronomy & Astrophysics **687**, A253 (2024)

Heß S., Kitaura F.-S., & Gottlöber S.: *Simulating Structure Formation of the Local Universe.* MNRAS **435**, 2065 (2013)

Hidding J., Shandarin S. F., & van de Weygaert R.: *The Zel'dovich Approximation: Key to Understanding Cosmic Web Complexity.* MNRAS **437**, 3442 (2014)

Hinshaw G., Banday A. J., Bennett C. L., Gorski K. M., Kogut A., Lineweaver C. H., Smoot G. F., & Wright E. L.: *2-point correlations in the COBE DMR 4-year anisotropy maps.* Astrophys. J. Lett. **464**, L25 (1996)

Hitomi Collaboration, Aharonian F., Akamatsu H., Akimoto F., Allen S. W., Angelini L., Audard M., Awaki H., Axelsson M., Bamba A., et al.: *Atmospheric Gas Dynamics in the Perseus Cluster Observed with Hitomi*.* Publications of the Astronomical Society of Japan **70**, 9 (2018)

Hoang D. N., Brüggen M., Zhang X., Bonafede A., Liu A., Liu T., Shimwell T. W., Botteon A., Brunetti G., Bulbul E., et al.: *A Search for Intercluster Filaments with LOFAR and eROSITA.* Monthly Notices of the Royal Astronomical Society **523**, 6320 (2023)

Hoffman Y. & Ribak E.: *Constrained Realizations of Gaussian Fields: A Simple Algorithm.* The Astrophysical Journal **380**, L5 (1991)

Hoffman Y., Lahav O., Yepes G., & Dover Y.: *The Future of the Local Large Scale Structure: The Roles of Dark Matter and Dark Energy.* J. Cosmology Astropart. Phys. **2007**, 016 (2007)

Hoffman Y.: *Gaussian Fields and Constrained Simulations of the Large-Scale Structure.* 565 (2009)

Hoffman Y., Courtois H. M., & Tully R. B.: *Cosmic Bulk Flow and the Local Motion from Cosmicflows-2.* Monthly Notices of the Royal Astronomical Society **449**, 4494 (2015)

Hogarth L. M., Saintonge A., Cortese L., Davis T. A., Croom S. M., Bland-Hawthorn J., Brough S., Bryant J. J., Catinella B., Fletcher T. J., et al.: *Centrally Concentrated Molecular Gas Driving Galactic-Scale Ionized Gas Outflows in Star-Forming Galaxies.* MNRAS **500**, 3802 (2021)

Hoosain M., Blyth S.-L., Skelton R. E., Kannappan S. J., Stark D. V., Eckert K. D., Hutchens Z. L., Carr D. S., & Kraljic K.: *The Effect of Cosmic Web Filaments on Galaxy Properties in the RESOLVE and ECO Surveys.* Monthly Notices of the Royal Astronomical Society **528**, 4139 (2024)

Hopp U., Bender R., Grupp F., Goessl C., Lang-Bardl F., Mitsch W., Riffeser A., & Ageorges N.: *Commissioning and Science Verification of the 2m-Fraunhofer Wendelstein Telescope.* In: *Ground-Based and Airborne Telescopes V.* **9145**, 872 (2014)

Hoyle F. & Lyttleton R. A.: *The Effect of Interstellar Matter on Climatic Variation.* Proceedings of the Cambridge Philosophical Society **35**, 405 (1939)

Hubble E. P.: *Extragalactic Nebulae.* **64** (1926)

Hubble E.: *A Relation between Distance and Radial Velocity among Extra-Galactic Nebulae.* Proceedings of the National Academy of Science **15**, 168 (1929)

Hudson D. S., Mittal R., Reiprich T. H., Nulsen P. E. J., Andernach H., & Sarazin C. L.: *What Is a Cool-Core Cluster? A Detailed Analysis of the Cores of the X-ray Flux-Limited HIFLUGCS Cluster Sample.* Astronomy & Astrophysics **513**, A37 (2010)

Hurier G., Macías-Pérez J. F., & Hildebrandt S.: *MILCA, a Modified Internal Linear Combination Algorithm to Extract Astrophysical Emissions from Multifrequency Sky Maps.* A&A **558**, A118 (2013)

Ichinohe Y., Simionescu A., Werner N., & Takahashi T.: *An Azimuthally Resolved Study of the Cold Front in Abell 3667.* Monthly Notices of the Royal Astronomical Society **467**, 3662 (2017)

Ikebe Y., Reiprich T. H., Böhringer H., Tanaka Y., & Kitayama T.: *A New Measurement of the X-ray Temperature Function of Clusters of Galaxies.* A&A **383**, 773 (2002)

Iodice E., Capaccioli M., Grado A., Limatola L., Spavone M., Napolitano N. R., Paolillo M., Peletier R. F., Cantiello M., Lisker T., et al.: *The Fornax Deep Survey with VST. I. The Extended and Diffuse Stellar Halo of NGC 1399 out to 192 Kpc.* The Astrophysical Journal **820**, 42 (2016)

Isopi G., Capalbo V., Hincks A., Di Mascolo L., Barbavara E., Battistelli E., Bond J., Cui W., Coulton W., De Petris M., et al.: *The Atacama Cosmology Telescope: A Census of Bridges between Galaxy Clusters.* Journal of Cosmology and Astroparticle Physics **2025**, 078 (2025)

Ivezić Ž., Kahn S. M., Tyson J. A., Abel B., Acosta E., Allsman R., Alonso D., AlSayyad Y., Anderson S. F., Andrew J., et al.: *LSST: From Science Drivers to Reference Design and Anticipated Data Products.* The Astrophysical Journal **873**, 111 (2019)

Jaffé Y. L., Smith R., Candlish G. N., Poggianti B. M., Sheen Y.-K., & Verheijen M. A. W.: *BUDHIES II: A Phase-Space View of H I Gas Stripping and Star Formation Quenching in Cluster Galaxies.* **448**, 1715 (2015)

Janka H.-T., Langanke K., Marek A., Martínez-Pinedo G., & Müller B.: *Theory of Core-Collapse Supernovae.* Physics Reports **442**, 38 (2007)

Jazayeri S., Sadr A. V., & Firouzjahi H.: *Primordial anisotropies from cosmic strings during inflation.* Phys. Rev. D **96**, 023512 (2017)

Jenkins A.: *Second-Order Lagrangian Perturbation Theory Initial Conditions for Resimulations.* Monthly Notices of the Royal Astronomical Society **403**, 1859 (2010)

Jôeveer M. & Einasto J.: *Has the Universe the Cell Structure?* Symposium - International Astronomical Union **79**, 241 (1978)

Jõeveer M., Einasto J., & Tago E.: *Spatial Distribution of Galaxies and of Clusters of Galaxies in the Southern Galactic Hemisphere.* Monthly Notices of the Royal Astronomical Society **185**, 357 (1978)

Jung G., Aghanim N., Sorce J. G., Seidel B., Dolag K., & Douspis M.: *Revisiting the CMB Large-Scale Anomalies: The Impact of the Sunyaev-Zeldovich Signal from the Local Universe.* A&A **692**, A180 (2024)

Kester C. E., Bernui A., & Hipólito-Ricaldi W. S.: *Probing statistical isotropy of the universe with the Planck CMB data.* (2023)

Khatri R.: *An Alternative Validation Strategy for the Planck Cluster Catalogue and Y-Distortion Maps.* A&A **592**, A48 (2016)

Kimmig L. C., Remus R.-S., Dolag K., & Biffi V.: *The Hateful Eight: Connecting Massive Substructures in Galaxy Clusters like A2744 to Their Dynamical Assembly State Using the Magneticum Simulations.* ApJ **949**, 92 (2023)

Kimmig L. C., Brough S., Dolag K., Remus R.-S., Bahé Y. M., Martin G., Pillepich A., Hatch N., Montes M., Ahad S. L., et al.: *Intra-Cluster Light as a Dynamical Clock for Galaxy Clusters: Insights from the MAGNETICUM, IllustrisTNG, Hydrangea and Horizon-AGN Simulations.* Astronomy & Astrophysics **700**, A95 (2025a)

Kimmig L. C., Remus R.-S., Seidel B., Valenzuela L. M., Dolag K., & Burkert A.: *Blowing Out the Candle: How to Quench Galaxies at High Redshift—An Ensemble of Rapid Starbursts, AGN Feedback, and Environment.* The Astrophysical Journal **979**, 15 (2025b)

Kimmig L. C.: *Rise and shine – the formation of structures from cosmic dawn to present day.* Text.PhDThesis, Ludwig-Maximilians-Universität München (2026)

Kitaura F.-S., Erdoğdu P., Nuza S. E., Khalatyan A., Angulo R. E., Hoffman Y., & Gottlöber S.: *Cosmic Structure and Dynamics of the Local Universe.* MNRAS **427**, L35 (2012)

Kleiner D., Koribalski B. S., Serra P., Whiting M. T., Westmeier T., Wong O. I., Kamphuis P., Popping A., Bekiaris G., Elagali A., et al.: *WALLABY Early Science – IV. ASKAP H i Imaging of the Nearby Galaxy IC 5201.* Monthly Notices of the Royal Astronomical Society **488**, 5352 (2019)

Kleiner D., Serra P., Maccagni F. M., Venhola A., Morokuma-Matsui K., Peletier R., Iodice E., Raj M. A., de Blok W. J. G., Comrie A., et al.: *A MeerKAT View of Pre-Processing in the Fornax A Group.* Astronomy & Astrophysics **648**, A32 (2021)

Kluge M., Hatch N. A., Montes M., Golden-Marx J. B., Gonzalez A. H., Cuillandre J.-C., Bolzonella M., Lançon A., Laureijs R., Saifollahi T., et al.: *Euclid: Early Release Observations – The Intracluster Light and Intracluster Globular Clusters of the Perseus Cluster.* A&A **697**, A13 (2025)

Klypin A., Kravtsov A. V., Valenzuela O., & Prada F.: *Where Are the Missing Galactic Satellites?* The Astrophysical Journal **522**, 82 (1999)

Knebe A., Devriendt J. E. G., Gibson B. K., & Silk J.: *Top-down Fragmentation of a Warm Dark Matter Filament.* Monthly Notices of the Royal Astronomical Society **345**, 1285 (2003)

Kobayashi C., Karakas A. I., & Lugaro M.: *The Origin of Elements from Carbon to Uranium.* ApJ **900**, 179 (2020)

Komatsu E., Smith K. M., Dunkley J., Bennett C. L., Gold B., Hinshaw G., Jarosik N., Larson D., Nolta M. R., Page L., et al.: *Seven-Year Wilkinson Microwave Anisotropy Probe (WMAP) Observations: Cosmological Interpretation.* **192**, 18 (2011)

Kosyra R., Gössl C., Hopp U., Lang-Bardl F., Riffeser A., Bender R., & Seitz S.: *The 64 Mpixel Wide Field Imager for the Wendelstein 2m Telescope: Design and Calibration.* Experimental Astronomy **38**, 213 (2014)

Kraljic K., Arnouts S., Pichon C., Laigle C., de la Torre S., Vibert D., Cadiou C., Dubois Y., Treyer M., Schimd C., et al.: *Galaxy Evolution in the Metric of the Cosmic Web.* Monthly Notices of the Royal Astronomical Society **474**, 547 (2018)

Kravtsov A. V. & Borgani S.: *Formation of Galaxy Clusters.* **50**, 353 (2012)

Kreckel K., Platen E., Aragón-Calvo M. A., van Gorkom J. H., van de Weygaert R., van der Hulst J. M., Kovač K., Yip C.-W., & Peebles P. J. E.: *ONLY THE LONELY: H i IMAGING OF VOID GALAXIES.* The Astronomical Journal **141**, 4 (2010)

Krumholz M. R., McKee C. F., & Tumlinson J.: *The Atomic-to-Molecular Transition in Galaxies. I. An Analytic Approximation for Photodissociation Fronts in Finite Clouds.* The Astrophysical Journal **689**, 865 (2008)

Krumholz M. R., McKee C. F., & Tumlinson J.: *THE ATOMIC-TO-MOLECULAR TRANSITION IN GALAXIES. II: H i AND H2 COLUMN DENSITIES.* The Astrophysical Journal **693**, 216 (2009)

Kuchner U., Aragón-Salamanca A., Rost A., Pearce F. R., Gray M. E., Cui W., Knebe A., Rasia E., & Yepes G.: *Cosmic Filaments in Galaxy Cluster Outskirts: Quantifying Finding Filaments in Redshift Space.* Monthly Notices of the Royal Astronomical Society **503**, 2065 (2021)

Kuutma T., Tamm A., & Tempel E.: *From Voids to Filaments: Environmental Transformations of Galaxies in the SDSS.* Astronomy & Astrophysics **600**, L6 (2017)

Ködel M.: *HI Gas in the Magneticum Simulations.* LMU, Master Thesis (2018)

Labbé I., van Dokkum P., Nelson E., Bezanson R., Suess K. A., Leja J., Brammer G., Whitaker K., Mathews E., Stefanon M., & Wang B.: *A Population of Red Candidate Massive Galaxies 600 Myr after the Big Bang.* Nature **616**, 266 (2023)

Laigle C., Pichon C., Arnouts S., McCracken H. J., Dubois Y., Devriendt J., Slyz A., Le Borgne D., Benoit-Lévy A., Hwang H. S., et al.: *COSMOS2015 Photometric Redshifts Probe the Impact of Filaments on Galaxy Properties.* Monthly Notices of the Royal Astronomical Society **474**, 5437 (2018)

Lebeau T., Ettori S., Aghanim N., & Sorce J. G.: *Can the splashback radius be an observable boundary of galaxy clusters?* A&A **689**, A19 (2024a)

Lebeau T., Sorce J. G., & Aghanim N.: *Projection Effects on Pressure Profiles: A Case Study of the Virgo Replica.* EPJ Web of Conferences **293**, 00028 (2024b)

Lebeau T., Sorce J. G., Aghanim N., Hernández-Martínez E., & Dolag K.: *Mass Bias in Clusters of Galaxies: Projection Effects on the Case Study of Virgo Replica.* A&A **682**, A157 (2024c)

Lee C. T., Primack J. R., Behroozi P., Rodríguez-Puebla A., Hellinger D., & Dekel A.: *Tidal Stripping and Post-Merger Relaxation of Dark Matter Haloes: Causes and Consequences of Mass-Loss.* MNRAS **481**, 4038 (2018)

Lehle K., Nelson D., Pillepich A., Truong N., & Rohr E.: *The Heart of Galaxy Clusters: Demographics and Physical Properties of Cool-Core and Non-Cool-Core Halos in the TNG-Cluster Simulation.* A&A **687**, A129 (2024)

Leja J., Speagle J. S., Johnson B. D., Conroy C., van Dokkum P., & Franx M.: *A New Census of the 0.2 < z < 3.0 Universe. I. The Stellar Mass Function.* The Astrophysical Journal **893**, 111 (2020)

Li C. & White S. D. M.: *The Distribution of Stellar Mass in the Low-Redshift Universe.* Monthly Notices of the Royal Astronomical Society **398**, 2177 (2009)

Libeskind N. I., Knebe A., Hoffman Y., Gottloeber S., Yepes G., & Steinmetz M.: *The Preferred Direction of Infalling Satellite Galaxies in the Local Group.* MNRAS **411**, 1525 (2011)

Libeskind N. I., van de Weygaert R., Cautun M., Falck B., Tempel E., Abel T., Alpaslan M., Aragón-Calvo M. A., Forero-Romero J. E., Gonzalez R., et al.: *Tracing the Cosmic Web.* Monthly Notices of the Royal Astronomical Society **473**, 1195 (2018)

Libeskind N. I., Carlesi E., Grand R. J. J., Khalatyan A., Knebe A., Pakmor R., Pilipenko S., Pawlowski M. S., Sparre M., Tempel E., et al.: *The Hestia Project: Simulations of the Local Group.* Monthly Notices of the Royal Astronomical Society **498**, 2968 (2020)

Lidman C., Suherli J., Muzzin A., Wilson G., Demarco R., Brough S., Rettura A., Cox J., DeGroot A., Yee H. K. C., et al.: *Evidence for Significant Growth in the Stellar Mass of Brightest Cluster Galaxies over the Past 10 Billion Years.* Monthly Notices of the Royal Astronomical Society **427**, 550 (2012)

Lilly S. J., Carollo C. M., Pipino A., Renzini A., & Peng Y.: *GAS REGULATION OF GALAXIES: THE EVOLUTION OF THE COSMIC SPECIFIC STAR FORMATION RATE, THE METALLICITY–MASS–STAR-FORMATION RATE RELATION, AND THE STELLAR CONTENT OF HALOS.* The Astrophysical Journal **772**, 119 (2013)

Linde A. D.: *A New Inflationary Universe Scenario: A Possible Solution of the Horizon, Flatness, Homogeneity, Isotropy and Primordial Monopole Problems.* Physics Letters B **108**, 389 (1982)

Liu A., Bulbul E., Kluge M., Ghirardini V., Zhang X., Sanders J. S., Artis E., Bahar Y. E., Balzer F., Brüggen M., et al.: *The SRG/eROSITA All-Sky Survey - First Catalog of Superclusters in the Western Galactic Hemisphere.* Astronomy & Astrophysics **683**, A130 (2024)

Loewenstein M.: *On Iron Enrichment, Star Formation, and Type Ia Supernovae in Galaxy Clusters.* ApJ **648**, 230 (2006)

Long A. S., Antwi-Danso J., Lambrides E. L., Lovell C. C., de la Vega A., Valentino F., Zavala J. A., Casey C. M., Wilkins S. M., Yung L. Y. A., et al.: *Efficient NIRCam Selection of Quiescent Galaxies at 3 < z < 6 in CEERS.* The Astrophysical Journal **970**, 68 (2024)

López P., van de Weygaert R., & Merchán M.: *Spinning Masters: On the Impact of Tidal Forces and Protohalo Size on Early Spin Evolution.* Monthly Notices of the Royal Astronomical Society **543**, 2222 (2025)

Ludlow A. D., Schaye J., & Bower R.: *Numerical Convergence of Simulations of Galaxy Formation: The Abundance and Internal Structure of Cold Dark Matter Haloes.* Monthly Notices of the Royal Astronomical Society **488**, 3663 (2019)

Lynden-Bell D., Faber S. M., Burstein D., Davies R. L., Dressler A., Terlevich R. J., & Wegner G.: *Photometry and Spectroscopy of Elliptical Galaxies. V. Galaxy Streaming toward the New Supergalactic Center.* ApJ **326**, 19 (1988)

Makarov D. & Karachentsev I.: *Galaxy Groups and Clouds in the Local (Z~ 0.01) Universe.* MNRAS **412**, 2498 (2011)

Malavasi N., Arnouts S., Vibert D., de la Torre S., Moutard T., Pichon C., Davidzon I., Kraljic K., Bolzonella M., Guzzo L., et al.: *The VIMOS Public Extragalactic Redshift Survey (VIPERS): Galaxy Segregation inside Filaments at $z \simeq 0.7$.* Monthly Notices of the Royal Astronomical Society **465**, 3817 (2017)

Malavasi N., Sorce J. G., Dolag K., & Aghanim N.: *The Cosmic Web around the Coma Cluster from Constrained Cosmological Simulations - I. Filaments Connected to Coma at $z = 0$.* A&A **675**, A76 (2023)

Marchesini D., van Dokkum P. G., Förster Schreiber N. M., Franx M., Labbé I., & Wuyts S.: *The Evolution of the Stellar Mass Function of Galaxies from $z = 4.0$ and the First Comprehensive Analysis of Its Uncertainties: Evidence for Mass-Dependent Evolution.* The Astrophysical Journal **701**, 1765 (2009)

Marin-Gilabert T., Valentini M., Steinwandel U. P., & Dolag K.: *The Role of Physical and Numerical Viscosity in Hydrodynamical Instabilities.* Monthly Notices of the Royal Astronomical Society **517**, 5971 (2022)

Masters K. L.: *A Zoo of Galaxies.* Highlights of Astronomy **16**, 1 (2015)

McAlpine S., Helly J. C., Schaller M., Sawala T., Lavaux G., Jasche J., Frenk C. S., Jenkins A., Lucey J. R., & Johansson P. H.: *SIBELIUS-DARK: A Galaxy Catalogue of the Local Volume from a Constrained Realization Simulation.* Monthly Notices of the Royal Astronomical Society **512**, 5823 (2022)

McCall H., Reiprich T. H., Veronica A., Pacaud F., Sanders J., Edler H. W., Brüggen M., Bulbul E., de Gasperin F., Gatuzz E., et al.: *The SRG/eROSITA All-Sky Survey - View of the Virgo Cluster.* Astronomy & Astrophysics **689**, A113 (2024)

McKee C. F. & Krumholz M. R.: *The Atomic-to-Molecular Transition in Galaxies. III. A New Method for Determining the Molecular Content of Primordial and Dusty Clouds.* The Astrophysical Journal **709**, 308 (2010)

McMillan P. J.: *The Mass Distribution and Gravitational Potential of the Milky Way.* Monthly Notices of the Royal Astronomical Society **465**, 76 (2017)

Mendel J. T., Proctor R. N., Forbes D. A., & Brough S.: *The Anatomy of the NGC 5044 Group – I. Group Membership and Dynamics.* MNRAS **389**, 749 (2008)

Merlin E., Fortuni F., Torelli M., Santini P., Castellano M., Fontana A., Grazian A., Pentericci L., Pilo S., & Schmidt K. B.: *Red and Dead CANDELS: Massive Passive Galaxies at the Dawn of the Universe.* Monthly Notices of the Royal Astronomical Society **490**, 3309 (2019)

Merloni A., Predehl P., Becker W., Böhringer H., Boller T., Brunner H., Brusa M., Dennerl K., Freyberg M., Friedrich P., et al.: *eROSITA Science Book: Mapping the Structure of the Energetic Universe.* arXiv.org (2012)

Merluzzi P., Busarello G., Haines C. P., Mercurio A., Okabe N., Pimbblet K. J., Dopita M. A., Grado A., Limatola L., Bourdin H., et al.: *Shapley Supercluster Survey: Galaxy Evolution from Filaments to Cluster Cores.* Monthly Notices of the Royal Astronomical Society **446**, 803 (2015)

Mohapatra R., Federrath C., & Sharma P.: *Turbulence in Stratified Atmospheres: Implications for the Intracluster Medium.* Monthly Notices of the Royal Astronomical Society **493**, 5838 (2020)

Monteiro-Oliveira R., Morell D. F., Sampaio V. M., Ribeiro A. L. B., & de Carvalho R. R.: *Unveiling the Internal Structure of the Hercules Supercluster.* Monthly Notices of the Royal Astronomical Society **509**, 3470 (2022)

Mukhanov S.: *Cosmological Perturbations from Inflation.* Journal of Physics A: Mathematical and Theoretical **40**, 6561 (2007)

Mukhanov V. F. & Chibisov G. V.: *Quantum Fluctuations and a Nonsingular Universe.* Soviet Journal of Experimental and Theoretical Physics Letters **33**, 532 (1981)

Mukhanov V. F. & Chibisov G. V.: *Energy of Vacuum and the Large-Scale Structure of the Universe.* Zhurnal Eksperimentalnoi i Teoreticheskoi Fiziki **83**, 475 (1982)

Muñoz R. P., Eigenthaler P., Puzia T. H., Taylor M. A., Ordenes-Briceño Y., Alamo-Martínez K., Ribbeck K. X., Ángel S., Capaccioli M., Côté P., et al.: *Unveiling a Rich System of Faint Dwarf Galaxies in the next Generation Fornax Survey.* **813**, L15 (2015)

Murante G., Calabrese M., De Lucia G., Monaco P., Borgani S., & Dolag K.: *A Warm Mode of Gas Accretion on Forming Galaxies.* ApJ **749**, L34 (2012)

Musso M., Cadiou C., Pichon C., Codis S., Kraljic K., & Dubois Y.: *How Does the Cosmic Web Impact Assembly Bias?* Monthly Notices of the Royal Astronomical Society **476**, 4877 (2018)

Muzzin A., Marchesini D., Stefanon M., Franx M., McCracken H. J., Milvang-Jensen B., Dunlop J. S., Fynbo J. P. U., Brammer G., Labbé I., & van Dokkum P. G.: *The Evolution of the Stellar Mass Functions of Star-forming and Quiescent Galaxies to z = 4 from the COSMOS/UltraVISTA Survey.* The Astrophysical Journal **777**, 18 (2013)

Nagamine K. & Loeb A.: *Future Evolution of Nearby Large-Scale Structures in a Universe Dominated by a Cosmological Constant.* New Astronomy **8**, 439 (2003)

Navarro J. F., Frenk C. S., & White S. D. M.: *A Universal Density Profile from Hierarchical Clustering.* ApJ **490**, 493 (1997)

Negri A., Dalla Vecchia C., Aguerri J. A. L., & Bahé Y.: *The Luminosity of Cluster Galaxies in the Cluster-EAGLE Simulations.* Monthly Notices of the Royal Astronomical Society **515**, 2121 (2022)

Nelson D., Springel V., Pillepich A., Rodriguez-Gomez V., Torrey P., Genel S., Vogelsberger M., Pakmor R., Marinacci F., Weinberger R., et al.: *The IllustrisTNG Simulations: Public Data Release.* arXiv preprint, 10.48550/arXiv.1812.05609 (2021)

Nelson D., Pillepich A., Ayromlou M., Lee W., Lehle K., Rohr E., & Truong N.: *Introducing the TNG-Cluster Simulation: Overview and Physical Properties of the Gaseous Intracluster Medium.* arXiv preprint, 10.48550/arXiv.2311.06338 (2024)

Neyrinck M., Aragon-Calvo M. A., Falck B., Szalay A. S., & Wang J.: *Halo Spin from Primordial Inner Motions.* The Open Journal of Astrophysics **3**, 3 (2020)

Nicastro F., Kaastra J., Krongold Y., Borgani S., Branchini E., Cen R., Dadina M., Danforth C. W., Elvis M., Fiore F., et al.: *Observations of the Missing Baryons in the Warm-Hot Intergalactic Medium.* Nature **558**, 406 (2018)

Nomoto K., Kobayashi C., & Tominaga N.: *Nucleosynthesis in Stars and the Chemical Enrichment of Galaxies.* A&A Rev. **51**, 457 (2013)

Obreschkow D., Glazebrook K., Bassett R., Fisher D. B., Abraham R. G., Wisnioski E., Green A. W., McGregor P. J., Damjanov I., Popping A., & Jørgensen I.: *Low Angular Momentum in Clumpy, Turbulent Disk Galaxies.* The Astrophysical Journal **815**, 97 (2015)

Odekon M. C., Jones M. G., Graham L., Kelley-Derzon J., & Halstead E.: *Infall Profiles for Supercluster-scale Filaments.* ApJ **935**, 130 (2022)

Odekon M. C., Viscardi T. W., Rabinowitz J., & Young B.: *Estimating the Masses of Supercluster-scale Filaments from Redshift Dispersions.* ApJ **977**, 28 (2024)

Oñorbe J., Garrison-Kimmel S., Maller A. H., Bullock J. S., Rocha M., & Hahn O.: *How to Zoom: Bias, Contamination and Lagrange Volumes in Multimass Cosmological Simulations.* **437**, 1894 (2014)

Oppenheimer B. D. & Davé R.: *Mass, Metal, and Energy Feedback in Cosmological Simulations.* Monthly Notices of the Royal Astronomical Society **387**, 577 (2008)

Osato K. & Nagai D.: *Baryon Pasting Algorithm: Halo-Based and Particle-Based Pasting Methods.* Monthly Notices of the Royal Astronomical Society **519**, 2069 (2023)

Ota N., Onzuka K., & Masai K.: *Density Profile of a Cool Core of Galaxy Clusters.* Publications of the Astronomical Society of Japan **65**, 47 (2013)

Panter B., Heavens A. F., & Jimenez R.: *The Mass Function of the Stellar Component of Galaxies in the Sloan Digital Sky Survey.* Monthly Notices of the Royal Astronomical Society **355**, 764 (2004)

Papovich C., Kawinwanichakij L., Quadri R. F., Glazebrook K., Labbé I., Tran K.-V. H., Forrest B., Kacprzak G. G., Spitler L. R., Straatman C. M. S., & Tomczak A. R.: *The Effects of Environment on the Evolution of the Galaxy Stellar Mass Function.* ApJ **854**, 30 (2018)

Pearson D. W. & Batuski D. J.: *Locating Bound Structure in an Accelerating Universe.* Monthly Notices of the Royal Astronomical Society **436**, 796 (2013)

Pearson D. W., Batiste M., & Batuski D. J.: *The Largest Gravitationally Bound Structures: The Corona Borealis Supercluster – Mass and Bound Extent.* MNRAS **441**, 1601 (2014)

Peebles P. J. E.: *Origin of the Angular Momentum of Galaxies.* The Astrophysical Journal **155**, 393 (1969)

Peebles P. J. E.: *The Large-Scale Structure of the Universe.* Princeton University Press (2020)

Peebles P. J. E.: *Flat Patterns in Cosmic Structure.* MNRAS **526**, 4490 (2023)

Penzias A. A. & Wilson R. W.: *A Measurement of Excess Antenna Temperature at 4080 Mc/s.* The Astrophysical Journal **142**, 419 (1965)

Pérez-González P. G., Rieke G. H., Villar V., Barro G., Blaylock M., Egami E., Gallego J., Gil de Paz A., Pascual S., Zamorano J., & Donley J. L.: *The Stellar Mass Assembly of Galaxies from z = 0 to z = 4: Analysis of a Sample Selected in the Rest-Frame Near-Infrared with Spitzer.* The Astrophysical Journal **675**, 234 (2008)

Persic M. & Salucci P.: *The Baryon Content of the Universe.* Monthly Notices of the Royal Astronomical Society **258**, 14P (1992)

Piffaretti R., Arnaud M., Pratt G. W., Pointecouteau E., & Melin J.-B.: *The MCXC: A Meta-Catalogue of x-Ray Detected Clusters of Galaxies.* A&A **534**, A109 (2011)

Pilipenko S., Yepes G., Gottlöber S., & Knollmann S.: *Ginnungagap – a massively parallel cosmological initial conditions generator.* arXiv e-prints, arXiv:2511 (2025)

Pillepich A., Springel V., Nelson D., Genel S., Naiman J., Pakmor R., Hernquist L., Torrey P., Vogelsberger M., Weinberger R., & Marinacci F.: *Simulating Galaxy Formation with the IllustrisTNG Model.* Monthly Notices of the Royal Astronomical Society **473**, 4077 (2018)

Pinzke A., Pfrommer C., & Bergström L.: *Prospects of Detecting Gamma-Ray Emission from Galaxy Clusters: Cosmic Rays and Dark Matter Annihilations.* Physical Review D **84**, 123509 (2011)

Planck Collaboration, Ade P. a. R., Aghanim N., Armitage-Caplan C., Arnaud M., Ashdown M., Atrio-Barandela F., Aumont J., Baccigalupi C., Banday A. J., et al.: *Planck 2013 Results. XVI. Cosmological Parameters.* A&A **571**, A16 (2014)

Planck Collaboration, Adam R., Ade P. A. R., Aghanim N., Akrami Y., Alves M. I. R., Argüeso F., Arnaud M., Arroja F., Ashdown M., et al.: *Planck 2015 Results. I. Overview of Products and Scientific Results.* Astronomy and Astrophysics **594**, A1 (2016a)

Planck Collaboration, Ade P. A. R., Aghanim N., Akrami Y., Aluri P. K., Arnaud M., Ashdown M., Aumont J., Baccigalupi C., Banday A. J., et al.: *Planck 2015 Results. XVI. Isotropy and Statistics of the CMB.* Astronomy and Astrophysics **594**, A16 (2016b)

Planck Collaboration, Ade P. A. R., Aghanim N., Arnaud M., Ashdown M., Aumont J., Baccigalupi C., Banday A. J., Barreiro R. B., Bartlett J. G., & al. e.: *Planck 2015 Results. XIII. Cosmological Parameters.* **594**, A13 (2016c)

Planck Collaboration, Aghanim N., Arnaud M., Ashdown M., Aumont J., Baccigalupi C., Banday A. J., Barreiro R. B., Bartlett J. G., Bartolo N., et al.: *Planck 2015 Results - XXII. A Map of the Thermal Sunyaev-Zeldovich Effect.* A&A **594**, A22 (2016d)

Planck Collaboration, Aghanim, N., Akrami, Y., Arroja, F., Ashdown, M., Aumont, J., Baccigalupi, C., Ballardini, M., Banday, A. J., Barreiro, R. B., et al.: *Planck 2018 Results - I. Overview and the Cosmological Legacy of Planck.* antike und abendland **641**, A1 (2020)

Planelles S., Borgani S., Fabjan D., Killedar M., Murante G., Granato G. L., Ragone-Figueroa C., & Dolag K.: *On the role of AGN feedback on the thermal and chemodynamical properties of the hot intracluster medium.* MNRAS **438**, 195 (2014)

Popesso P., Biviano A., Marini I., Dolag K., Vladutescu-Zopp S., Csizi B., Biffi V., Lamer G., Robothan A., Bravo M., et al.: *The Hot Gas Mass Fraction in Halos - From Milky Way-like Groups to Massive Clusters.* Astronomy & Astrophysics **707**, A362 (2026)

Porciani C., Dekel A., & Hoffman Y.: *Testing Tidal-Torque Theory – I. Spin Amplitude and Direction.* Monthly Notices of the Royal Astronomical Society **332**, 325 (2002)

Predehl P., Andritschke R., Arefiev V., Babyshkin V., Batanov O., Becker W., Böhringer H., Bogomolov A., Boller T., Borm K., et al.: *The eROSITA X-ray Telescope on SRG.* Astronomy & Astrophysics **647**, A1 (2021)

Press W. H. & Schechter P.: *Formation of Galaxies and Clusters of Galaxies by Self-Similar Gravitational Condensation.* ApJ **187**, 425 (1974)

Proust D., Quintana H., Carrasco E. R., Reisenegger A., Slezak E., Muriel H., Dünner R., Sodré L., Drinkwater M. J., Parker Q. A., & Ragone C. J.: *Structure and Dynamics of the Shapley Supercluster: Velocity Catalogue, General Morphology and Mass.* Astronomy & Astrophysics **447**, 133 (2006)

Ragagnin A., Tchipev N., Bader M., Dolag K., & Hammer N.: *Exploiting the Space Filling Curve Ordering of Particles in the Neighbour Search of Gadget3.* 411 (2016)

Ragone-Figueroa C., Granato G. L., Ferraro M. E., Murante G., Biffi V., Borgani S., Planelles S., & Rasia E.: *BCG Mass Evolution in Cosmological Hydro-Simulations.* Monthly Notices of the Royal Astronomical Society **479**, 1125 (2018)

Rahmati A., Pawlik A. H., Raičević M., & Schaye J.: *On the Evolution of the H I Column Density Distribution in Cosmological Simulations.* Monthly Notices of the Royal Astronomical Society **430**, 2427 (2013)

Raj M. A., Awad P., Peletier R. F., Smith R., Kuchner U., van de Weygaert R., Libeskind N. I., Canducci M., Tino P., & Bunte K.: *The Large-Scale Structure around the Fornax-Eridanus Complex.* arXiv preprint, 10.48550/arXiv.2407.03225 (2024)

Rees M. J. & Ostriker J. P.: *Cooling, Dynamics and Fragmentation of Massive Gas Clouds: Clues to the Masses and Radii of Galaxies and Clusters.* MNRAS **179**, 541 (1977)

Reiprich T. H. & Böhringer H.: *The Mass Function of an X-Ray Flux-limited Sample of Galaxy Clusters.* The Astrophysical Journal **567**, 716 (2002)

Reiprich T. H., Veronica A., Pacaud F., Ramos-Ceja M. E., Ota N., Sanders J., Kara M., Erben T., Klein M., Erler J., et al.: *The Abell 3391/95 Galaxy Cluster System - A 15 Mpc Intergalactic Medium Emission Filament, a Warm Gas Bridge, Infalling Matter Clumps, and (Re-) Accelerated Plasma Discovered by Combining SRG/eROSITA Data with ASKAP/EMU and DECam Data.* Astronomy & Astrophysics **647**, A2 (2021)

Reiprich T. H., Veronica A., Pacaud F., Stöcker P., Nazaretyan V., Srivastava A., Pandya A., Dietl J., Sanders J. S., Yeung M. C. H., et al.: *The SRG/eROSITA All-Sky Survey - View of the Fornax Galaxy Cluster.* Astronomy & Astrophysics **703**, A9 (2025)

Reisenegger A., Quintana H., Carrasco E. R., & Maze J.: *The Shapley Supercluster. III. Collapse Dynamics and Mass Ofthe CentralConcentration.* The Astronomical Journal **120**, 523 (2000)

Remus R.-S., Burkert A., & Dolag K.: *A 'Universal' Density Profile for the Outer Stellar Halos of Galaxies.* Proceedings of the International Astronomical Union **11**, 84 (2016)

Remus R.-S., Dolag K., & Hoffmann T.: *The Outer Halos of Very Massive Galaxies: BCGs and Their DSC in the Magneticum Simulations.* Galaxies **5**, 49 (2017)

Remus R.-S., Dolag K., & Dannerbauer H.: *The Young and the Wild: What Happens to Protoclusters Forming at Redshift $z \approx 4$?* ApJ **950**, 191 (2023)

Remus R.-S. & Kimmig L. C.: *Relight the Candle: What Happens to High-redshift Massive Quenched Galaxies.* The Astrophysical Journal **982**, 30 (2025)

Retana-Montenegro E., Hese E. V., Gentile G., Baes M., & Frutos-Alfaro F.: *Analytical Properties of Einasto Dark Matter Haloes.* Astronomy & Astrophysics **540**, A70 (2012)

Riess A. G., Filippenko A. V., Challis P., Clocchiatti A., Diercks A., Garnavich P. M., Gilliland R. L., Hogan C. J., Jha S., Kirshner R. P., et al.: *Observational Evidence from Supernovae for an Accelerating Universe and a Cosmological Constant.* The Astronomical Journal **116**, 1009 (1998)

Riess A. G., Yuan W., Macri L. M., Scolnic D., Brout D., Casertano S., Jones D. O., Murakami Y., Anand G. S., Breuval L., et al.: *A Comprehensive Measurement of the Local Value of the Hubble Constant with 1 Km S-1 Mpc-1 Uncertainty from the Hubble Space Telescope and the SH0ES Team.* The Astrophysical Journal Letters **934**, L7 (2022)

Rindler W.: *Visual Horizons in World Models.* Monthly Notices of the Royal Astronomical Society **116**, 662 (1956)

Rines K., Mahdavi A., Geller M. J., Diaferio A., Mohr J. J., & Wegner G.: *X-Ray-emitting Groups in the Infall Region of Abell 2199.* ApJ **555**, 558 (2001)

Roberts-Borsani G. W. & Saintonge A.: *The Prevalence and Properties of Cold Gas Inflows and Outflows around Galaxies in the Local Universe.* Monthly Notices of the Royal Astronomical Society **482**, 4111 (2019)

Roberts M. S. & Whitehurst R. N.: *The Rotation Curve and Geometry of M31 at Large Galactocentric Distances.* The Astrophysical Journal **201**, 327 (1975)

Roediger E., Lovisari L., Dupke R., Ghizzardi S., Brüggen M., Kraft R. P., & Machacek M. E.: *Gas Sloshing, Cold Fronts, Kelvin–Helmholtz Instabilities and the Merger History of the Cluster of Galaxies Abell 496.* Monthly Notices of the Royal Astronomical Society **420**, 3632 (2012)

Rohr E., Pillepich A., Nelson D., Ayromlou M., & Zinger E.: *The Hot Circumgalactic Media of Massive Cluster Satellites in the TNG-Cluster Simulation: Existence and Detectability.* A&A **686**, A86 (2024)

Romano L. E. C., Behrendt M., & Burkert A.: *SISSI: Supernovae in a Stratified, Shearing Interstellar Medium - I. The Geometry of Supernova Remnants.* Astronomy & Astrophysics **702**, A12 (2025)

Rottgering H. J. A., Wieringa M. H., Hunstead R. W., & Ekers R. D.: *The Extended Radio Emission in the Luminous X-ray Cluster A3667.* Monthly Notices of the Royal Astronomical Society **290**, 577 (1997)

Saintonge A., Catinella B., Tacconi L. J., Kauffmann G., Genzel R., Cortese L., Davé R., Fletcher T. J., Graciá-Carpio J., Kramer C., et al.: *xCOLD GASS: The Complete IRAM 30 m Legacy Survey of Molecular Gas for Galaxy Evolution Studies.* The Astrophysical Journal Supplement Series **233**, 22 (2017)

Sakuma E., Ota N., Sato K., Sato T., & Matsushita K.: *Suzaku Observations of Metal Distributions in the Intracluster Medium of the Centaurus Cluster.* PASJ **63**, S979 (2011)

Sala L., Valentini M., Biffi V., & Dolag K.: *Supermassive Black Hole Spin Evolution in Cosmological Simulations with OPENGADGET3.* Astronomy & Astrophysics **685**, A92 (2024)

Salvati L., Douspis M., Ritz A., Aghanim N., & Babul A.: *Mass Bias Evolution in tSZ Cluster Cosmology.* A&A **626**, A27 (2019)

Sandage A.: *The Hubble Atlas of Galaxies.* (1961)

Sanders J. S., Fabian A. C., Allen S. W., & Schmidt R. W.: *Mapping Small-Scale Temperature and Abundance Structures in the Core of the Perseus Cluster.* Monthly Notices of the Royal Astronomical Society **349**, 952 (2004)

Santini P., Fontana A., Grazian A., Salimbeni S., Fontanot F., Paris D., Boutsia K., Castellano M., Fiore F., Gallozzi S., et al.: *The Evolving Slope of the Stellar Mass Function at $0.6 \leq z < 4.5$ from Deep WFC3 Data.* Astronomy and Astrophysics **538**, A33 (2012)

Sarazin C. L. & White R. E., III: *Steady State Cooling Flow Models for Normal Elliptical Galaxies.* The Astrophysical Journal **320**, 32 (1987)

Sarkar P. & Bharadwaj S.: *The Local Dimension: A Method to Quantify the Cosmic Web.* Monthly Notices of the Royal Astronomical Society: Letters **394**, L66 (2009)

Sawala T., McAlpine S., Jasche J., Lavaux G., Jenkins A., Johansson P. H., & Frenk C. S.: *The SIBELIUS Project: E Pluribus Unum.* Monthly Notices of the Royal Astronomical Society **509**, 1432 (2022)

Sawala T., Teeriaho M., Frenk C. S., Helly J., Jenkins A., Racz G., Schaller M., & Schaye J.: *The Emperor's New Arc: Gigaparsec Patterns Abound in a ΛCDM Universe.* ArXiv e-prints **2502.03515** (2025)

Schaye J., Crain R. A., Bower R. G., Furlong M., Schaller M., Theuns T., Dalla Vecchia C., Frenk C. S., McCarthy I. G., Helly J. C., et al.: *The EAGLE Project: Simulating the Evolution and Assembly of Galaxies and Their Environments.* Monthly Notices of the Royal Astronomical Society **446**, 521 (2015a)

Schaye J., Crain R. A., Bower R. G., Furlong M., Schaller M., Theuns T., Dalla Vecchia C., Frenk C. S., McCarthy I. G., Helly J. C., et al.: *The EAGLE Project: Simulating the Evolution and Assembly of Galaxies and Their Environments.* Mon Not R Astron Soc **446**, 521 (2015b)

Schaye J., Kugel R., Schaller M., Helly J. C., Braspenning J., Elbers W., McCarthy I. G., van Daalen M. P., Vandenbroucke B., Frenk C. S., et al.: *The FLAMINGO Project: Cosmological Hydrodynamical Simulations for Large-Scale Structure and Galaxy Cluster Surveys.* Monthly Notices of the Royal Astronomical Society **526**, 4978 (2023)

Schaye J., Chaikin E., Schaller M., Ploeckinger S., Huško F., McGibbon R. J., Trayford J. W., Benítez-Llambay A., Correa C., Frenk C. S., et al.: *The COLIBRE Project: Cosmological Hydrodynamical Simulations of Galaxy Formation and Evolution.* Monthly Notices of the Royal Astronomical Society **548**, stag375 (2026)

Schechter P.: *An Analytic Expression for the Luminosity Function for Galaxies.* The Astrophysical Journal **203**, 297 (1976)

Schreiber C., Glazebrook K., Nanayakkara T., Kacprzak G. G., Labbé I., Oesch P., Yuan T., Tran K.-V., Papovich C., Spitler L., & Straatman C.: *Near Infrared Spectroscopy and Star-Formation Histories of 3 ≤ z ≤ 4 Quiescent Galaxies.* Astronomy & Astrophysics **618**, A85 (2018)

Schwarz D. J., Copi C. J., Huterer D., & Starkman G. D.: *CMB Anomalies after Planck.* Classical and Quantum Gravity **33**, 184001 (2016)

Seidel B. A., Dolag K., Remus R.-S., Sorce J. G., Hernández-Martínez E., Khabibullin I., & Aghanim N.: *Simulating the LOcal Web (SLOW) - IV. Not All That Is Close Will Merge in the End: Superclusters and Their Lagrangian Collapse Regions.* A&A **702**, A243 (2025a)

Seidel B. A., Remus R.-S., Valenzuela L. M., Kimmig L. C., & Dolag K.: *Go with the Flow: The Self-Similar and Non-Linear Behaviour of Large-Scale in- and Outflows and the Impact of Accretion Shocks from Galaxies to Galaxy Clusters.* Astronomy & Astrophysics **701**, A192 (2025b)

Sembolini F., Yepes G., De Petris M., Gottlöber S., Lamagna L., & Comis B.: *The MUSIC of Galaxy Clusters – I. Baryon Properties and Scaling Relations of the Thermal Sunyaev–Zel'dovich Effect.* Mon Not R Astron Soc **429**, 323 (2013)

Serra P., Maccagni F. M., Kleiner D., de Blok W. J. G., van Gorkom J. H., Hugo B., Iodice E., Józsa G. I. G., Kamphuis P., Kraan-Korteweg R., et al.: *Neutral Hydrogen Gas within and around NGC 1316.* Astronomy and Astrophysics **628**, A122 (2019)

Sérsic J. L.: *Influence of the Atmospheric and Instrumental Dispersion on the Brightness Distribution in a Galaxy.* Boletin de la Asociacion Argentina de Astronomia La Plata Argentina **6**, 41 (1963)

Shahidi A., Mobasher B., Nayyeri H., Hemmati S., Wiklind T., Chartab N., Dickinson M., Finkelstein S. L., Pacifici C., Papovich C., et al.: *Selection of Massive Evolved Galaxies at 3 ≤ z ≤ 4.5 in the CANDELS Fields.* The Astrophysical Journal **897**, 44 (2020)

Sheth R. K., Mo H. J., & Tormen G.: *Ellipsoidal Collapse and an Improved Model for the Number and Spatial Distribution of Dark Matter Haloes.* Monthly Notices of the Royal Astronomical Society **323**, 1 (2001)

Sheth R. K. & van de Weygaert R.: *A Hierarchy of Voids: Much Ado about Nothing.* Monthly Notices of the Royal Astronomical Society **350**, 517 (2004)

Sheth R. K. & Diaferio A.: *How Unusual Are the Shapley Supercluster and the Sloan Great Wall?* Monthly Notices of the Royal Astronomical Society **417**, 2938 (2011)

Shi X.: *Locations of Accretion Shocks around Galaxy Clusters and the ICM Properties: Insights from Self-Similar Spherical Collapse with Arbitrary Mass Accretion Rates.* MNRAS **461**, 1804 (2016)

Shu F. H.: *Six Decades of Spiral Density Wave Theory.* Annual Review of Astronomy and Astrophysics **54**, 667 (2016)

Slipher V. M.: *Radial Velocity Observations of Spiral Nebulae.* The Observatory **40**, 304 (1917)

Snowden S. L., Egger R., Freyberg M. J., McCammon D., Plucinsky P. P., Sanders W. T., Schmitt J. H. M. M., Trümper J., & Voges W.: *ROSAT Survey Diffuse X-Ray Background Maps. II.* ApJ **485**, 125 (1997)

Sommer J. S., Dolag K., Böss L. M., Khabibullin I., Liang X., Waerbeke L. V., Zhitnitsky A., Majidi F., Sorce J. G., Seidel B., & Hernández-Martínez E.: *The Glow of Axion Quark Nugget Dark Matter - II. Galaxy Clusters.* Astronomy & Astrophysics **691**, A38 (2024)

Song M., Finkelstein S. L., Ashby M. L. N., Grazian A., Lu Y., Papovich C., Salmon B., Somerville R. S., Dickinson M., Duncan K., et al.: *The Evolution of the Galaxy Stellar Mass Function at z = 4-8: A Steepening Low-mass-end Slope with Increasing Redshift.* The Astrophysical Journal **825**, 5 (2016)

Sorce J. G., Courtois H. M., Gottlöber S., Hoffman Y., & Tully R. B.: *Simulations of the Local Universe Constrained by Observational Peculiar Velocities.* MNRAS **437**, 3586 (2014)

Sorce J. G.: *Minimization of Biases in Galaxy Peculiar Velocity Catalogues.* Monthly Notices of the Royal Astronomical Society **450**, 2644 (2015)

Sorce J. G., Hoffman Y., & Gottlöber S.: *Towards an Optimal Sampling of Peculiar Velocity Surveys for Wiener Filter Reconstructions.* Monthly Notices of the Royal Astronomical Society **468**, 1812 (2017)

Sorce J. G. & Tempel E.: *How Does the Grouping Scheme Affect the Wiener Filter Reconstruction of the Local Universe?* Monthly Notices of the Royal Astronomical Society **469**, 2859 (2017)

Sorce J. G.: *Galaxy Clusters in Local Universe Simulations without Density Constraints: A Long Uphill Struggle.* MNRAS **478**, 5199 (2018)

Sorce J. G. & Tempel E.: *Galaxy Clusters in Simulations of the Local Universe: A Matter of Constraints.* Monthly Notices of the Royal Astronomical Society **476**, 4362 (2018)

Sorce J. G., Dubois Y., Blaizot J., McGee S. L., Yepes G., & Knebe A.: *I – A Hydrodynamical Clone of the Virgo Cluster of Galaxies to Confirm Observationally Driven Formation Scenarios.* Monthly Notices of the Royal Astronomical Society **504**, 2998 (2021)

Sorce J. G., Mohayaee R., Aghanim N., Dolag K., & Malavasi N.: *Distortions of the Hubble Diagram: Line-of-sight Signatures of Local Galaxy Clusters.* Astronomy & Astrophysics **687**, A85 (2024)

Sousbie T.: *The Persistent Cosmic Web and Its Filamentary Structure – I. Theory and Implementation.* Monthly Notices of the Royal Astronomical Society **414**, 350 (2011)

Springel V., White S. D. M., Tormen G., & Kauffmann G.: *Populating a Cluster of Galaxies – I. Results at z = 0.* MNRAS **328**, 726 (2001)

Springel V. & Hernquist L.: *Cosmological Smoothed Particle Hydrodynamics Simulations: A Hybrid Multiphase Model for Star Formation.* Monthly Notices of the Royal Astronomical Society **339**, 289 (2003)

Springel V.: *The Cosmological Simulation Code Gadget-2.* Monthly Notices of the Royal Astronomical Society **364**, 1105 (2005)

Springel V., di Matteo T., & Hernquist L.: *Modelling Feedback from Stars and Black Holes in Galaxy Mergers.* MNRAS **361**, 776 (2005)

Springel V.: *E Pur Si Muove: Galilean-invariant Cosmological Hydrodynamical Simulations on a Moving Mesh.* Monthly Notices of the Royal Astronomical Society **401**, 791 (2010)

Stefanon M., Bouwens R. J., Labbé I., Illingworth G. D., Gonzalez V., & Oesch P. A.: *Galaxy Stellar Mass Functions from z 10 to z 6 Using the Deepest Spitzer/Infrared Array Camera Data: No Significant Evolution in the Stellar-to-halo Mass Ratio of Galaxies in the First Gigayear of Cosmic Time.* The Astrophysical Journal **922**, 29 (2021)

Steinborn L. K., Dolag K., Hirschmann M., Prieto M. A., & Remus R.-S.: *A Refined Sub-Grid Model for Black Hole Accretion and AGN Feedback in Large Cosmological Simulations.* **448**, 1504 (2015)

Steinmetz M. & White S. D. M.: *Two-body heating in numerical galaxy formation experiments.* MNRAS **288**, 545 (1997)

Steinwandel U. P., Dolag K., Böss L. M., & Marin-Gilabert T.: *Toward Cosmological Simulations of the Magnetized Intracluster Medium with Resolved Coulomb Collision Scale.* ApJ **967**, 125 (2024)

Stephenson H., Stott J., Butler J., Webster M., & Head J.: *Evidence That Pre-Processing in Filaments Drives the Anisotropic Quenching of Satellite Galaxies in Massive Clusters.* arXiv preprint, 10.48550/arXiv.2412.07834 (2024)

Stone J. M., Gardiner T. A., Teuben P., Hawley J. F., & Simon J. B.: *Athena: A New Code for Astrophysical MHD.* The Astrophysical Journal Supplement Series **178**, 137 (2008)

Stone J. M., Tomida K., White C. J., & Felker K. G.: *The Athena++ Adaptive Mesh Refinement Framework: Design and Magnetohydrodynamic Solvers.* The Astrophysical Journal Supplement Series **249**, 4 (2020)

Straatman C. M. S., Labbé I., Spitler L. R., Allen R., Altieri B., Brammer G. B., Dickinson M., van Dokkum P., Inami H., Glazebrook K., et al.: *A SUBSTANTIAL POPULATION OF MASSIVE QUIESCENT GALAXIES AT z ∼ 4 FROM ZFOURGE*.* The Astrophysical Journal Letters **783**, L14 (2014)

Stuber S. K., Saito T., Schinnerer E., Emsellem E., Querejeta M., Williams T. G., Barnes A. T., Bigiel F., Blanc G., Dale D. A., et al.: *Frequency and Nature of Central Molecular Outflows in Nearby Star-Forming Disk Galaxies.* A&A **653**, A172 (2021)

Su Y., Kraft R. P., Roediger E., Nulsen P., Forman W. R., Churazov E., Randall S. W., Jones C., & Machacek M. E.: *Deep Chandra Observations of NGC 1404: Cluster Plasma Physics Revealed by an Infalling Early-type Galaxy.* The Astrophysical Journal **834**, 74 (2017a)

Su Y., Nulsen P. E. J., Kraft R. P., Roediger E., ZuHone J. A., Jones C., Forman W. R., Sheardown A., Irwin J. A., & Randall S. W.: *Gas Sloshing Regulates and Records the Evolution of the Fornax Cluster.* The Astrophysical Journal **851**, 69 (2017b)

Sunyaev R. A. & Zeldovich Ya. B.: *The Spectrum of Primordial Radiation, Its Distortions and Their Significance.* Comments on Astrophysics and Space Physics **2**, 66 (1970)

Tanner R., Weaver K. A., & Ogorzałek A.: *Simulations of Galactic Outflows Driven by Active Galactic Nuclei and Starbursts.* The Astrophysical Journal **992**, 90 (2025)

Teklu A. F., Remus R.-S., Dolag K., Beck A. M., Burkert A., Schmidt A. S., Schulze F., & Steinborn L. K.: *CONNECTING ANGULAR MOMENTUM AND GALACTIC DYNAMICS: THE COMPLEX INTERPLAY BETWEEN SPIN, MASS, AND MORPHOLOGY.* ApJ **812**, 29 (2015)

Tessore N., Joachimi B., Loureiro A., Hall A., Cañas-Herrera G., Tutusaus I., Jeffrey N., Naidoo K., McEwen J. D., Amara A., et al.: *Euclid Preparation - LIX. Angular Power Spectra from Discrete Observations.* Astronomy & Astrophysics **694**, A141 (2025)

Tevlin L., Berlok T., Pfrommer C., Talbot R. Y., Whittingham J., Puchwein E., Pakmor R., Weinberger R., & Springel V.: *Magnetic Dynamos in Galaxy Clusters: The Crucial Role of Galaxy Formation Physics at High Redshifts.* A&A **701**, A114 (2025)

Teyssier R.: *Cosmological Hydrodynamics with Adaptive Mesh Refinement - A New High Resolution Code Called RAMSES.* A&A **385**, 337 (2002)

Tinker J., Kravtsov A. V., Klypin A., Abazajian K., Warren M., Yepes G., Gottlöber S., & Holz D. E.: *Toward a Halo Mass Function for Precision Cosmology: The Limits of Universality.* The Astrophysical Journal **688**, 709 (2008)

Tomczak A. R., Quadri R. F., Tran K.-V. H., Labbé I., Straatman C. M. S., Papovich C., Glazebrook K., Allen R., Brammer G. B., Kacprzak G. G., et al.: *Galaxy Stellar Mass Functions from ZFOURGE/CANDELS: An Excess of Low-mass Galaxies since z = 2 and the Rapid Buildup of Quiescent Galaxies.* The Astrophysical Journal **783**, 85 (2014)

Tormen G., Bouchet F. R., & White S. D. M.: *The Structure and Dynamical Evolution of Dark Matter Haloes.* **286**, 865 (1997)

Tornatore L., Borgani S., Dolag K., & Matteucci F.: *Chemical Enrichment of Galaxy Clusters from Hydrodynamical Simulations.* MNRAS **382**, 1050 (2007)

Tremmel M., Karcher M., Governato F., Volonteri M., Quinn T. R., Pontzen A., Anderson L., & Bellovary J.: *The Romulus Cosmological Simulations: A Physical Approach to the Formation, Dynamics and Accretion Models of SMBHs.* **470**, 1121 (2017)

Tremmel M., Quinn T. R., Ricarte A., Babul A., Chadayammuri U., Natarajan P., Nagai D., Pontzen A., & Volonteri M.: *Introducing RomulusC: A Cosmological Simulation of a Galaxy Cluster with Unprecedented Resolution.* (2018)

Tremmel M., Wright A. C., Brooks A. M., Munshi F., Nagai D., & Quinn T. R.: *The Formation of Ultradiffuse Galaxies in the RomulusC Galaxy Cluster Simulation.* Monthly Notices of the Royal Astronomical Society **497**, 2786 (2020)

Truong N., Pillepich A., Nelson D., Zhuravleva I., Lee W., Ayromlou M., & Lehle K.: *X-Ray-Inferred Kinematics of the Core Intracluster Medium in Perseus-like Clusters: Insights from the TNG-Cluster Simulation.* A&A **686**, A200 (2024)

Tully R. B. & Fisher J. R.: *A New Method of Determining Distances to Galaxies.* Astronomy and Astrophysics **54**, 661 (1977)

Tully R. B., Courtois H. M., Dolphin A. E., Fisher J. R., Héraudeau P., Jacobs B. A., Karachentsev I. D., Makarov D., Makarova L., Mitronova S., et al.: *COSMICFLOWS-2: THE DATA.* The Astronomical Journal **146**, 86 (2013)

Tully R. B., Courtois H., Hoffman Y., & Pomarède D.: *The Laniakea Supercluster of Galaxies.* Nature **513**, 71 (2014)

Tully R. B.: *GALAXY GROUPS: A 2MASS CATALOG.* The Astronomical Journal **149**, 171 (2015)

Tully R. B., Courtois H. M., & Sorce J. G.: *Cosmicflows-3.* The Astronomical Journal **152**, 50 (2016)

Tully R. B., Kourkchi E., Courtois H. M., Anand G. S., Blakeslee J. P., Brout D., de Jaeger T., Dupuy A., Guinet D., Howlett C., et al.: *Cosmicflows-4.* The Astrophysical Journal **944**, 94 (2023)

Tumlinson J., Peeples M. S., & Werk J. K.: *The Circumgalactic Medium.* Annual Review of Astronomy and Astrophysics **55**, 389 (2017)

Valade A., Libeskind N., Pomarède D., Stiskalek R., Hoffman Y., Gottlöber S., & Tully R. B.: *Constraining Cosmological Simulations with Peculiar Velocities: A Forward-Modeling Approach.* arXiv preprint, 10.48550/arXiv.2602.03699 (2026)

Valentino F., Brammer G., Gould K. M. L., Kokorev V., Fujimoto S., Jespersen C. K., Vijayan A. P., Weaver J. R., Ito K., Tanaka M., et al.: *An Atlas of Color-selected Quiescent Galaxies at z > 3 in Public JWST Fields.* The Astrophysical Journal **947**, 20 (2023)

Valenzuela L. M., Remus R.-S., Dolag K., & Seidel B. A.: *Galaxy Shapes in Magneticum - I. Connecting Stellar and Dark Matter Shapes to Dynamical and Morphological Galaxy Properties and the Large-Scale Structure.* Astronomy & Astrophysics **690**, A206 (2024)

Vallés-Pérez D., Planelles S., & Quilis V.: *On the Accretion History of Galaxy Clusters: Temporal and Spatial Distribution.* MNRAS **499**, 2303 (2020)

van de Weygaert R. & Bond J. R.: *Clusters and the Theory of the Cosmic Web.* 335 (2008)

van den Bosch F. C.: *The Universal Mass Accretion History of Cold Dark Matter Haloes.* MNRAS **331**, 98 (2002)

van Weeren R. J., Timmerman R., Vaidya V., Gendron-Marsolais M.-L., Botteon A., Roberts I. D., Hlavacek-Larrondo J., Bonafede A., Brüggen M., Brunetti G., et al.: *LOFAR High-Band Antenna Observations of the Perseus Cluster - The Discovery of a Giant Radio Halo.* Astronomy & Astrophysics **692**, A12 (2024)

Vazza F., Roediger E., & Brüggen M.: *Turbulence in the ICM from Mergers, Cool-Core Sloshing, and Jets: Results from a New Multi-Scale Filtering Approach.* Astronomy & Astrophysics **544**, A103 (2012)

Vazza F., Brüggen M., Gheller C., & Wang P.: *On the Amplification of Magnetic Fields in Cosmic Filaments and Galaxy Clusters.* Monthly Notices of the Royal Astronomical Society **445**, 3706 (2014)

Venturi T., Rossetti M., Bardelli S., Giacintucci S., Dallacasa D., Cornacchia M., & Kantharia N. G.: *Radio Emission at the Centre of the Galaxy Cluster Abell 3560: Evidence for Core Sloshing?* A&A **558**, A146 (2013)

Venturi T., Giacintucci S., Merluzzi P., Bardelli S., Busarello G., Dallacasa D., Sikhosana S. P., Marvil J., Smirnov O., Bourdin H., et al.: *Radio Footprints of a Minor Merger in the Shapley Supercluster: From Supercluster down to Galactic Scales.* A&A **660**, A81 (2022)

Veronica A., Su Y., Biffi V., Reiprich T. H., Pacaud F., Nulsen P. E. J., Kraft R. P., Sanders J. S., Bogdan A., Kara M., et al.: *The eROSITA View of the Abell 3391/95 Field: The Northern Clump - The Largest Infalling Structure in the Longest Known Gas Filament*

Observed with eROSITA, XMM-Newton, and Chandra. Astronomy & Astrophysics **661**, A46 (2022)

Vielva P.: *A Comprehensive Overview of the Cold Spot.* Advances in Astronomy **2010**, 592094 (2010)

Villaescusa-Navarro F., Planelles S., Borgani S., Viel M., Rasia E., Murante G., Dolag K., Steinborn L. K., Biffi V., Beck A. M., & Ragone-Figueroa C.: *Neutral Hydrogen in Galaxy Clusters: Impact of AGN Feedback and Implications for Intensity Mapping.* Monthly Notices of the Royal Astronomical Society **456**, 3553 (2016)

Vogelsberger M., Marinacci F., Torrey P., Genel S., Springel V., Weinberger R., Pakmor R., Hernquist L., Naiman J., Pillepich A., & Nelson D.: *The Uniformity and Time-Invariance of the Intra-Cluster Metal Distribution in Galaxy Clusters from the IllustrisTNG Simulations.* MNRAS **474**, 2073 (2018)

Voit G. M., Donahue M., Bryan G. L., & McDonald M.: *Regulation of Star Formation in Giant Galaxies by Precipitation, Feedback and Conduction.* Nature **519**, 203 (2015)

Vurm I., Nevalainen J., Hong S. E., Bahé Y. M., Vecchia C. D., & Heinämäki P.: *Cosmic Gas Highways in C-EAGLE Simulations.* A&A **673**, A62 (2023)

Walker S., Simionescu A., Nagai D., Okabe N., Eckert D., Mroczkowski T., Akamatsu H., Ettori S., & Ghirardini V.: *The Physics of Galaxy Cluster Outskirts.* Space Sci. Rev. **215**, 7 (2019)

Wang L., Dutton A. A., Stinson G. S., Macciò A. V., Penzo C., Kang X., Keller B. W., & Wadsley J.: *NIHAO Project - I. Reproducing the Inefficiency of Galaxy Formation across Cosmic Time with a Large Sample of Cosmological Hydrodynamical Simulations.* **454**, 83 (2015)

Wang Y., Pearce F., Knebe A., Yepes G., Cui W., Power C., Arth A., Gottlöber S., De Petris M., Brown S., & Feng L.: *The Three Hundred Project: The Influence of Environment on Simulated Galaxy Properties.* The Astrophysical Journal **868**, 130 (2018)

Watkins E. J., Kreckel K., Groves B., Glover S. C. O., Whitmore B. C., Leroy A. K., Schinnerer E., Meidt S. E., Egorov O. V., Barnes A. T., et al.: *Quantifying the Energetics of Molecular Superbubbles in PHANGS Galaxies.* A&A **676**, A67 (2023)

Weaver J. R., Kauffmann O. B., Ilbert O., McCracken H. J., Moneti A., Toft S., Brammer G., Shuntov M., Davidzon I., Hsieh B. C., et al.: *COSMOS2020: A Panchromatic View of the Universe to Z∼10 from Two Complementary Catalogs.* The Astrophysical Journal Supplement Series **258**, 11 (2022)

Weaver J. R., Davidzon I., Toft S., Ilbert O., McCracken H. J., Gould K. M. L., Jespersen C. K., Steinhardt C., Lagos C. D. P., Capak P. L., et al.: *COSMOS2020: The Galaxy Stellar Mass Function. The Assembly and Star Formation Cessation of Galaxies at $0.2< z \leq 7.5$.* Astronomy and Astrophysics **677**, A184 (2023)

Weinberger R., Springel V., Hernquist L., Pillepich A., Marinacci F., Pakmor R., Nelson D., Genel S., Vogelsberger M., Naiman J., & Torrey P.: *Simulating Galaxy Formation with Black Hole Driven Thermal and Kinetic Feedback.* Monthly Notices of the Royal Astronomical Society **465**, 3291 (2017)

Weller E. J., Pacucci F., Ni Y., Hernquist L., & Park M.: *Discrepancies between JWST Observations and Simulations of Quenched Massive Galaxies at $z > 3$: A Comparative Study with IllustrisTNG and ASTRID.* The Astrophysical Journal **979**, 181 (2025)

Whittaker E. T. & Watson G. N.: *A Course of Modern Analysis.* Cambridge University Press (2021)

Wicker R., Douspis M., Salvati L., & Aghanim N.: *Constraining Hydrostatic Mass Bias and Cosmological Parameters with the Gas Mass Fraction in Galaxy Clusters.* EPJ Web of Conferences **257**, 00046 (2022)

Wiersma R. P. C., Schaye J., & Smith B. D.: *The Effect of Photoionization on the Cooling Rates of Enriched, Astrophysical Plasmas.* MNRAS **393**, 99 (2009)

Wilde O.: *The Importance of Being Earnest: A Trivial Comedy for Serious People.* Leonard Smithers and Company (1899)

XRISM Collaboration, Audard M., Awaki H., Ballhausen R., Bamba A., Behar E., Boissay-Malaquin R., Brenneman L., Brown G. V., Corrales L., et al.: *XRISM Forecast for the Coma Cluster: Stormy, with a Steep Power Spectrum.* ApJL **985**, L20 (2025)

XRISM Science Team: *XRISM Quick Reference.* arXiv preprint, 10.48550/arXiv.2202.05399 (2022)

Xu Y., Kronberg P. P., Habib S., & Dufton Q. W.: *A Faraday Rotation Search for Magnetic Fields in Large-scale Structure.* ApJ **637**, 19 (2006)

Yang Q.-R., Zhu W., Yu G.-Y., Mo J.-F., Zheng Y., & Feng L.-L.: *On the Width and Profiles of Cosmic Filaments.* The Astrophysical Journal **989**, 187 (2025)

Yao Y., Shull J. M., Wang Q. D., & Cash W.: *DETECTING THE WARM–HOT INTERGALACTIC MEDIUM THROUGH X-RAY ABSORPTION LINES.* The Astrophysical Journal **746**, 166 (2012)

York D. G., Adelman J., Anderson J. E., Jr., Anderson S. F., Annis J., Bahcall N. A., Bakken J. A., Barkhouser R., Bastian S., Berman E., et al.: *The Sloan Digital Sky Survey: Technical Summary.* **120**, 1579 (2000)

Yoshida N., Sheth R. K., & Diaferio A.: *Non-Gaussian cosmic microwave background temperature fluctuations from peculiar velocities of clusters.* MNRAS **328**, 669 (2001)

Yu B. P. B., Owen E. R., Pan K.-C., Wu K., & Ferreras I.: *Outflows from Starburst Galaxies with Various Driving Mechanisms and Their X-ray Properties.* MNRAS **508**, 5092 (2021)

Zapartas E., de Mink S. E., Izzard R. G., Yoon S.-C., Badenes C., Götberg Y., de Koter A., Neijssel C. J., Renzo M., Schootemeijer A., & Shrotriya T. S.: *Delay-Time Distribution of Core-Collapse Supernovae with Late Events Resulting from Binary Interaction.* Astronomy & Astrophysics **601**, A29 (2017)

Zaroubi S., Hoffman Y., Fisher K. B., & Lahav O.: *Wiener Reconstruction of the Large-Scale Structure.* The Astrophysical Journal **449**, 446 (1995)

Zaroubi S., Hoffman Y., & Dekel A.: *Wiener Reconstruction of Large-Scale Structure from Peculiar Velocities.* The Astrophysical Journal **520**, 413 (1999)

Zeldovich Ya. B. & Sunyaev R. A.: *The Interaction of Matter and Radiation in a Hot-Model Universe.* Astrophysics and Space Science **4**, 301 (1969)

Zel'dovich Ya. B.: *Gravitational Instability: An Approximate Theory for Large Density Perturbations.* Astronomy and Astrophysics **5**, 84 (1970)

Zhang C., Churazov E., Dolag K., Forman W. R., & Zhuravleva I.: *Encounters of Merger and Accretion Shocks in Galaxy Clusters and Their Effects on Intracluster Medium.* MNRAS **494**, 4539 (2020)

Zhang C., Zhuravleva I., Heinrich A., Bellomi E., Truong N., ZuHone J., Churazov E., Eckart M. E., Fujita Y., Hlavacek-Larrondo J., et al.: *Mapping the Perseus Galaxy Cluster with XRISM - Gas Kinematic Features and Their Implications for Turbulence.* Astronomy & Astrophysics **707**, A109 (2026)

Zhang X., Bulbul E., Malavasi N., Ghirardini V., Comparat J., Kluge M., Liu A., Merloni A., Zhang Y., Bahar Y. E., et al.: *The SRG/eROSITA All-Sky Survey: X-ray Emission from the Warm-Hot Phase Gas in Long Cosmic Filaments.* Astronomy and Astrophysics **691**, A234 (2024a)

Zhang Y., Comparat J., Ponti G., Merloni A., Nandra K., Haberl F., Locatelli N., Zhang X., Sanders J., Zheng X., et al.: *The Hot Circumgalactic Medium in the eROSITA All-Sky Survey - I. X-ray Surface Brightness Profiles.* Astronomy & Astrophysics **690**, A267 (2024b)

Zhao D., Aragón-Salamanca A., & Conselice C. J.: *Evolution of the Brightest Cluster Galaxies: The Influence of Morphology, Stellar Mass and Environment.* Monthly Notices of the Royal Astronomical Society **453**, 4444 (2015)

Zöller R., Kluge M., Bender R., Pippert J.-N., Seidel B., Gössl C., Hopp U., Kellermann H., Ries C., Riffeser A., et al.: *Galaxy Luminosity Function of the Coma Cluster from Deep $u'-g'-r'$ Wendelstein Imaging Data.* arXiv preprint, 10.48550/arXiv.2510.26889 (2025)

Zonca A., Singer L., Lenz D., Reinecke M., Rosset C., Hivon E., & Gorski K.: *Healpy: Equal Area Pixelization and Spherical Harmonics Transforms for Data on the Sphere in Python.* The Journal of Open Source Software **4**, 1298 (2019)

Zucca E., Zamorani G., Scaramella R., & Vettolani G.: *All-Sky Catalogs of Superclusters of Abell-ACO Clusters.* ApJ **407**, 470 (1993)

Zwicky F.: *On the Masses of Nebulae and of Clusters of Nebulae.* The Astrophysical Journal **86**, 217 (1937)

Acknowledgements

This thesis and the work presented within it would not have been possible without a long list of people: First, I want to thank Klaus Dolag for being a great supervisor and collaborator since the beginning of my Masters' project. Thank you very much for all the ideas, scientific connections, and, last but definitely not least for your humour during the nearly five years I worked with you. It has been – and will hopefully continue to be – a pleasure. I would additionally like to thank Andreas Burkert, whose CAST group provided a nourishing environment for discussions and the exchange of scientific ideas, often kickstarted by the energetic professor himself. Thank you also to the entire CAST group and all my PhD and postdoc colleagues. Special thanks are in order to Frederick Groth, for proofreading my contraction of his work.

An immeasurable amount of gratitude is owed to Rhea-Silvia Remus, who continuously contributed ideas and questions to almost everything I worked on and was an amazing scientific mentor. A few weeks ago, you found a box of chocolates on your desk reading "Du bist Gold wert" on the lid. While I wholeheartedly agree with the sentiment, I would – as is to be expected of me – like to disagree on a technicality: The value of gold is arbitrary and temporary. The value of the leadership, guidance and encouragement I had the privilege to receive from you during the past few years is not. Thank you for everything.

I would like to thank her entire DRAGONS team, namely Lucas Valenzuela, Lucas Kimmig, Silvio Fortuné, Tadziu Hoffmann, Anna Ivleva, Johannes Stoiber, Anita Schiller, Alexandra Konrad and Shubhan Bhatia. You were an amazing team to work with and proved time and again what collaboration and co-creativity is worth in science.

Silvio Fortuné deserves an additional honorable mention for being my office mate during my entire time at USM. The fact that you didn't go mad from my constant blabbering and the deafening strokes of my keyboard is truly a testament to your resilience (especially your eardrums'). It will not be the same without you.

I also want to thank Ludwig Böss and Lucas Valenzuela for the development and maintenance of `GadgetIO` and again Lucas Valenzuela for providing additional post-processing libraries and getting me hooked on `Julia`.

Any person in the "just the IT guy" role I will work with in the future will have their work cut out for them. That is due to the amazing Tadziu Hoffmann, whose knowledgeability, curiosity and inexhaustible scientific mind offers so much more than just the monumental efforts to keep the CAST machines running against the tides of Master and PhD students (and often Master students who become PhD students) sloshing against the infrastructure. Thank you for being truly inspiring. Additional minor thanks for sometimes laughing at my jokes!

Outside of Munich I owe gratitude to the LOCALIZATION collaboration, especially Jenny Sorce and Nabila Aghanim. Thank you both for your insight, ideas and help and for welcoming me into the collaboration. I hope the future holds many more interesting projects in the Local Universe.

I want to thank my marvellous partner in crime for making disappearing from the face of the earth for a couple of months to write this thesis that much more bearable by being

their hilarious and loving self. Thank you also for proofreading quite a large part of the text! Never stop being you.

Finally I would like to thank my family for all the encouragement, curiosity, laughter and – most importantly – cake, that helped me go along with my projects and follow the fascination of a little boy staring through a telescope for the first time. Every single one of you made me who I am. For that I will be eternally grateful.

And so end four years of scientific work, of fun, cool plots, interesting concepts and sometimes, in delightfully moderate doses, stress and frustration. Nonetheless this, once again, feels more like a starting point than an ending. There is much to be excited about scientifically, many more questions to answer and riddles to solve. The data from ongoing and upcoming observations, in combination with the simulations and techniques presented in this work will help us understand the multi-scalar evolution of structures in even more detail.

Or, to leave the final words to Oscar Wildes' character Gwendolen in *The Importance of Being Earnest*: "This suspense is terrible. I hope it will last." (Wilde, 1899).

Selbstständigkeitserklärung

Hiermit erkläre ich, die vorliegende Arbeit selbstständig verfasst zu haben und keine anderen als die in der Arbeit angegebenen Quellen und Hilfsmittel benutzt zu haben.

München, [19.05.2026]

_____

Benjamin Andreas Seidel